Atomic characteristics and high-order harmonic spectra: extension of ab-initio numerical calculations to larger systems

by

Ran Brynn Reiff

B.A., University of Colorado Boulder, 2015

M.S., University of Colorado, 2018

A thesis submitted to the

Faculty of the Graduate School of the

University of Colorado in partial fulfillment

of the requirements for the degree of

Doctor of Philosophy

Department of Physics

2021

Committee Members:

Andreas Becker, Chair

Agnieszka Jaroń-Becker

John Bohn

Bengt Fornberg

Margaret Murnane

Reiff, Ran Brynn (Ph.D., Physics)

Atomic characteristics and high-order harmonic spectra: extension of ab-initio numerical calculations to larger systems

Thesis directed by Prof. Andreas Becker

High-order harmonic generation (HHG) is a highly nonlinear process where an electron driven by an intense, typically infrared, laser pulse ionizes, accelerates in the laser field and recombines with the parent ion, emitting a photon with frequency many times that of the driving field. The coherent radiation emitted from many atoms in the focus of the driving laser leads to the generation of an ultrashort ultraviolet or x-ray laser pulse. Numeric solution of the time-dependent Schrödinger equation (TDSE) accurately describes the single-electron process, including the low-energy region of the emission spectrum for which the atomic potential and excited states play a significant role. The coherent macroscopic response (e.g., from a gas jet) involves the emission of a very large number of atomic radiators (e.g., 10^{15}) that each interacts with the driving laser at different peak intensities and carrier-envelope phases. Full ab-initio simulation of the macroscopic response using exact numeric single-electron calculations are not feasible.

In this thesis, we present results of three projects related to high-order harmonic generation with a focus on the below- and near-threshold regime, in which excited states of the atom and the specific form of the atomic potential play an important role. First, we present a reproducible ab-initio method to produce benchmark tests between calculations based on the time-dependent Schrödinger equation (TDSE) in the single-active-electron approximation (SAE) and time-dependent density functional theory (TDDFT) in the highly nonlinear multiphoton and tunneling regime of strong-field physics. As key to the benchmark comparison we obtain an analytic form of SAE potentials based on density functional theory, which we have applied for different atoms, ions, and molecules. Using these potentials, we find remarkable agreement between the results of the two independent numerical approaches (TDDFT and SAE-TDSE) for the high-order

harmonic yields in helium, demonstrating the accuracy of the SAE potentials as well as the predictive power of SAE-TDSE and TDDFT calculations for the nonperturbative and highly nonlinear strong-field process of high harmonic generation in the ultraviolet and visible wavelength regime.

Next, we investigate resonance enhancement of near-threshold HHG, identifying similar resonance effects in broad parameter regimes, including hydrogen driven by near- and mid-infrared pulses as well as helium with 400 nm lasers. We differentiate behavior that may be explicable through semi-classical trajectory models (generally at higher intensity) from features which are not consistent with these models.

In the last part of the thesis, we develop a macroscopic description of high-order harmonic radiation resulting from the interaction of atomic systems with an intense laser pulse using ab-initio solutions of the time-dependent Schrödinger equation (TDSE). We show that for this highly nonlinear process, interpolation can be performed across laser intensity for a given wavelength, limiting the number of full time-dependent Schrödinger equation calculations to about one hundred. The significantly reduced computational time as compared to more sophisticated methods opens a path toward the extension of macroscopic high harmonic calculations based on ab-initio microscopic results to more complex targets and interactions. We investigate the near-threshold regime of the spectra, showing that the degree of coherence of the off-harmonic radiation generated during the pulse is much lower than that of the harmonics, but this radiation extends to larger divergence angles than the harmonic signals – providing the option for separation of the different signals in this part of the spectrum. Finally, we analyze high harmonic generation from the spatial phase distribution for broadband Gaussian pulses with a negative Porras factor, showing an interference pattern in the angular distribution of below- and near-threshold harmonics, which is not present for the monochromatic Gouy phase distribution.

Dedication

To my wife, Lorien.

Acknowledgements

First, my research mentors and colleagues. The Ultrafast AMO Theory group has welcomed me since I began an undergraduate research project in 2014. Profs. Andreas Becker and Agnieszka Jaroń-Becker introduced me to research, and have since taught me countless things about physics, research, academia, and teaching. Senior grad students Dr. Michelle Miller and Dr. Cory Goldsmith were particularly important to my onboarding, both scientific and social. Later, I was lucky enough to grow and work alongside Erez Shani, Dr. Joel Venzke, and Dr. Tennesse Joyce. We complemented each other well with our different perspectives and approaches, leading to many productive debates at the white board. Newer graduate students (Spencer Walker, Yonas Gebre, Andres Mora, and Bejan Ghomashi) and undergraduates (Lucas Kolanz and Zetong Xue) challenged me to rethink and repackage my knowledge, expanding it in the process. As a postdoc at JILA and later, Dr. Carlos Hernandez-Garcia provided crucial expertise and I am indebted to his aid on my work understanding macroscopic HHG.

Teachers beyond physics have played a vital role in cultivating ways of thinking and communicating necessary for research. I do not have the words (or space) to convey the impact each of these individuals had on my life and worldview: Peg Bemis (literature), Marco de Martino & Anissa Butler (history, sociology, and writing), Kira Hall (sociolinguistics), Christian Kopff (classics), Valerie Otero (pedagogy and systemic change).

My research has been bolstered by the community and ways of thinking that I developed doing equity work. Without that support and motivation, I would not have completed this thesis. I am especially grateful to Dr. Miller for bringing me into this work via CU-Prime, from which I

extended my involvement into many other groups (R-Cubed, JEDI, APS-IDEA, and GASP). The friendship and shared mission of improving physics have continually buoyed me when I struggled in research and life.

Finally, I must thank my mother, my wife, and my friends, who encouraged the persistent spirit of lifelong learning, thoughtful collaboration, and critical thinking necessary for research.

Contents

Chapter

List of Tables

Table

List of Figures

Figure

Chapter 1

Introduction

1.1 Background

Lasers are widely used in medicine, industry, defense, and scientific research. The ability to precisely apply power is important itself, but lasers offer other benefits, especially in the broad realm of detection and measurement. Observing reflection of light off of and absorption into materials has consistently exposed otherwise inaccessible information. One form of light is particularly relevant for its uses in this way: x-ray imaging and x-ray diffraction off crystals. The short wavelength and high photon energy of x-ray radiation makes it a tool for detailed observation and analysis that easily pierces obscuring materials (e.g., flesh). Ultraviolet (UV) lasers tuned to energies relevant in atoms and molecules serve as a different sort of probe. The main interest of this thesis is in modeling the generation of ultrashort UV laser pulses from a theoretical perspective with the goal of deepening our understanding and control of the sources and the underlying physical processes.

1.1.1 Single- and multi-photon absorption

In 1887, it was observed that metals exposed to light would release electrons with kinetic energy related only to the color (frequency) of the light and not its intensity [7]. In 1905, Albert Einstein described this effect as resulting from the quantization of light [8]. Electrons would absorb energy from light in the form of single photons with energy proportional to the frequency, but would not absorb more than one photon no matter the photon density (i.e., intensity). In 1930, Maria Göppert-Mayer suggested that a sufficiently intense light would allow electrons to absorb

multiple photons, reaching higher kinetic energies than allowed by Einstein's rule [9]. With the advent of lasers in 1961, her prediction was verified – two-photon absorption was observed [10]. As laser technology advanced to allow higher intensities, multiphoton absorption involving more than two photons became possible.

1.1.2 Applications

Short duration, high energy laser pulses have applications in many disciplines [11, 12]. First, lasers with shorter wavelength (higher frequency) allow use of light as "microscopes" with finer spatial resolution. Likewise, taking "pictures" of rapid processes requires the use of measurement techniques that operate on a similar time scale, or the behavior of interest will be blurred out. Finally, controlling a process requires tools that can be applied at the characteristic frequency or energy scale of the process. X-rays in general have wavelengths smaller than 10 nm and energies above 100 eV; the subject of this thesis, high-order harmonic generation, in particular leads to pulses with durations in the attosecond (10^{-18} s) to femtosecond (10^{-15} s) range [13, 14]. This time scale corresponds to that of single-electron motion in valence shells and bulk-electron motion in larger molecules – such as those found in biology. In combination with fine spatial resolution, HHG lasers can benefit chemical and biological research and engineering via their ability to "film" and control chemical reactions [15, 16]. Other methods of creating x-ray lasers, involving kilometer-long electron accelerators, have greatly increased our understanding of proteins, photosynthesis, and many other chemical reactions. In contrast, HHG can produce well-controlled lasers – with a wide range of wavelengths – on a tabletop scale, allowing scientists in smaller labs access to a powerful research tool. Finally, the process of HHG itself can be used to probe atomic and molecular structure [17–19].

1.1.3 Hartree atomic units

When discussing physical phenomena, it is useful to use a unit system with an appropriate scale. For example, consider various temperature systems – Fahrenheit is useful for gauging human

Dimension	Constant	Conversion (1 a.u. = ...)
Charge	electron charge, e	1.60218×10^{-19} C
Mass	electron mass, m_e	9.10938×10^{-31} kg
Energy	2x hydrogen ionization potential	27.2110 eV
Angular momentum	$\hbar$	1.05457×10^{-34} J*s
Length	Bohr radius, a_0	0.05292 nm
Time	1st Bohr orbital period / 2π	24.18884 as
Permittivity	Coulomb's constant $k_e = 1/4\pi\varepsilon_0$	8.98755×10^9 Nm^2/C^2
Speed of light	$c = 1/\alpha = 137.03500$	

Table 1.1: Description of Hartree atomic units, including reference constants and conversion to common units.

comfort and safety (corresponding roughly to $0° - 100°F$), while Celsius more intuitively describes water (freezing and boiling at $0°C$ and $100°C$, respectively), and Kelvin is important for applications where total thermal energy is relevant (since temperatures in K are proportional to the thermal energy, unlike in Fahrenheit or Celsius).

In strong-field atomic physics, one natural scale is that of the electron. Rather than talking about masses smaller than 10^{-25} kilograms, charges as multiples of 1.6×10^{-19} C, and so forth, we use a unit system where as many dimensions as possible are scaled so that electronic behavior is described in numbers of order 1. Most relevant constants are set to 1, but consistency is maintained, requiring some (notably the speed of light, c) to have other values. Generally, constants with unity values are left out of equations. Also, the unit abbreviation, a.u., is the same for all atomic units regardless of dimension. In certain circumstances, equivalence is sensible (e.g., a photon with frequency ω a.u. will always also have energy ω a.u.), but in other cases is not (that same photon will have wavelength $\lambda = \frac{2\pi c}{\omega}$ a.u.). Table 1.1 includes a few of the most important conversions.

1.2 Strong field ultrafast physics

Classically, a free electron in a laser field of the form

$$E(t) = E_0 \sin(\omega t), \tag{1.1}$$

with intensity $I = E_0^2$ and frequency ω, will move as follows

$$a = \frac{qE}{m} = -E_0 \sin(\omega t) \tag{1.2}$$

$$v = \int a dt = \frac{E_0}{\omega} \cos(\omega t) + v_0 \tag{1.3}$$

$$x = \int v dt = \frac{E_0}{\omega^2} \sin(\omega t) + v_0 t + x_0 \tag{1.4}$$

where x_0 and v_0 are the initial position and velocity, respectively. From this, we can define characteristic values for the field. First, the characteristic length of electron motion is simply the amplitude of the oscillation – the so-called quiver radius

$$r_q = \frac{E_0}{\omega^2}. \tag{1.5}$$

Similarly, we can consider a characteristic kinetic energy associated with field motion, the ponderomotive energy U_P. Excluding energy associated with the average velocity of the electron (or, transforming to a frame where this is zero), we have

$$T = \frac{1}{2} m v^2 = \frac{E_0^2}{2\omega^2} \cos^2(\omega t), \tag{1.6}$$

$$U_P = \langle T \rangle = \frac{E_0^2}{4\omega^2} = \frac{I}{4\omega^2}. \tag{1.7}$$

The ponderomotive energy in particular appears often, as well as being used to define several dimensionless parameters [20]:

$$\gamma = \sqrt{\frac{I_P}{2U_P}} \tag{1.8}$$

$$z_f = \frac{U_P}{2mc^2} \tag{1.9}$$

$$z = \frac{U_P}{\omega}, \tag{1.10}$$

where the Keldysh parameter γ describes ionization as occurring through tunneling ($\gamma \ll 1$) or multiphoton ionization ($\gamma \gg 1$); the free-electron intensity parameter z_f describes the significance of relativistic effects (minimal for all fields used in this thesis, where $z_f \ll 10^{-3}$); and, the non-perturbative intensity parameter z naturally describes how non-perturbative interactions will be. z will also appear later in its role as a measure of the typical number of photons involved in the interaction with the field.

1.2.1 Laser pulses

In contrast to the idealized continuous wave (CW) lasers above (Eq. (1.1)), strong-field lasers have a finite extent in time and driving laser pulses are given by:

$$E(t) = f(t)E_0 \sin(\omega t + \phi), \tag{1.11}$$

where $E_0 = \sqrt{I}$ is the amplitude of the electric field for peak intensity I, $\omega = 2\pi c/\lambda$ is the central frequency for wavelength λ, ϕ is the carrier-envelope phase (CEP), and $f(t)$ is some envelope function, such as the sine-squared or Gaussian envelope

$$f_{sin^2}(t) = \sin^2\left(\frac{\pi t}{\tau}\right) \tag{1.12}$$

$$f_{Gauss}(t) = \exp\left(-\ln(2)\left(\frac{2t}{\tau}\right)^2\right) \tag{1.13}$$

with $\tau = 2\pi N_\tau/\omega$ being the pulse duration for a pulse of N_τ cycles. As is typical, we define durations as full width for sine-squared, and full width half max (FWHM) for Gaussian envelopes. In this thesis, we do not report results with Gaussian envelopes, but do additionally use variations of the sine envelope with faster rise or fall:

$$f_{sin^n sin^m}(t) = \begin{cases} \sin^n\left(\frac{\pi t}{\tau}\right) & t \leq 0 \\ \sin^m\left(\frac{\pi t}{\tau}\right) & t \geq 0 \end{cases} \tag{1.14}$$

for even integers n, m.

1.2.2 Tunnel and multiphoton ionization

With laser pulses of moderate intensity (roughly $10^{13}-10^{15}$ W/cm^2) and wavelengths near the visible (hundreds of nanometers), two pathways contribute to ionization, with dominance predicted roughly by the Keldysh parameter γ: multiphoton ionization ($\gamma > 1$, at shorter λ and lower I) and tunnel ionization ($\gamma > 1$, at longer λ and higher I). The diagram in Fig. 1.1 shows both processes. An electron is initially in the ground ($1s$) state of an atomic potential (black curve).

In the case of tunnel ionization, the potential is distorted (blue curve), leading to a finite potential barrier. After tunnel ionization, the electron is assumed to start at rest at the tunnel exit, x_0. The rate of ionization depends exponentially on the instantaneous value of the electric field [21], resulting in bursts of ionization every half-cycle. In the case of multiphoton ionization (three-photon ionization shown here), the electron absorbs several photons of energy ω (purple arrows), resulting in non-zero kinetic energy, T_0 at the moment of ionization. For weak fields, perturbation theory gives a rate of I^{N_γ}, where N_γ is the number of photons involved in ionization. However, non-perturbative, above-threshold ionization (ATI) – in which more photons than the minimum required for ionization are absorbed – is an area of active research not discussed in this thesis (cf. [22–24]).

1.3 AC Stark shift[1]

In the presence of an alternating electric field, the energies of states shift. For states whose eigenenergy E_n is much less than the photon energy ω, this shift becomes simply U_P [25]

$$E'_n = E_n + U_P. \tag{1.15}$$

As a result, the effective ionization potential also shifts

$$I'_P = I_P + U_P, \tag{1.16}$$

and as a consequence, multiphoton ionization channels may close. In Fig. 1.2, we show the shifted energies (in ω) of ionization (I'_P, black dashed line) and excitation from $1s$ to hydrogen $n = 2$ (i.e., $E'_{2s} - E_0$ and $E'_{2p} - E_0$, blue line) and $n = 3$ (e.g., $E'_{3s} - E_0$, orange line) shells. When the minimum energy to ionize an electron exceeds the energy of an N_γ-photon process (i.e., $I'_P > N_\gamma\omega$), multiphoton ionization must occur primarily through absorption of $N_\gamma + 1$ (or more) photons, and we say the N_γ-photon channel has closed. For transition into bound states, resonant excitation has greatly enhanced probability if $E'_n - E_0 = N_\gamma\omega$. For short intense pulses, the energy shift as

[1] The results of this Section are also presented in [3].

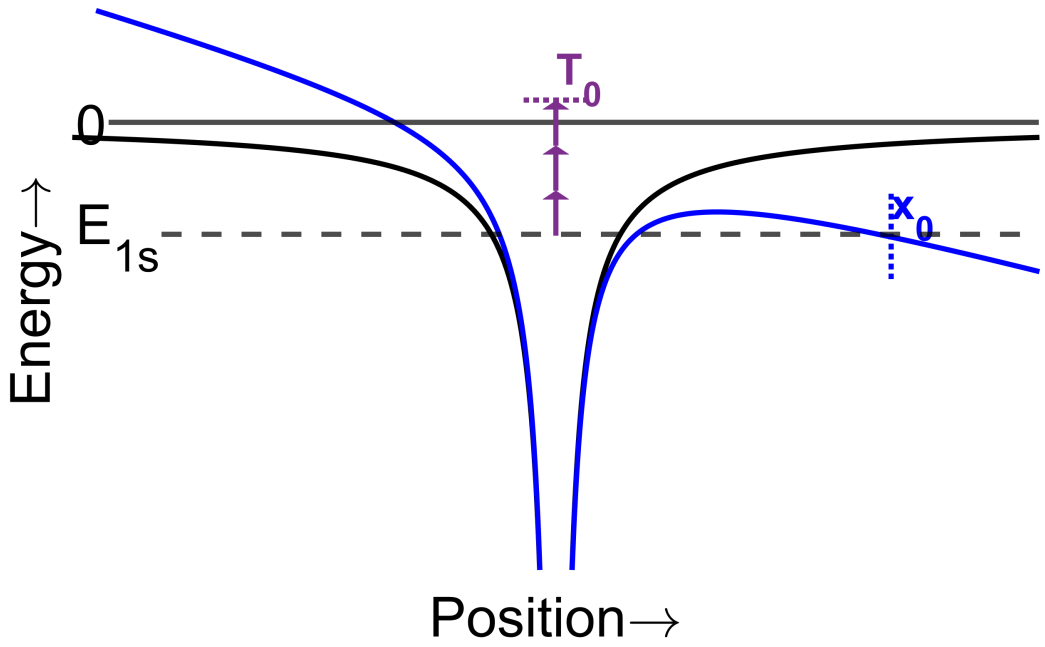

Figure 1.1: Diagram of ionization processes. (black) Field-free atomic potential and $1s$ bound state energy. (blue) Tunnel ionization: Potential distorted by external field, resulting in tunnel exit x_0. (purple) Three-photon ionization resulting in excess kinetic energy T_0.

a function of time may also be relevant (Fig. 1.3). For this purpose, we define an approximate time-dependent shift [26, 27]

$$E'_n(t) = E_n + U_P(t) \tag{1.17}$$

where

$$U_P(t) \equiv \frac{|\vec{E}(t)|^2}{4\omega^2}. \tag{1.18}$$

In [3], we investigated the impact of such channel closings and resonances on the distribution of Rydberg state population after a pulse. To this end, we considered peak intensities such that $n = 8$ states shifted into multiphoton resonance with $N_\gamma = 10, 11, \ldots 15$ at central frequency ω, corresponding to a wavelength of 800 nm. Due to the finite duration of laser pulses (versus monochromatic CW fields), more than one manifold of states can be resonantly excited. For example, the bandwidth of a 20 o.c. $\sin^2$ pulse at 800 nm covers all excited states $n \gtrapprox 6$ within the same N_γ photon process. We further note that in the present cases, the $n = 3$ and $n = 2$ states are approximately resonant via $N_\gamma - 1$ and $N_\gamma - 2$ photon processes, respectively, assuming that the energy shift of these states equals the ponderomotive energy as well.

The population in each quantum state (n, l) at the end of the pulse is shown in Fig. 1.4 for intensities between 10^{13} and 10^{14} W/cm^2. The results shown in the left (right) column correspond to cases in which the Rydberg states are resonant with an even (odd) number of photons. In all cases, we see that the highest angular momentum states ($l > 7$) are not much populated, in agreement with previous studies [28] and semi-classical estimates [29]. In the results, we observe signatures of selection rules resulting in dominant population of states with an even (odd) angular momentum quantum number for the absorption of even (odd) photons in the plots on the left (right). This shows that in the intensity regime of 10^{13} to 10^{14} W/cm^2 the parity selection rules, previously studied for monochromatic fields and flat-top pulses, are effective for long pulses of about 20 cycles. However, we observe that the contrast between the population in even and odd states is stronger at lower intensities.

The results also show that for an odd parity process (right column) predominantly one angular

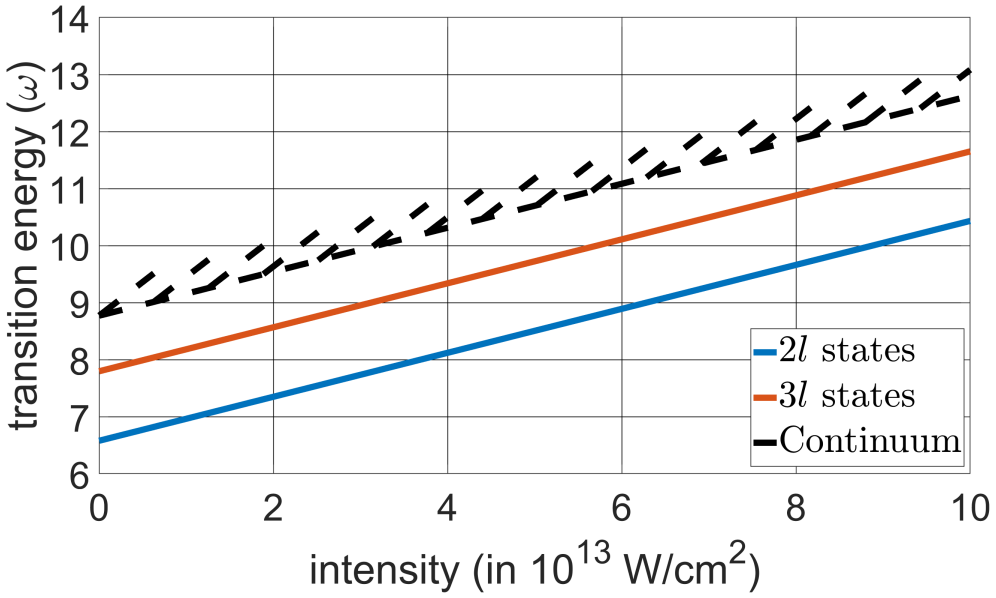

Figure 1.2: Diagram of the AC Stark shift as a function of laser intensity for a wavelength of 800 nm. (solid lines) Excitation and (dashed line) ionization energies are given in units of ω. As the intensity increases, N-photon ionization channels close (e.g., the 9-photon channel at intensities above about 6×10^{12} W/cm^2) and excited states shift across resonances.

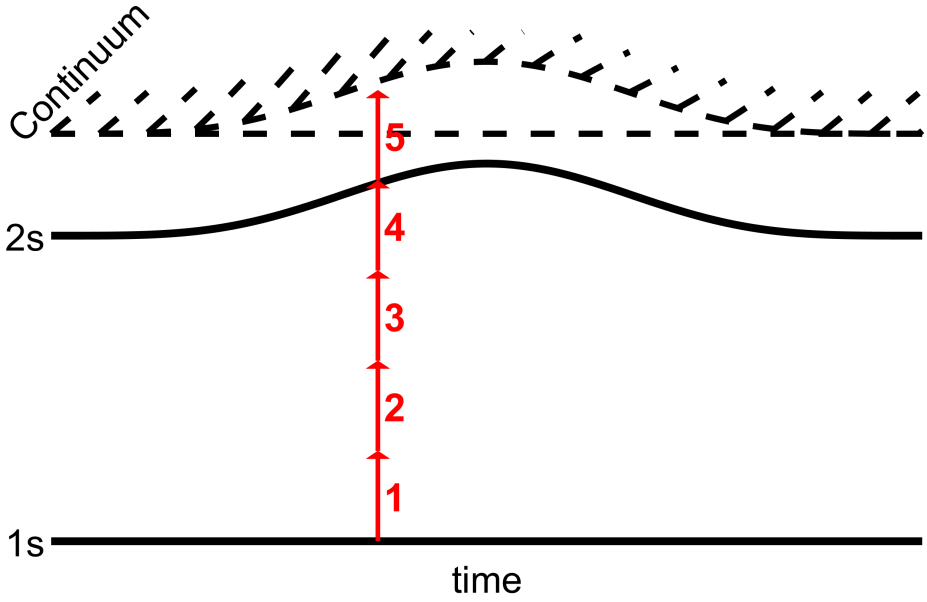

Figure 1.3: Diagram of the time-dependent AC Stark shift. Near the peak of the pulse, the effective ionization potential (top dashed line) rises above the energy of five photons (red arrows), while the $2s$ state energy (top solid line) shifts briefly into 4-photon resonance.

momentum state ($l = 5$) is populated. This is in agreement with the results presented by Li et al. [30], who conjectured that electrons in the low angular momentum states more easily absorb additional photons resulting in suppression of population in these states due to ionization. However, our results for even parity processes exhibit a pattern, alternating in l, showing that both low and high angular momentum states, except for the s-states, remain populated at the end of the pulse.

Chapter 3 investigates related processes in resonance-enhanced HHG.

1.3.1 High-order harmonic generation

In high-order harmonic generation (HHG), an atom or molecule is exposed to a high-intensity, low-frequency laser. An electron absorbs many photons (up to thousands [31]) before being driven back into the atom; all of the absorbed energy is then emitted as a single photon. When a laser shines on a gas consisting of many such atoms, the emitted photons form high-frequency laser light with lower intensity. The emitted photons have a large range of frequencies with similar intensities – an unusual and useful trait. Of primary interest are the high-energy portions (into the x-ray regime) and the incredibly short duration of these laser pulses.

HHG is characterized by a so-called plateau where radiation occurs with consistent intensity at odd multiples of the driving laser frequency, ω. In Fig. 1.5, we show a schematic HHG spectrum. The first few harmonics (1ω, 3ω, 5ω, and 7ω) below the ionization threshold (I_P) show exponentially-decreasing intensity as predicted by perturbation theory. However, the next several odd harmonics (through 21ω) appear at the same intensity, forming the plateau. After a so-called "cut-off" energy (21ω), the intensity of harmonics again decreases exponentially.

HHG can be understood through a three-step semi-classical model [32–34] (Fig. 1.6). An electron is initially in the ground state of an atomic Coulomb potential. Then, an intense field initiates tunnel ionization. The freed electron oscillates purely under the influence of the external field (Eq. (1.4)), gaining kinetic energy. When the electron again approaches the vicinity of the nucleus, it has a chance to recombine back to the ground state. In doing so, it emits the excess energy as a single high-energy photon. Semi-classical trajectory analysis (Sec. 1.4.1) predicts the

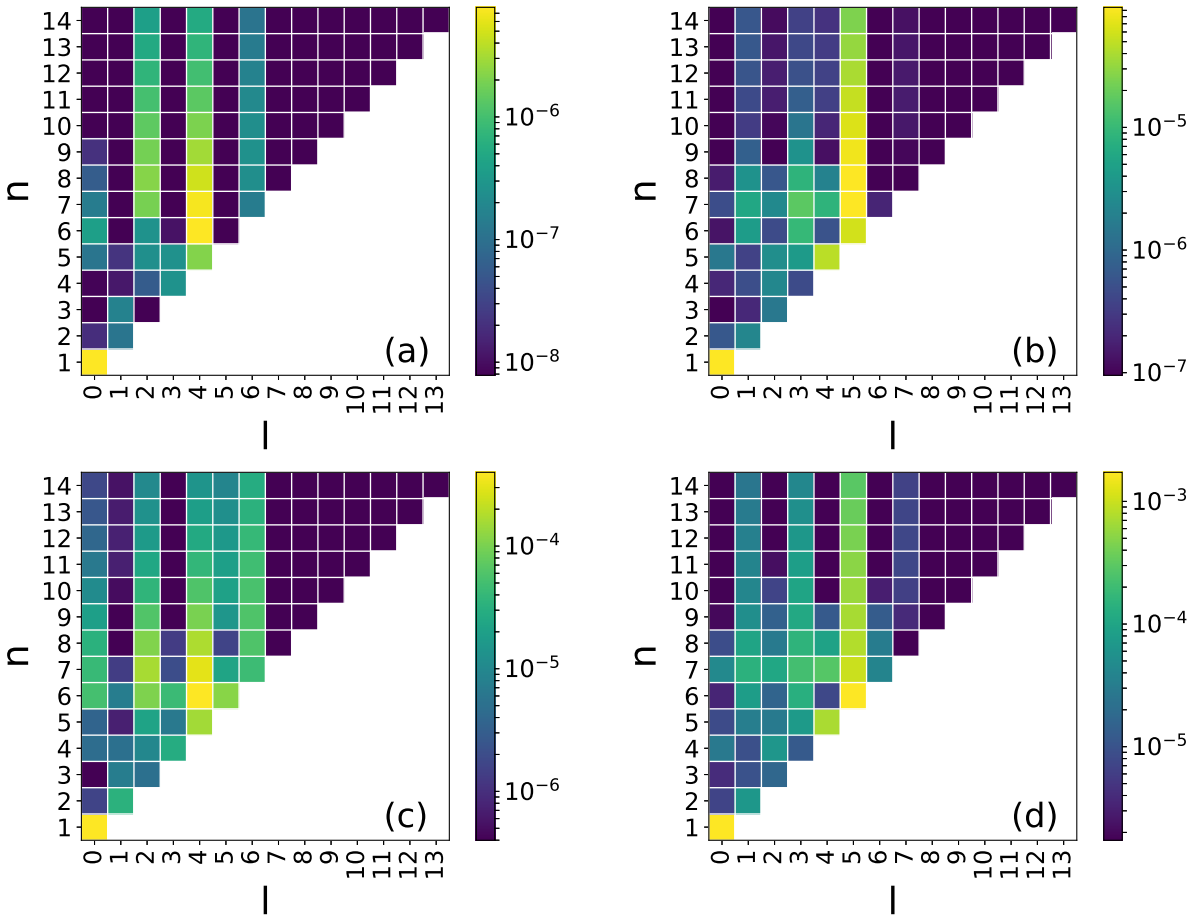

Figure 1.4: Excited state distribution as function of quantum numbers n (vertical axis) and l (horizontal axis) at the end of 800 nm, 20 cycle pulses with sine-squared envelope and peak intensities: (a) $I_0 = 3.4 \times 10^{13}$ W/cm^2, (b) $I_0 = 6.0 \times 10^{13}$ W/cm^2, (c) $I_0 = 8.6 \times 10^{13}$ W/cm^2, and (d) $I_0 = 11.2 \times 10^{13}$ W/cm^2. Left (right) column corresponds to cases in which the Rydberg states are resonant with an even (odd) number of photons. (Taken from [3].)

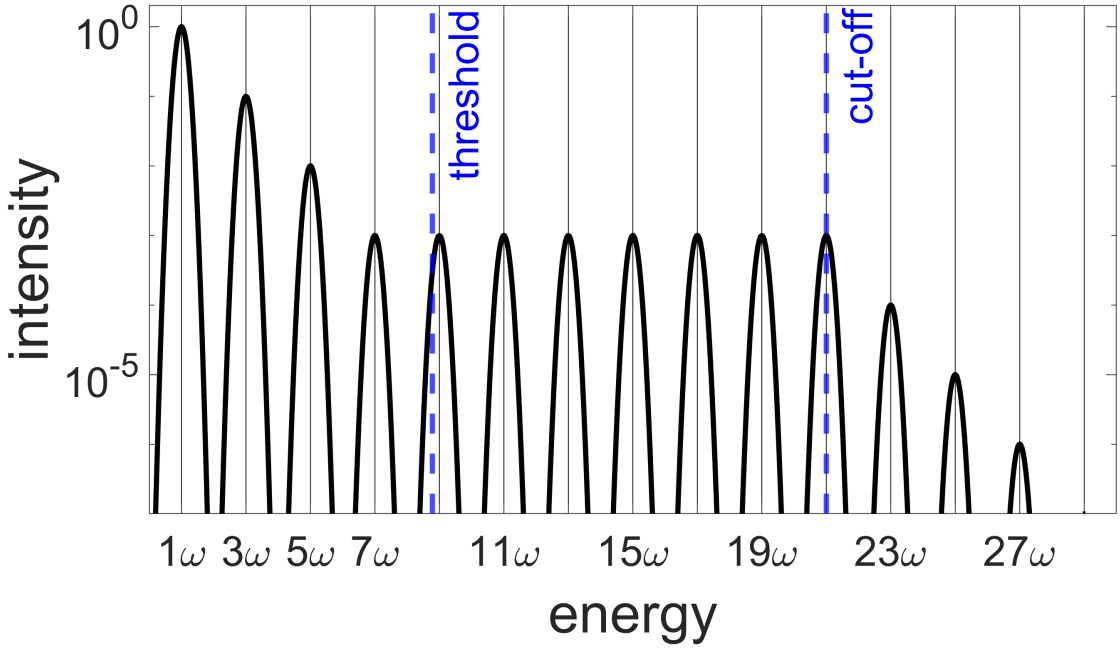

Figure 1.5: Diagram of a high-order harmonic generation spectrum marked by a plateau of radiation at similar intensities.

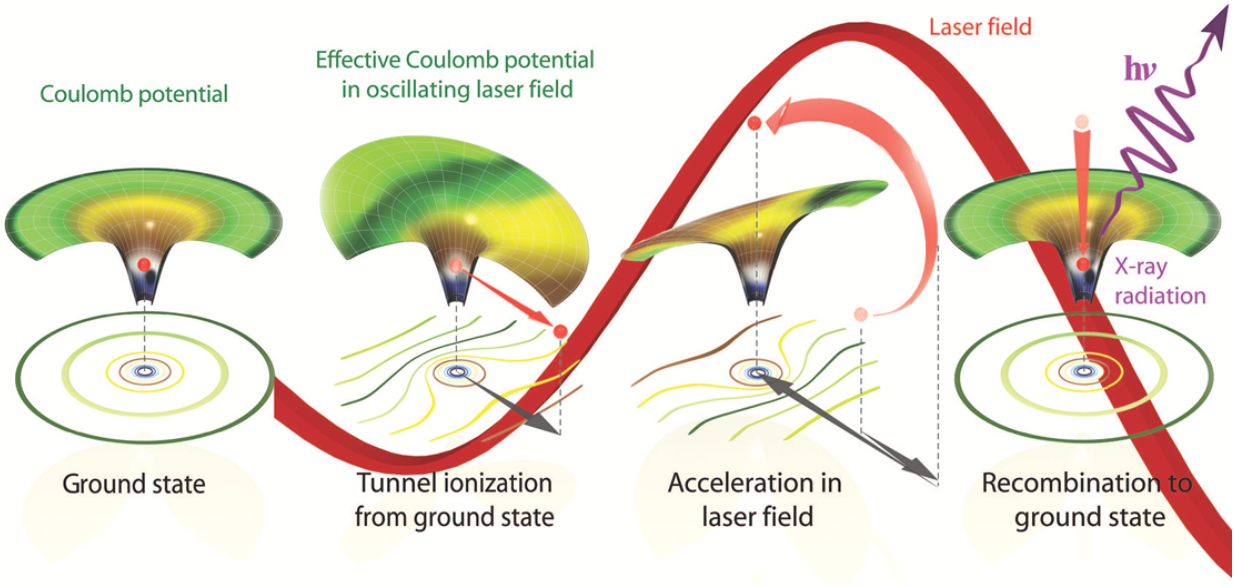

Figure 1.6: Diagram of the 3-step model of high-order harmonic generation. (Taken from [4].)

maximum kinetic energy upon return as $3.17U_P$, resulting in the radiation cut-off of $I_P + 3.17U_P$. Various additional considerations result in a more complicated interaction and may allow for higher return energies, including inclusion of the Coulomb force in classical trajectories, the presence of quantum trajectories, and multiphoton ionization.

As with perturbative harmonics, atomic inversion symmetry across the laser polarization direction prohibits even-harmonic radiation [35]. This symmetry is not present in other systems (e.g., most molecules) or when significant electron density departs the ground state.

HHG has been a subject of intense research for decades, for a variety of reasons. Firstly, unlike other methods of generating high energy photons (e.g., linear accelerators such as at SLAC [36]), HHG can be performed on the tabletop scale. Additionally, HHG allows a higher level of coherence and control of various parameters including the CEP, polarization, and angular momentum of the laser [37, 38].

1.3.2 Free-induction decay

In the context of strong-field physics, free-induction decay (FID) is simply the process whereby electrons in excited np states decay to the ground state and emit photons with the corresponding energy $\omega = E_n - E_0$ [39]. The bandwidth of this radiation is generally quite small relative to that of harmonic radiation, appearing as sharp peaks. Additionally, FID continues well after the end of the driving laser pulse, unlike most other radiative processes. In our numeric methods, FID is not fully captured since the vacuum field necessary for spontaneous emission is absent – FID radiation appears due to the oscillation of electrons in a superposition state, but the excited population never decays to the ground state and energy is not conserved. Fortunately, the timescale of spontaneous decay is generally orders of magnitude longer than the duration of our pulses, and the approximation of infinite lifetime is good.

1.4 Numeric methods

This thesis does not cover the development of new methods for simulation of single-electron behavior, but we briefly describe tools developed by others – in some cases implemented during the course of this research.

1.4.1 Semi-classical trajectories

From the 3-step model of HHG, one may derive an approximative description where electron motion is simulated through simple Newtonian methods. Namely, the initial position and momentum of the electron are set by ionization conditions (typically, placing the electron at the tunnel exit with zero initial velocity) and motion then proceeds according to the classical equations of motion, often excluding the effect of the Coulomb potential. In this case, motion may be analytically predicted (i.e., Eq. (1.4)), but when the full force is included:

$$F(x,t) = F_E(t) + F_C(x) = -E_0 \sin(\omega t) - \frac{x}{|x^3|}, \tag{1.19}$$

numeric solutions are required, such as Verlet integration [40] where the position and velocity are computed for progressive steps in time, $t_{i+1} = t_i + dt$:

$$x(t_{i+1}) = x(t_i) + v(t_i)dt + 0.5a(t_i)dt^2 \tag{1.20}$$

$$a(t_{i+1}) = F\left(x(t_{i+1}), t_{i+1}\right) \tag{1.21}$$

$$v(t_{i+1}) = v(t_i) + 0.5\left(a(t_{i+1}) + a(t_i)\right)dt. \tag{1.22}$$

Radiation is then predicted whenever x crosses 0, and the resulting energy is given by the kinetic energy $T = 1/2v^2$ plus I_P.

A broader discussion of semi-classical trajectories can be found in Hostetter et al. [41], including: methods to avoid issues with the singularity in the Coulomb field and derive the radiation phase computed from classical action; and, an alternate set of initial conditions meant to represent multiphoton ionization. We do not present results of calculations of semi-classical trajectories in this thesis, but any remarks are based on a reproduction of the algorithm as presented in [41].

1.4.2 Finite difference and eigenstate problems

For the vast majority of Schrödinger equation cases, there is no analytic solution to even the time-independent problem. Thus, we proceed with numerical solution through discretization of space and time, for example the wavefunction $\psi(x,t) \rightarrow \psi(x_i, t_j)$ with indices $i, j = 0, 1, ...$ In this thesis, all discretization occurs on uniformly-spaced grids and with uniform time steps, so $x_{i+1} = x_i + \Delta x$ and $t_{j+1} = t_j + \Delta t$.

Spatial derivatives are then computed through finite differences, for example the 2nd-order approximations:

$$\frac{\partial}{\partial x}\psi(x_i) \approx \frac{-\psi(x_{i-1}) + \psi(x_{i+1})}{\Delta x} \tag{1.23}$$

$$\frac{\partial^2}{\partial x^2}\psi(x_i) \approx \frac{\psi(x_{i-1}) - 2\psi(x_i) + \psi(x_{i+1})}{\Delta x^2}, \tag{1.24}$$

which may be expressed as matrix equations, such as

$$\frac{\partial^2\psi(x_i)}{\partial x^2} = \frac{1}{\Delta x^2}\begin{bmatrix} 2 & -1 & & & & \\ -1 & 2 & -1 & & & \\ & \ddots & \ddots & \ddots & & \\ & & -1 & 2 & -1 & \\ & & & -1 & 2 & \end{bmatrix}\begin{bmatrix} \psi(x_0) \\ \psi(x_1) \\ \vdots \\ \psi(x_{N-1}) \\ \psi(x_N) \end{bmatrix}. \tag{1.25}$$

The time-independent Schrödinger equation (in one dimension)

$$E_n\psi_n(x) = \left[-\frac{\partial^2}{\partial x^2} + V(x)\right]\psi(x) \tag{1.26}$$

becomes an eigenvalue/eigenvector problem. Our early eigenstate solutions were based on a trick of the time-dependent numeric propagator (called Imaginary Time Propagation, see Sec. 1.4.3.2). However, more recently we have utilized [42] the Arnoldi method of eigenvalue solutions [43].

While the TISE has spherical symmetry for atomic potentials, we often require eigenstates as the initial conditions for further time-dependent interactions with laser fields without such symmetry. For all results of this thesis, linearly-polarized lasers are used and the electron density remains in the subspace where magnetic/azimuthal quantum number $m = 0$. Thus, we perform computations with discretization in cylindrical (ρ_i, z_i) or spherical (r_i, Y_l^0) coordinates.

1.4.3 Time-dependent Schrödinger equation

Solutions to the TDSE (length gauge)

$$i\frac{\partial}{\partial t}\psi(\vec{r},t) = H\psi(\vec{r},t) = \left[-\frac{\nabla^2}{2} + V(\vec{r}) + \vec{E}(t) * \vec{r}\right]\psi(\vec{r},t) \tag{1.27}$$

naturally require propagation in time. Considering the propagator formulation

$$\psi(\vec{r},t) = e^{-iH\Delta t}\psi(\vec{r},t), \tag{1.28}$$

we may achieve numerical tractability through the Cayley form [44]

$$e^{-iH\Delta t} \approx \frac{1 - i\frac{\Delta t}{2}H}{1 + i\frac{\Delta t}{2}H}, \tag{1.29}$$

and the Crank-Nicolson method [45]:

$$\left(1 + i\frac{\Delta t}{2}H\right)\psi(t + \Delta t) = \left(1 - i\frac{\Delta t}{2}H\right)\psi(t). \tag{1.30}$$

The resulting problem in multiple dimensions may be performed either through approximating the effect of the Hamiltonian along each dimension (e.g., $H = H_{x_1} + H_{x_2}$):

$$e^{-iH\Delta t} \approx e^{-iH_{x_1}\frac{\Delta t}{2}} e^{-iH_{x_2}\Delta t} e^{-iH_{x_1}\frac{\Delta t}{2}}, \tag{1.31}$$

or through direct solution relying on modern sparse-matrix methods, such as the Generalized Minimal Residual method [46]. The former is simpler to code, but the latter benefits from better parallelization on large computational systems. Results in this thesis comprise both methods, which we have previously shown to give consistent results [3].

1.4.3.1 Exterior complex scaling

One issue with simulations on discrete grids is that the grid cannot have infinite extent – we are in practice placing our interaction in a box. For weak fields, it may be possible to use numerical grids large enough that no appreciable electron density reaches the edge, but this is not feasible for simulations in the strong-field regime of interest. Instead, one must ensure that behavior of interest (e.g., HHG trajectories) fits within the extend of the grid, and appropriately handle departure of ionized electron density. The former is generally a matter of checking numeric convergence by scanning the box size, but we have found a radius of three times the quiver radius $r_q = \frac{E_0}{\omega^2}$ to generally suffice for HHG simulations. For the escaping density, we use Exterior Complex Scaling (ECS) [47, 48], where the edges of the grid are rotated into complex space by an angle $\eta = \pi/4$:

$$\rho \ (or \ r) = \begin{cases} \rho & \rho \leq \rho_0 \\ \rho_0 + (\rho - \rho_0)e^{i\eta} & \rho \geq \rho_0 \end{cases} \tag{1.32}$$

$$z = \begin{cases} -z_0 + (z + z_0)e^{i\eta} & z \leq -z_0 \\ z & -z_0 \leq z \leq z_0 \\ z_0 + (z - z_0)e^{i\eta} & z \geq z_0. \end{cases} \tag{1.33}$$

We apply this transformation only to the kinetic energy term of the Hamiltonian to avoid undesirable density-explosion from the oscillating electric field [49].

1.4.3.2 Imaginary Time Propagation

Given a numeric library for solution of the TDSE, Imaginary Time Propagation (ITP) is a simple and popular method of generating initial states similar to the power method. An initial wavefunction guess $\psi(\vec{r}, t = 0)$ is made based on analytic solutions or random generation. The wavefunction is then propagated in steps of imaginary time $\psi_i(\vec{r}, t = -iN\Delta t)$ and normalizing $|\psi|^2 = 1$ until reaching numeric convergence. This functions by replacing eigenstate quantum oscillation:

$$\psi(\vec{r}, t) = \sum_n c_n \psi_n(\vec{r}, t = 0) e^{-iE_n t} \tag{1.34}$$

with exponential enhancement of the ground state (i.e., state with most negative energy):

$$\psi(\vec{r}, t = -iN\Delta t) = \sum_n c_n \psi_n(\vec{r}, t = 0) e^{-E_n N \Delta t}. \tag{1.35}$$

The first excited state may be acquired by projecting out the ground state after each iteration (via Gram-Schmidt orthogonalization), and so forth for additional states.

ITP has the advantage of building on tools already developed for (real) time propagation, and generally converges rapidly for the first few states. However, it becomes inefficient for higher excited states (when repeated orthogonalization is required) and may cease functioning altogether due to limitations of machine precision. For this reason, methods better-grounded in linear algebra (e.g., the Arnoldi method) are preferable.

1.4.3.3 Simulating spectra

To derive the radiation spectrum from simulation of electron motion, we evaluate the dipole acceleration $\mathbf{a}(t)$ using the Ehrenfest theorem

$$\mathbf{a}(t) = \langle \nabla V \rangle \,, \tag{1.36}$$

and compute the spectrum as its Fourier transform:

$$P(\omega) = \left| \int_0^T \mathbf{a}(t) e^{-i\omega t} dt \right|^2 , \tag{1.37}$$

where T is the final time of the simulation. Often, we apply a window function as described in Sec. 1.5.1.

The dipole acceleration can generally be extracted from the integration of the wavefunction at each time step during simulation without dramatically reducing efficiency. If necessary, it may be output at a lower time resolution ($dt = 0.1$ a.u. is generally sufficient for resolving spectra, but at times propagation of the wavefunction requires finer steps).

1.5 Tools for analyzing HHG

To understand HHG, we must be able to analyze the effects of several different pathways. Consideration of HHG spectra or time-domain pulses independently can be useful (e.g., to identify or measure attosecond pulses), but insight into the underlying processes based on this information is often limited. There are several possible tools to enhance our understanding of the mechanisms and physics:

(1) focus on a simpler approximate theory (e.g., strong-field approximation (SFA) [50–52], classical trajectories), which can provide different access to what is going on than numerical solutions of TDSE;

(2) perform analysis in a mixture of the time and frequency domains; or,

(3) widely scan laser and target parameters to seek trends, which can be especially useful given how noisy HHG spectra often are.

When analyzing radiation emitted near the ionization threshold, many approximative methods fail due to the complex impact of excited states and atomic potential – which are, for example, entirely ignored in the basic strong-field approximation [32, 50–52] and still poorly represented in its extensions [53, 54]. Considering laser parameters that fall in the strong-field multiphoton (vs. the tunneling or perturbative multiphoton) regime of ionization and excitation similarly precludes the use of most other approximate methods, or at least complicates them greatly, and therefore limits intuitive insights based on the results (as in the case of generalized semi-classical trajectory methods, cf. Sec. 1.4.1). Therefore, we primarily utilize numeric solutions to the full time-dependent Schrödinger equation (TDSE). The resultant spectra, however, often include many radiation peaks, sidebands, and other features with sufficient magnitude to be of interest. On the other hand, the temporal response during the pulse is consistently dominated by the low harmonics – i.e., one domain contains too much information and the other too little. Performing scans of laser (or target) parameters will often at least clarify which radiation features are stable versus those existing only in narrow slices of parameter space – and thus not likely to survive macroscopic propagation (see Ch. 4) or appear in experiment. This can illuminate the mechanisms behind a subset of features with simple dependence (e.g., FID signals which appear at the field-free $|0\rangle \rightarrow |np\rangle$ transition energies). Often, though, understanding mechanisms requires simultaneous parsing of time and frequency information, and frequently in conjunction with parameter scans. In the following subsections, we will discuss the particulars of a few forms of time-frequency analysis and some remarks on parameter scanning.

1.5.1 Temporal windowing

Perhaps the simplest way to gain insight into the interplay between time and frequency in radiation is to consider a windowed Fourier transform of the dipole acceleration,

$$P(\omega) = \left| \int_{-\infty}^{\infty} \mathbf{a}(t) W(t) e^{-i\omega t} dt \right|^2 , \tag{1.38}$$

with $W(x) \in [0,1]$ being some window function. We already introduced the commonly-used Blackman window $W_{Blackman}(x,T) = 0.42 - 0.5\cos(2\pi x/T) + 0.08\cos(4\pi x/T)$ [55]. By convention, most numeric HHG spectra are reported using a Blackman window with width T equal to the laser pulse duration. This eliminates radiation occurring after the end of the laser and generally smooths the spectra.

However, windowing can also provide additional information, for example comparing the spectra windowed to the span of the pulse versus one including extended propagation past the end of the pulse. In a previous paper [3], we used this technique to demonstrate the impact of populations of excited states with dipole-allowed transitions to the ground state on the spectra: FID lines appearing as sharp peaks in the post-pulse radiation (see Fig. 1.7).

More generally, we may window to particular sections of the pulse (e.g., first half, peak ± 2 o.c., etc.) to identify the radiation emitted during different periods. The primary limitations of windowing are loss of spectral precision – since fewer data points in the Fourier transform include actual data – and identifying windows that provide useful information.

1.5.2 Spectral filtering and temporal profiles

In the other direction, we may consider the temporal profile of radiation for particular spectral regions. For example, we could ask what pulse would be produced by filtering to the radiation near the 9th harmonic. This is accomplished by Fourier transforming the dipole acceleration into the frequency domain, applying a spectral filter, R, then inverse Fourier transforming back to the time domain

$$P(t;R) = \left|\mathcal{F}^{-1}\left[R(\omega')\mathcal{F}[\mathbf{a}(t')]\right]\right|^2. \tag{1.39}$$

Unless otherwise noted, we use for such studies a filter with a two-harmonic flat top and

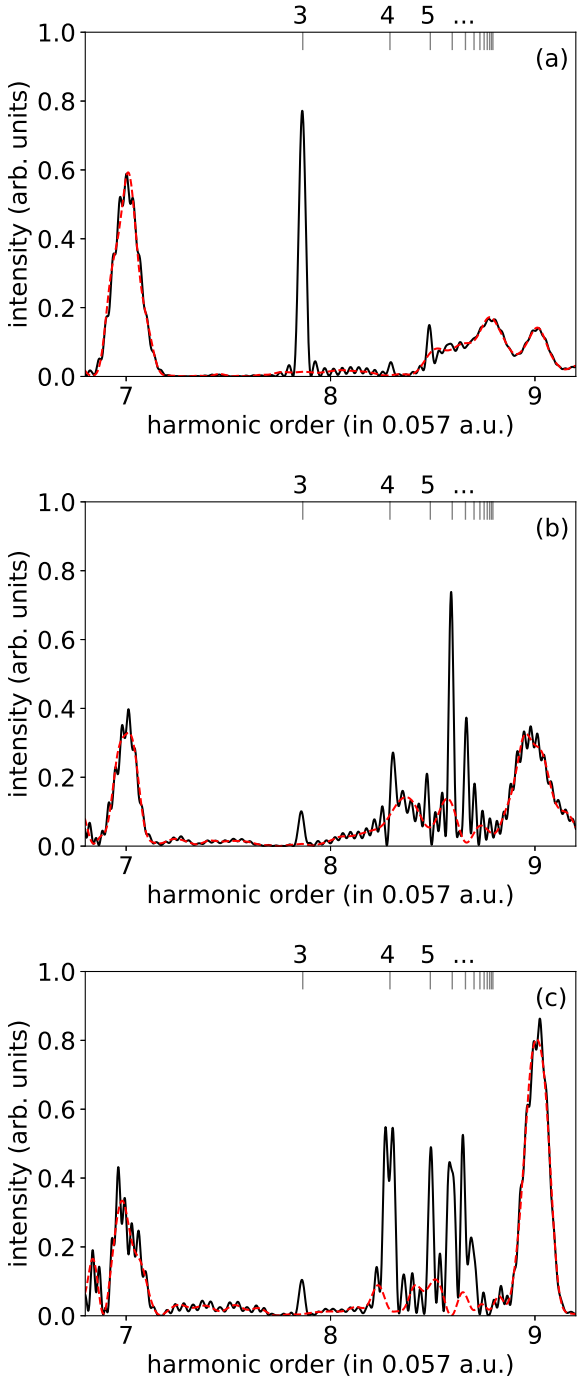

Figure 1.7: Radiation spectra generated during the pulse (red dashed lines) and those including line emissions after the pulse (black solid lines) are shown for hydrogen driven by a 20 o.c. sine-squared, 800-nm pulse with peak intensities: (a) $I_0 = 3.4 \times 10^{13}$ W/cm^2, (b) $I_0 = 6.0 \times 10^{13}$ W/cm^2, and (c) $I_0 = 16.4 \times 10^{13}$ W/cm^2. The vertical gray lines show the field free energy differences between the np energy levels (up to $14p$) and the $1s$ ground state. (Taken from [3].)

Gaussian falloff with $\sigma = 0.1$ harmonics, centered at harmonic N:

$$R_N(q\omega_0) = \begin{cases} \exp\left[-\frac{1}{2}(\frac{q-(N-1))}{0.1})^2\right] & q \leq N-1 \\ 1 & N-1 \leq q \leq N+1 \\ \exp\left[-\frac{1}{2}(\frac{q-(N+1))}{0.1})^2\right] & q \geq N+1 \end{cases} \tag{1.40}$$

Spectral filtering in this way can be quite powerful – especially when combined with parameter scans – but it is important to recognize artifacts of the filtering technique, including:

- Fourier transforms and windows/filters involve a sometimes surprising number of factors and phases which must be managed carefully to avoid unintentional shifts in time or magnitude scaling.
- If spectral filters are narrower than peaks or near-constant regions, it is possible to introduce spurious frequencies, which can appear as temporal beating.
- Sidelobes resulting from too-sharp filter cut-offs, which may be appealing when attempting to isolate narrow features.

1.5.3 Wavelet analysis

True time-frequency analysis provides information on the intensity of a signal in regions of *both* time and frequency, together. The simplest method is to scan the center of a temporal window across the duration of data, then stack the windowed frequency response. This has a variety of drawbacks including those already mentioned. Many are resolved using a more complex method, such as the continuous wavelet transform [56–58]. We specifically utilize a Morlet wavelet

$$f(\omega, t; t_f) \propto \int_{min(t_E)}^{max(t_E)} \frac{\omega}{\Omega_0} E_R(t') e^{-i\omega(t'-t) - \frac{1}{2}\left(\frac{\omega}{\Omega_0}(t'-t)\right)^2} dt' \tag{1.41}$$

where

$$E_R(t_E) = \int_0^{\omega_{max}} E_R(\omega) e^{i\omega t_E} d\omega \,, \tag{1.42}$$

ω is the frequency of the wavelet, and t and Ω_0 are the center and the variance of the Gaussian window. The parameter Ω_0 allows control of the time vs. frequency resolution of the wavelet. In this thesis, we have chosen $\Omega_0 = 6$ or 54, which provide a good resolution in time or frequency, respectively, for 800 nm lasers. We note that Eq. (1.41) provides the high harmonic spectrum for $\Omega_0 \to \infty$:

$$f_{HHG}(\omega; t_f) \propto \int_{-\infty}^{t_f} a(t')e^{-i\omega t'}dt'. \tag{1.43}$$

While wavelet plots provide a great deal of information, there are drawbacks. Firstly, the differences in scale (e.g., between different harmonics) require careful selection of color axis limits to avoid either hiding important features or enhancing noise to the point of obscuring details. This in turn leads to difficulties in comparing wavelet plots for different laser parameters. Even when consistent and informative color scales are achieved, the sheer volume of information conveyed can make comparisons visually complex.

1.5.4 Parameter scans

One of the strongest tools to understand any physical phenomena is to see what happens under variation ("Does the heavier ball fall faster?"). In the context of theoretical physics, this is particularly easy, as we may set any arbitrary laser or target parameters and analyze the simulation results. In the simplest case of scalar observables, results may be plotted as a line against parameters (e.g., probability of ionization vs. driving intensity). For radiation, though, this is generally not as productive. For instance, plotting the intensity of a given harmonic obscures important features (red/blue-shift, sidebands, width) and becomes unstable to deviations from the expected behavior (e.g., when the "9th harmonic" is not centered at 9ω, or when nearby off-harmonic peaks have greater intensity). For this reason, heatmaps are popular – allowing for plotting the full harmonic spectrum as a function of some parameter. Similarly, we find great benefit in plotting scans of the temporal profile of a given harmonic across, e.g., intensity. Finally, there are cases where the results from a single simulation are already multidimensional, and scans can often not be visually

processed without separate images (incl. slideshows and animated media). While important for our research process, we avoid including such visualizations in this thesis.

1.6 Outline of this thesis

The rest of this thesis comprises three projects on high-order harmonic generation tied together by an emphasis on investigation of near-threshold harmonics and their connection to atomic characteristics (including the potential and excited states). Additionally, methods are presented for efficient simulation and analysis applicable to broad parameter regimes.

In Chapter 2, we will discuss single-active-electron (SAE) potentials for atoms, ions, and molecules. These potentials allow the use of existing single-electron methods (especially numeric TDSE libraries) for simulation of more complex targets. We outline a method for generating SAE potentials based on analytic forms fit to density functional theory potentials – without any parameters modified by hand. Using one such potential, novel agreement is shown with time-dependent density functional theory calculations for simulation of a strong-field process, namely HHG. We introduce additional applications to HHG from multi-orbital atoms, and nonlinear polarization and ionization of molecules.

In Chapter 3, we analyze the impact of field-shifted resonances on near-threshold HHG. We focus on a particular set of spectro-temporal features associated with the $3p$ state of the hydrogen atom shifting into 9-photon resonance, investigating the dependence on a variety of laser and target parameters. We show that aspects of the behavior are quite general, and similar features appear in a broad range of parameters, including more intense near-IR driving lasers, weak mid-IR pulses, and helium driven by intense 400 nm pulses.

In Chapter 4, we introduce an efficient method of macroscopic summation built upon a manageable set of TDSE simulations. Specifically, the response of macroscopic gas jets are determined through Monte Carlo summation of relatively few ($10^5 - 10^7$) point-like radiators. The acceleration response from each radiator is interpolated from a small set (100-1000) of full TDSE calculations. This method allows for accurate simulation of near-threshold HHG – for the thin medium or low

gas density regimes that are free from longitudinal phase-matching effects – which is not possible with approximate methods such as the Strong-Field Approximation. The method is immediately extensible to long wavelengths and to other atomic and molecular targets, and results are presented for mid-IR pulses and helium driven by 400 nm pulses. We additionally demonstrate a distinct interference pattern in the angular distribution of HHG for focal phase distributions associated with highly-focused pulses.

Finally, in Chapter 5, we conclude with a summary of the topics discussed within this thesis and consider future directions of the field supported by this work.

Chapter 2

Single-Active-Electron Potentials[1]

A widely-used method to study nonlinear effects in larger laser-driven atoms involves numerical solutions of the time-dependent Schrödinger equation (TDSE) within the single-active-electron (SAE) approximation. In the SAE approximation, it is assumed that the laser field only interacts with one – typically the most weakly-bound – electron in the atom or molecule, considering all other electrons as frozen spectators to the evolving physics. SAE-TDSE calculations have the advantage of being a straightforward extension from common hydrogen TDSE codes. These calculations are computationally efficient and scale well to parameter regimes (e.g., long wavelength and/or high intensity) that are often infeasible to explore with multielectron codes. In cases where multielectron calculations are possible, single-electron approximations still have value, since SAE-TDSE simulations can serve in initial exploratory parameter sweeps before running more expensive calculations to identify multielectron effects.

Furthermore, ab-initio SAE calculations can provide important benchmark results for more sophisticated multielectron methods in parameter regimes where electron correlation effects are small. In the perturbative interaction regime, such a comparison between results of time-dependent density functional theory (TDDFT) simulations and ab-initio calculations using lowest-order perturbation theory has been done recently and a good agreement has been found [59]. This established the applicability of TDDFT calculations for perturbative multiphoton processes. We are not aware of a similar study at higher intensities for highly nonlinear and nonperturbative processes. A few

[1] Some results of this chapter are also presented in [1]

rare studies reporting a comparison between TDDFT and SAE-TDSE results for nonperturbative strong-field processes typically attribute differences to the impact of multielectron effects [60, 61] without establishing a benchmark test between SAE-TDSE and TDDFT calculations. The absence of such benchmark tests partially contributes to the misconception in parts of the strong-field community that TDDFT studies cannot provide quantitative predictions for highly nonlinear processes involving the continuum. In this Chapter, we show – by carefully constructing an SAE potential – that indeed agreement between SAE-TDSE benchmark results and TDDFT results can be found. Hence, we establish a method to check the accuracy of TDDFT calculations in view of multielectron effects and disprove the misconception about the quantitative predictive power of TDDFT calculations. We further extend the SAE framework to the generation of simple, but accurate, potentials for molecular dimers. Throughout, we place an emphasis on technical obstacles we encountered and advice on how others may similarly overcome them in future work.

In Sec. 2.1 we present the method to obtain analytical forms of SAE potentials based on DFT calculations (which is essential for the benchmark tests). We establish the accuracy of the SAE potentials by presenting predictions for energies of the ground state and singly excited states of various atoms within the single-active-electron approximation (Sec. 2.1.4). In Sec. 2.2, we compare results for high harmonic generation (HHG) from helium within the single-active-electron approximation with those from TDDFT calculations based on the same DFT approach for a few highly nonlinear cases. Next, we show as another application of the SAE potentials results for high-order harmonic generation from outer and inner valence shells (Sec. 2.2.3). Finally, we discuss SAE potentials for molecules and an application to nonlinear polarization and ionization in O_2 (Sec. 2.3). We summarize our results in Sec. 2.4 along with a brief description of published work by others based on the SAE potentials.

2.1 Constructing SAE potentials

In this section, we discuss the construction of SAE potentials for atomic systems, based on fitting to an effective Kohn-Sham potential. First, we discuss the concept in constructing the SAE

potential for the benchmark tests before we briefly reiterate the density functional theory formalism used to obtain the Kohn-Sham potential. Then we present the approach used to approximate the Kohn-Sham potential via analytical functions and discuss strategies to determine the coefficients in the model potential. Finally, we present the methods used to perform the ab-initio SAE-TDSE and TDDFT calculations.

The construction of a potential to model single-active-electron behavior has been pursued through several different strategies (e.g., [62–69]). SAE models are frequently developed using analytic functions with free parameters that are fit to accurately simulate experimental behavior in the scenario of interest (often by matching the ionization potential for the single active valence electron to the experimental value, since many strong field processes – such as tunneling ionization – strongly depend on it). Besides the long-range behavior of the SAE potential – which is essential for the determination of the ionization behavior – electron dynamics driven by a strong laser pulse also probe the short-range properties of the potential (e.g., excited states). Constructing an SAE potential that reproduces well ground, inner, and excited state energies, is therefore useful for studying laser-driven processes from the valence as well as inner shells. Furthermore, it provides a reliable ground for benchmarking TDDFT calculations against ab-inito SAE-TDSE results, as we will demonstrate in Sec. 2.2.2. Conceptually, the SAE potential should therefore be based on the same DFT approach used in the TDDFT calculations without any free parameter adjustment.

To this end, we have obtained analytical forms of single-active-electron potentials, using density functional theory (DFT) and physical reasoning regarding the electronic structure of an atomic system. Fits to the effective Kohn-Sham potential are made without using ad-hoc free parameters. We establish the accuracy of the potentials by comparing ionization and excitation energies. Basing the approaches on the same functional we are set up to make an accurate quantitative comparison between SAE-TDSE and TDDFT calculations for HHG from helium at intensities in the nonperturbative regime. We further note that by providing analytical forms of the SAE potentials, the SAE-TDSE vs. TDDFT comparisons can be reproduced or extended in the future.

2.1.1 Density Functional Theory

In the Kohn-Sham density functional theory (DFT) formulation of multielectron systems [70, 71], each orbital $\psi^{KS}_{i,\sigma}(\mathbf{r})$ $(i = 1, \ldots N)$ involved in the ground state of the spin-polarized N-electron system is determined by solving a set of Schrödinger-like eigenvalue equations given by

$$\left[-\frac{1}{2}\nabla^2 + V_{eff,\sigma}(\mathbf{r})\right]\psi^{KS}_{i,\sigma}(\mathbf{r}) = E^{KS}_{i,\sigma}\psi^{KS}_{i,\sigma}(\mathbf{r}), \tag{2.1}$$

where

$$V_{eff,\sigma}(\mathbf{r}) = V_{ext}(\mathbf{r}) + V_H(\mathbf{r}) + V_{xc,\sigma}(\mathbf{r}) \tag{2.2}$$

is the effective Kohn-Sham potential and σ denotes the spin of the electron. The terms in Eq. (2.2) represent the external Coulomb potential $V_{ext}(\mathbf{r}) = -\frac{Z}{r}$, the Hartree potential $V_H(\mathbf{r}) = \int \frac{\rho(\mathbf{r}')}{|\mathbf{r}-\mathbf{r}'|}d\mathbf{r}'$ accounting for the electron-electron repulsion with the total electron density $\rho(\mathbf{r}) = \sum_\sigma \rho_\sigma(\mathbf{r}) = \sum_\sigma \sum_{i=1}^{N_\sigma} \rho_{i,\sigma}(\mathbf{r})$ with $\rho_{i,\sigma}(\mathbf{r}) = \left|\psi^{KS}_{i,\sigma}(\mathbf{r})\right|^2$, and the exchange correlation term $V_{xc,\sigma}(\mathbf{r})$.

An exact expression for V_{xc} is not known and several popular approximations to this quantity exist. We make use of the strategy proposed by Krieger, Li, and Iafrate [72] and extended in [73]. We choose a sum of local (spin-)density approximation (LDA) exchange and correlation functionals:

$$v^{LDA}_{xc,\sigma}(\mathbf{r}) = \mu^{LDA}_{x,\sigma}(\rho_\uparrow(\mathbf{r}), \rho_\downarrow(\mathbf{r})) + \mu^{LDA}_{c,\sigma}(\rho_\uparrow(\mathbf{r}), \rho_\downarrow(\mathbf{r})) \tag{2.3}$$

where $\mu^{LDA}_{x,\sigma}(\mathbf{r}) = -\left(\frac{6}{\pi}\rho_\sigma(\mathbf{r})\right)^{\frac{1}{3}}$ and with $\mu^{LDA}_{c,\sigma}$, as defined in Appendix C of [74], and apply a self-interaction correction [74]:

$$\begin{aligned} v^{LDA-SIC}_{xc,i,\sigma}(\mathbf{r}) = v^{LDA}_{xc,\sigma}(\mathbf{r}) &- \mu^{LDA}_{x,\sigma}(\rho_i(\mathbf{r}), 0) \\ &- \mu^{LDA}_{c,\sigma}(\rho_i(\mathbf{r}), 0) - \int \frac{\rho_{i,\sigma}(\mathbf{r}')}{|\mathbf{r}-\mathbf{r}'|}d\mathbf{r}' \,. \end{aligned} \tag{2.4}$$

This results in an orbital-dependent potential, but the Optimized Effective Potential procedure from [72] resolves this via

$$V^{KLI}_{xc,\sigma}(\mathbf{r}) = \sum_{i=1}^{N_\sigma} \frac{\rho_{i,\sigma}(\mathbf{r})}{\rho_\sigma(\mathbf{r})}(v_{xc,i,\sigma}(\mathbf{r}) + X_{i,\sigma}) \,, \tag{2.5}$$

where $X_{i,\sigma}$ is the solution to the set of linear equations:

$$(\delta_{ji} - (M_\sigma)_{ji})X_{i,\sigma} = \bar{V}^S_{xc,j,\sigma} - \bar{v}_{xc,j,\sigma}, \tag{2.6}$$

with

$$(M_\sigma)_{ji} = \int \rho_{j,\sigma}(\mathbf{r})\frac{\rho_{i,\sigma}(\mathbf{r})}{\rho_\sigma(\mathbf{r})}d\mathbf{r}\,, \tag{2.7}$$

$$\bar{V}^S_{xc,j,\sigma} = \int \rho_{j,\sigma}(\mathbf{r})\left(\sum_{i=1}^{N_\sigma}\frac{\rho_{i,\sigma}(\mathbf{r})}{\rho_\sigma(\mathbf{r})}v_{xc,i,\sigma}(\mathbf{r})\right)d\mathbf{r}\,, \tag{2.8}$$

$$\bar{v}_{xc,i,\sigma} = \int \rho_{j,\sigma}(\mathbf{r})v_{xc,j,\sigma}(\mathbf{r})d\mathbf{r}\,. \tag{2.9}$$

and note $X_{m,\sigma} = 0$ where m is the index of the highest occupied orbital (or indices for a degenerate set), so those terms are ignored. The potential $V^{KLI}_{xc,\sigma}(\mathbf{r})$ has been found self-consistently by guessing a set of orbitals, i.e., $\rho_{i,\sigma}$, then using the orbitals to calculate an exchange correlation potential (Eq. (2.5)), which is then used to update the orbital set as the lowest energy eigenstates of the effective Kohn-Sham potential (Eq. (2.2)), repeating until convergence is reached. The DFT calculations have been completed on a 1D spherical grid with spacing $dr = 0.0025$ a.u. and length $L = 80$ a.u., requiring that the valence orbital energy $E^{KS}_{m,\sigma}$ converges to a difference below 10^{-10} a.u. between iterations. Note this DFT implementation was coded entirely independently of the Octopus [75–77] and Libxc [78] libraries used for our TDDFT comparison.

2.1.2 Notes on implementing DFT

While we are by no means experts on density functional theory or its implementations, we do have some observations which may be of use to other strong-field researchers venturing into DFT. As with much of programming, the best solution is not to do it yourself. There are plenty of pre-existing libraries (such as Octopus) that should suffice for most purposes. These are the result of years of careful thought and optimization. Here, we chose to write a DFT code from scratch so as to allow fully independent comparison with Octopus TDDFT. The following few tips may be helpful when coding a new DFT implementation:

- Many simple DFT algorithms function through iterative convergence. This necessitates both that individual iterations have high accuracy, and that non-convergent behavior is avoided. An advantage, however, is that individual iterations can be manually adjusted, as long as final convergence is achieved.

- As a simple example, any initial density distribution is valid. It may not converge, but it will not converge to an incorrect answer.

- Especially for weakly-bound valence electrons (e.g., in lithium or negative ions), the density tail of the DFT potential may extend further than expected. If the tail is not properly constrained, small errors may compound, resulting in poor long-range behavior of the DFT potential. If, for example, the density is too high far from the atom in one iteration, the potential for the next iteration will be too shallow, resulting in even greater, incorrect density. We managed this by using grids with a large extent and fixing the long range tail to an exponential decay for the initial and middle iterations. Additionally, the iterative process was cancelled when the tail was found to be flat or growing rather than decaying.

- For our process, an exceedingly common result involved two- or three-iteration loops. Instead of converging toward a single energy, the energy would consistently switch between two or three energies (and, presumably, corresponding states and potentials). Generally, none of these energies would be close to the correct one (estimated by other DFT results or experiment, or compared after the fact). One method to avoid this involves mixing multiple previous iterations to set the initial conditions for the next one [79]. We did this at the level of the density, mixing according to $\rho_{input,i} = (1-\alpha)\rho_{output,i-1} + \alpha\rho_{input,i-1}$. The mixing parameter α limits the rate of change between iterations while also acting simply as a non-physical dial to seek convergent behavior – according to our experience, calculations with $\alpha = 0.7$ often converged and with decent speed, but it was frequently necessary to scan α to achieve convergence.

- Computing a set of lowest eigenstates of some potential is a key component of the iteration. The popular Imaginary Time Propagation (ITP) method [80] is ill-suited to this for a number of reasons. Firstly, it is relatively slow, especially when computing eigenstates above the ground state. Similarly, the accuracy falls off as higher eigenstates require manual orthogonalization. Replacing ITP with the Arnoldi method [42] reduced the iteration time by orders of magnitude, allowing for the generation of DFT potentials for atoms as large as xenon. (Note: Arnoldi has similar benefits for generating initial TDSE states.)

- Whether using a DFT potential directly or fitting to an analytic form, it is important that the short range behavior (generally a Coulomb singularity, with a constant offset as seen in Figs. 2.1 and 2.2) is accurately captured. We made use of (constant) grids much finer than practical for time-dependent calculations and visually checked that $V_{xc,\sigma}(r \to 0)$ approached a constant.

2.1.3 Analytic fitting

One can proceed by using the DFT potential numerically; it is however instructive and useful to provide an analytical form of the SAE potential as:

$$V_{SAE}(r) = V_{long} + V_{short} + V_{shell}, \tag{2.10}$$

where V_{long} is the long-range Coulomb term:

$$V_{long}(r) = -\frac{C_0}{r}, \tag{2.11}$$

and V_{short} is a screened Coulomb (or "Yukawa") potential

$$V_{short}(r) = -\frac{Z_c e^{-cr}}{r}\,. \tag{2.12}$$

In test calculations we left C_0 and Z_c as free parameters in the fitting procedure. The results, shown in Table 2.1, are close to the expected values of $C_0 = Z - (N_e - 1)$, where Z is the charge of the nucleus and N_e the number of electrons in the atom or ion, and $Z_c = Z - C_0$ accounts for the

Species	C_0	Z_c	$C_0 + Z_c$
He	0.999441	1.000562	2.000002
Ne	1.066567	8.933208	9.999777
Ar	0.985250	17.014712	17.999962

Table 2.1: Fitting results for charge parameters C_0 and Z_c in SAE potentials for rare gas atoms helium, neon, and argon.

remainder of the charge. For this reason we did not vary these parameters in the remainder of our studies.

V_{shell} captures the effective SAE potential at intermediate distances with one exponential term for each of the n orbital shells:

$$V_{shell}(r) = -\sum_{i=1}^{n} a_i e^{-b_i r} \,. \tag{2.13}$$

This is motivated by the comparison of electron density and exchange correlation potential based on DFT calculations (see Figs. 2.1 and 2.2) where we identify one smooth region per shell. We have applied the above potential form to both atoms and ions up to argon. For a given species the same potential is found for both valence and inner orbitals. We note that for larger atoms, the present approach based on an orbital shell picture may need to be modified, since in such atoms subshell densities are more strongly overlapping (see Sec. 2.2.4).

The effective single-active-electron potential V_{SAE}:

$$V_{SAE}(r) = -\frac{C_0}{r} - \frac{Z_c e^{-cr}}{r} - \sum_{i=1}^{n} a_i e^{-b_i r} \tag{2.14}$$

depends on n linear parameters (a_i) and $n+1$ nonlinear parameters (b_i, c). We fit $V_{SAE}(r)$ to $V_{eff,\uparrow}(r)$ using the Levenberg-Marquardt (LM) least-squares curve fitting algorithm [81, 82] implemented in the LMFIT library [83]. The LM algorithm involves methods to avoid local minima, resulting in nonlocal fitting based on initial parameter guesses. As an extra check, the parameters b_i in the exponentials have been scanned across a range of initial guesses, selecting as final fit the one with lowest chi-squared value. In Table 2.2 we show the results for the parameters of our fits for a number of atomic and ionic species. The relative error between the fit and the actual DFT

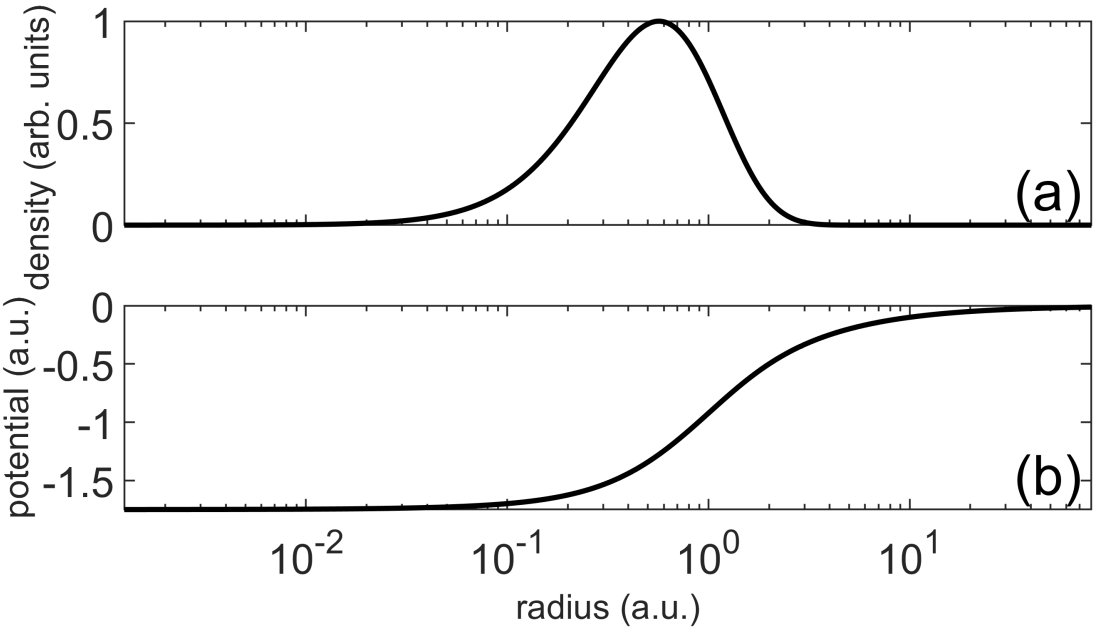

Figure 2.1: Results of DFT calculations for (a) electron density and (b) exchange correlation potential of the helium atom (Taken from [1]).

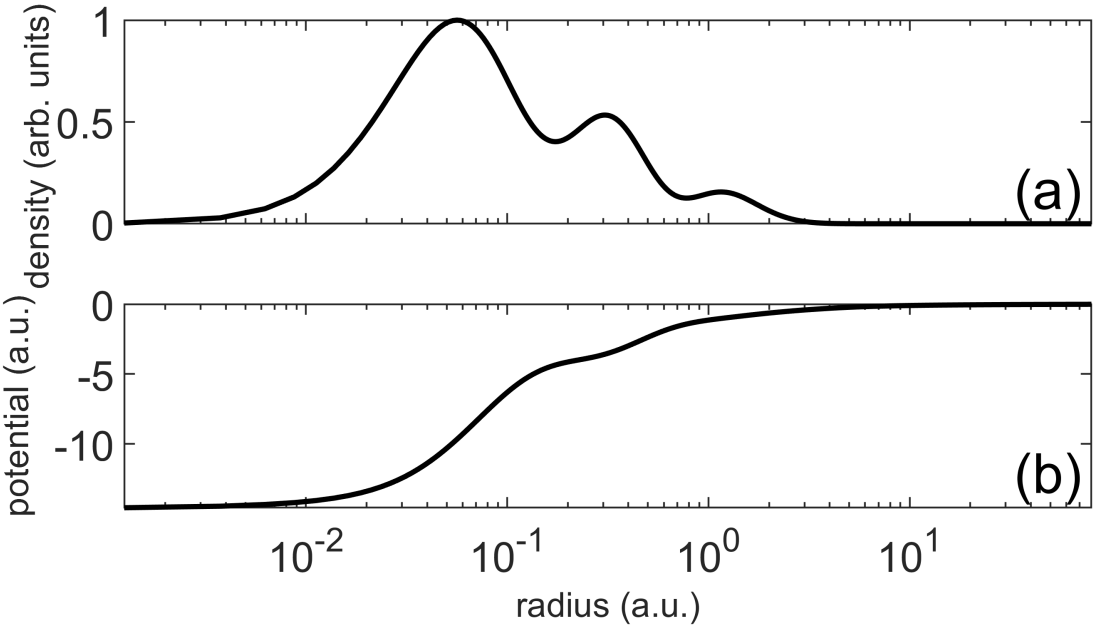

Figure 2.2: Same as Fig. 2.1 but for the argon atom (Taken from [1]).

	C_0	Z_c	c	a_1	a_2	a_3	a_4	a_5	b_1	b_2	b_3	b_4	b_5
He	1	1	2.0329	0.3953					6.1805				
Li	1	2	15.9594	9.1124	19.3145				3.6040	11.3082			
Be	1	3	2.0481	0.5294	0.3219				0.8475	37.5567			
Ne	1	9	0.8870	-9.9286	-5.9950				1.3746	3.7963			
Na	1	10	1.4927	-11.3552	-2.0302	1.6028			2.5597	10.1466	47.9542		
Mg	1	11	1.4248	-14.5892	-1.9433	1.8141			2.7001	12.3150	51.7100		
Ar	1	17	0.8103	-15.9583	-27.7467	2.1768			1.2305	4.3946	86.7179		
Ar^+	2	16	0.8698	-16.0391	-26.9860	2.1780			1.3146	4.4514	88.3315		
Ar^{2+}	3	15	0.8792	-16.4007	-26.6805	2.1681			1.3486	4.4656	90.3068		
Ar^{3+}	4	14	0.9445	-16.4800	-25.8243	2.1550			1.4521	4.5171	94.5151		
Ar^{4+}	5	13	0.8529	-17.4441	-26.0893	2.1135			1.4141	4.4613	101.5018		
Ar^{5+}	6	12	0.8929	-17.5407	-25.4398	2.0818			1.5024	4.4823	108.4695		
Li^+	2	1	3.3926	0.7669					8.3981				
Li^-	0	3	1.9849	0.3089	1.8401				0.3910	1.4335			
C	1	5	1.2052	-4.4396	0.5516				2.3838	48.6696			
N	1	6	1.3720	-5.2033	0.6921				2.7581	50.9204			
O	1	7	1.6000	-5.4268	0.7737				3.1481	60.7533			
F	1	8	1.7868	-5.9589	0.9084				3.4888	63.8907			
Ne^+	2	8	2.1416	-6.1507	1.0293				3.8371	69.9272			
Na^+	2	9	1.0754	-11.6217	-5.8563				1.6453	4.1576			
Cl^-	0	17	0.7375	-14.1508	-26.3671	1.9457			1.1359	4.0661	96.3853		
Ar^{6+}	7	11	16.0036	23.4319	98.1002	3.7337			4.1702	11.2679	62.3281		
K+	2	17	0.8826	-17.8493	-29.0486	2.4104			1.3365	4.7361	77.5565		
Ca	1	19	8.9221	7.4822	56.3383	39.6268	2.0380		1.2798	3.9896	8.9347	144.0899	
Kr	1	35	0.8356	-30.9586	-65.9241	-102.2050	72.7813		1.2065	3.3382	18.6001	23.9322	
Rb	1	36	1.0860	-36.3604	-58.1493	-122.5379	94.5717	0*	1.6439	3.8530	20.2399	24.7360	0*
Sr	1	37	1.1039	-39.7948	-59.0982	-97.8013	69.8723	0*	1.7337	4.0363	20.4979	26.7700	0*
Cd	1	47	0.7202	0.0776	-32.4798	-61.0621	-95.5870	7.9444	0*	1.0178	2.6748	10.7140	148.2401
Xe	1	53	0.8608	0.1039	-44.7989	-67.7122	-104.9326	9.8085	0*	1.2148	3.4041	12.4774	133.1390

Table 2.2: Parameters for V_{SAE} (Eq. (2.14)) obtained in analytical fits of single-active-electron potentials for various atoms and ions. (The upper part of this Table also appears in [1].) (*) For Rb, Sr, Cd, and Xe, see Sec. 2.2.4.

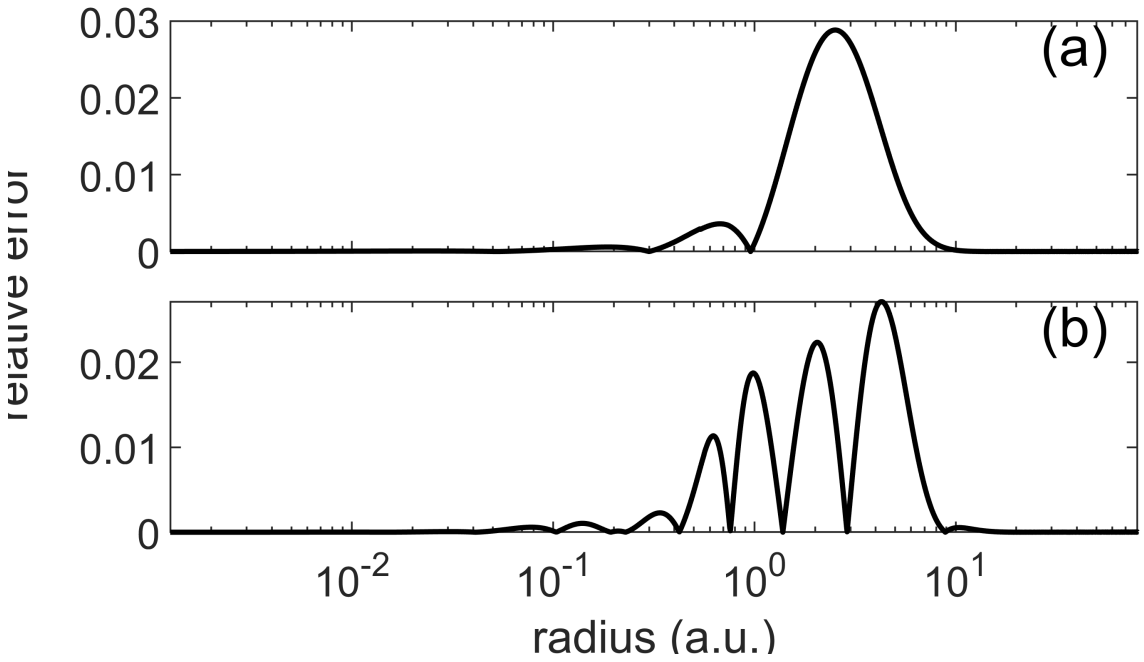

Figure 2.3: Relative error between results of the analytical fit and DFT calculations for the single-active-electron potentials for (a) helium and (b) argon (Taken from [1]).

Species	Experiment	DFT	SAE
He	0.9037	0.9453	0.944
Li	0.1981	0.1970	0.200
Be	0.3425	0.3262	0.326
Ne	0.7927	0.8353	0.834
Na	0.1888	0.2151	0.228
Mg	0.2811	0.2979	0.302
Ar	0.5792	0.6003	0.607
Ar^{+}	1.0154	1.0715	1.078
Ar^{2+}	1.4972	1.5850	1.593
Ar^{3+}	2.1980	2.1589	2.166
Ar^{4+}	2.7570	2.7835	2.791
Ar^{5+}	3.3446	3.4419	3.446

Table 2.3: Comparison of first ionization energies: Experimental data [2], DFT calculations, and analytical potential fit (SAE) (Taken from [1]).

results for $V_{eff,\uparrow}$ is presented in Fig. 2.3 for helium and argon.

2.1.4 Ionization and excitation energies

We have obtained energies for the ground state and (singly) excited states of the atoms and ions for the analytical SAE potential fits using the Implicitly Restarted Arnoldi Method [43]. For the analytical SAE potentials we have performed calculations on the same 1D spherical grid as for the DFT calculations, with $dr = 0.0025$ a.u. and $L = 80$ a.u..

In Table 2.3 we compare the ground state energies for the atoms and ions studied, obtained in the DFT calculations and with the analytical SAE potential fits, with the experimental data from the NIST Atomic Spectra Database [2]. The SAE potential results reproduce the DFT results remarkably well, showing the success of the fitting procedure. The same conclusion holds for the ionization energies of inner orbitals, as the example for neon atom in Table 2.4 shows. Further improvement concerning the agreement between the theoretical results and experimental data requires more advanced DFT calculations (investigations suggest the next step up the functional ladder – the Generalized Gradient Approximation – is *not* sufficient to noticeably improve agreement). In Tables 2.5 and 2.6 we present a comparison between experimental data [2] and the predictions

State	Experiment	DFT	SAE
1s	35.1590	30.8598	30.9051
2s	1.8134	1.6723	1.6770

Table 2.4: Same as Table 2.3 but for ionization energies of inner orbitals in neon (Taken from [1]).

State	Experiment	SAE
2s	-0.14595	-0.15969
2p	-0.12382	-0.12847
3s	-0.06126	-0.064999
3p	-0.05514	-0.056679
3d	-0.05561	-0.055581

Table 2.5: Comparison of experimental data [2] and predictions using the analytical potential fit (SAE) for ionization energies of excited states in helium (Taken from [1]).

State	Experiment	SAE
4s	-0.14834	-0.17196
4p	-0.08937	-0.10843
3d	-0.05606	-0.07170
5s	-0.05581	-0.06463

Table 2.6: Same as Table 2.5 but for $3p^5(^2P^\circ_{1/2})$X argon excited states (Taken from [1]).

obtained using the SAE potentials for some singly excited state energies of the helium and argon atoms, which shows a reasonable agreement.

2.2 HHG with SAE potentials

2.2.1 SAE-TDSE and TDDFT methods

To obtain HHG spectra in the SAE-TDSE calculations, we have propagated the wavefunction using the static potential $V_{SAE}(\mathbf{r})$ and the time-dependent laser interaction potential described in length gauge as:

$$V_I(t) = \mathbf{r} \cdot \mathbf{E}(t), \tag{2.15}$$

where $\mathbf{E}$ is the electric field of the laser. In the present calculations, the initial state was set as the ground state of the helium SAE potential. We have discretized the wavefunction and (radial) potential on a cylindrical 2D grid with $d\rho = dz = 0.03$ a.u, and grid sizes up to $\rho_{max} = 50$ a.u. and $z_{max} = \pm 100$ a.u.. We have applied the 2nd order Crank-Nicolson method and the split-operator approximation to propagate the wavefunction starting from the initial state.

To study the accuracy of the SAE potentials, we compare results of SAE-TDSE calculations with those of TDDFT calculations (performed by Tennesse Joyce). For the latter, the wavefunction has been propagated using the Kohn-Sham orbitals obtained by solving the time-dependent Kohn-Sham equations

$$\left[-\frac{1}{2}\nabla^2 + V_{eff,\sigma}(\mathbf{r},t)\right]\psi^{KS}_{i,\sigma}(\mathbf{r},t) = i\frac{\partial}{\partial t}\psi^{KS}_{i,\sigma}(\mathbf{r},t), \tag{2.16}$$

with

$$V_{eff,\sigma}(\mathbf{r},t) = V_{ext}(\mathbf{r},t) + V_H(\mathbf{r},t) + V_{xc,\sigma}(\mathbf{r},t)\,, \tag{2.17}$$

where

$$V_{ext}(\mathbf{r},t) = -\frac{Z}{r} + V_I(t) \tag{2.18}$$

and the Hartree and exchange correlation terms depend now on the time-dependent density $\rho(\mathbf{r},t)$. The TDDFT calculations have been performed using the Octopus code [75–77] on a Cartesian 3D

grid with spacing $dx = 0.3$ a.u. in a cylindrical box of length at least 70 a.u. in the z-direction, and diameter at least 40 a.u. in the xy-plane. An additional 20 a.u. in every direction outside the box was added for the complex absorbing potential. Note that use of 4th-order finite difference allows for coarser dx here.

We have taken the laser to be linearly polarized in the z-direction, with a $\sin^2$ pulse envelope, variable central frequency ω_0, and full-width duration $T = 8\pi/\omega_0$ corresponding to four optical cycles. That is,

$$\mathbf{E}(t) = E_0 \sin^2\left(\frac{\pi t}{T}\right) \sin(\omega_0 t)\hat{\mathbf{z}} \tag{2.19}$$

for $0 \leq t \leq T$. We have evaluated the dipole acceleration $\mathbf{a}(t)$ using the Ehrenfest theorem

$$\mathbf{a}(t) = \langle \nabla V \rangle + \mathbf{E}(t). \tag{2.20}$$

where $V = V_{SAE}$ (for SAE-TDSE) and $V = -Z/r$ (for TDDFT). In the case of TDDFT, the dipole accelerations from all orbitals are added together, and other interaction terms cancel. The harmonic spectrum $P(\omega)$ is then obtained by taking the windowed Fourier transform of the dipole acceleration,

$$P(\omega) = \left| \int_0^T \mathbf{a}(t) W(t/T) e^{-i\omega t} dt \right|^2, \tag{2.21}$$

where $W(x) = 0.42 - 0.5\cos(2\pi x) + 0.08\cos(4\pi x)$ is the Blackman window [55].

2.2.2 Comparison of SAE-TDSE and TDDFT results

The good agreement between analytical fit and DFT results provides the grounds to proceed with the quantitative comparison between TDDFT and SAE-TDSE calculations for HHG. In Fig. 2.4, we compare results of SAE-TDSE and TDDFT calculations for the HHG spectrum driven by a 4-cycle laser pulse with peak intensity of $I_{peak} = 10^{15}$ W/cm^2 at central wavelengths of (a) $\lambda = 267$ nm ($\omega_{267} = 4.65$ eV), (b) $\lambda = 400$ nm ($\omega_{400} = 3.10$ eV), and (c) $\lambda = 600$ nm ($\omega_{600} = 2.07$ eV). For each comparison, we have matched the two results at one point, namely the energy of the driving laser pulse. We used the helium atom as a target, this being the simplest atomic system with electron correlation effects. For laser wavelengths in the ultraviolet and optical regime, we

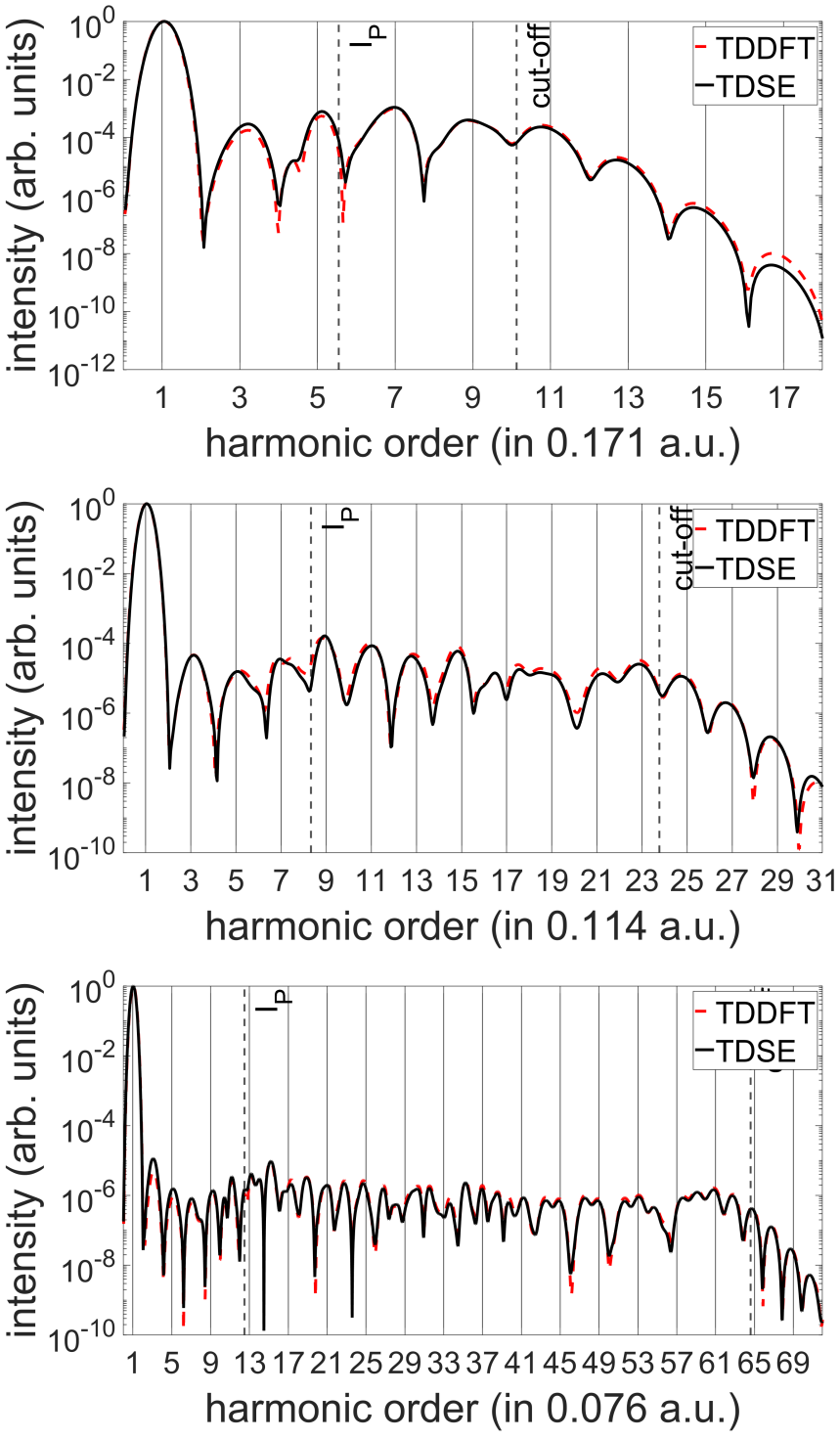

Figure 2.4: Comparison of TDDFT results (dashed red line) and SAE-TDSE (solid black line) results for HHG spectra generated in the interaction of a helium atom with a 4-cycle laser pulse at peak intensity of 10^{15} W/cm^2 and central wavelengths of (a) 267 nm, (b) 400 nm, and (c) 600 nm. Vertical dashed lines denote the ionization potential I_P and expected HHG cut-off energy for each calculation. (Taken from [1].)

expect that the correlation effects on the nonlinear and nonperturbative dynamics may be small. Thus, the single-active-electron approximation should be applicable and, hence, constitute a test bed for the comparison.

At the shortest wavelength (panel (a)), it requires six photons to exceed the field-free ionization potential $I_p = 25.7$ eV (cf. Table 2.3), while the energy of seven photons is needed to exceed the field-shifted ionization threshold of $I_p + U_p = 32.3$ eV where $U_p = 9.3 \times 10^{-5}\ I_{peak}$ [PW/cm^2] λ^2 [nm] is the ponderomotive energy of a free electron in a laser field at the peak intensity. Furthermore, the HHG cut-off energy of $3.17U_p + I_p = 46.7$ eV $\approx 10\,\omega_{267}$. The results of the TDDFT and SAE-TDSE calculations are in excellent agreement over the whole spectrum, up to the expected cut-off and even beyond. The position of the maxima and minima, the form of the odd high-order harmonic lines, as well as the cut-off in the spectrum, are nearly identical in the results of both independent calculations. We note small deviations between the results in the region of the 3rd and 5th harmonics, which either may be related to differences in the excited state spectra for the two calculations or may indicate minor electron correlation effects. However, overall the comparison shows that electron correlation effects appear to be negligible for this nonlinear process in helium at a UV driver laser wavelength.

Similarly good agreement is found at the longer central wavelengths of 400 nm (b) and 600 nm (c); the other laser parameters are held the same as for the calculations at 267 nm. We note that while the 267 nm calculation was in the so-called multiphoton regime, the Keldysh parameter $\gamma = 0.62$ [50] indicates that the process at 600 nm occurs in the tunneling interaction regime. Due to the longer wavelength, the ponderomotive energies are significantly larger. This results in larger field-shifted ionization potentials and corresponding HHG cutoffs of 73.1 eV (b) and 132.2 eV (c), corresponding to the 24th and 64th harmonic of the driving frequencies, respectively. While the differences between the results of the two independent calculations are slighter larger than at the UV driver wavelength, they remain overall clearly less than a factor of two. The largest deviations are again found in the energy region near the ionization threshold. We note that at higher energies, even subtle features are in excellent agreement for the two calculations.

The agreement between the results demonstrates the accuracy and applicability of the single-atom potentials and shows the capability of TDDFT to provide reliable results for nonperturbative strong-field processes in this parameter regime. The deviations in the ionization threshold region may be attributed to a minor role of electron correlation and/or excited states during the process. We note that studies reporting a comparison between TDDFT and SAE-TDSE results for non-perturbative strong-field processes are rare [60, 61] and we are not aware of another study in the strong-field and tunneling regime reporting agreement in parameter regimes of small correlation effects. Typically, differences between results have been interpreted as the effect of correlation effects [60], even in parameter regimes in which we find excellent agreement between SAE-TDSE and TDDFT results. This demonstrates the importance of the method in constructing SAE potentials used in the present study and the general benchmark tests performed. It also clarifies the sometimes expressed misconception that TDDFT calculation cannot provide accurate results in the highly nonlinear multiphoton and tunneling regimes.

2.2.2.1 Subtleties of convergence

Informal discussions suggest that other groups have sought to compare TDSE and TDDFT simulations of HHG and generally found poor agreement. We therefore think it is valuable to address the process behind our final results, including various obstacles.

First off, TDDFT calculations are generally more expensive than TDSE calculations. Obviously, the extra computations required to periodically update the DFT potential contribute; but additionally, TDDFT codes usually have different goals than TDSE codes and are optimized correspondingly. In the case of linear polarization and atomic targets, most modern TDSE codes use a spherical harmonic basis (as in our current TDSE code) or at least exploit azimuthal symmetry (as the code used for the comparisons in this Chapter) for speed. Since most targets in TDDFT codes do not have spherical symmetry, the option is rarely included. Thus, even single-electron calculations (e.g., hydrogen) will often be much more expensive when run with a TDDFT library, even though the actual physics is identical.

As a result of this expense – and the differing needs of common calculations – TDDFT simulations are often run with larger grid spacing and smaller box size than is common in TDSE simulations. Consequently, HHG convergence tests may (and, in our case, did) begin with the TDDFT parameters far from being converged. This led to more complicated interactions between simulation parameters than is typical for almost-converged TDSE cases. As one example, increasing the box size along the laser polarization led to worse agreement! After further investigation, we came to the conclusion that the issue was related to the relatively narrow box perpendicular to polarization – electron wavepackets were artificially reflecting off the boundaries, leading to unexpected interference behavior as a function of box length. After increasing the box width sufficiently, changes in the box length displayed a more normal convergence behavior.

On a different note, HHG depends significantly on the ionization potential. When this does not agree between SAE-TDSE and TDDFT simulations, the spectra will differ. This suggests first the utility of basing the two simulations on a shared potential formulation (e.g., a particular DFT functional, in our case with one being static and fit to an analytic form). As above, it is also important that both codes be converged for the ground state energy (here, grid spacing is most important). Some of these notes may seem obvious, but when the result is a month-long TDDFT calculation, there is the incentive to cut corners and assume that the simulation is sufficiently converged when it may not be.

Finally, we provide a few notes relevant to any comparison of HHG calculations, including those using different TDSE implementations. In principal, HHG can be computed equivalently via the dipole moment, the dipole velocity, or the dipole acceleration. Since the dipole moment is the simplest to compute, this approach may look most attractive. However, the equal treatment of electron density anywhere on the grid leads to errors when ionized wavepackets must be absorbed. Using the dipole acceleration (specifically via the Ehrenfest theorem, as shown above) minimizes these issues and we have generally found that method to provide better convergence behavior with respect to various numeric parameters, especially box size. The quality of the HHG spectrum using the dipole velocity falls between the other two, but we have generally found its accuracy to be

closer to calculations based on the dipole moment. Thus, we highly recommend the use of dipole acceleration, even if adding it to a library appears complicated. For a thorough investigation and discussion of more theoretical background, see [84].

Another potential issue can arise when a team is using multiple libraries since it is easy for different definitions of parameters to come into conflict. Often, the results will only differ slightly, making it feasible that the difference is intrinsic to methods rather than a result of miscommunication. A few examples:

- Is the "length of the box" defined by diameter or radius?
- How, *exactly* are the laser wavelength and frequency defined? For example, is the wavelength exactly 800.0 nm or is the frequency set to 0.0570 a.u.?
- Is the duration of the pulse measured in FWHM (Gaussian) or full width (sine-squared)? Are reported durations in fs rounded or does the pulse have a non-integer number of cycles?
- Is the laser field defined by an expression for electric field or for vector potential? The difference introduces a CEP offset and frequency shift [85], both especially relevant for short pulses. This is independent of gauge as the other field may be derived through numeric or analytic differentiation/integration.

Lastly, one needs to be careful to ensure consistency of HHG calculations using the dipole acceleration. Perhaps the simplest method is to pass the raw acceleration data through the same plotting script. Otherwise, one needs to be aware of the following considerations:

- Is the acceleration windowed before applying the Fourier transform? If so, what window is used?
- Are the Fourier transform conventions consistent? If not, an overall factor may appear.
- Do signals have consistent time sampling and padding? This is mostly a technical issue for plotting, but important to consider when things go wrong.

2.2.3 Multiple SAE-TDSE for larger atoms

Beyond the application for benchmark-testing TDDFT calculations, the present SAE potential can of course be applied for other studies as well. Recently, the influence of inner valence shells on high harmonic generation has been studied [86–89]. The effects in the spectra are often interpreted by multielectron or intershell correlation, so accurate single-active-electron calculations can serve as a useful tool for comparison and, hence, identification of the correlation effects.

Using the potentials for neon, we have obtained high harmonic spectra from the outermost $2p$ shell ($m = 0$) and the inner $2s$ valence shell. In the calculations, we have applied a laser pulse of 4 optical cycles at 800 nm and a peak intensity of 10^{14} W/cm^2. Both spectra (cf. Fig. 2.5(a) and (b)) show the characteristic features of an HHG spectrum with plateau and cut-off. However, in both spectra there occurs a prominent peak between the 15th and 17th harmonic, at the energy corresponding to the energy difference between the $2p$ and $2s$ states in our SAE potentials for neon. The peak is an artifact of the SAE-TDSE calculations which allow for transitions between the sub-shells, although they are filled in the real multielectron atom. However, the unphysical feature is completely removed once the amplitudes for the processes driven from the two sub-shells are added and the full HHG spectrum (Fig. 2.5(c)) is obtained. This is another indication of the accuracy of the single-active-electron potentials obtained with the present method, which therefore can be applied for single-active-electron reference calculations, e.g., for the identification of multielectron correlation effects.

2.2.4 Notes on SAE for large atoms

For larger atoms, the above analytic form, Eq. (2.14), does not always capture the shape of the DFT potential well. The resulting poor quality fits are generally easy to spot from the output of the fitting function. A few red flags are:

- The error is much higher than for similar atoms.
- Parameter values fall very close to the limits of the parameter range.

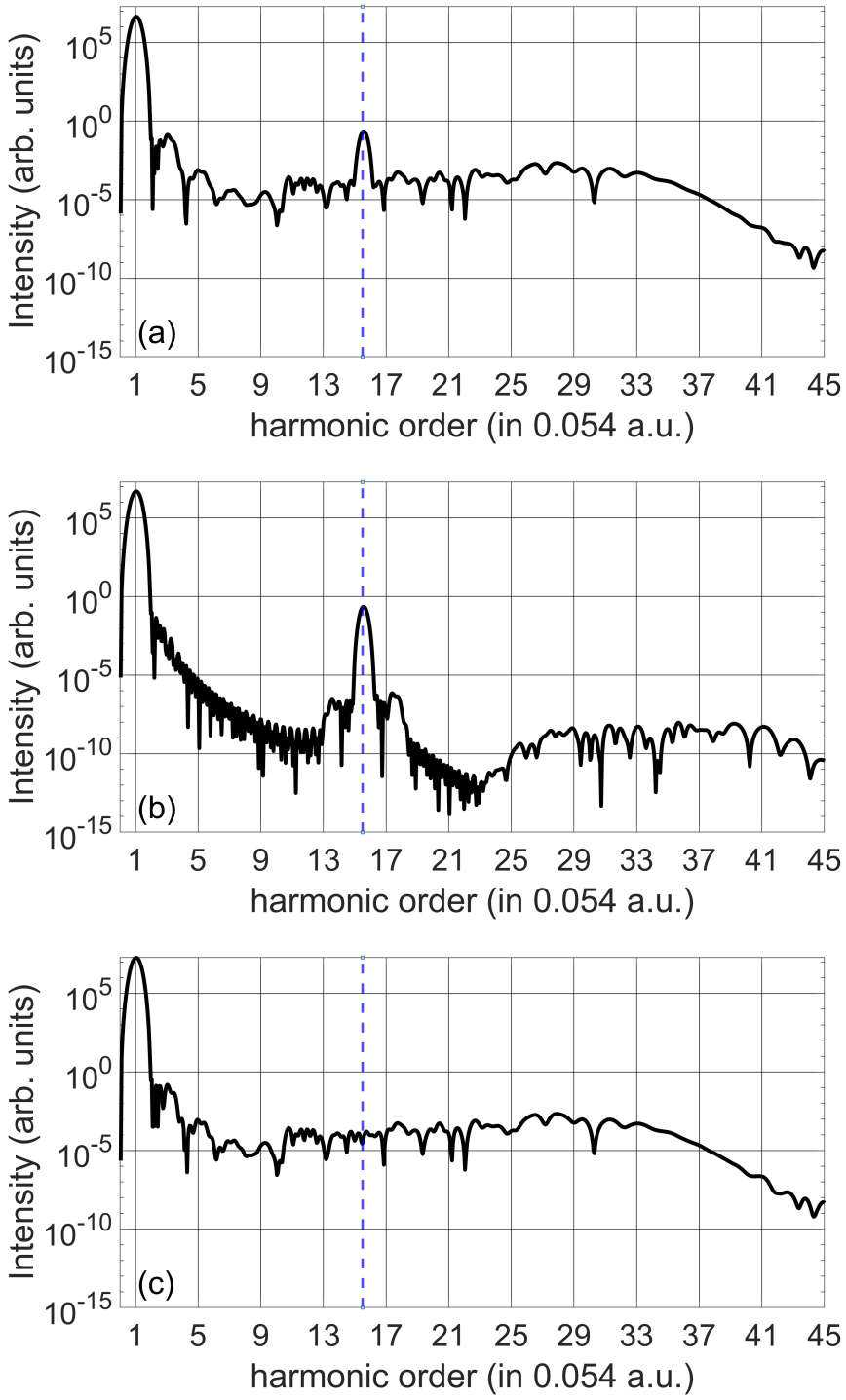

Figure 2.5: Results of SAE calculations for high-order harmonic spectra generated from (a) $2p$-shell and (b) $2s$-shell in neon by a 4-cycle laser pulse at peak intensity of 10^{14} W/cm^2 and wavelength of 800 nm. The vertical dashed line indicates the $2s - 2p$ transition energy at which an artificial peak occurs in the spectra from the two sub-shells, which is removed once the the amplitudes for both processes are added (Panel (c)). (Taken from [1]).

- Parameter values for different terms are close together, or nearly opposite. For example, we have encountered cases where $b_1 \approx b_2$ and $a_1 \approx -a_2$.
- Correlations between terms are reported as 1.0.
- The uncertainty in fitted parameter values is high (esp. when $> 100\%$).
- Other warnings from the program, such as "Reached maximum iterations without achieving requested tolerance."

Often, these issues can be resolved by modifying the fitting options, such as increasing the allowed parameter ranges, the number of iterations, or the initial parameter guesses. But, when problems persist, it is useful to reconsider the analytic form.

For our SAE potentials, we have identified a few species where the predicted number of exponential terms overfits the data. Specifically, neutral Rubidium and Strontium (with $5s$ valence shell) produce poor fits with five exponential terms. Aside from a high fit error, the corresponding fits display nearly every red flag mentioned above. However, when fit with four exponential terms, the issues disappear while the fit error remains reasonable. These are the fits reported in Table 2.2.

For the two largest atoms considered, cadmium and xenon, we encountered different behavior. Namely, one of the "exponential" terms in fact fit to a constant (i.e., $b_1 = 0.00$ with nonzero a_1). Interestingly, no other red flags appeared. Reducing the number of terms to four or three decreased the fit accuracy but did not eliminate the constant terms. Physically, constant potential terms are not reasonable but it is unclear whether the issue is related to the DFT potential or that our analytic form is missing some characteristic of these large atoms.

2.2.5 Effects of manual SAE parameter modification

Since many previous SAE potentials have included manual modification of parameters to match experimental ionization potentials, we briefly explore the effects of various modifications of V_{SAE} on a helium HHG spectrum. For this particular investigation, we included only the exchange

terms in Eqs. (2.3-2.4):

$$v_{x,i,\sigma}^{LDA-SIC}(\mathbf{r}) = \mu_{x,\sigma}^{LDA}(\rho_\uparrow(\mathbf{r}), \rho_\downarrow(\mathbf{r})) - \mu_{x,\sigma}^{LDA}(\rho_i(\mathbf{r}), 0) - \int \frac{\rho_{i,\sigma}(\mathbf{r}')}{|\mathbf{r} - \mathbf{r}'|} d\mathbf{r}' \,. \tag{2.22}$$

The resulting I_P values are lower than those for the v_{xc} functional by up to about 5%, and fitting parameters also vary. However, we do not expect this to affect the manner in which HHG *changes* as a function of parameter values.

To begin, we have investigated the effects of removing individual terms from V_{SAE} and modifying other parameters to keep I_P constant. We have performed the matching on the actual 2D cylindrical grid used for HHG calculations, with radius $R = 40$ a.u., length $L = 120$ a.u., and grid spacing $dx = 0.1$ a.u.. Due to limitations of convergence in this older code, $I_P = 0.9477$ differs from the converged value for the eigenstate of the potential, -0.918 (consistent for numeric V_{eff} and fitted V_{SAE}, on the finer grid described in Sec. 2.1.4). We have determined the parameter values necessary to match I_P – to at least three decimal places – using a simple secant search. In Table 2.7, we show six such parameter sets with parameters and eigenstate energies on the cylindrical grid. The first three potentials share nearly identical energies for all states, while the remaining three differ greatly (up to 140%), or lack bound excited states entirely.

In Fig. 2.6, we show HHG with a driving laser of 10^{15} W/cm^2, 4 o.c., and 800 nm for each of these potentials. The results are indistinguishable for the first three, so we merge the legend entries. After the 80th harmonic, the spectra show decent agreement – despite significant alterations to: the short- and long-range behavior of the potentials, and the excited state spectra. In this highly non-perturbative ($\frac{U_P}{\omega} = 38$) and tunneling-dominated ($\gamma = 0.47$) regime, the value of the ionization potential appears to be the sole target feature influencing the shape of higher harmonics. However, radiation near and below the ionization threshold is strongly impacted by the atomic potential (and, as discussed in Ch. 3, excited state spectrum). This is especially clear for the short-range potential, YE-a, which lacks excited states. In this case below-threshold radiation is strongly suppressed relative to the plateau harmonics, as well as compared to below-threshold radiation of other potentials.

	CYE	**CE-a**	**CY-c**	**CE-b**	**YE-a**	**C-C_0**
V_{SAE}	$-\frac{1}{r}-\frac{e^{-cr}}{r}-ae^{-br}$	$-\frac{1}{r}-a'e^{-br}$	$-\frac{1}{r}-\frac{e^{-c'r}}{r}$	$-\frac{1}{r}-ae^{-b'r}$	$-\frac{e^{-cr}}{r}-a'e^{-br}$	$-\frac{C_0'}{r}$
C_0	1	1	1	1	0	1.3682
Z_c	1	0	1	0	1	0
c	2.3526	2.3526	2.0640	2.3526	2.3526	2.0640
a	0.6628	7.0910	0	0.6628	16.8190	0
b	4.0762	4.0762	4.0762	0.3130	4.0762	4.0762
1s	-0.948	-0.948	-0.948	-0.948	-0.948	-0.948
2s	-0.160	-0.159	-0.160	-0.354	n/a	-0.236
2p	-0.128	-0.128	-0.128	-0.306	n/a	-0.234
3s	-0.065	-0.065	-0.065	-0.153	n/a	-0.105
3p	-0.056	-0.056	-0.057	-0.131	n/a	-0.104
3d	-0.056	-0.056	-0.056	-0.113	n/a	-0.104
4s	-0.035	-0.035	-0.035	-0.057	n/a	-0.059
4p	-0.032	-0.032	-0.032	-0.057	n/a	-0.059
4d	-0.031	-0.031	-0.031	-0.053	n/a	-0.059
4f	-0.031	-0.031	-0.031	-0.049	n/a	-0.059

Table 2.7: Modifications of helium SAE potential keeping $I_P = 0.948$. In the first row, potentials are labeled by which terms are included (Coulomb, Yukawa, Exponential) and which term is modified from the base parameters. The second row defines the form of the modified potential, with specific parameter values given in the following rows. Finally, the eigenstate energies are given through E_{4f}. The potential without a Coulomb term (**YE-a**) does not support bound states above $|1s\rangle$. We note the consistency of state energies (and, as will be seen, HHG) for the first three potentials.

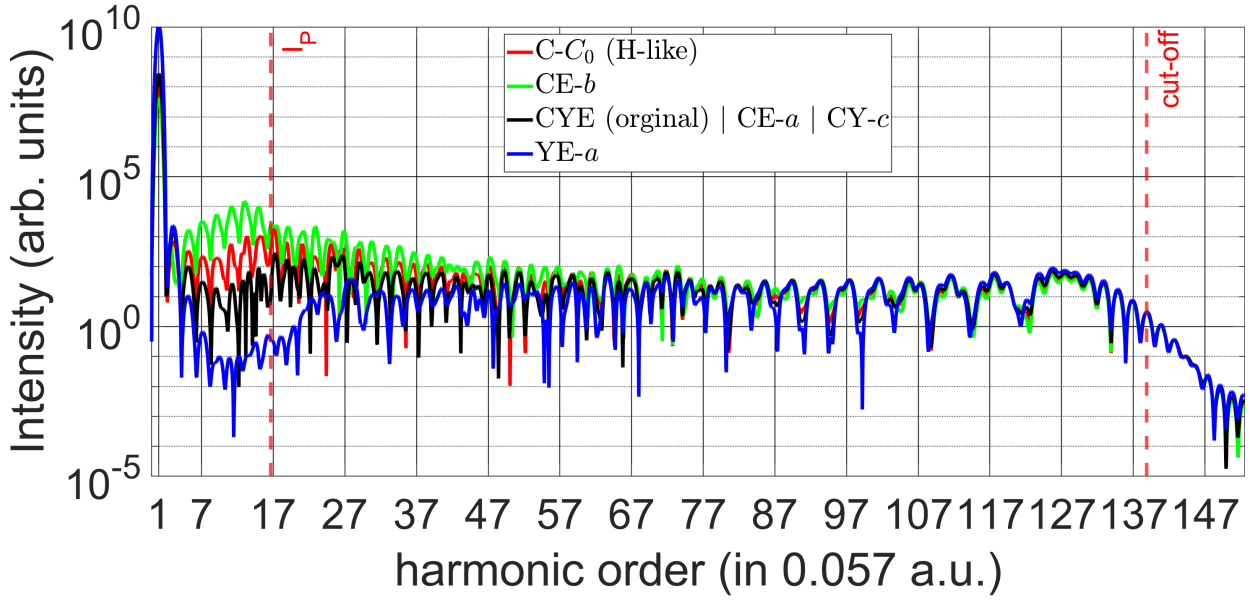

Figure 2.6: Results of SAE calculations for high-order harmonic spectra generated in the interaction of a helium atom with a 4-cycle laser pulse at peak intensity of 10^{15} W/cm^2 and central wavelength of 800 nm. Each line represents results for an SAE potential defined in Table 2.7. The black line corresponds to the original potential as well as two other potentials with indistinguishable spectra. Vertical dashed lines denote the shared ionization potential ($I_P = 0.948$ a.u.) and HHG cut-off (8.0 a.u.). Results have been normalized to the intensity at the cut-off.

Additionally, we have performed calculations in which we have varied the SAE potential to match the experimental ionization potential. These HHG spectra (not shown) differed from those in Fig. 2.6, but the areas of agreement between different potentials and qualitative differences remained consistent. We note that the modified full potential produced indistinguishable state energies and HHG regardless of whether the a, b, or c parameter was chosen for modification.

2.3 Molecular SAE[2]

Here, we extend the SAE formulation to the oxygen molecule for investigation of nonlinear polarization and ionization. In particular, we collaborated with the group of M. Kolesik (University of Arizona) in extending their previous applications of the Metastable Electronic State Approach (MESA) [90] to O_2. In a previous paper, their group investigated molecular nitrogen using multi-electron calculations [91], but attempts to use a simplistic model potential for O_2 did not achieve the expected level of agreement with experimental data. Our construction of the molecular SAE potential follows primarily the same procedure as that for atomic SAE potentials above.

The effective Kohn-Sham potential $V_{eff,\sigma}(\mathbf{r}) = V_{ext}(\mathbf{r}) + V_H(\mathbf{r}) + V_{xc,\sigma}(\mathbf{r})$ is here calculated using the Octopus code (our separate DFT implementation is limited to species with radial symmetry) on a cylindrical 2D (ρ, z) grid with spacing 0.05 a.u. and length of 10 a.u. in both dimensions. The $V_H + V_{xc,\sigma}$ terms have the same form as in Sec. 2.1.1 above, now with two Coulomb terms for the interaction with the nuclei, so

$$V_{ext}(\mathbf{r}) = -\frac{8}{|\mathbf{r} - \mathbf{r}_1|} - \frac{8}{|\mathbf{r} - \mathbf{r}_2|}. \tag{2.23}$$

As above, all core electrons are included in the calculations (i.e., no pseudopotential is used). Here, the valence electrons are spin-polarized.

For the analytic form, we use a pair of radially-symmetric functions centered at each nucleus plus a cylindrically-symmetric term along the molecular axis. This approximately captures the details of the potential from the core and valence electrons while retaining a simple form. Thus,

[2] The results of this Section are also presented in [5]

for a molecule aligned with the o-axis, we fit an analytic potential of the form

$$V(o,p,q) = f\left(\sqrt{(o-L/2)^2+p^2+q^2}\right) + f\left(\sqrt{(o+L/2)^2+p^2+q^2}\right) + g\left(o,\sqrt{p^2+q^2}\right), \quad (2.24)$$

where $L = 2.3$ a.u. is the bond length,

$$f(r) = -\frac{C_0}{2r} - \frac{Z_c e^{-r/c}}{2r} + a_1 e^{-r/b_1} \quad (2.25)$$

with the net charge seen by the active electron, $C_0 = Z - (N_e - 1) = 1$ split evenly across the two nuclei, as well as the shielded charge, $Z_c = Z - C_0 = 15$, where Z (N_e) is the total number of protons (electrons) in the molecule, and

$$g(o,\rho) = de^{-(o/c_o)^2-(\rho/c_\rho)^2} \quad (2.26)$$

with the parameters obtained from a least-squares fit, $c = 1.326$, $a_1 = 10.804$, $b_1 = 0.466$, $c_o = 3.248$, $c_\rho = 2.778$, and $d = 1.643$ (all in Hartree atomic units).

The radial functions $f(r)$ are a truncated form of the above atomic SAE potentials, dropping the second ($n = 2$) exponential term for efficient fitting. Note that the parameter definitions are different from above (for one, nonlinear parameters are here given as distances). The additional cylindrical Gaussian term $g(x,\rho)$ with three fitting parameters coarsely captures the effect of molecular bonding orbitals.

The numerical effective Kohn-Sham potential from the Octopus code is fitted to the analytic form (2.24) using a similar least-squares fitting procedure to that above. Fitting of the radial term is facilitated by (Fourier) transforming the 2D potential to a radial form. This improves the speed of the fit, but is not strictly necessary. The accuracy of the fit can be seen from the comparison of the analytical SAE fit with the numeric DFT potential in Fig. 2.7. Shown are cuts along (a) and perpendicular to (b) the internuclear axis, as well as the relative error as a function of the coordinates (c). Since the electron-nucleus potential V_{ext} is the same in the two forms of the potential, we have excluded it from the visualization to enhance the comparison. We further note that the ionization potential of the analytic fit ($I_p = 0.43$ a.u.) agrees well with that of the Octopus calculations ($I_P = 0.40$ a.u.).

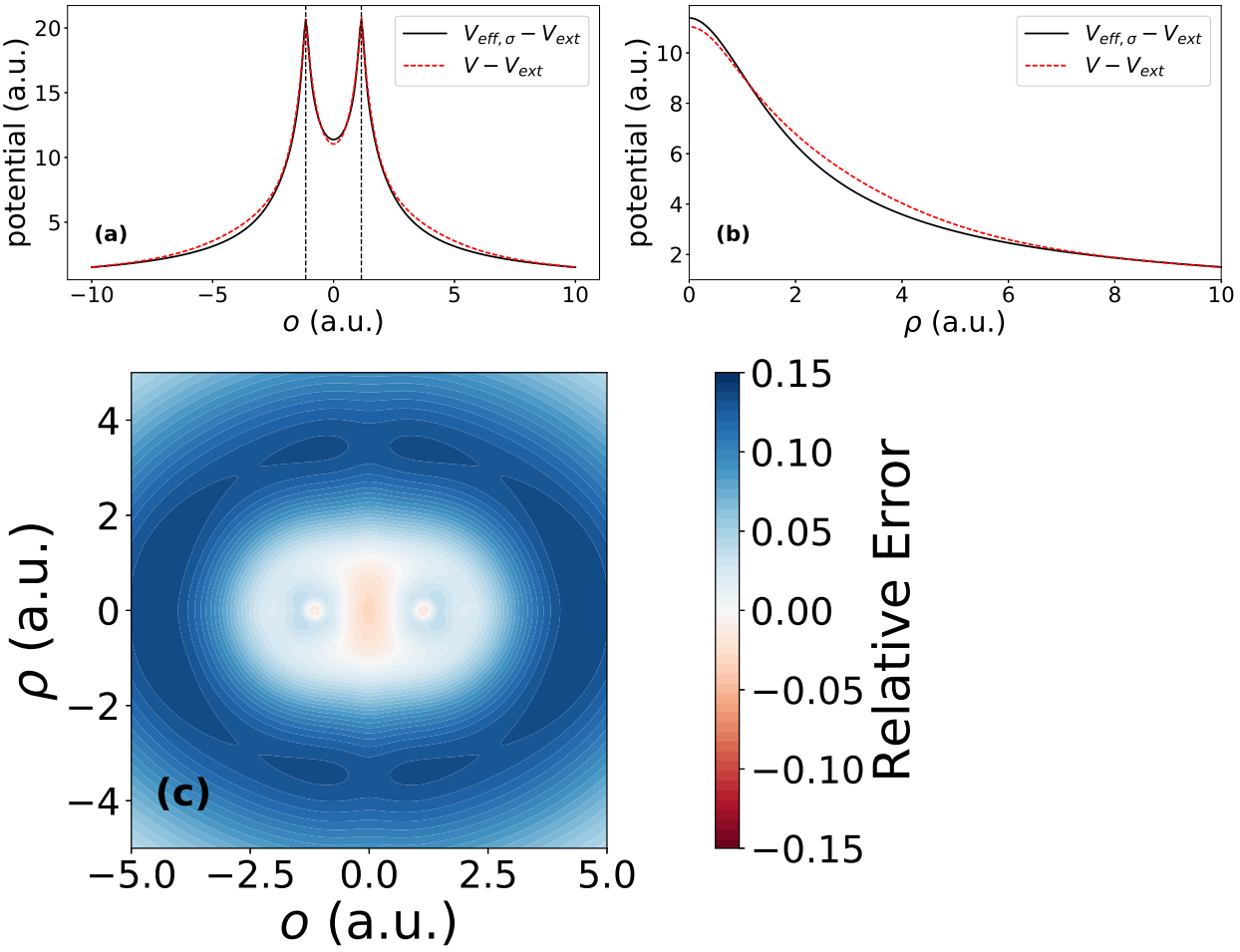

Figure 2.7: Top row: Comparison of the analytical SAE potential fit (dashed red line) and the numeric DFT potential (solid black line) (a) along the molecular axis ($\rho = 0$) and (b) for a line bisecting the molecular axis at the origin ($o = 0$). Bottom row: (c) Relative error between numeric DFT potential and analytic SAE fit (Eq. (2.24)). Note that the error, within a range of ≈ 1.5 a.u. from the nuclei, is $\leq 5\%$ (Taken from [5]).

	L	C_0	Z_c	c	c_o	c_ρ	d	a_1	b_1
H_2	1.4314	1	1	0.316	13.841	18.637	-0.162	1.205	0.497
O_2	2.3000	1	15	1.326	3.248	2.778	1.643	10.804	0.466

Table 2.8: Parameters for molecular V_{SAE} (Eq. (2.24-2.26)) obtained in analytical fits of single-active-electron potentials for various molecules.

2.3.1 Potentials for other molecules

We have also begun to construct analytic fits to other molecules – thus far, H_2 based on Octopus DFT calculations completed by Lauren Bauerle. For this and later symmetric dimer molecules, we use the same analytic form, Eq. (2.24-2.26). The fitting process is unchanged and we achieve similar results. For future work on asymmetric dimers such as CO, we suggest several modifications:

(1) Consider additional or different bridge terms g_j.

(2) Utilize separate parameters (excl. bond parameters L, d, c_o, c_ρ) for each atom.

(3) Allow charge coefficients $C_{0,i}$ and $Z_{c,i}$ to vary in the fit, while retaining a fixed sum.

2.4 Summary

To summarize, we have presented analytical forms for atomic and molecular SAE potentials, which are based on results of DFT calculations. The potential fits are shown to provide a good agreement with the DFT results for the energy of the ground state as well as with experimental data for the energies of ground and excited states, and inner shells, of different atoms and ions, without any ad hoc adjustment of parameters in the analytical forms. Using the potentials, a benchmark test between SAE-TDSE and TDDFT calculations has been performed and a remarkable agreement throughout the whole HHG spectra at ultraviolet and visible wavelengths has been achieved. Since the calculations are based on two different approaches and different numerical codes, the agreement indicates the accuracy of the SAE potentials as well as the capability of TDDFT to provide reliable

results for a nonperturbative, highly nonlinear process such as high harmonic generation in this parameter regime. Additionally, results of SAE calculations for HHG spectra from different shells in neon reveal an artificial large peak at the transition energy between the $2s$ and $2p$-states, which is removed once the amplitudes of the processes from the two sub-shells are added up. Finally, we discuss construction of SAE potentials for a usage beyond HHG, in the nonlinear polarization and ionization of O_2.

2.4.1 Usage in other work

In addition to projects with my direct involvement (above), other members of our group successfully use the generated potentials for a variety of investigations, including on EUV ionization of helium [92] and IR ionization of alkali and alkaline earth metals [93]. With the recent publication of parameters and demonstrated agreement in helium HHG, we contribute to an ongoing discourse on HHG from more complex atoms and molecules, including the first external citation [94].

Chapter 3

Resonance-Enhanced High-order Harmonic Generation

In the near-threshold region of the spectrum, off-harmonic spectral features, red-shifted with respect to the harmonics, have recently received new attention in experiment and theory [39, 95–101], since they cannot be interpreted using the standard three-step picture of high-order harmonic generation. Instead, different interpretations based on resonant excitation followed by free induction decay [39, 96, 99], resonant enhanced harmonic generation [100], as well as population of excited states through frustrated tunneling ionization followed by free induction decay [101], have been put forward.

In this Chapter, we investigate this spectral region with a particular focus on a set of radiation features we associate with enhancement by the field-shifted $9\omega \rightarrow 3p$ resonance in hydrogen atoms. In Sec. 3.1, we introduce this feature through spectral results for an illustrative case, and discussion of variations within the parameter space. Sec. 3.2 summarizes the prior work and semi-classical trajectory hypothesis of another group. We then demonstrate a method for identifying and verifying radiation associated with enhancement from a particular resonance and its associated delay(s) in Sec. 3.3 before applying these insights to several distinct features, which appear across a wider range of driving intensities (Sec. 3.4). Next, in Sec 3.5 we return to the trajectory hypothesis and demonstrate that it explains some but not all observations. In Sec. 3.6, we investigate deviations from our model by keeping our core feature (resonance time) constant through simultaneous scans across multiple parameters. In the remaining Sections, we provide a brief discussion of results in the distinct parameter regimes of: short and very long pulses (Sec. 3.7), the helium atom driven

by a 400 nm laser (Sec. 3.8.1), and hydrogen atoms driven by a mid-infrared pulse (Sec. 3.8.2). Finally, we provide a summary and discussion of future prospects in Sec. 3.9.

3.1 Spectral features

In Fig. 3.1, we show an example of a spectrum with harmonic peaks at $\omega, 3\omega, 5\omega, 7\omega$, and 11ω, in which the radiation near the 9th harmonic is strongly suppressed relative to both nearby frequencies and neighboring harmonics. Additionally, there is an extra peak below the 7th harmonic (near the $1s \rightarrow 2p$ transition energy of 6.58ω) with similar intensity. These radiation features occur during the pulse, and do not have the narrow width characteristic of field-free decay from excited states (cf. Fig. 1.7).

In order to gain further insights we have performed a series of calculations, for different peak intensities, in which the wavefunction has been propagated during the pulse and over a period of four times the pulse duration after the pulse. The results are shown in Fig. 3.2 as a function of peak intensity. It is seen that the spectral structure below the 9th harmonic, observed in the results shown above, is present over a certain range of intensities at about 3.8×10^{13} W/cm^2. However, the structure can be clearly distinguished from the free induction decay lines arising due to population of excited states after the pulse ends – in Fig. 3.2(b) denoted and marked by red dashed lines.

In Fig. 3.3, results from similar sets of calculations varying driving laser wavelength (top panel) and pulse duration (bottom panel) reinforce this conclusion, while highlighting trends in the energy of the off-harmonic peaks. As either parameter is decreased, the side peaks clearly separate further from 9ω. For shorter wavelengths (than about 790 nm), the 9ω radiation is dominant, but the sidebands are still present. For the shortest pulses (less than about 7 o.c.), other structures appear more intensely than both on-harmonic radiation and the feature present at longer durations.

Comparing spectral intensity and phase as a function of intensity in Fig. 3.4, the off-harmonic feature appears to have less phase variation than the weaker lower-energy features, and to be related to the on-harmonic emission at higher intensities. Combined with its significant strength within a moderate volume of parameter space, one would expect the off-harmonic radiation to be visible in

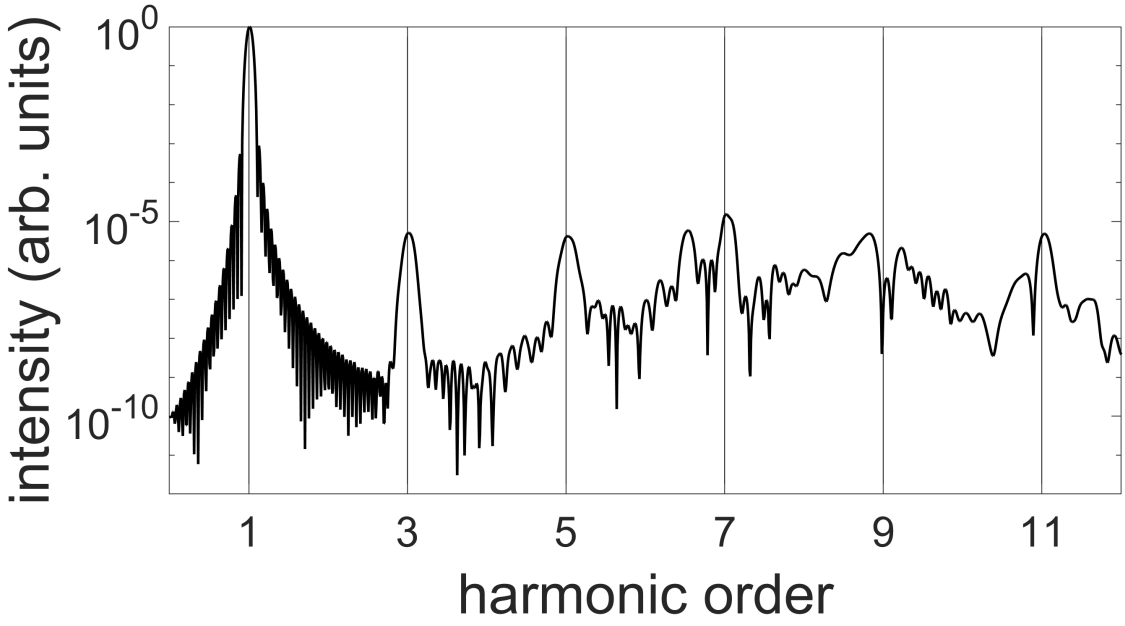

Figure 3.1: High harmonic spectrum generated in atomic hydrogen, exhibiting a rich structure in the near-threshold region of the spectrum between harmonics 5 and 12. The hydrogen ionization threshold of 0.5 a.u. $= 8.77\omega$, where $\omega = 0.057$ a.u. corresponds to the central driver wavelength of 800 nm. Other laser parameters: $\sin^2$ pulse of 20 optical cycles with peak intensity of 3.8×10^{13} W/cm^2. Note that the intensity of the spectrum is scaled by the signal at the fundamental frequency.

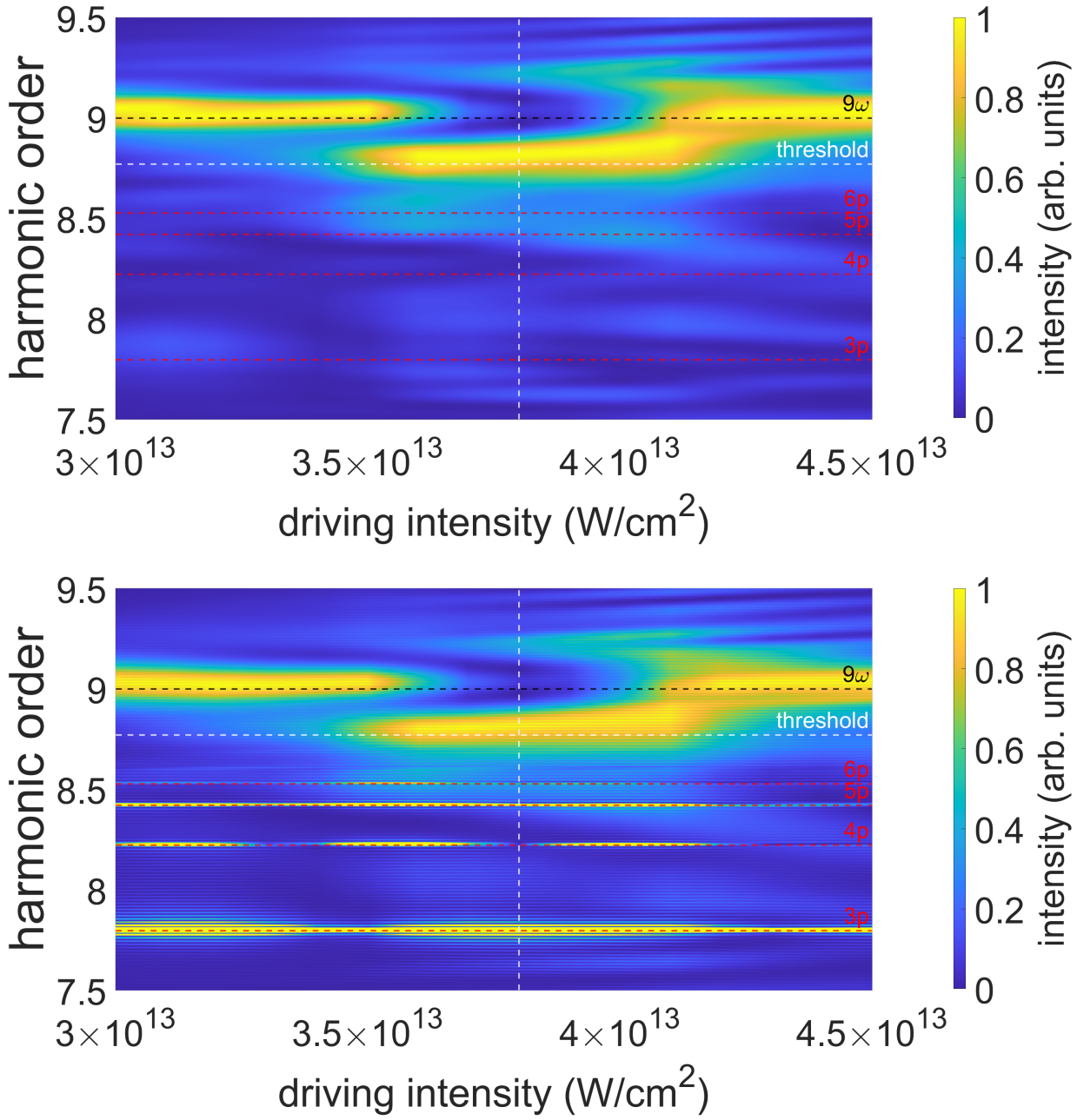

Figure 3.2: HHG spectra as a function of peak intensity for (top) radiation during the pulse (as in Fig. 3.1) and (bottom) for propagation of the wavefunction over a period of four times the pulse duration after the end of the pulse. Results for each intensity have been normalized to the maximum signal in the region between 8.75ω and 9.5ω. Red dashed lines denote field-free excited state transition energies.

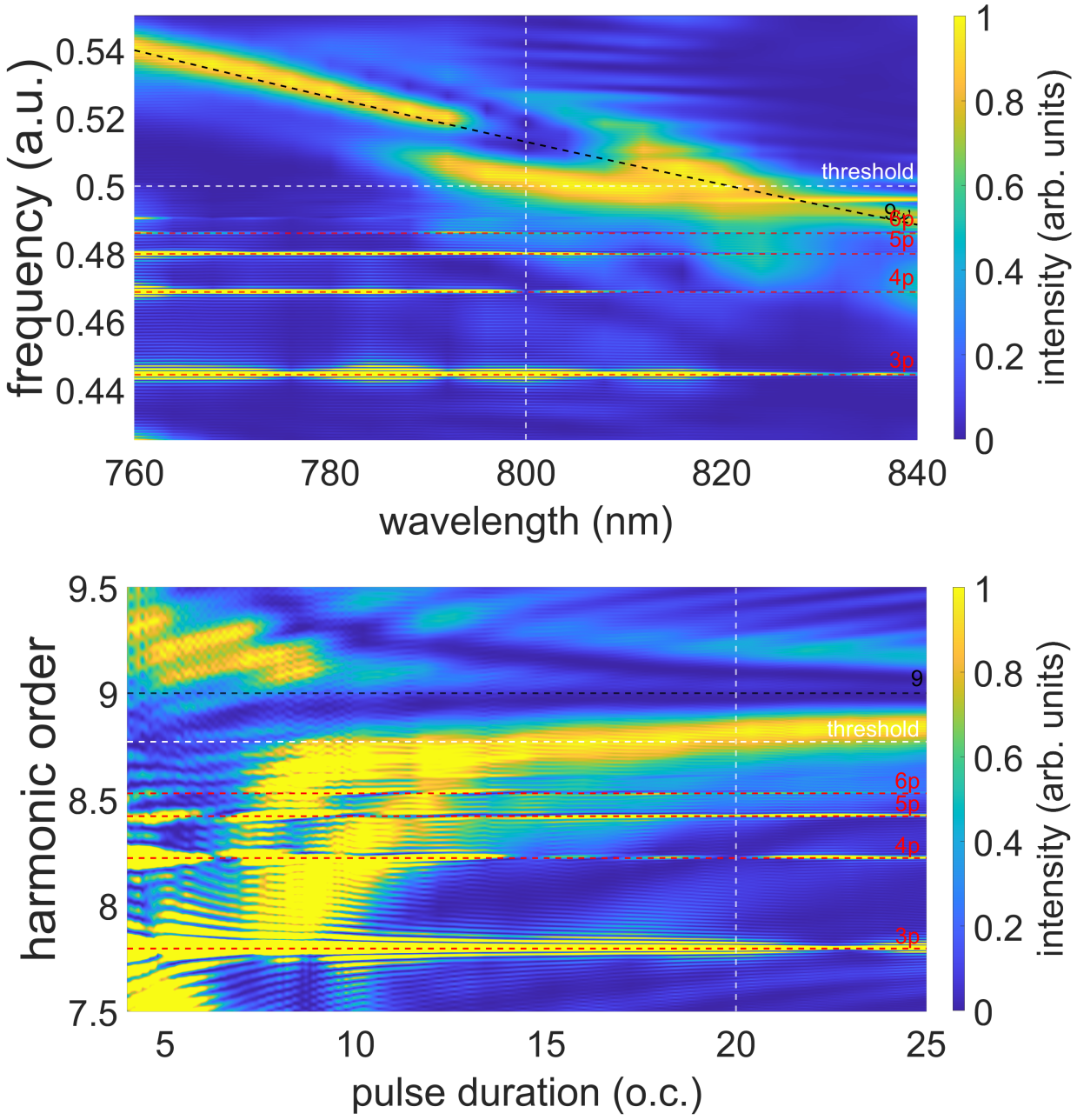

Figure 3.3: HHG spectra as (top) a function of the driving wavelength at $N_\tau = 20$ o.c., and (bottom) a function of pulse duration at $\lambda = 800$ nm. For both plots, driving intensity $I_0 = 3.8\times10^{13}$ W/cm^2. Results include spectral contributions (free induction decay) for propagation of the wavefunction over a period of four times the pulse duration after the end of the pulse. Results for each wavelength (top) or each duration (bottom) have been normalized to the maximum signal in the region between 8.75ω and 9.5ω. Red dashed lines denote field-free excited state transition energies.

experiment (this is further supported by macroscopic calculations in Sec. 4.4.2).

3.2 Resonantly-initiated quantum trajectories

A similar structure in HHG from argon was previously explained by Camp et al. in Ref. [100] via trajectories initiated by a resonantly-enhanced response through Stark-shifted excited states. In pulses of moderate duration (e.g., 20 o.c.), the envelope varies slowly enough to consider adiabatically-shifting states, but rapidly enough that the envelope cannot be considered constant over the scale of the travel time of an HHG trajectory. Assuming that excited states shift with $U_P(t) = \frac{|\vec{E}(t)|^2}{4\omega^2}$ as described in Sec. 1.3, the resonance condition for $\sin^2$ pulses is given by:

$$\frac{I}{4\omega^2}\cos^4\left(\pm\frac{T_r\pi}{N_\tau}\right) = N_\gamma - (E_n - E_0)\,, \tag{3.1}$$

where T_r is the resonance time in o.c. relative to the envelope peak, N_γ is the number of photons to be absorbed for the transition, E_n is the field-free energy of the resonant state, I is the peak laser intensity, ω is the central frequency, and N_τ is the pulse duration (full width) in o.c.. In their analysis, the radiation occurred at a specific delay after the resonances, t_d, measured in optical cycles, dependent on the particular resonance but not on laser parameters. This delay was attributed at least partially to the time associated with a semi-classical trajectory.

Camp et al. then claim the slope of the laser envelope is imprinted through the phase $\alpha U_P/\omega$, which depends on time of recombination – thus resulting in a red-shift (blue-shift) when recombination occurs on the falling (rising) side of the pulse:

$$\Delta\omega = \alpha\frac{dU_P/\omega}{dt}\bigg|_{t=\pm T_r+t_d} \tag{3.2}$$

The scale of the phase is left as a free parameter, α, used to fit the predicted shift to the observed radiation. We note that two other parameters – the degree of state shift as a fraction of U_P, and delay between resonance and emission – are modified to achieve agreement between temporal profiles of radiation and the predicted emission time. The values of these free parameters are justified as falling roughly within the range of previous studies (esp. on semi-classical trajectories).

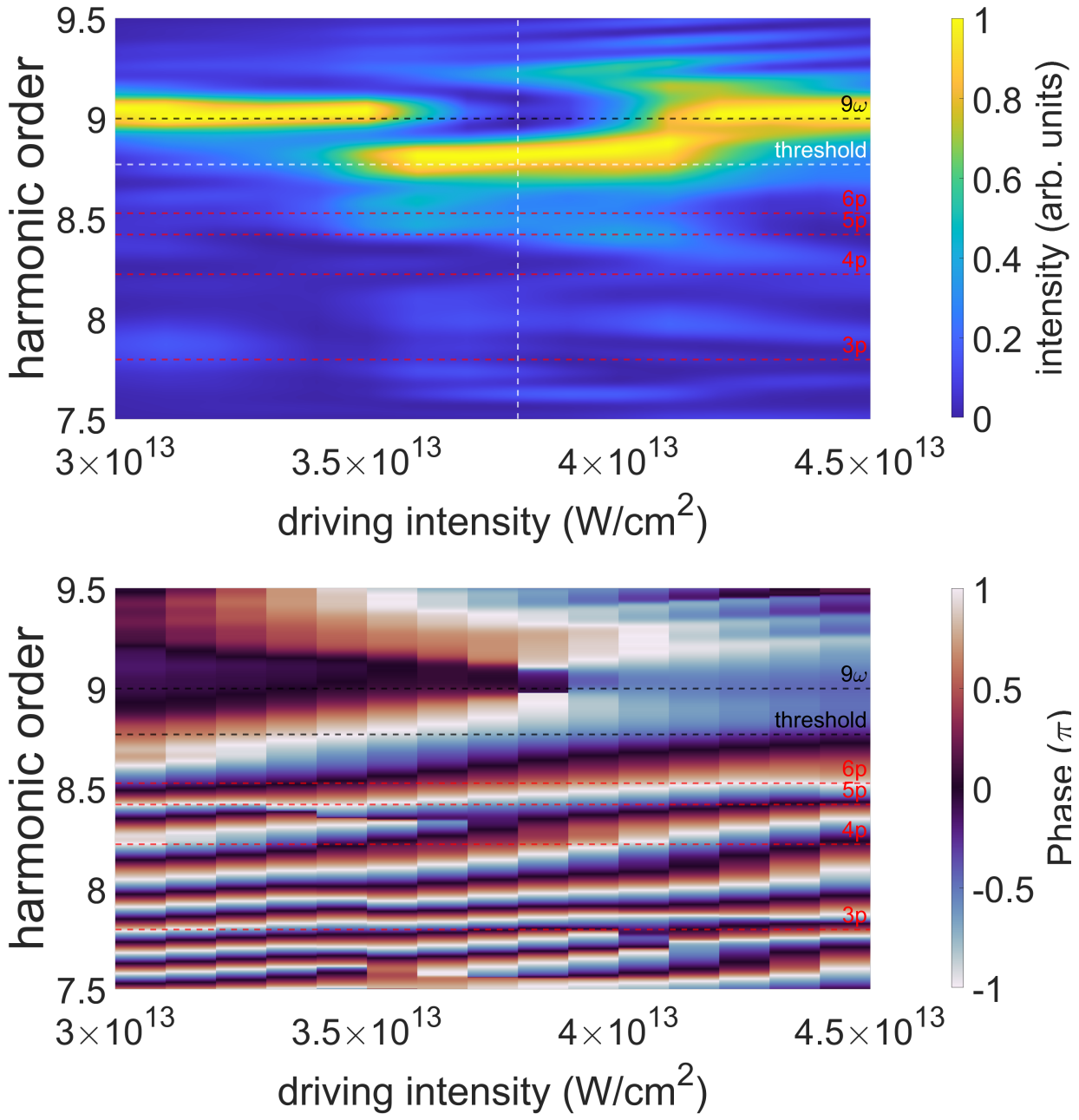

Figure 3.4: HHG spectral (top) intensity and (bottom) phase as a function of peak intensity for radiation during the pulse (other parameters as in Fig. 3.1).

Our own investigations, below, confirm the association of temporal radiation with delays after field-induced resonances (without by-hand modification – setting $\Delta E = U_P(t)$). However, in Sec. 3.5, we find features not explained by the $\Delta\omega$ prediction and present results suggesting that semi-classical trajectories do not apply at the parameters of our primary attention (specifically, intensities roughly at and below 3.8×10^{13} W/cm^2). Interestingly, we do find evidence of trajectory-like radiation at higher intensities.

3.3 Identifying resonances with temporal profiles

By windowing the spectrum and inverse-Fourier transforming, we may analyze the temporal profile of particular harmonics. Here, the dipole acceleration is first Blackman-windowed and then a flat-top spectral window of width 2ω with Gaussian fall-off of width 0.2ω is applied. We identify resonance times as a function of laser parameters according to Eq. (3.1). In the Figures below, we draw these as lines connecting the times for discrete values of a scan. This generally leads to gaps near the point where rising- and falling-side resonances meet (e.g., when the exactly-resonant peak intensity condition is not sampled), but allows for marking resonances on arbitrary scans of one or more parameters.

A central benefit of these visualizations is the ability to match radiation features to particular resonance features. This is done by comparing the timing of radiation to that of various resonances. While several resonances may occur during a given pulse, we will generally be able to identify a single specific resonance as only this one will consistently follow the timing of the radiation across all parameter scans (and usually just 1-2 scans are sufficient). We then denote these resonances as $N_\gamma\omega \to |n\rangle$ – for example, $9\omega \to 3p$. Additionally, we often include the delay between resonance and radiation, t_d, in optical cycles and which side of the envelope peak the resonance occurs, in phrases such as: $rising$ $9\omega \to 3p$ $+1.8$ *o.c.* or $falling$ $9\omega \to 3p$ $+0.5$ *o.c.*. For the radiation features in Figs. 3.1-3.3, we will now outline the steps of identifying the associated resonance ($9\omega \to 3p$) and delays ($0.5, 1.8, 3.0$ *o.c.*). In later sections, we primarily present the results of this process, where associated resonances and corresponding delays have already been identified.

To begin, it is useful to plot a temporal profile scan as a function of driving pulse duration N_τ, as shown in Fig. 3.5. In these scans, most dimensionless parameters ($U_P/\omega, I_P/\omega$, HHG cut-off, etc.) remain constant, as does the set of resonances which occur during the pulse. The timing of resonances T_r does change, as measured in optical cycles or absolute time (e.g., fs), though not in fractions of the pulse duration. In Fig. 3.5, we identify four temporal features of the 9th harmonic. This radiation is primarily generated through a feature on the trailing end of the pulse. A somewhat weaker contribution occurs on the rising edge, which seems to merge with the strong feature in the trailing part for short pulses. Additionally, for longer pulses (more than about 8 and 15 cycles, respectively) there are two additional radiation features close to the pulse peak, varying in relative intensity as a function of pulse duration (strongest near $N_\tau = 15$ and 25 o.c., respectively). To the eye, the slopes of all these features in the Figure, except for the strong feature on the trailing edge, appear to be similar.

Next, in Fig. 3.6(a), we indicate the resonance times T_r for different transitions via dashed lines in the same plot as shown in Fig. 3.5. According to Eq. (3.1), T_r is proportional to the cycle duration N_τ. Therefore, resonances appear as straight lines with slopes depending on the resonance chosen (and the other, fixed, laser parameters). As such, it is fairly simple to check which resonance lines match the slope of radiation features and identify the delay t_d. In this case, the central six lines – $(9\omega \to 4p), (9\omega \to 3p), (8\omega \to 2s)$, rising and falling – seem promising as matches to the slopes of the various radiation features. Upon checking, it becomes obvious that $9\omega \to 3p$ agrees quite well with all features, while the other resonances do not. At the same time, it is possible to estimate the delays between this resonance and the radiation, finding $t_d \approx 0.5, 1.8, 3.0$ *o.c.*.

In Fig. 3.6(b), we draw only the $9\omega \to 3p$ resonances, with delays t_d. Contrary to our expectations, it appears the rising $9\omega \to 3p$ resonance produces radiation at three distinct delays. While the difference between the consecutive delays ($\Delta t_d = 1.3$ and 1.2 o.c.) is approximately equal, our investigations have uncovered no further examples to mark this as more than a coincidence. (For example, we have not found radiation matching $9\omega \to 3p\ + 4.25$ *o.c.*, nor other resonances associated with radiation at more than a single delay.) As a side note, the unexpected result of these

multiple delays led us through a detour investigating the effects of pulse envelope and radiation in longer pulses, which will be discussed in Secs. 3.5.1 and 3.7, respectively.

After identifying the resonance and delays associated with the radiation features in the present results, we verify our conclusions by scanning other parameters. Firstly in Fig. 3.7, we present results obtained by varying the driving intensity. In this case, the only dimensionless parameter to remain constant is the energy (in ω) of field-free ionization (I_P/ω) or excitation (E_n/ω). Additionally, the resonance condition Eq. (3.1) is achieved at different times with a dependence on intensity that is not linear (namely, $\propto \mathrm{acos}\left(\sqrt{I}\right)$). Again, in Fig. 3.7(b) we see good agreement with the rising $9\omega \to 3p$ resonance delayed as above. The falling resonance appears to have the correct shape, but appears slightly later than a delay of $t_d = 0.5$ cycles.

Next, we scan the driving wavelength (results in Fig. 3.8); the conclusion is similar, though the width of the scan window is larger, so we see more different features. Generally, radiation features appear at certain times (0-2 o.c. after the peak of the pulse) then a split occurs at larger wavelengths. The dependence is clearly nonlinear (and without a familiar analytic form; see Eq. (3.1)). Usually – but not always – the falling-edge radiation is somewhat more intense than the rising-edge. Again, the best/only resonance candidate for the emitted radiation for wavelengths near 800 nm is $9\omega \to 3p$, with fairly good agreement (incl. offset). For other wavelengths, some features show similar bowl-like structure, while others have a zig-zag pattern of radiation time w.r.t wavelength.

An additional parameter accessible for variation in computation but, in general, not in experiment is the atomic potential. In Sec. 3.8.1, we will consider helium atoms in the single-active-electron approximation, but this introduces many differences since the form of the potential changes (affecting different states differently) and equivalent dimensionless parameters require moving to a different wavelength and intensity region. Instead, here we consider continuous variations from the hydrogen atom case by altering the nuclear charge, Z, without other modifications. This results in the single effect that all transition energies scale by Z^2. We expect $1s \to$(field-free-)continuum and $1s \to 3p$ to have the greatest impact here, but cannot necessarily parse out the consequences of

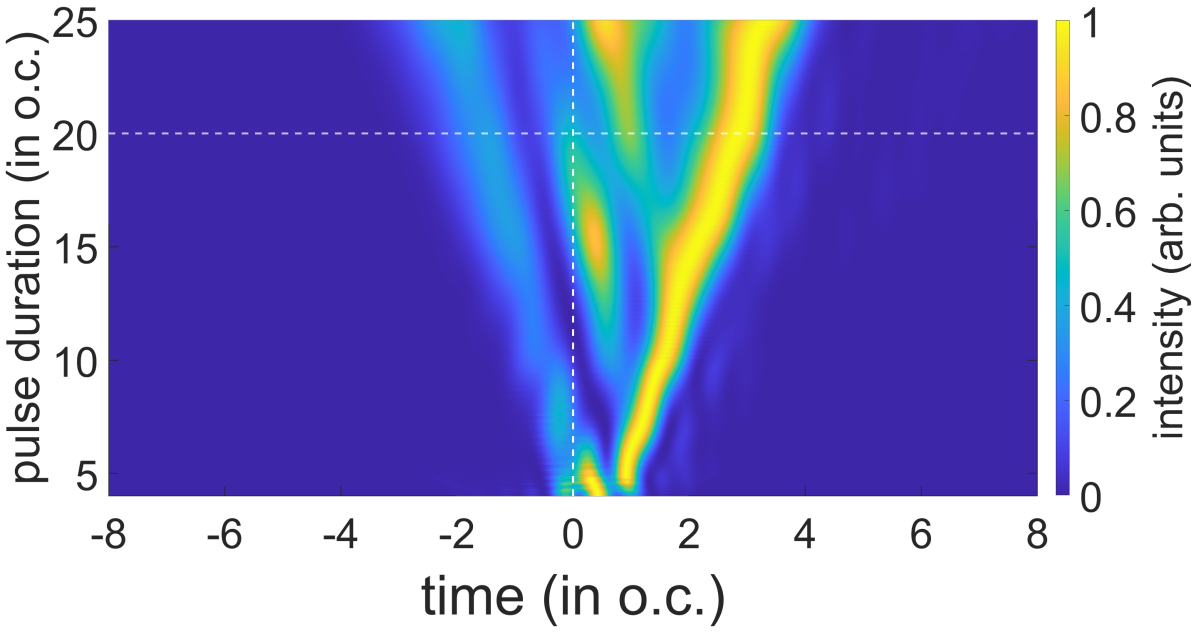

Figure 3.5: Temporal profile of radiation within 1ω of the 9th harmonic as a function of pulse duration in atomic hydrogen for an 800 nm, 3.8×10^{13} W/cm^2 pulse. For each duration the results have been normalized to a maximum of 1 for sake of comparison. A vertical dashed line denotes the peak of the laser and a horizontal dashed line identifies the pulse parameters used as a base in this Chapter (i.e., 20-cycle duration).

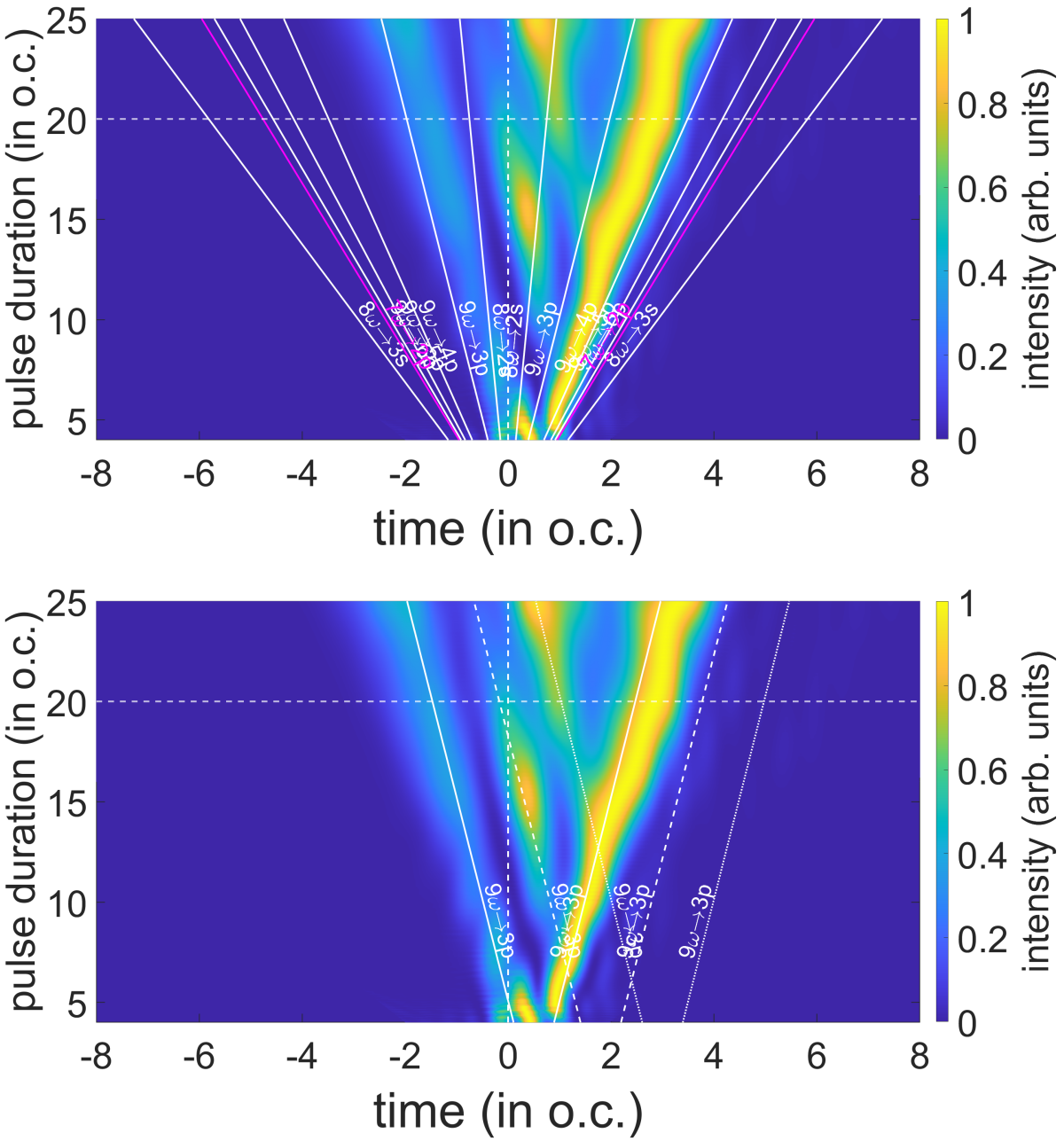

Figure 3.6: Same as Fig. 3.5, but overlaid with lines denoting: (top) resonance times for 7- (magenta) and 8- or 9- (white) photon resonances (there are no resonances with a smaller or larger number of photons involved for these parameters) for $2s - 6p$, and (bottom) $9\omega \to 3p$ resonances delayed by 0.5 (solid), 1.8 (dashed), and 3.0 (dotted) optical cycles.

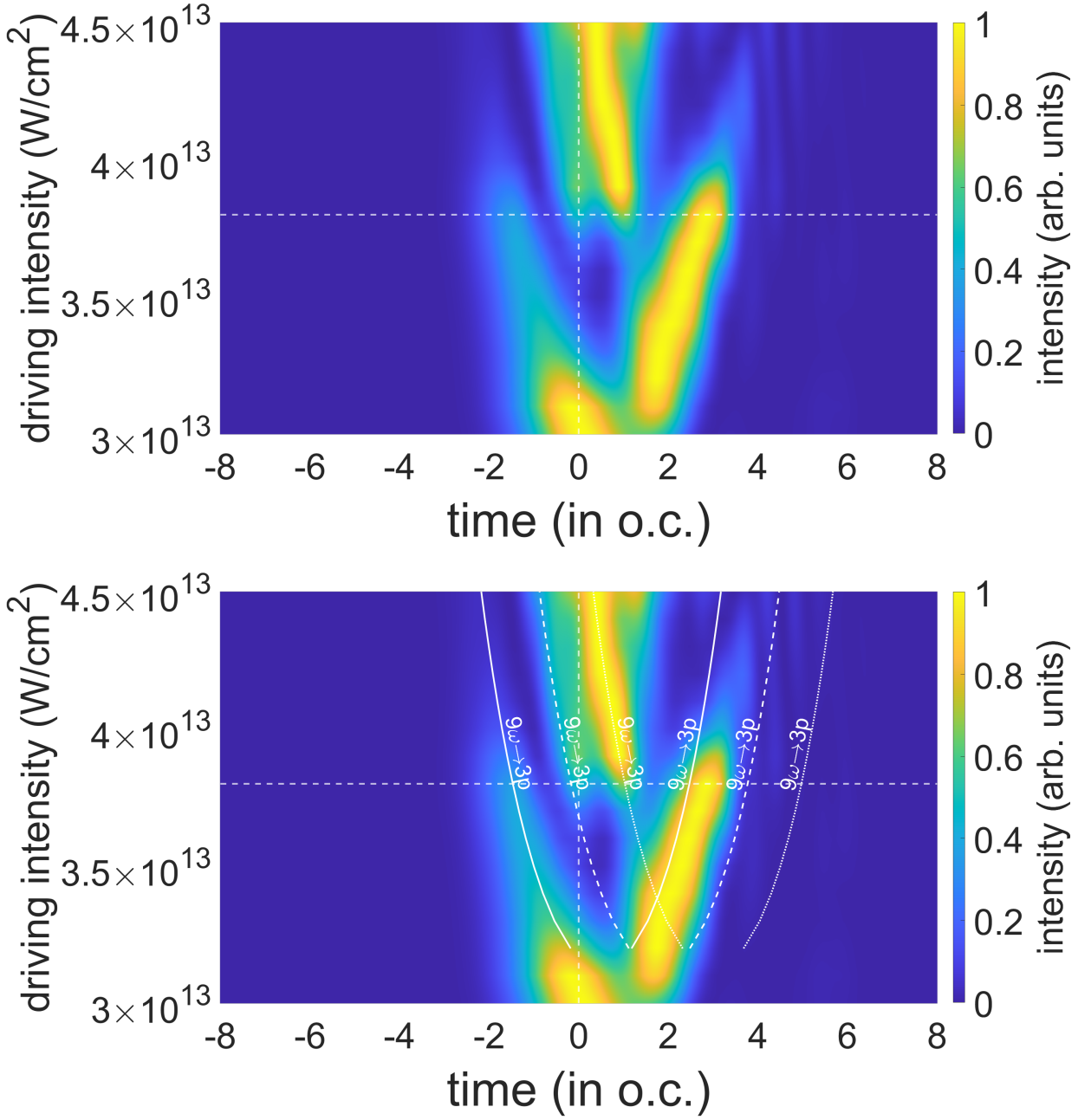

Figure 3.7: Temporal profile of radiation within 1ω of the 9th harmonic as a function of driving pulse intensity in atomic hydrogen for an 800 nm, 20 o.c. pulse. For each intensity the results have been normalized to a maximum of 1 for sake of comparison. A vertical dashed line denotes the peak of the laser and a horizontal dashed line identifies the pulse parameters used as a base in this Chapter (i.e., 3.8×10^{13} W/cm^2 intensity). Panels show identical radiation data, but the lower is overlaid with lines denoting $9\omega \rightarrow 3p$ resonances delayed by 0.5 (solid), 1.8 (dashed), and 3.0 (dotted) optical cycles.

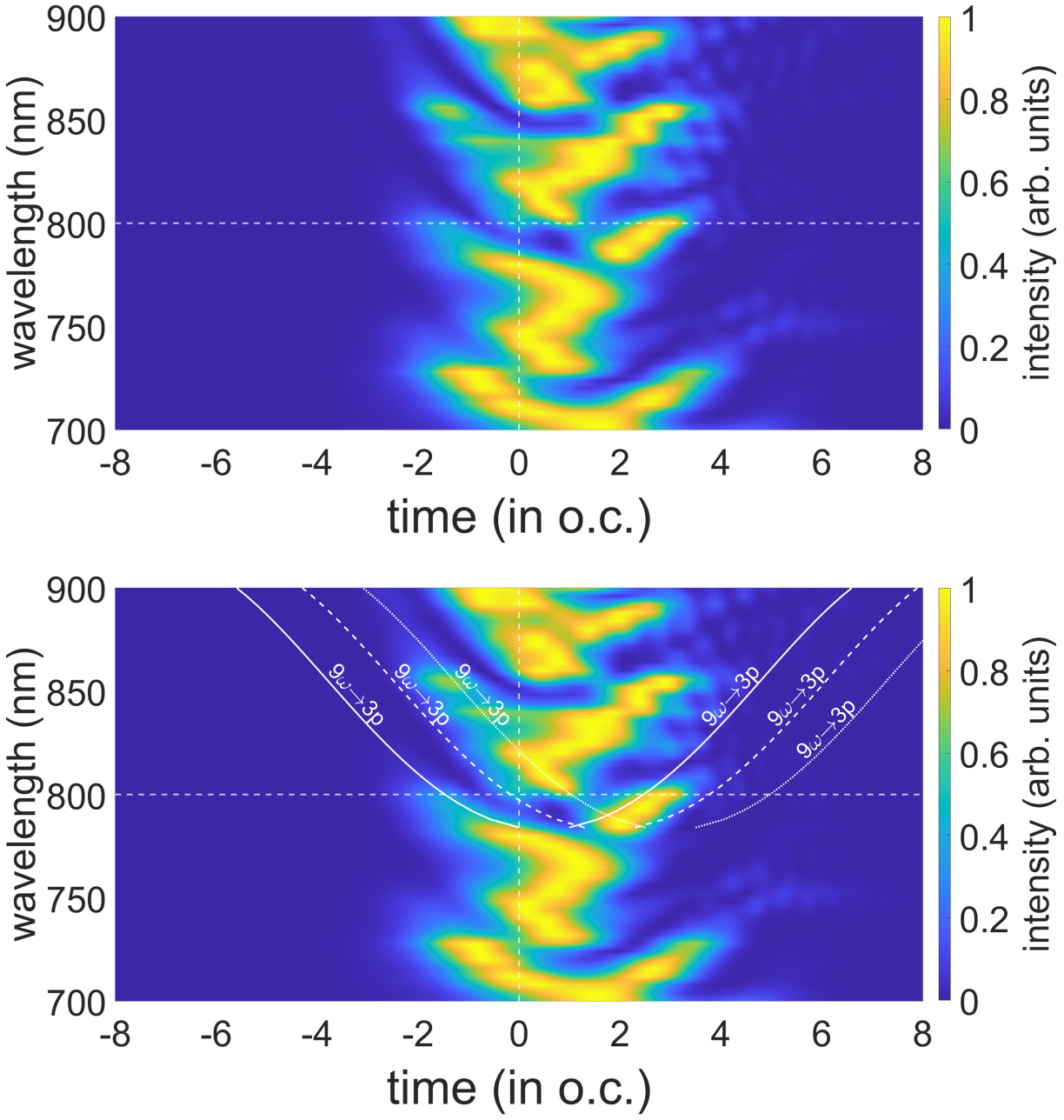

Figure 3.8: Temporal profile of radiation within 1ω of the 9th harmonic as a function of driving wavelength in atomic hydrogen for a 20 o.c. pulse at 3.8×10^{13} W/cm^2. For each wavelength the results have been normalized to a maximum of 1 for sake of comparison. A vertical dashed line denotes the peak of the laser and a horizontal dashed line identifies the pulse parameters used as a base in this Chapter (i.e., 800 nm wavelength). Panels show identical radiation data, but the lower is overlaid with lines denoting $9\omega \rightarrow 3p$ resonances delayed by 0.5 (solid), 1.8 (dashed), and 3.0 (dotted) optical cycles.

other state shifts. We note that the field-shifted transition energies do not scale in this same way since U_P does not depend on the potential of the target.

The results of the respective scan are shown in Fig. 3.9, and we see a variety of features quite similar to those present in the wavelength scan in Fig. 3.8. Again, there are a number of "bowl" features which match the shape of resonance lines, as well as a few zig-zags that do not. The initial parameters ($Z = 1, \lambda = 800$, and $I = 3.8 \times 10^{13}$ W/cm^2) all seem to place us just at the transition point between dominance of two different features, associated with the $falling$ $9\omega \rightarrow 3p$ $+0.5$ *o.c.* and the $rising$ $9\omega \rightarrow 3p$ $+3.0$ *o.c.* delayed resonance lines.

From these scans, we conclude the identified resonances are correct, and the delays at least are approximately correct (the falling-side delay consistently appears to be slightly longer than 0.5 cycles, but for now we leave the rising/falling delays equal). Further off of the base parameters, some of the radiation diverges slightly from the $9\omega \rightarrow 3p$ predictions, while other features clearly do not correspond to it at all. The deviations are explored in Sec. 3.6, while other resonances may be identified using the process outlined above for different base scan intensities.

3.4 Radiation at other driving intensities

While Figs. 3.2 and 3.7 show how the generated radiation varies close to 3.8×10^{13} W/cm^2, it is also valuable to consider a broader range in intensities. In Fig 3.10, we plot the spectrum for driving intensities ranging from $0.5 - 9.0 \times 10^{13}$ W/cm^2. From this scan we identify and select five intensities of particular interest (vertical white lines):

- 2.0×10^{13} W/cm^2: Here are radiation features near 9ω similar to the case of 3.8×10^{13} W/cm^2, studied previously. However, there is additional strong radiation in the region of the Rydberg state transition energies.

- 3.0×10^{13} W/cm^2: A "normal" case where the harmonic radiation at 9ω clearly dominates over any off-harmonic radiation.

- 3.8×10^{13} W/cm^2: The case we have investigated most closely, where radiation just below

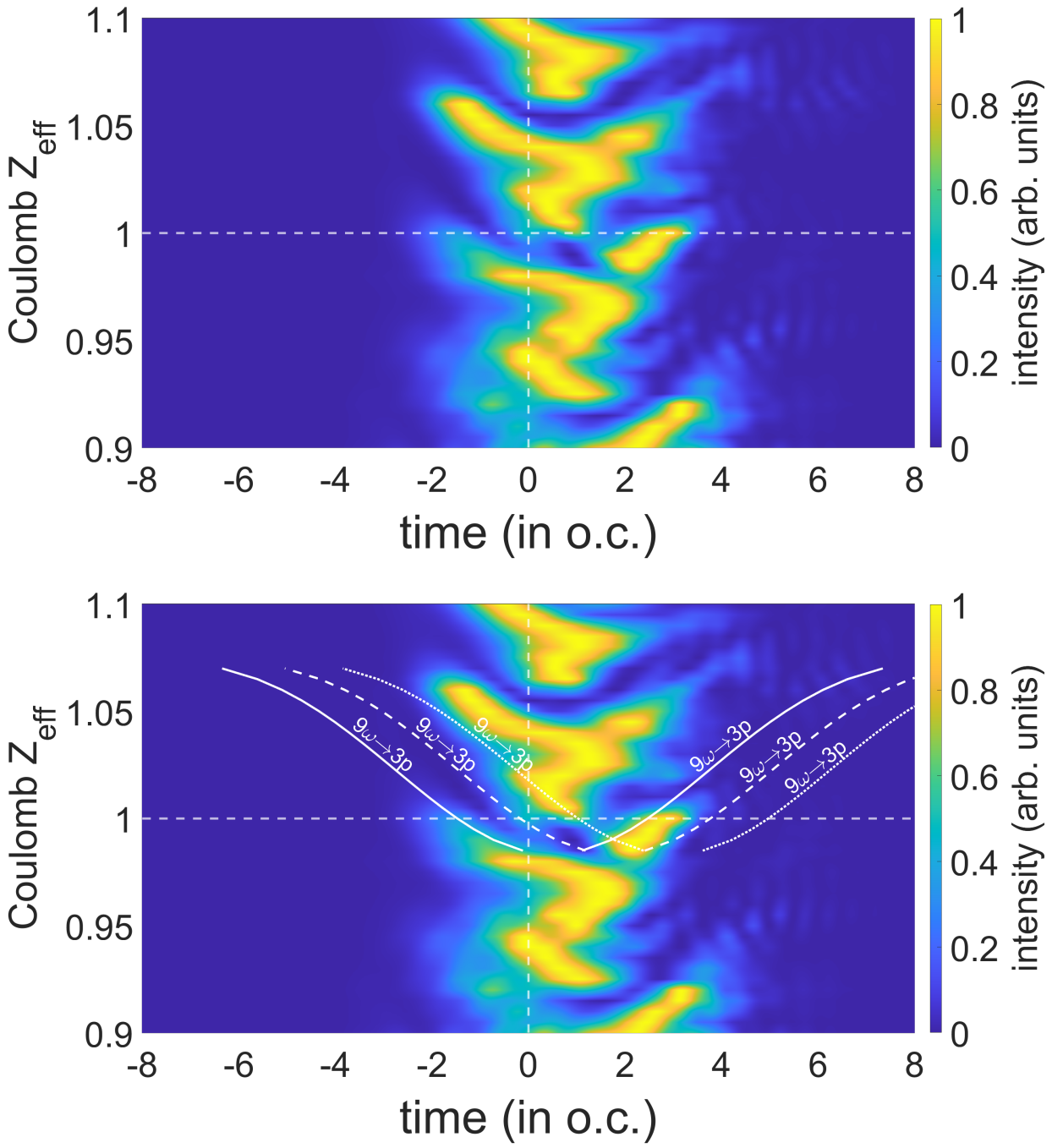

Figure 3.9: Temporal profile of radiation within 1ω of the 9th harmonic as a function of atomic nuclear charge Z in a hydrogen-like atom for an 800 nm, 20 o.c. pulse at 3.8×10^{13} W/cm^2. For each Z the results have been normalized to a maximum of 1 for sake of comparison. A vertical dashed line denotes the peak of the laser and a horizontal dashed line identifies the pulse parameters used as a base in this Chapter (hydrogen, i.e., $Z = 1$). Panels show identical radiation data, but the lower is overlaid with lines denoting $9\omega \rightarrow 3p$ resonances delayed by 0.5 (solid), 1.8 (dashed), and 3.0 (dotted) optical cycles.

$N_\gamma\omega \to \lvert n\rangle$		t_d (o.c.)	line style	
$9\omega \to 3p$		0.5	white	solid
$9\omega \to 3p$		1.8	white	dashed
$9\omega \to 3p$		3.0	white	dotted
$10\omega \to 4s$	(or $4d$)	0.5	magenta	
$10\omega \to 3s$	(or $3d$)	1.2	red	
$9\omega \to 2p$		0.8	cyan	
$7\omega \to 2p$		0.8	yellow	
$9\omega \to 6p$	(or $6f$ or $6h$)	0.8	green	

Table 3.1: Identified resonances, delays, and line styles. We note that due to l-independent energies in hydrogen atoms, some of the resonances can be ascribed to different states with the same l parity, namely: $3s$ and $3d$, $4s$ and $4d$, $6p$ and $6f$ or $6h$.

and above 9ω dominates over that at the harmonic.

- 5.6×10^{13} W/cm^2: Similar features to the radiation generated at 3.8×10^{13} W/cm^2, but with strong and clearly-separated sidebands well above and below 9ω.

- 7.0×10^{13} W/cm^2: Here, again the radiation emitted at 9ω dominates, but weaker sidebands are still present.

For each of these base intensities we have performed the same process to identify resonances and delays. As above, we generally have considered – in order – scans across pulse duration, driving intensity, and driving wavelength. From each scan, we can eliminate potential resonances which do not match the shape of the radiation curves, while estimating delays for the remaining possibilities. Through this, we identified resonances and delays, accounting for most of the clear radiation structures. In the Figures below, we plot all identified resonance-delays, labeled by resonance and denoted by color defined in Table 3.1. As mentioned above, $9\omega \to 3p$ is the only resonance for which we have identified multiple delays, differentiated by line style.

First, in Figs. 3.11 and 3.12, we show scans of pulse duration for each chosen intensity. As above, all resonance conditions are straight lines versus pulse duration, so it is simple to identify radiation connected to resonances. As in Fig. 3.5, which radiation feature is dominant often depends on pulse duration. However, we are not able to identify a systematic rule or trend for this variation. We note a plotting artifact visible in some figures (esp. in the lower part of Fig. 3.11's top panel):

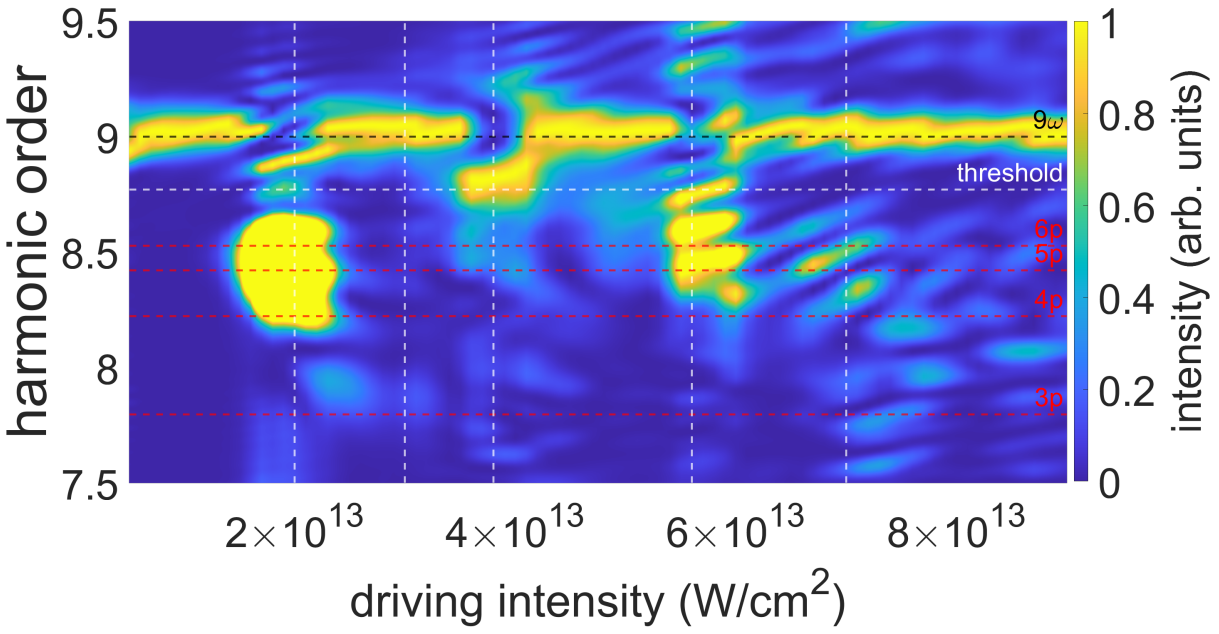

Figure 3.10: HHG spectra as a function of peak intensity for radiation during the pulse. Results for each intensity have been normalized to the maximum signal in the region between 8.75ω and 9.5ω. Red dashed lines denote field-free excited state transition energies.

As a function of duration, it appears that radiation rapidly transitions between peaks and nodes. This is a result of relatively coarse sampling, not a physical effect – radiation is slice-normalized for each sampled duration, but smoothing in the Figure interpolates lower values for pixels between actual data.

For 2.0×10^{13} W/cm^2 (Fig. 3.11 top), a duration-independent radiation feature just after the peak of the pulse dominates. This feature corresponds to the "normal" harmonic emission at 9ω, without resonant enhancement. However, for all durations, there are two additional duration-dependent radiation features visible, which we identify to correspond to rising and falling resonances. Specifically, the $7\omega \rightarrow 2p + 0.8$ *o.c.* (yellow) and $9\omega \rightarrow 6p + 0.8$ *o.c.* (green) delayed resonances both agree well with these features on both the rising and falling sides (incl. across other scans, see below). From the present results, we can however not determine conclusively which one (or both) is the origin of the generated radiation. We note that the same resonances occur at all higher intensities, but are in the rising and falling edge of the pulse far from the peak and in those cases they do not appear to provide significant radiation.

In the spectra at 3.0×10^{13} W/cm^2 (Fig. 3.11 bottom) the dominant radiation occurs just after the peak of the pulse for durations up to about 15 o.c., then it shifts to earlier times with increase of the pulse duration. This suggests that resonances do not play a strong role for shorter pulses at this intensity. We have not definitively identified a resonance associated with the longer-pulse radiation. There is some agreement (across different scans) with a much larger delay of the resonances identified at the lower intensities ($7\omega \rightarrow 2p$ and $9\omega \rightarrow 6p$), specifically 4.3 o.c.. Unfortunately, the agreement is generally good only in small portions of each scan near the base parameters (800 nm, 20 o.c., 3.0×10^{13} W/cm^2). Unlike the delayed resonances listed in Table 3.1, here the features do not correspond with radiation in different and broader scans (for example, in Fig. 3.12, we do not identify radiation features with the same slopes as the green/yellow lines at later delays).

For 5.6×10^{13} W/cm^2 (Fig. 3.12 top), there are two primary radiation structures corresponding to the $10\omega \rightarrow 4s + 0.5$ *o.c.* delayed resonance (magenta), but other structures are also present.

Firstly, unlike for 3.8×10^{13} W/cm^2, there are particular times (separated by 0.5 o.c.) when radiation is emitted regardless of pulse duration. The intensity of this radiation increases strongly when it coincides with resonance lines (esp. $10\omega \to 4s$). This suggests a combined influence of the field and envelope, which we will further investigate in Sec. 3.5. We note also the presence of other resonance lines. *Rising* $9\omega \to 3p$ $+1.8$ *o.c.* may be responsible for broadening and "smearing" the rising radiation feature, and weaker features line up with other resonances.

Finally, at 7.0×10^{13} W/cm^2 (Fig. 3.12 bottom) we can see a single strong radiation feature corresponding to rising $10\omega \to 3s$ $+1.2$ *o.c.* (red) and $9\omega \to 2p$ $+0.8$ *o.c.* (cyan) resonances, but a great deal of weaker radiation features are also present. Similarly to 5.6×10^{13} W/cm^2, radiation is enhanced at particular times, but the effect is not as sharp.

In Fig. 3.13, we present the temporal profile of radiation for the full intensity range. Before considering individual radiation features, we may make some general observations. As for intensities near 3.8×10^{13} W/cm^2, the radiation appears in several "bowl" shapes centered just after the peak of the pulse. For lower intensities ($\lessapprox 5 \times 10^{13}$), the structure of radiation tends to be smoother and be strongest within the first three cycles after the peak of the pulse. At the higher intensities, other structures are visible (e.g., discrete radiation times independent of intensity). Similarly, we observe more complexity in radiation structures occurring after the peak of the pulse compared to those before the peak.

With good agreement we have included identified resonances and delays in Fig. 3.13 (bottom panel), which clearly explain the majority of radiation features. In regions where two or more delayed resonances overlap, the radiation features broaden, but the number of resonances does not appear to predict which radiation will dominate (cf. the $5 - 6 \times 10^{13}$ W/cm^2 range).

Scanning the wavelength for each of the four intensities (Figs. 3.14 and 3.15) serves as an important additional check in resonance identification since the timing has a more complex dependence than in either the intensity or duration scans. In general, the agreement is quite good within a range of 50 nm centered about 800 nm. Beyond this range, there are radiation features which appear to correspond to unidentified resonances. In other cases identified resonances seem to have

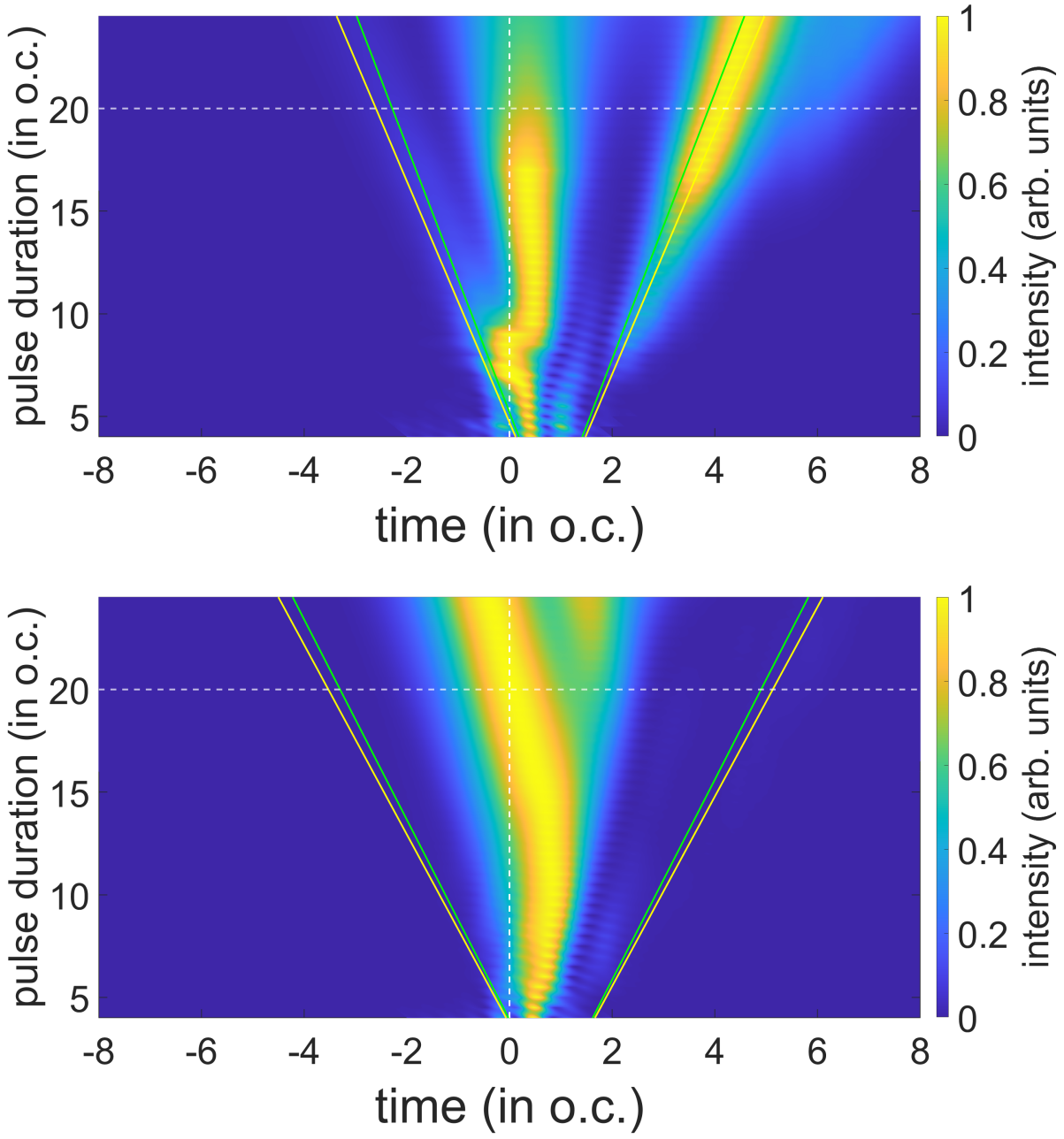

Figure 3.11: Temporal profile of radiation within 1ω of the 9th harmonic as a function of pulse duration in atomic hydrogen for an 800 nm pulse at (top) 2.0×10^{13} W/cm^2 and (bottom) 3.0×10^{13} W/cm^2. For each duration the results have been normalized to a maximum of 1 for sake of comparison. A vertical dashed line denotes the peak of the laser and a horizontal dashed line identifies the pulse duration used as a base in this Chapter (i.e., 20 o.c.). Lines are drawn for delayed resonances as outlined in Table 3.1.

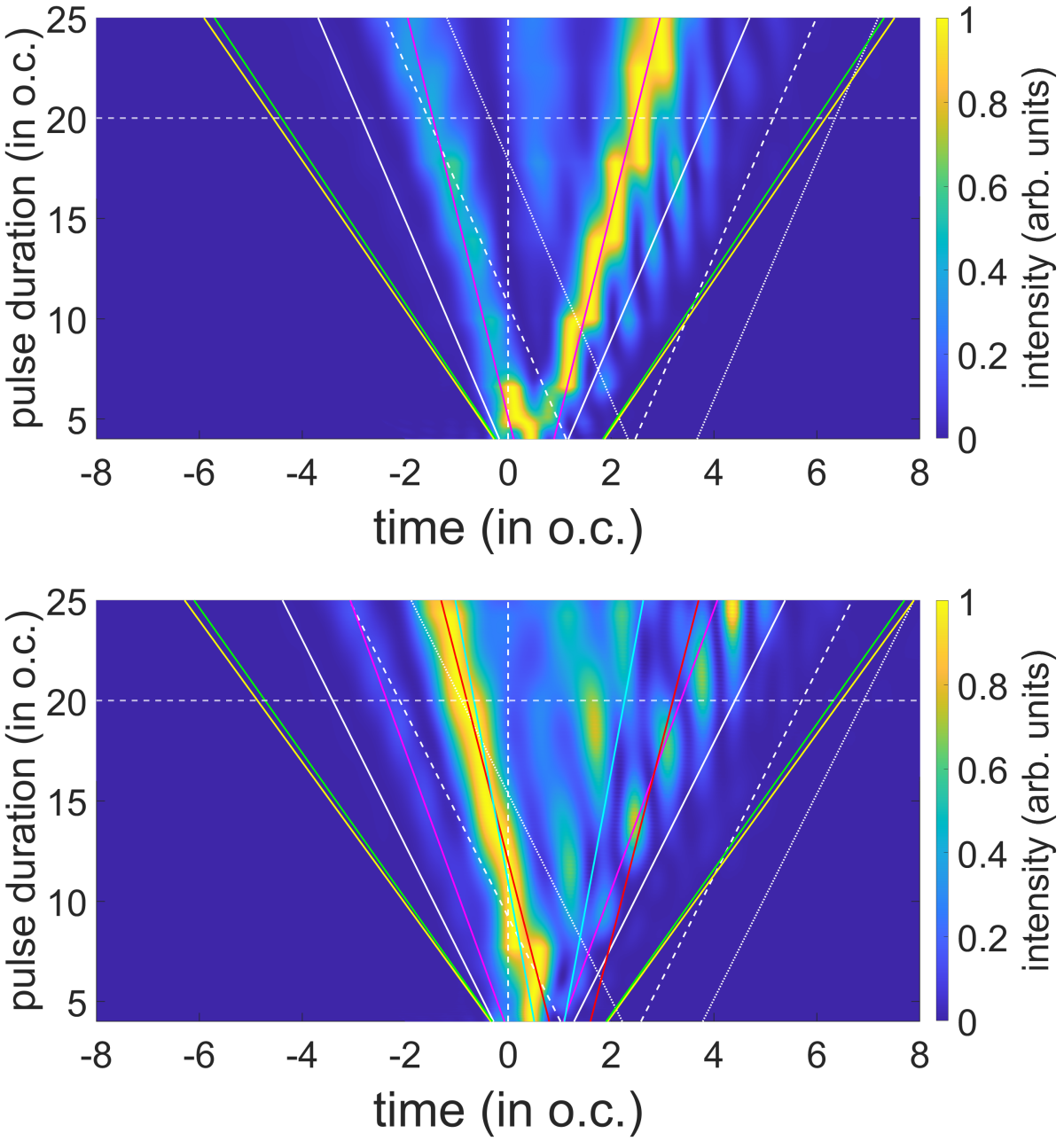

Figure 3.12: Same as Fig. 3.11, but for (top) 5.6×10^{13} W/cm^2 and (bottom) 7.0×10^{13} W/cm^2.

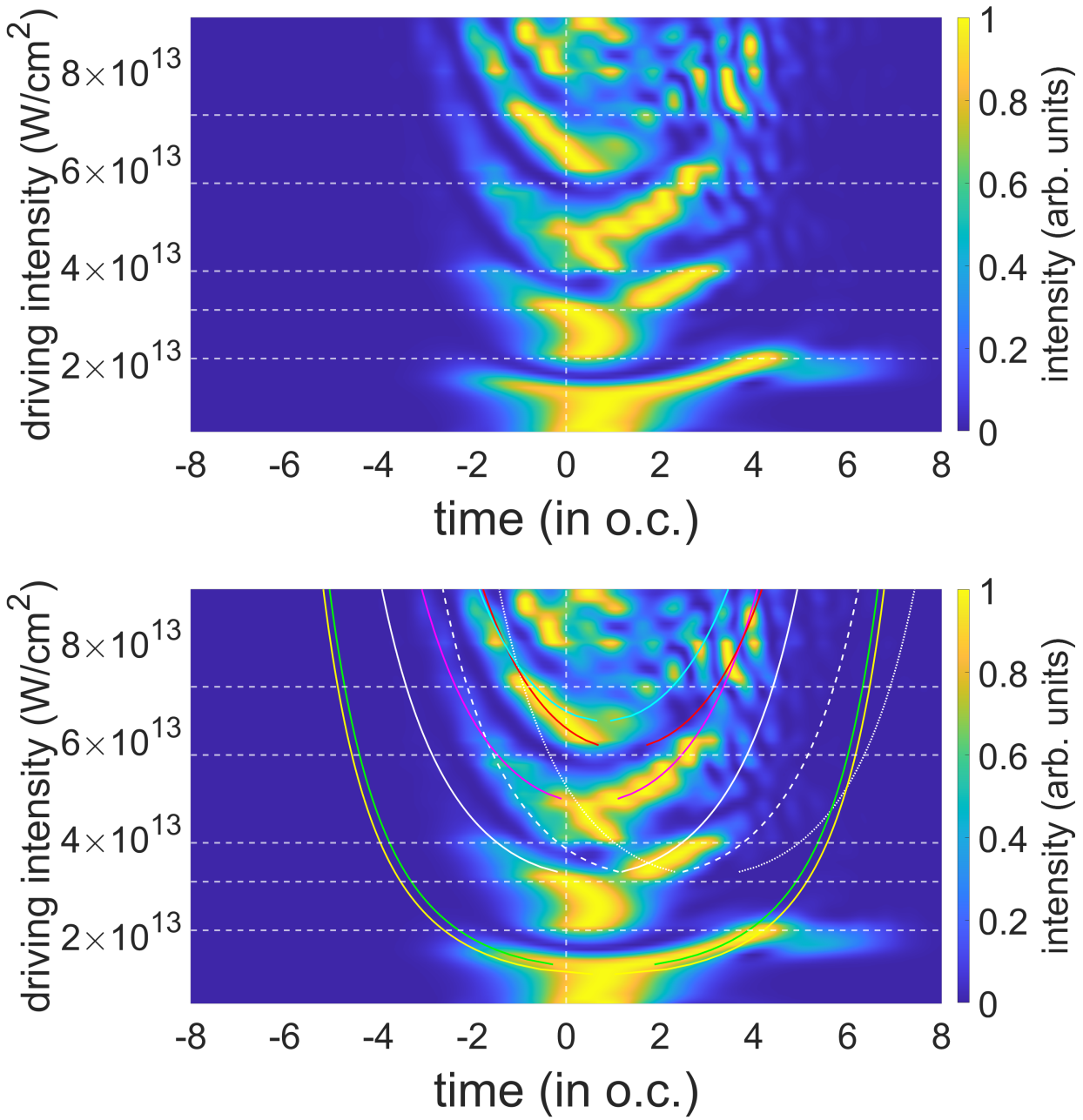

Figure 3.13: Temporal profile of radiation within 1ω of the 9th harmonic as a function of driving pulse intensity in atomic hydrogen for an 800 nm, 20 o.c. pulse. For each intensity the results have been normalized to a maximum of 1 for sake of comparison. A vertical dashed line denotes the peak of the laser and horizontal dashed lines identify the intensities selected above. (lower plot) Lines are drawn for delayed resonances as outlined in Table 3.1.

the correct behavior with changing wavelength, but occur at larger wavelengths than the corresponding radiation (i.e., lines appear at vertical offsets from radiation peaks). Identifying these additional resonances would require more simulations (e.g., scanning various parameters around a base pulse of 700 nm and 2.0×10^{13} W/cm^2 or 875 nm and 5.6×10^{13} W/cm^2). Deviations in the already-predicted resonances are more interesting, potentially highlighting approximations in our model; we will therefore investigate these in Sec. 3.6.

3.5 CEP and the trajectory model

Previously, Camp et al. [100] ascribed similar features to resonantly-initiated trajectories, and described their free parameters as falling within the range of predictions from the group's earlier semi-classical trajectory calculations in [41]. Using a classical trajectory code based off the description in this paper, we however did not find consistent initial conditions leading to trajectories of the correct durations $(0.5, 1.8, 3.0$ o.c.$)$ for our radiation at 3.8×10^{13} W/cm^2.

We have also tested the semi-classical model based on the following considerations. If semi-classical trajectories are involved in the observed radiation, we would expect a clear dependence of the radiation features on the carrier-envelope phase (CEP) since in any semi-classical trajectory model, field values between ionization and recombination times will determine the travel time and recombination energies possible. In "normal" HHG, the timing of radiation at a given energy is constrained by the phase of the laser at time of ionization. Further, in the tunneling regime, the field strength at moment of ionization determines both the ionization probability and the initial parameters of trajectories (location of the tunnel exit). In a theoretical study where time of ionization was gated by application of a second, VUV laser, field values at the moment of ionization continued to strongly impact the spectral and temporal character of HHG [102]. Results from a generalized semi-classical trajectory model mimicking trajectories initiated by multiphoton ionization showed a dependence at least on the direction of the field, differentiating "uphill" and "downhill" trajectories [41].

In Fig. 3.16, we investigate the CEP dependence for two intensities – (top panel) $3.8 \times$

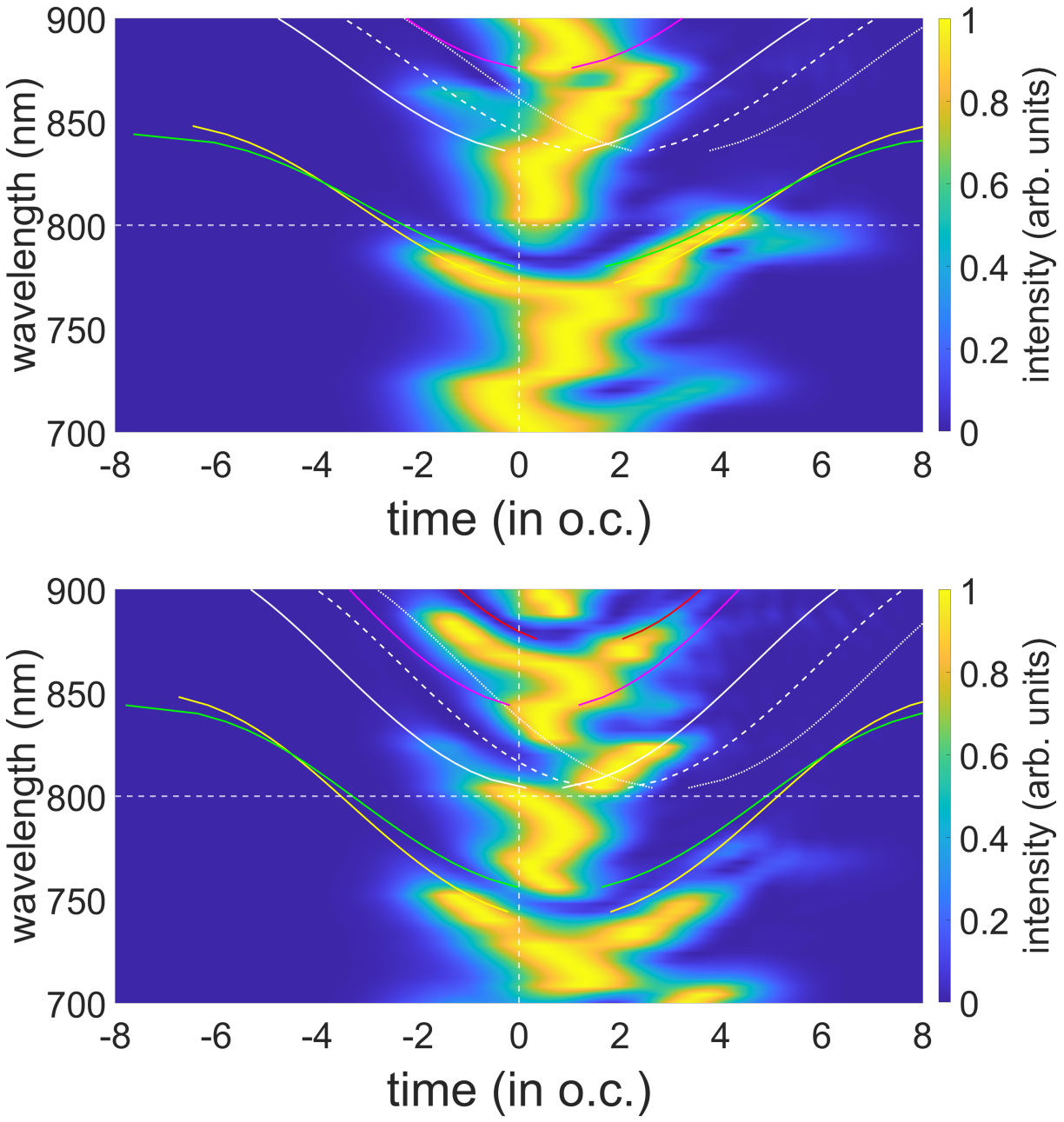

Figure 3.14: Temporal profile of radiation within 1ω of the 9th harmonic as a function of driving pulse wavelength in atomic hydrogen for a 20 o.c. pulse at (top) 2.0×10^{13} W/cm^2 and (bottom) 3.0×10^{13} W/cm^2. For each wavelength the results have been normalized to a maximum of 1 for sake of comparison. A vertical dashed line denotes the peak of the laser and a horizontal dashed line identifies the laser wavelength used as a base in this Chapter (i.e., 800 nm). Lines are drawn for delayed resonances as outlined in Table 3.1.

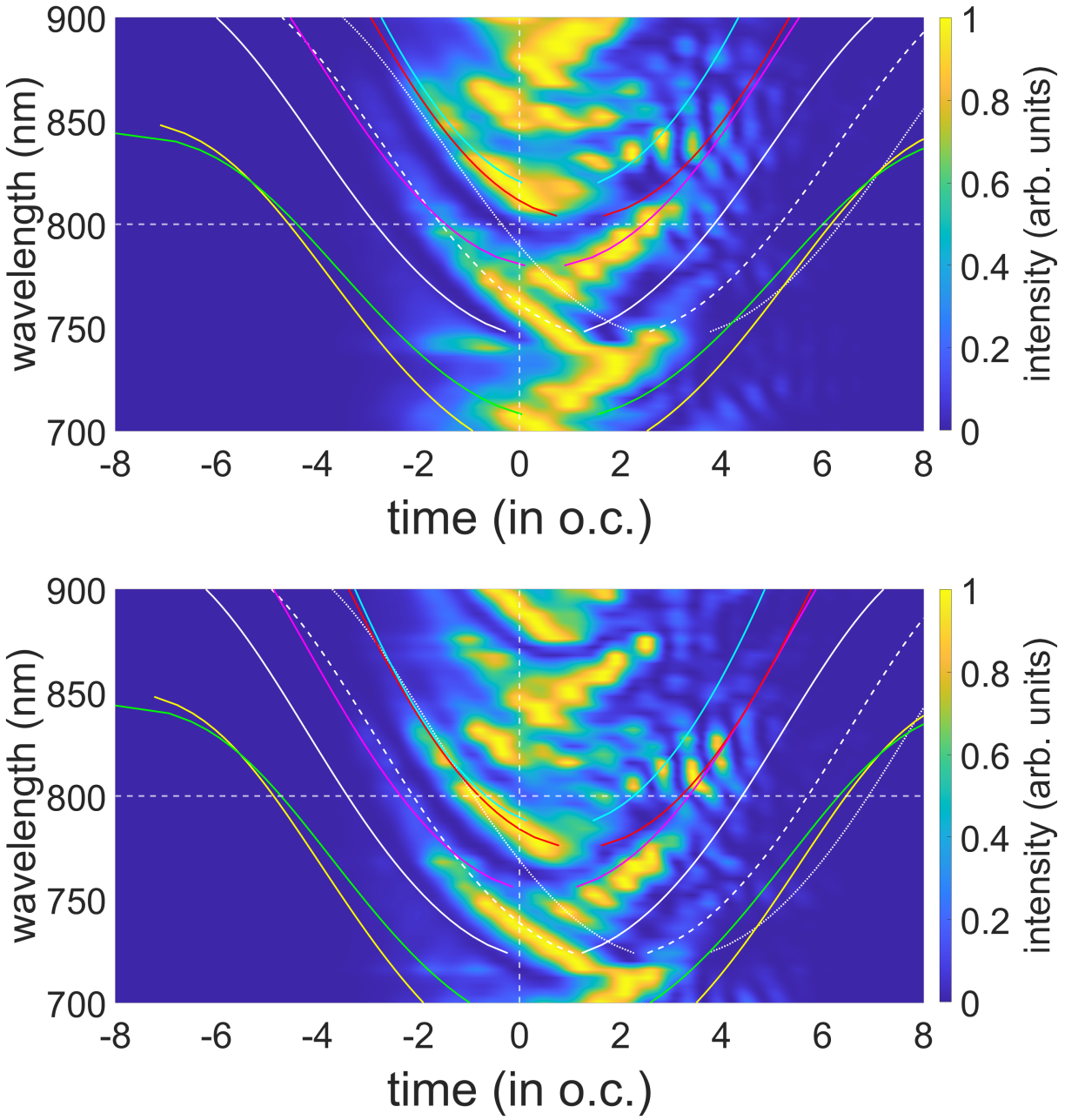

Figure 3.15: Same as Fig. 3.14, but for (top) 5.6×10^{13} W/cm^2 and (bottom) 7.0×10^{13} W/cm^2.

10^{13} W/cm^2, and (bottom) 5.6×10^{13} W/cm^2 – and discover an interesting contrast. For the lower intensity, radiation appears to be completely independent of CEP, consistently agreeing with delayed resonance times. This suggests that the semi-classical trajectory model is not applicable here. However, for the higher intensity, we see a clear effect, where the timing of the dominant radiation peak shifts linearly with CEP. As in earlier scans, the radiation is strongest at discrete times (every half-cycle) especially when close to the timing of the delayed resonance ($falling\ 10\omega \rightarrow 4s\ + 0.5\ o.c.$). While in previous scans, these discrete times were fixed, here they shift in the same way as the electric field, with a slope of 0.5 cycles per π-phase shift. The consistent timing of radiation – independent of resonance enhancement to its intensity – suggests similarity between multiphoton- and tunnelling-initiated trajectories at this intensity. Further study at the higher intensities will be necessary to verify this observation.

Thus, at lower intensities (3.8×10^{13} W/cm^2, as well as 2.0 and 3.0×10^{13} W/cm^2, not shown), this resonant radiation appears to be fully controlled by the laser envelope independent of the specific phase of the electric field. In contrast, at higher intensities (5.6 and 7.0×10^{13} W/cm^2), there is an interplay between the envelope effect (resonance time) and the field effect (trajectories and/or time of tunnel ionization). We however also note that the Keldysh parameter, typically used to separate multiphoton ($\gamma > 1$) from tunneling ($\gamma < 1$) behavior, falls in the multiphoton regime for all intensities – $\gamma = 1.7$ at 3.8×10^{13} W/cm^2 and $\gamma = 1.4$ at 5.6×10^{13} W/cm^2.

In Fig. 3.17, we apply the frequency-offset prediction of [100] (Eq. (3.2)) with $\alpha = 2\pi$ for scans of intensity and wavelength. We observe good agreement for certain features (e.g., red-shifted radiation near 6×10^{13} W/cm^2). However, the model does not well account for the majority of blue-shifted radiation – especially that near 2×10^{13} W/cm^2 – which displays a clear left-opening shape in contrast to the right-opening predictions.

3.5.1 Varying pulse envelope

In seeking to parse the effect of the field at the time of resonance versus the time of radiation, we additionally vary the envelope of the electric field. Specifically, we steepen either the rising or

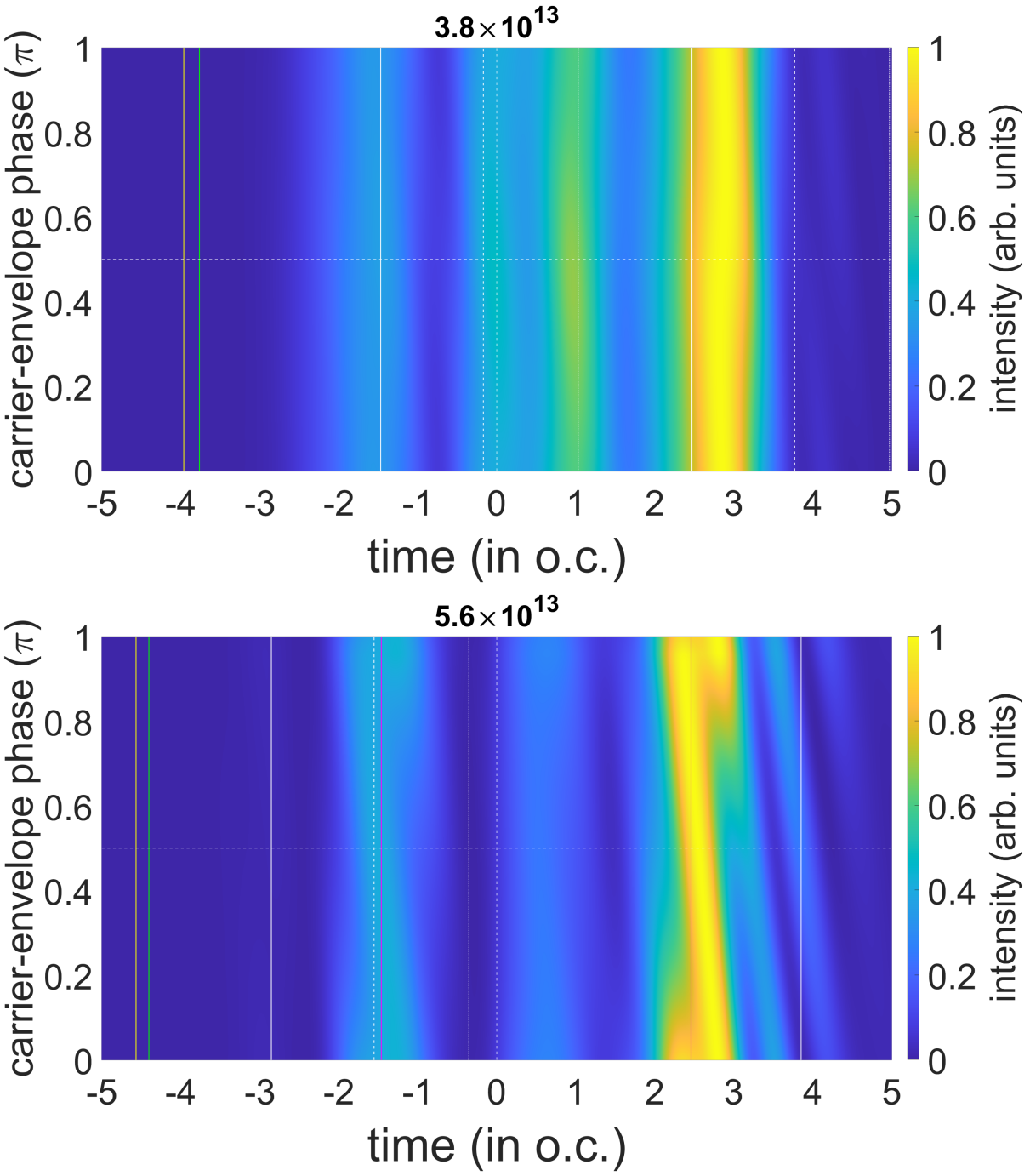

Figure 3.16: Temporal profile of radiation within 1ω of the 9th harmonic as a function of driving pulse CEP in atomic hydrogen for an 800 nm, 20 o.c. pulse at (top) 3.8×10^{13} W/cm^2, and (bottom) 5.6×10^{13} W/cm^2. A vertical dashed line denotes the peak of the laser and horizontal dashed lines identify the CEP shown in other scans ($\phi = \pi/2$). Lines are drawn for delayed resonances as outlined in Table 3.1.

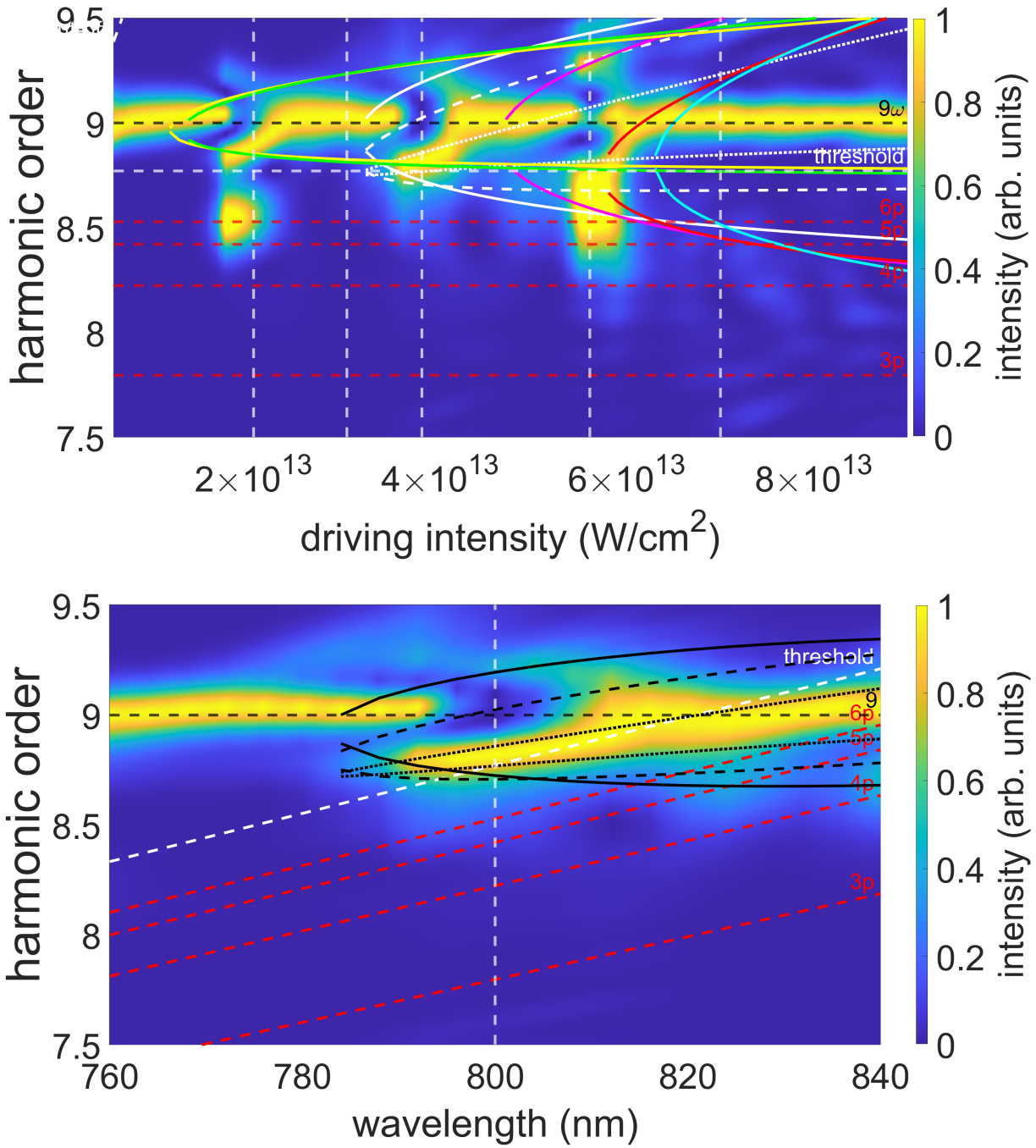

Figure 3.17: HHG spectra as a function of (top) peak intensity at $\lambda = 800$ nm and (bottom) driving wavelength at $I = 3.8 \times 10^{13}$ W/cm^2, in atomic hydrogen for a 20 o.c. pulse. We applied a Blackman window to dipole acceleration, and results for each intensity (top) or each wavelength (bottom) have been normalized to the maximum signal in the region between 8.75ω and 9.5ω. Overlaid curves denote the $\Delta\omega$ prediction, Eq. (3.2), for (top) delayed resonances as outlined in Table 3.1 and (bottom) $9\omega \to 3p$ resonances delayed by 0.5 (solid black), 1.8 (dashed black), and 3.0 (dotted black) optical cycles.

falling half of the envelope by using higher powers of the sine function – $\sin^4, \sin^6$ or $\sin^8$ rather than the standard $\sin^2$. We note that these even-integer powers retain necessary continuity and differentiability. Varying the envelope serves also as a tool for identifying resonance delays, and was valuable in the initial identification of the $9\omega \rightarrow 3p$ resonance and delays.

In Fig. 3.18, we plot temporal profiles for various envelopes. We note that plotting of this discrete scan differs from other Figures, with results for each envelope appearing as an independent horizontal bar. We first observe that the most intense (last) feature is minimally affected (timing or intensity) by modification of the rising side of the pulse, but shifts earlier when the falling side steepens. Likewise, the earliest feature is unaffected by the falling side (as required by causality) but shifts later as the rising side steepens. Considering the second feature – which occurs right at the peak of the pulse for $\sin^2$ ramp-up – we see it shifts in time similarly to the first, with a slight increase in intensity for envelopes with steeper rise. Finally, the third feature's (most noticeable for the original $\sin^2$ envelope) position does not change when the back of the pulse steepens, but shifts later (merging with the fourth) as the front of the pulse steepens. The intensity of the third feature does not appear to change greatly, but it is difficult to distinguish from the fourth feature for both steepest envelopes. In summary, the character of the earliest three radiation features appears to be controlled by the rising side of the pulse, including the feature occurring a full cycle after the peak.

3.6 Deviations from predicted resonance times

In various scans above, we noted that the observed radiation features generally fit well with predictions of delayed resonances, but that the two sometimes disagreed somewhat for parts of the scan. Thus, we sought to further test the consistency of these delays. A simple way to do this is to choose a particular resonance and fix the resonance time, T_r (in cycles from peak) across scans. One would then expect that the respective radiation feature will occur along vertical lines on temporal profile scans, thus clearly highlighting potential deviations and trends.

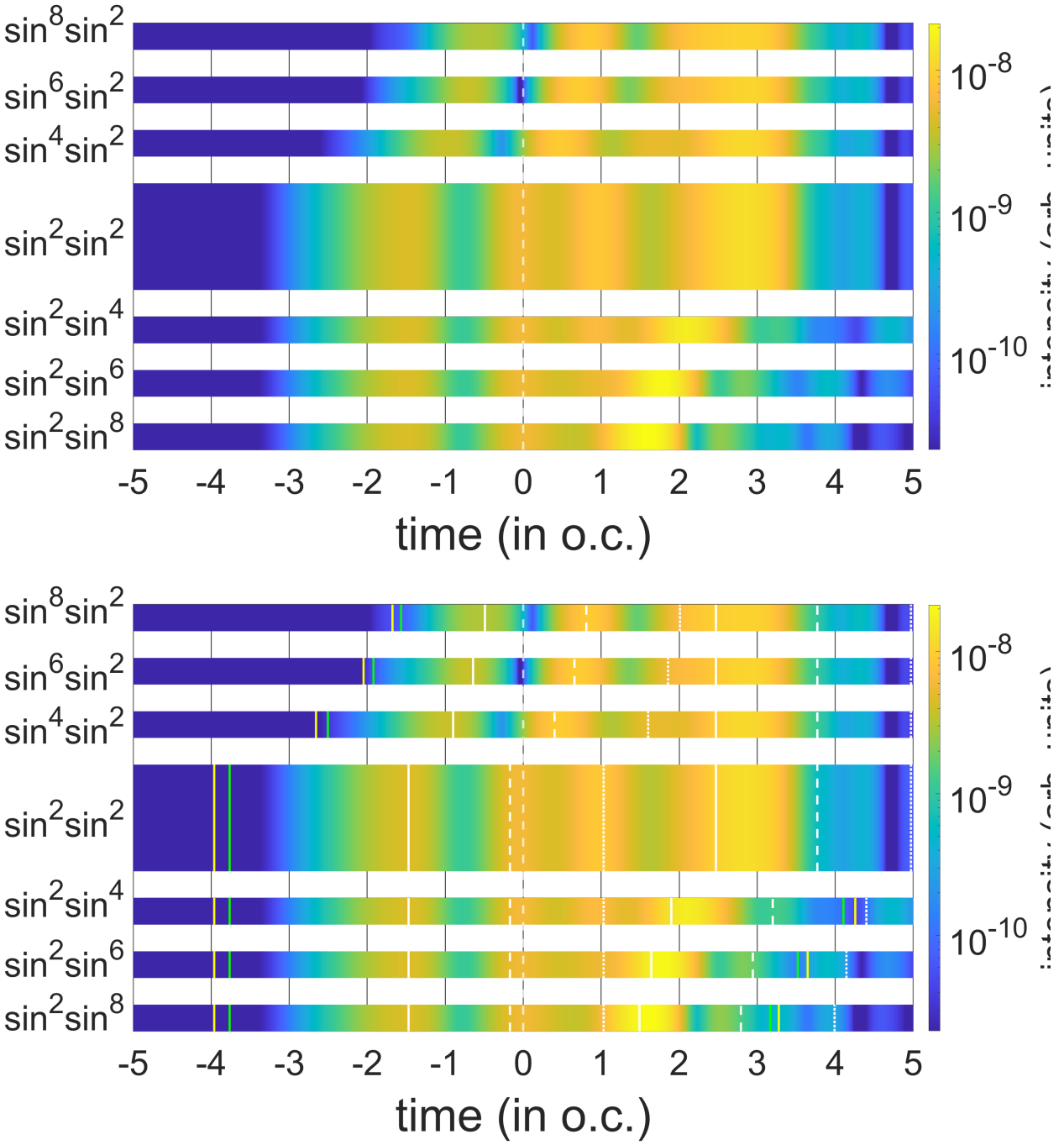

Figure 3.18: Temporal profile of radiation within 1ω of the 9th harmonic for a selection of electric field envelopes (horizontal bars) in atomic hydrogen for an 800 nm, 20 o.c. pulse at 3.8×10^{13} W/cm^2. We note that the results have **not** been normalized. A vertical dashed line denotes the peak of the laser. The center bar corresponds to the sine-squared envelope used elsewhere in this thesis. In the lower panel, lines are drawn for delayed resonances as outlined in Table 3.1.

To this end, we again consider the resonance condition

$$\frac{I}{4\omega^2}\cos^4\left(\pm\frac{T_r\pi}{N_\tau}\right) = N_\gamma - Z^2(E_n - E_0), \tag{3.3}$$

as in Eq. (3.1). Here, we however fix E_i as the hydrogen atom energies but allow variation of the Coulomb charge, Z. In order to keep T_r fixed, it is required to vary multiple parameters together. Still, many different variations are possible within the parameter space. To constrain our investigation, we vary pairs of continuous parameters: pulse duration in cycles (N_τ), Coulomb charge (Z), wavelength ($\lambda \propto 1/\omega$), and intensity (I). We did not vary the envelope shape since only discrete $\sin^{2n}$ envelopes are viable, and excluded the CEP as a parameter since it does not affect resonance time or – as shown previously – radiation at low peak intensities. These considerations result in six distinct scans for each resonance (defined by fixing N_γ and E_n), where we scan one parameter over a certain range while changing the second parameter accordingly to keep T_r constant, as described in Table 3.2. The parameter range is chosen such that the HHG cut-off at $I_P + 3.17U_P$ remains consistently larger than 10ω.

3.6.1 Deviations in radiation features around 9-photon resonance to 3p state

To investigate the $9\omega \to 3p$ resonance, we consider scans in the parameter subspace defined by $N_\gamma = 9$, $E_n = E_{|3p\rangle} = -0.056$ a.u., and $T_r = 2.0$ o.c., which includes our primary case of investigation analyzed in detail above, i.e., $I_0 = 3.8 \times 10^{13}$ W/cm^2, $\lambda_0 = 800$ nm ($\omega_0 = 0.057$ a.u.), $N_{\tau,0} = 20$ o.c., $Z_0 = 1$. As mentioned above, by scanning along a variety of curves with constant T_r, we intend to identify the stability of radiation features as well as the potential effects of the three dimensionless parameters. In particular, all scans shown in Table 3.2 have the common signature that $z = \frac{U_P}{\omega}$ decreases or remains fixed along the scan, while there are different trends for $\frac{I_P}{\omega}$ and $\frac{U_P}{I_P}$.

First, we demonstrate the importance of dimensionless parameters by considering a three-parameter scan which keeps simultaneously constant all of: $\frac{U_P}{\omega}, \frac{I_P}{\omega}, \frac{U_P}{I_P}$, and T_r for *each* of the resonances. We do this by scanning Z (from 0.9 to 1.1) and fixing $\lambda = \frac{800}{Z^2}$ nm ($\omega \propto Z^2$) and

Title	N_τ o.c.	Z	λ nm	I W/cm^2	$z = \frac{U_P}{\omega}$	$\frac{I_P}{\omega}$	$\frac{U_P}{I_P}$	$\frac{I_P+U_P}{\omega}$
$Z - \lambda$	20	$0.90, 0.905$ $...1.10$	numeric solve	3.8×10^{13}	$2.2 \searrow 1.0$	$8.1 \nearrow 9.2$	$0.27 \searrow 0.10$	$10.3 \searrow 10.2$
$Z - I$	20	$0.95, 0.9525$ $...1.05$	800	$\frac{4\omega_0^2\left(N_\gamma\omega_0 - Z^2(E_n - E_0)\right)}{\cos^4\left(\pm\frac{T_r\pi}{N_{\tau,0}}\right)}$	$2.4 \searrow 0.5$	$7.9 \nearrow 9.7$	$0.30 \searrow 0.05$	$10.3 \searrow 10.2$
$\lambda - I$	20	1	$750, 755$ $...850$	$\frac{4\omega^2\left(N_\gamma\omega - Z_0^2(E_n - E_0)\right)}{\cos^4\left(\pm\frac{T_r\pi}{N_{\tau,0}}\right)}$	$2.1 \searrow 0.9$	$8.2 \nearrow 9.3$	$0.25 \searrow 0.09$	$10.3 \searrow 10.2$
$N_\tau - Z$	$10, 10.5$ $...30$	$\sqrt{\frac{N_\gamma\omega_0 - \frac{I_0}{4\omega_0^2}\cos^4\left(\pm\frac{T_r\pi}{N_\tau}\right)}{E_n - E_0}}$	800	3.8×10^{13}	1.5	$9.4 \searrow 8.6$	$0.16 \nearrow 0.17$	$10.9 \searrow 10.1$
$N_\tau - \lambda$	$10, 10.5$ $...30$	1	numeric solve	3.8×10^{13}	$1.7 \searrow 1.4$	$9.3 \searrow 8.7$	$0.19 \searrow 0.16$	$11.0 \searrow 10.1$
$N_\tau - I$	$10, 10.5$ $...30$	1	800	$I_0\frac{\cos^4\left(\pm\frac{T_r\pi}{N_{\tau,0}}\right)}{\cos^4\left(\pm\frac{T_r\pi}{N_\tau}\right)}$	$2.8 \searrow 1.3$	8.8	$0.32 \searrow 0.15$	$11.6 \searrow 10.1$
Base	20	1	800	3.8×10^{13}	1.47	8.78	0.167	10.24

Table 3.2: Classification of two-parameter scans keeping $9\omega \to 3p$ resonance time T_r fixed. For each scan, two parameters are fixed at their base values and two are varied: one parameter is given as a range of equally-spaced values, while the other is determined by solving Eq. (3.3) analytically or numerically. The final four columns describe the range and trends of dimensionless parameters across the scans.

$I = Z^6 * 3.8 \times 10^{13}$ W/cm^2. With this variation for the TDSE in length gauge:

$$i\frac{\partial}{\partial t}\psi(\vec{r},t) = \left[-\frac{\nabla^2}{2} + -\frac{1}{r} + \vec{E}(t)\cdot\vec{r}\right]\psi(\vec{r},t), \tag{3.4}$$

with $E \to E_0\sqrt{I} = E_0 Z^3$ and $-\frac{1}{r} \to -\frac{Z}{r}$, we get

$$i\frac{\partial}{\partial t}\psi(\vec{r},t) = \left[-\frac{\nabla^2}{2} + -\frac{Z}{r} + Z^3\vec{E_0}(t)\cdot\vec{r}\right]\psi(\vec{r},t), \tag{3.5}$$

which is equivalent to Eq. (3.4) under the transform $t \to \frac{t'}{Z^2}$ and $\vec{r} \to \frac{\vec{r}'}{Z}$:

$$i\frac{\partial}{\partial t}\psi\left(\frac{\vec{r}'}{Z},\frac{t'}{Z^2}\right) = \left[-\frac{\nabla^2}{2} + -\frac{Z^2}{r'} + Z^3\vec{E_0}\left(\frac{t'}{Z^2}\right)\cdot\frac{\vec{r}'}{Z}\right]\psi\left(\frac{\vec{r}'}{Z},\frac{t'}{Z^2}\right). \tag{3.6}$$

Thus, the system has merely been rescaled (please note that the derivation is much the same in the velocity gauge). Consistently, the results in Fig. 3.19 demonstrate that a simultaneous variation of wavelength across $660 - 988$ nm and intensities from $2.0 - 6.7 \times 10^{13}$ W/cm^2 along with a variation of the Coulomb charge Z produces the same radiation (up to a factor). Beyond pure mathematical interest, this highlights a utility of dimensionless parameters over traditional ones. This also happens to be a fair test of the numerical stability of our code – we did not alter our grid or other numerical parameters and yet achieved consistent observables (incl. those not shown such as full complex spectrum through the cut-off, total ionization, and excited state population after the pulse).

Now, we turn to scans of more practical interest for the present purpose. We begin by considering the first three types of scans in Table 3.2. In each of these scans, two of the three parameters Z, λ, and I are varied. This results in a change of all three dimensionless parameters, however the trends for the dimensionless parameters are the same across the scans ($\frac{U_P}{\omega}$ and $\frac{U_P}{I_P}$ decreasing, $\frac{I_P}{\omega}$ increasing). Since the trends are opposite for $\frac{I_P}{\omega}$ (increasing) and $\frac{U_P}{\omega}$ (decreasing), the energy (in ω) required for field-shifted ionization, $\frac{I_P+U_P}{\omega}$, and for resonant excitation, $\frac{E_n+U_P}{\omega}$, at the peak of the pulse remains almost the same, up to about 0.1.

The results of the respective scans are shown in Fig. 3.20 and surprisingly show similar radiation trends in each of these scans. To avoid implying a specific association between trends and a particular parameter (e.g., Z or $\frac{U_P}{\omega}$), we discuss the results in terms of progress along a scan or

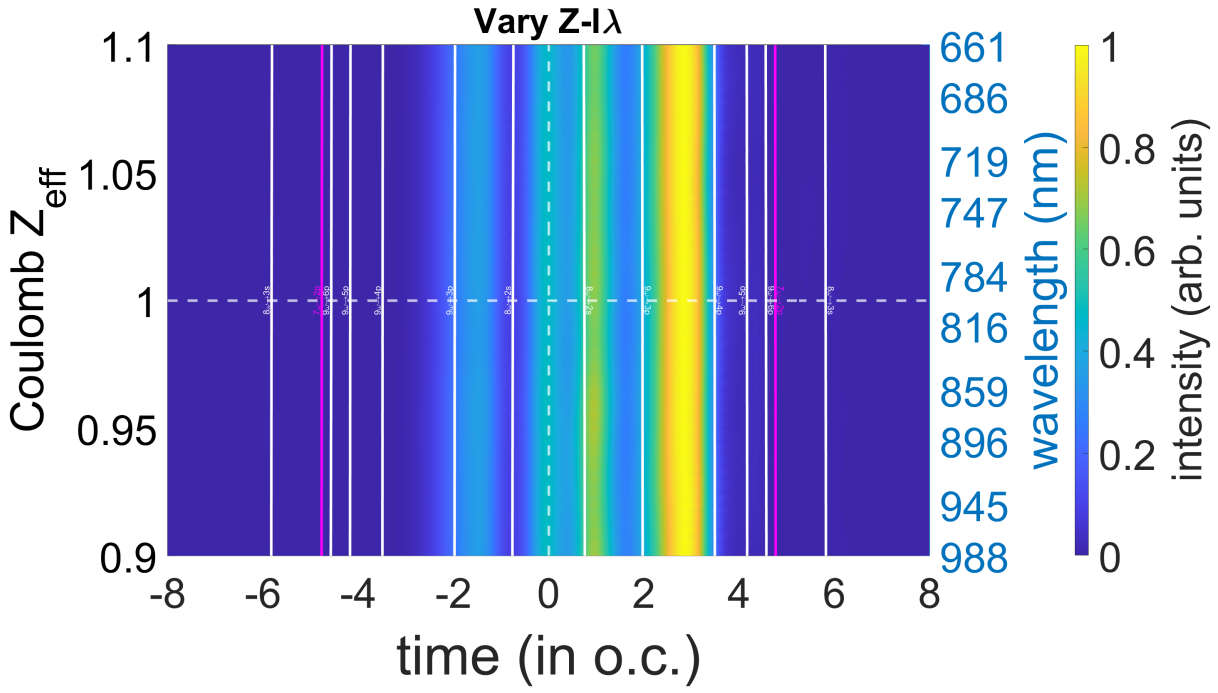

Figure 3.19: Temporal profile of radiation within 1ω of the 9th harmonic as a function of atomic nuclear charge Z in a hydrogen-like atom while also varying wavelength ($\lambda = \frac{800}{Z^2}$ nm) and intensity ($I = Z^6 * 3.8 \times 10^{13}$ W/cm^2) to keep resonance times fixed. A 20 o.c. pulse was used throughout. For each Z the results have been normalized to a maximum of 1 for sake of comparison (note: spectral intensity here scales roughly $\propto \sqrt{Z}$). A vertical dashed line denotes the peak of the laser and a horizontal dashed line identifies the pulse parameters used as a base in this Chapter (i.e., $Z = 1, I = 3.8 \times 10^{13}$ W/cm^2, $\lambda = 800$ nm). Overlaid with lines denoting resonance times for 7- (magenta) and 8- or 9- (white) photon resonances.

location in the associated figure, where "up" is further up on the respective plot, and corresponds to an increase of the first scanned variable. We first observe a transition between dominance of the outer radiation features (earlier associated with *rising* and *falling* $9\omega \rightarrow 3p\ + 0.5$ *o.c.*) and the inner ones (*rising* $9\omega \rightarrow 3p\ + 1.8$ *o.c.* and *rising* $9\omega \rightarrow 3p\ + 3.0$ *o.c.*) near the base parameters, which are denoted by the horizontal white line in each plot. Above this point (e.g., $Z > 1$ for the top panel), the outer features dominate, while the inner features dominate below it. Additionally, the outer radiation features shift inwards significantly toward the top of the scans, tending to occur closer to the peak of the pulse. At the same time these features decrease in magnitude, as can be best seen in Fig. 3.21, where we show the same data as in Fig. 3.20 (top panel) but this time un-normalized. Near the bottom of the scans, the inward trend is smaller, but still noticeable. The inner radiation also decreases in magnitude, even more rapidly, when moving up the scan, but the timing is more consistent. The peak of the second feature (*rising* $9\omega \rightarrow 3p\ + 1.8$ *o.c.*) appears slightly earlier in time as one moves down in the scan. Actually, the prediction for the resonance time is best matched slightly below the base parameters. However, the un-normalized plot (cf. Fig. 3.21) suggests that the radiation feature is indeed more widening in time than shifting. The third feature stays well-matched with the prediction for all portions of the scans, as long as it is distinguishable. Other identified resonance delays do not appear to play a role, nor do resonances not previously associated match the shape of radiation curves. From these results, we can again definitively state that radiation behavior depends not on traditional parameters (I, λ, Z) but rather on an alternate set such as the dimensionless parameters of Table 3.2. Despite very different traditional parameter changes across the three scans, radiation looks much the same for each scan. Unfortunately, we cannot tease out which dimensionless parameter(s) predict behavior – $\frac{U_P}{\omega}$, $\frac{U_P}{I_P}$, and $\frac{I_P}{\omega}$ have similar trends for all three scans. Further, the $Z - I$ scan has the widest range for each parameter, consistent with the impression of Fig. 3.20). Thus, the loss of agreement with resonance predictions may be attributed to: perturbative behavior (decreasing $\frac{U_P}{\omega}$), greater multiphoton dominance over tunneling (decreasing $\frac{U_P}{I_P}$), more photons involved in field-free interactions (increasing $\frac{I_P}{\omega}$), or some combination.

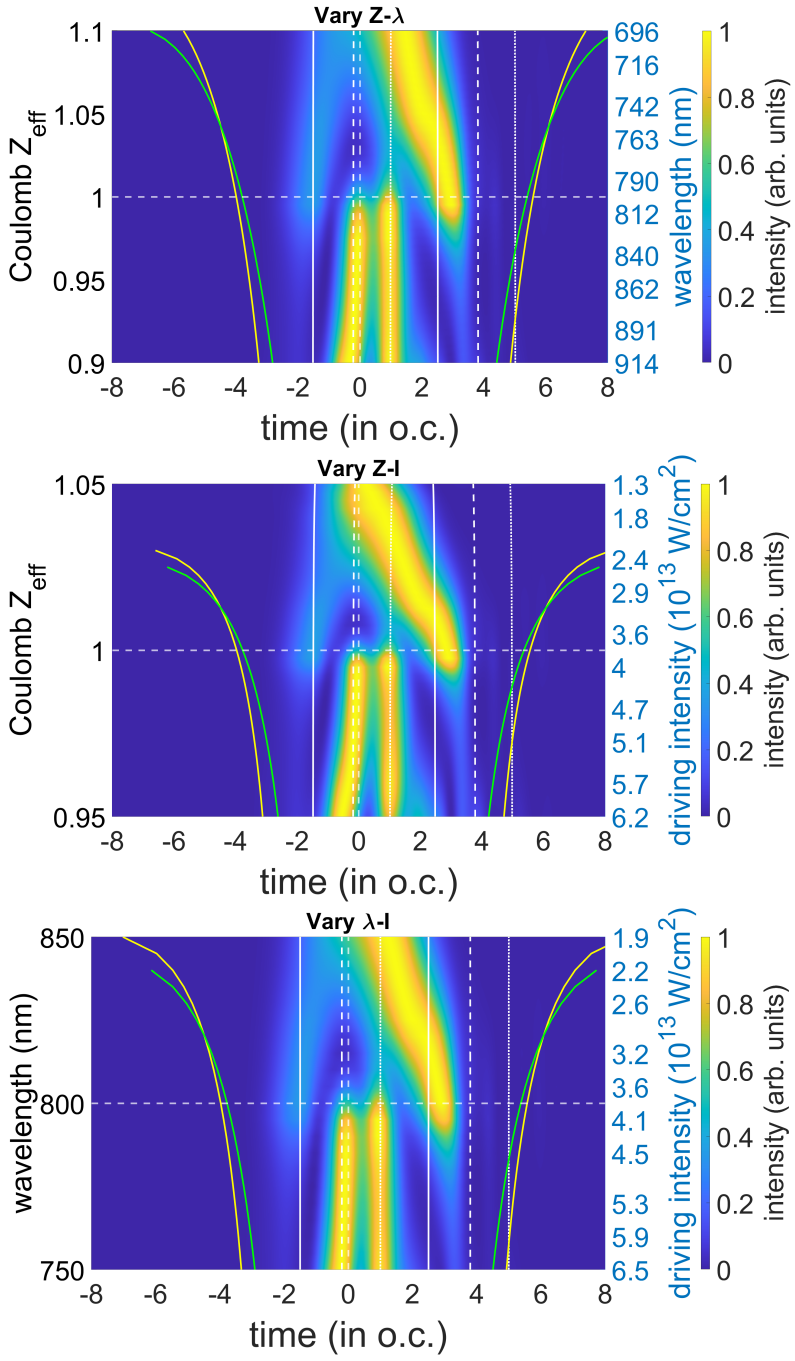

Figure 3.20: Temporal profile of radiation within 1ω of the 9th harmonic for scans of: (top) atomic nuclear charge Z and wavelength λ, (middle) Z and intensity I, and (bottom) λ and I. For all scans, the $9\omega \rightarrow 3p$ resonance time is kept fixed. A 20 o.c. pulse was used throughout. For each element of the scan (i.e., horizontal slice), the results have been normalized to a maximum of 1 for sake of comparison. A vertical dashed line denotes the peak of the laser and a horizontal dashed line identifies the pulse parameters used as a base in this Chapter (i.e., $Z = 1, I = 3.8 \times 10^{13}$ W/cm^2, $\lambda = 800$ nm). Lines are drawn for delayed resonances as outlined in Table 3.1.

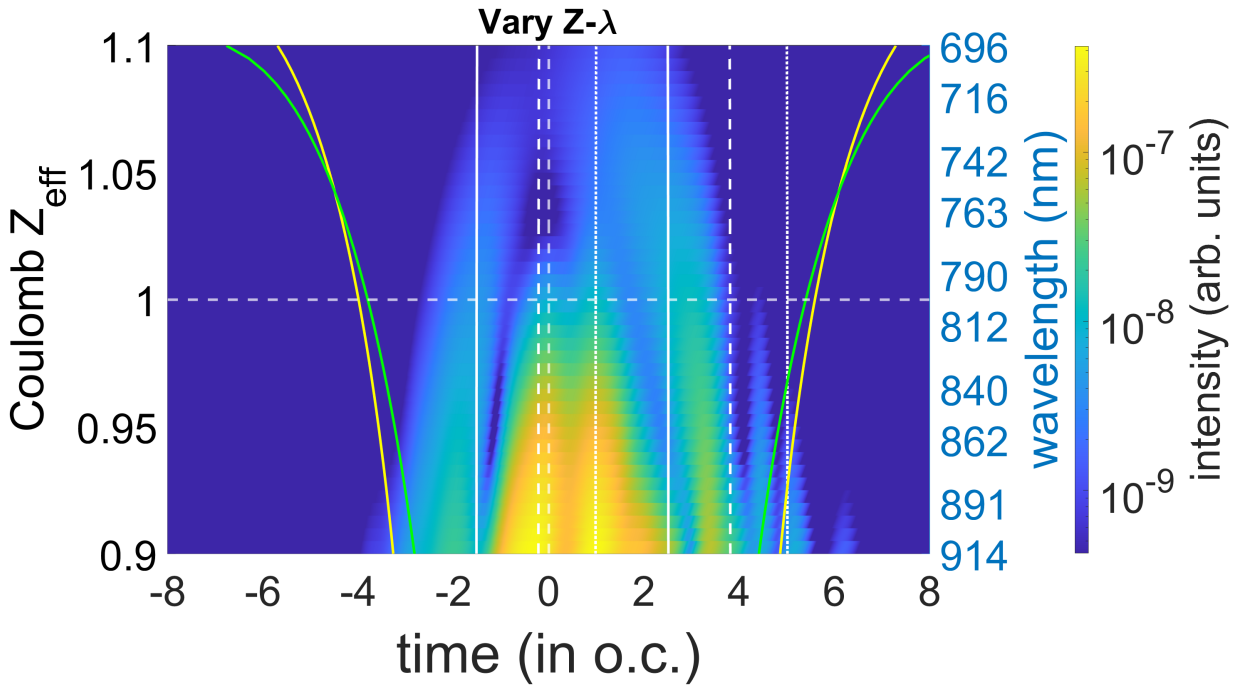

Figure 3.21: Same as top panel of Fig. 3.20, but with **no** normalization for each Z and on a logarithmic scale. Unscaled versions for other panels show similar trends, except with an overall $\approx I^4$ scaling of the radiation magnitude.

For the remainder of the scans, the primary scanned variable is pulse duration in optical cycles, with I, λ, or Z adjusted to keep $T_r = 2$. For these scans the set of three dimensionless parameters vary differently (see Table 3.2), though $\frac{I_P+U_P}{\omega}$ and $\frac{E_n+U_P}{\omega}$ do have similar trends. Additionally, it is worth considering N_τ itself as a meaningful dimensionless parameter describing the (inverse) spectral bandwidth and the inter-cycle envelope stability.

In Fig. 3.22, there is a similar transition in dominance of the features across the base parameters that we have noticed in the first three scans. The outer (inner) radiation dominates at the top (bottom) of the scans. In this case, the absolute intensity of the outer features increases up the scan, while the inner ones decrease (cf. un-normalized plot Fig. 3.23). The peaks of the outer features (*rising* and *falling* $9\omega \rightarrow 3p\ + 0.5$ *o.c.*) show a clear 'V'-like trend away from the peak of the pulse. This follows the shape of the lower-intensity resonance lines such as $9\omega \rightarrow 4p$, possibly suggesting that the $3p$ state shifts slightly less than U_P and the scans are highlighting this deviation. On the other hand, the results in Fig. 3.23 de-emphasize the shifting of the peaks and again more clearly show that the outer features widen away from the prediction. The timing of the second radiation feature (*rising* $9\omega \rightarrow 3p\ + 1.8$ *o.c.*) appears consistent with the prediction – constant. The third feature (*rising* $9\omega \rightarrow 3p\ + 3.0$ *o.c.*) – which dominates the radiation for shorter-than-base pulses – is more complicated, with the peak appearing to oscillate slightly earlier and later (overall slightly earlier than prediction). At the bottom of the scans, radiation diverges from the $9\omega \rightarrow 3p$ resonances and appears to correspond to other resonances (namely, $10\omega \rightarrow 4s$, $10\omega \rightarrow 3s$ and/or $9\omega \rightarrow 2p$). For the three scans, we contrast the similarity of radiation structures to the differences in trends of the dimensionless parameters $\frac{U_P}{\omega}$, $\frac{U_P}{I_P}$, and $\frac{I_P}{\omega}$. Therefore, it seems likely that the effects are a result of increasing pulse duration itself (potentially via extending durations of resonance) and altering the resonances occurring during the pulse (for which $\frac{I_P+U_P}{\omega}$ serves as a proxy).

Continuing the discussion of the first three scans, we note that values of $\frac{I_P}{\omega} \approx 9.3$ found at the top of Fig. 3.20 do not appear to disrupt resonant behavior near the bottom of the upper panels in Fig. 3.22. However, low values of $\frac{U_P}{\omega}(\lessapprox 1)$ and $\frac{U_P}{I_P}(\lessapprox 0.1)$ are not included in these latter

scans, so we may make no further conclusions to their roles. Overall, the two trios of scans seem to explore somewhat orthogonal spaces.

When varying more than two parameters simultaneously, it is possible to construct scans with other trends of dimensionless parameters (e.g., keeping $\frac{U_P}{I_P}$ constant while varying $\frac{U_P}{\omega}$ and $\frac{I_P}{\omega}$), and we recommend this for future investigation.

3.7 Short and long pulses

In prior results, we have focused on pulses with durations near 20 cycles. It is valuable now to briefly discuss effects when the driving pulse has either much shorter or much longer duration. For short pulses, the envelope variation may be significant even within a single cycle, and the "average" energy $U_P(t)$ becomes less sensible. On the other hand for long pulses, the relative intensity stability means both that resonances occur over longer stretches of the pulse and that the envelope does not vary significantly over the period between resonance and radiation.

For a 4-cycle pulse of 3.8×10^{13} W/cm^2, we perform a scan of CEP (Fig. 3.24). We observe radiation at CEP-dependent times, suggesting trajectory-like behavior as seen only at the higher intensity in Sec. 3.16. However, this radiation shows no enhancement when it coincides with predicted radiation times. Instead, radiation is strongest just at and after the peak of the pulse, as expected for "normal HHG."

In Fig. 3.25, we extend the scan of Fig. 3.6 through 50 o.c.. For pulses longer than about 30 o.c., the radiation predictions begin to break down. First, the majority of radiation occurs within the first two cycles after the laser peak, not matching any of the previously-identified resonance delays. Secondly, the earliest radiation feature begins to shift earlier than the *rising* $9\omega \rightarrow 3p$ + 0.5 *o.c.* delayed resonance. Agreement with other resonances would require large delays (greater than 3 cycles) and initial investigations find poor agreement.

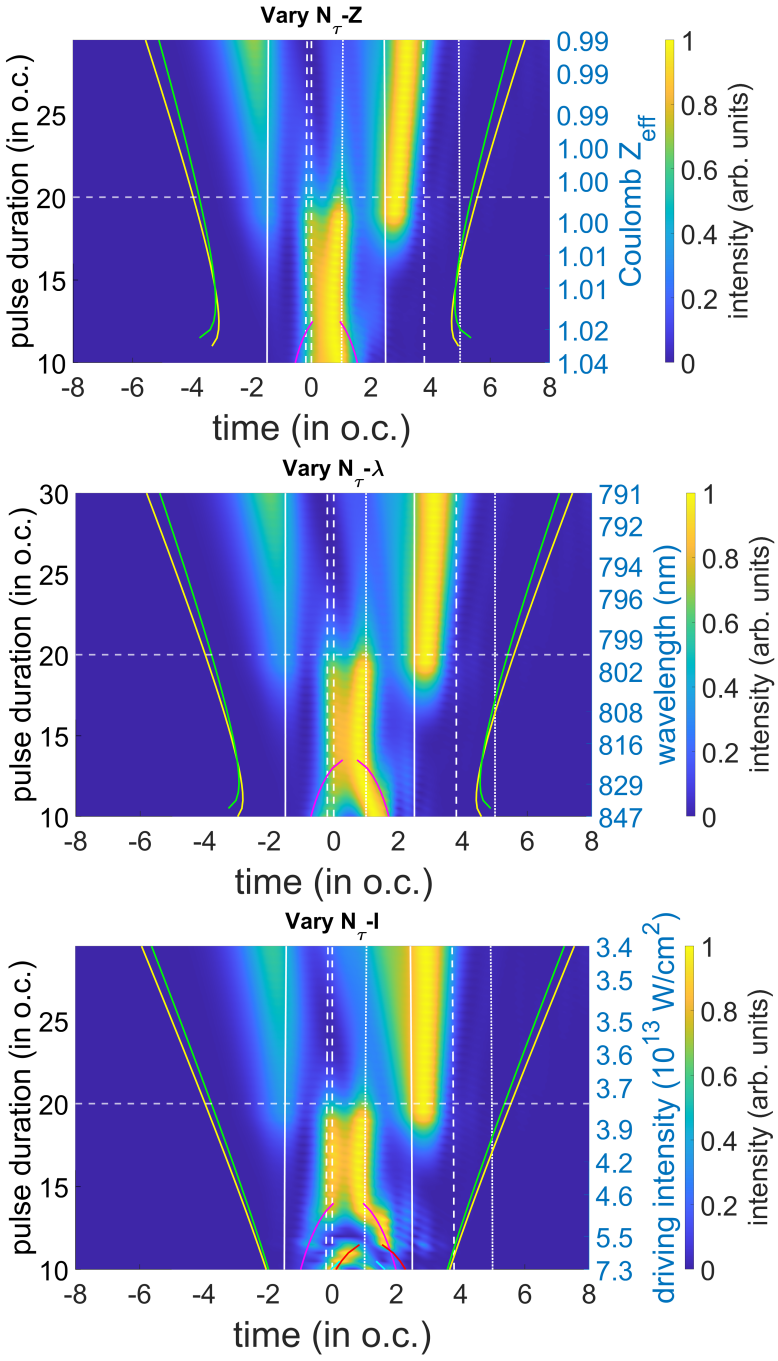

Figure 3.22: Temporal profile of radiation within 1ω of the 9th harmonic for scans of pulse duration, N_τ, in optical cycles and (top) atomic nuclear charge Z, (middle) wavelength λ, and (bottom) intensity I. For all scans, the $9\omega \rightarrow 3p$ resonance time is kept fixed. For each element of the scan (i.e., horizontal slice), the results have been normalized to a maximum of 1 for sake of comparison. A vertical dashed line denotes the peak of the laser and a horizontal dashed line identifies the pulse parameters used as a base in this Chapter (i.e., $Z = 1, N_\tau = 20$ o.c., $I = 3.8 \times 10^{13}$ W/cm^2, $\lambda = 800$ nm). Lines are drawn for delayed resonances as outlined in Table 3.1.

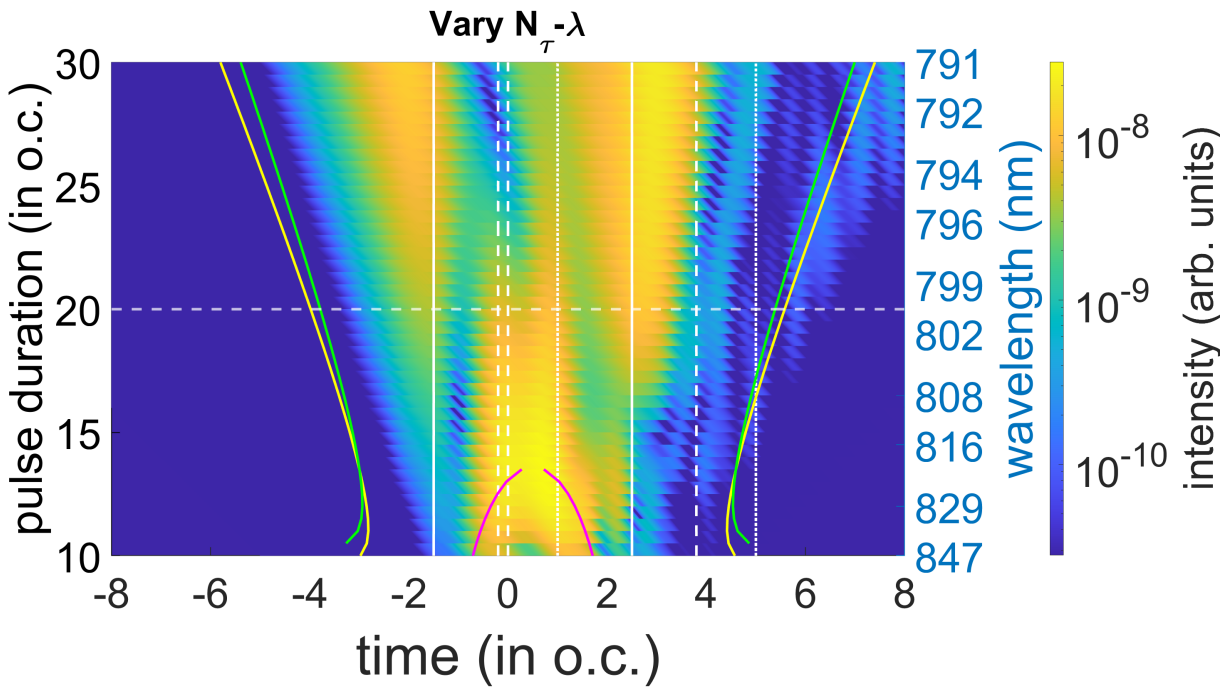

Figure 3.23: Same as middle panel of Fig. 3.22, but with **no** normalization for each N_τ and on a logarithmic scale. Unscaled versions for other panels show similar trends, except with an overall $\approx I^4$ scaling of the radiation magnitude.

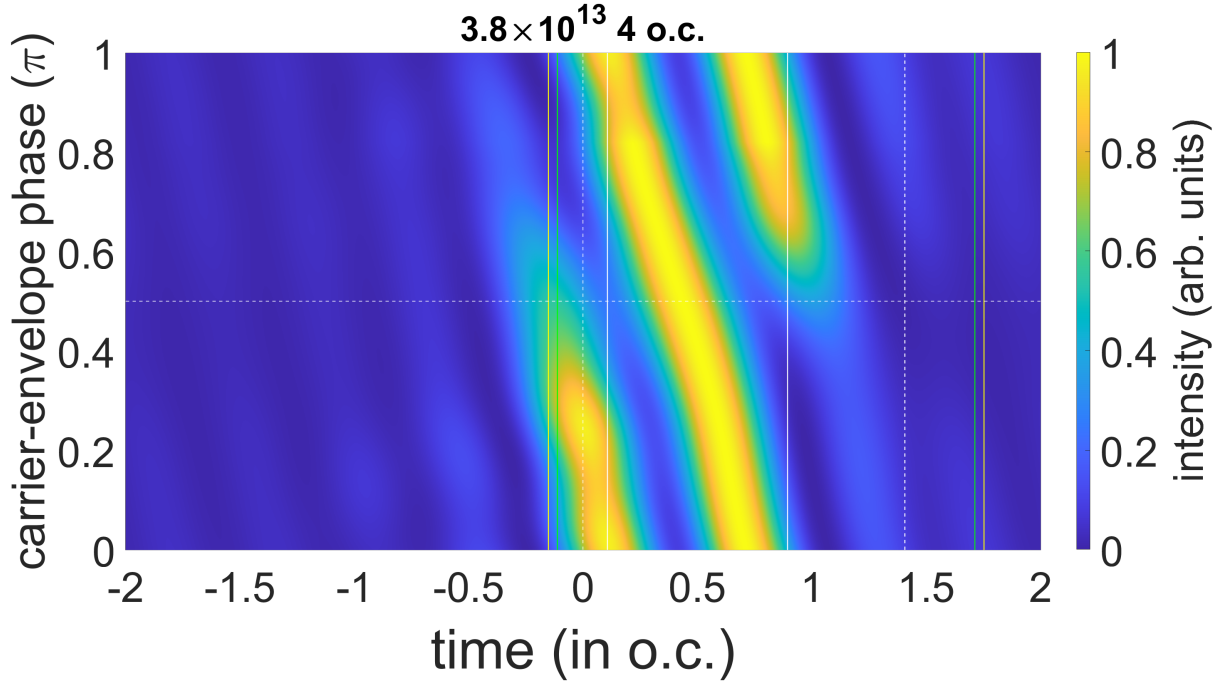

Figure 3.24: Temporal profile of radiation within 1ω of the 9th harmonic as a function of driving pulse CEP in atomic hydrogen for an 800 nm, 4 o.c. pulse at 3.8×10^{13} W/cm^2. A vertical dashed line denotes the peak of the laser. Lines are drawn for delayed resonances as outlined in Table 3.1.

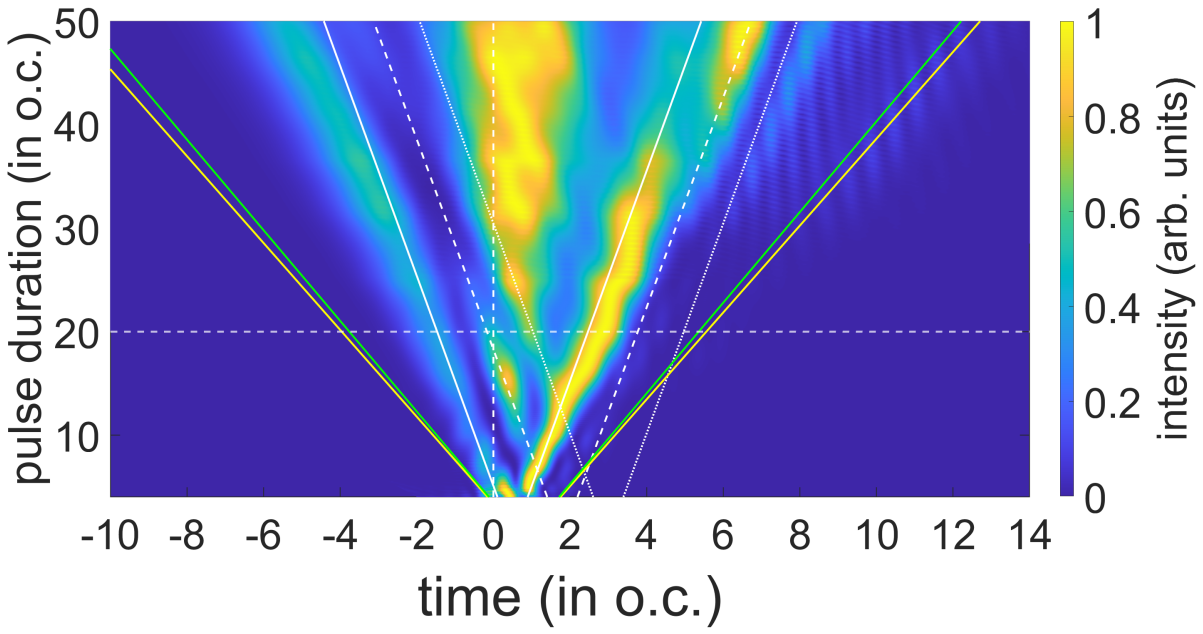

Figure 3.25: Same as Fig. 3.5, but extending to durations up to 50 o.c..

3.8 Appearance in other parameter regimes

While the appearance of this resonance-enhanced behavior requires a great deal of further study within the relatively narrow parameter space described above, we would emphasize that the effects are not limited to hydrogen or near-IR lasers. To that end, we present preliminary results for atomic hydrogen driven by a mid-infrared (1600 nm) laser and helium atoms driven by a laser on the edge close to the UV regime (400 nm). We also recall that Camp et al.'s investigation [100] was for argon atoms driven by a near-IR laser.

3.8.1 400 nm helium

For helium, we perform simulations using the SAE potential presented in Ch. 2, and select a laser with similar dimensionless parameters to that of the 3.8×10^{13} W/cm^2 hydrogen results above. Namely, we select a wavelength of 400 nm such that $U_P/\omega = 8.1$ (vs. 8.8 above), and an intensity 3.3×10^{14} W/cm^2 such that energy in units of ω remains similar for the HHG cut-off (13.1ω vs. 13.4ω) and the ponderomotive energy (1.6ω vs. 1.5ω), as well as a similar Keldysh parameter ($\gamma = 1.6$ vs. 1.7). We retain the same number of cycles, i.e., 20. The most notable features of the resultant spectrum (Fig. 3.26) are a peak below 7ω (broader and weaker than for hydrogen) and a 9ω radiation suppressed relative to both nearby frequencies and neighboring harmonics, just like in hydrogen. Varying driving laser intensity around 3.3×10^{14} W/cm^2 and wavelength around 400 nm, we again see (Fig. 3.27) a clear region where radiation below and above 9ω dominates that at the harmonic frequency. In Fig. 3.28, we show temporal profiles for scans of (top) duration, (middle) peak intensity, and (bottom) driving wavelength. The structures appear consistent with those found for hydrogen atoms (Figs. 3.5-3.8).

3.8.2 1600 nm hydrogen

HHG driven by mid-infrared pulses has received growing interest in recent years [103–105]. Due to the scaling of the HHG cut-off ($I_P + 3.17\frac{I}{4\omega^2}$) and lower probabilities of ionization (i.e., higher

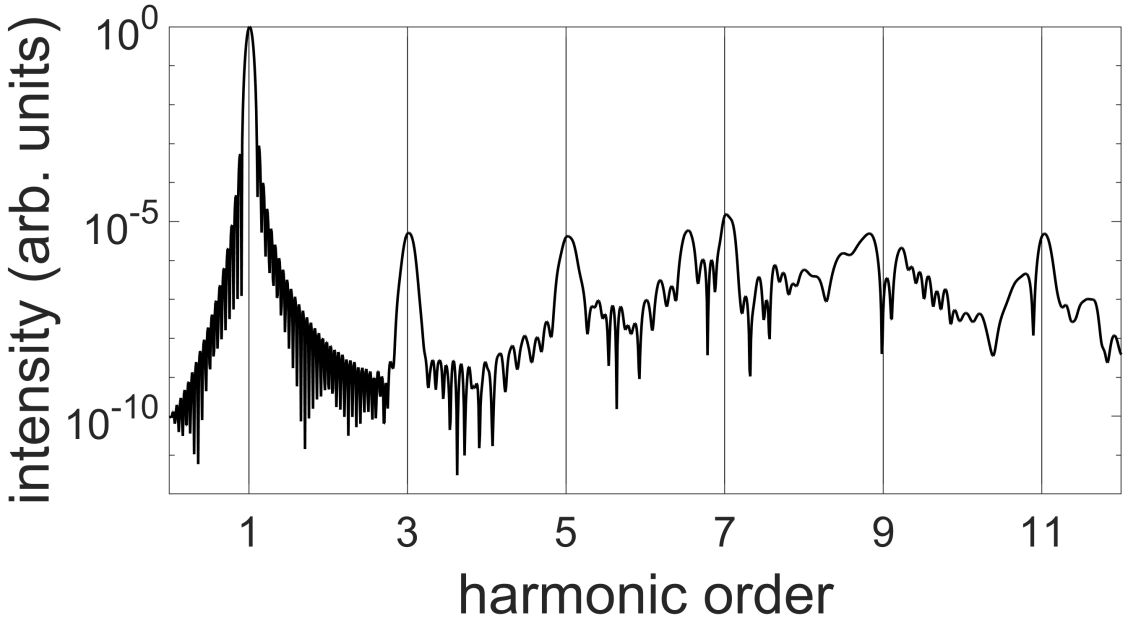

Figure 3.26: High harmonic spectrum generated in helium, exhibiting a rich structure in the near-threshold region of the spectrum between harmonics 5 and 12. The helium ionization threshold of 0.94 a.u. $= 8.1\omega$, where $\omega = 0.114$ a.u. corresponds to the central driver wavelength of 400 nm. Other laser parameters: $\sin^2$ pulse of 20 optical cycles with peak intensity of 3.3×10^{14} W/cm^2. Note that the intensity of the spectrum is scaled by the signal at the fundamental frequency. (cf. hydrogen results in Fig. 3.1).

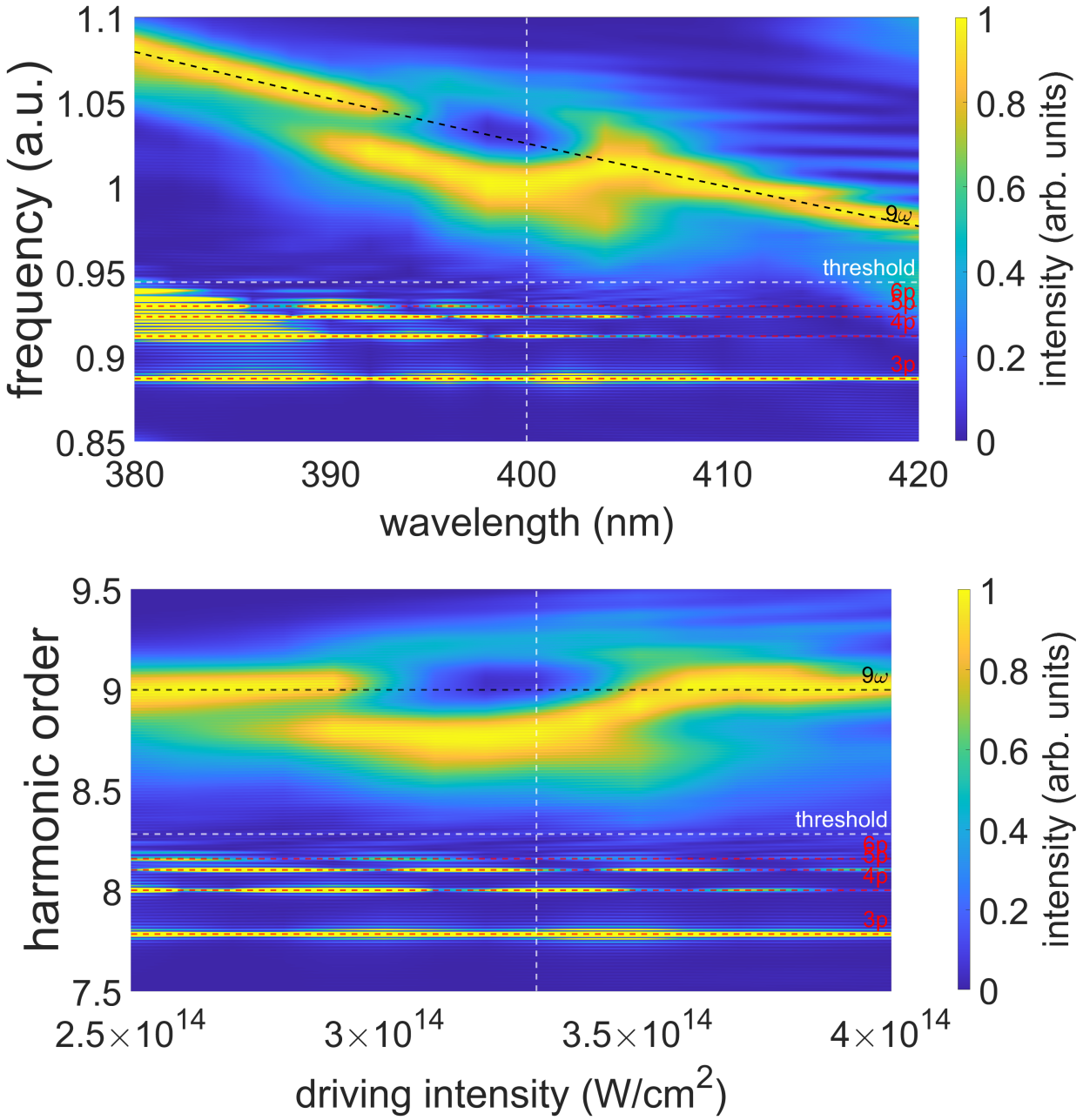

Figure 3.27: HHG spectra as (top) a function of driving wavelength at $I = 3.3 \times 10^{14}$ W/cm^2 and (bottom) a function of peak intensity at $\lambda = 400$ nm. $N_\tau = 20$ o.c. for both panels. Results for each wavelength (top) or each intensity (bottom) have been normalized to the maximum signal in the region between 8.75ω and 9.5ω. Red dashed lines denote field-free excited state transition energies. (cf. hydrogen results in Fig. 3.2 and Fig. 3.3).

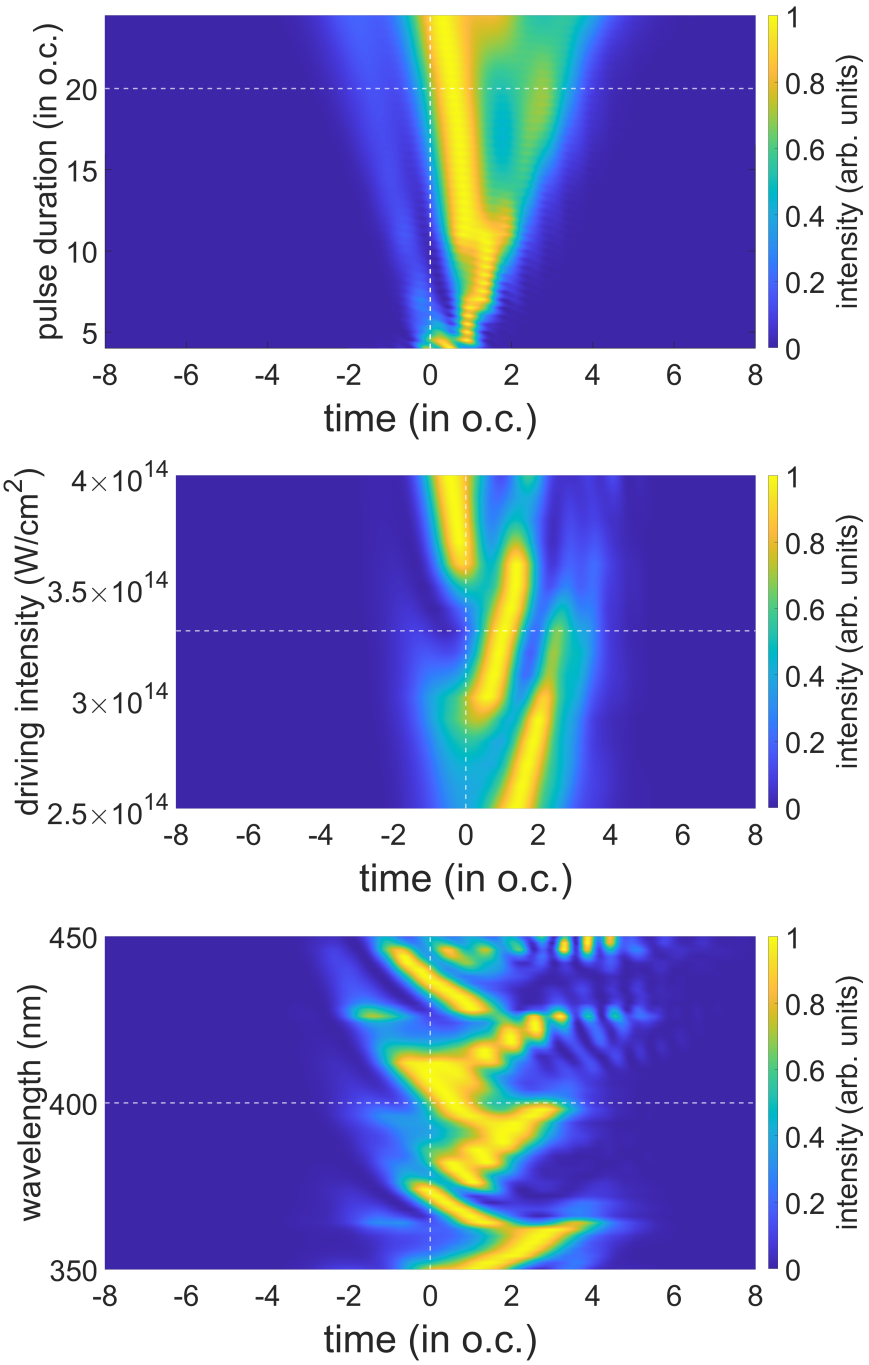

Figure 3.28: Temporal profile of radiation within 1ω of the 9th harmonic as a function of (top) pulse duration, (middle) peak intensity, and (bottom) driving wavelength. All in helium atom for a pulse of (unless specified) 20 o.c., 400 nm, and 3.3×10^{14} W/cm^2. For each element of the scans (i.e., horizontal slice), the result has been normalized to a maximum of 1. A vertical dashed line denotes the peak of the laser and a horizontal dashed line identifies the base pulse parameters.

saturation intensities), longer driving wavelengths allow for production of bright high-harmonic supercontinua extending into keV energies [31]. Much of the research on mid-IR HHG focuses on high driving laser intensities and the resulting ultrahigh harmonics. Here, we seek to investigate the near-threshold response, where low photon energies and large U_P mean that many states cross through resonance.

In the case of a 1600 nm laser, the field-free $1s \rightarrow 3p$ transition energy is nearly resonant with the 13th harmonic ($E_{1s\rightarrow 3p} = 13.16\omega$), and radiation at this energy is consistently more intense than other harmonics (excl. ω and 3ω). In Fig. 3.29, we show full (top panel) and near-threshold (bottom panel) HHG spectra for two driving intensities. Above I_P, the majority of radiation peaks do not clearly correspond to odd harmonics. Below I_p, harmonic radiation is dominant, but other structures are also present, similar to those found with 800 nm pulses.

Fig. 3.30 demonstrates the complex temporal structure of the 13th and 17th harmonics as a function of peak intensity. We note that many field-shifted resonances occur in this range – overlaying resonance conditions would cover nearly half of the Figure pixels within 3 o.c. of the peak. For most intensities (above about 10^{13} W/cm^2), dominant radiation occurs within about two cycles of the peak of the pulse. The specific timing, however, is highly dependent on driving intensity, with few consistent trends. Radiation does seem to occur most often centered at $0.5, 1.0, 1.5$, and 2.0 cycles – as would be expected for trajectory-driven HHG (see Sec. 3.5) – though we do not observe patterns as to which of these times will show the strongest radiation.

Considering the lowest intensities, 13th harmonic radiation shows cleaner structure, and we investigate this in Fig. 3.31. Here, the majority of radiation occurs before the peak of the pulse, following the shape of various rising-side resonances (esp. $17\omega \rightarrow 5p$ (*or* $5f$) and $16\omega \rightarrow 3s$ (*or* $3d$)). Additional weaker (and later) structures show similar trends, suggesting the role of multiple resonances and/or delays.

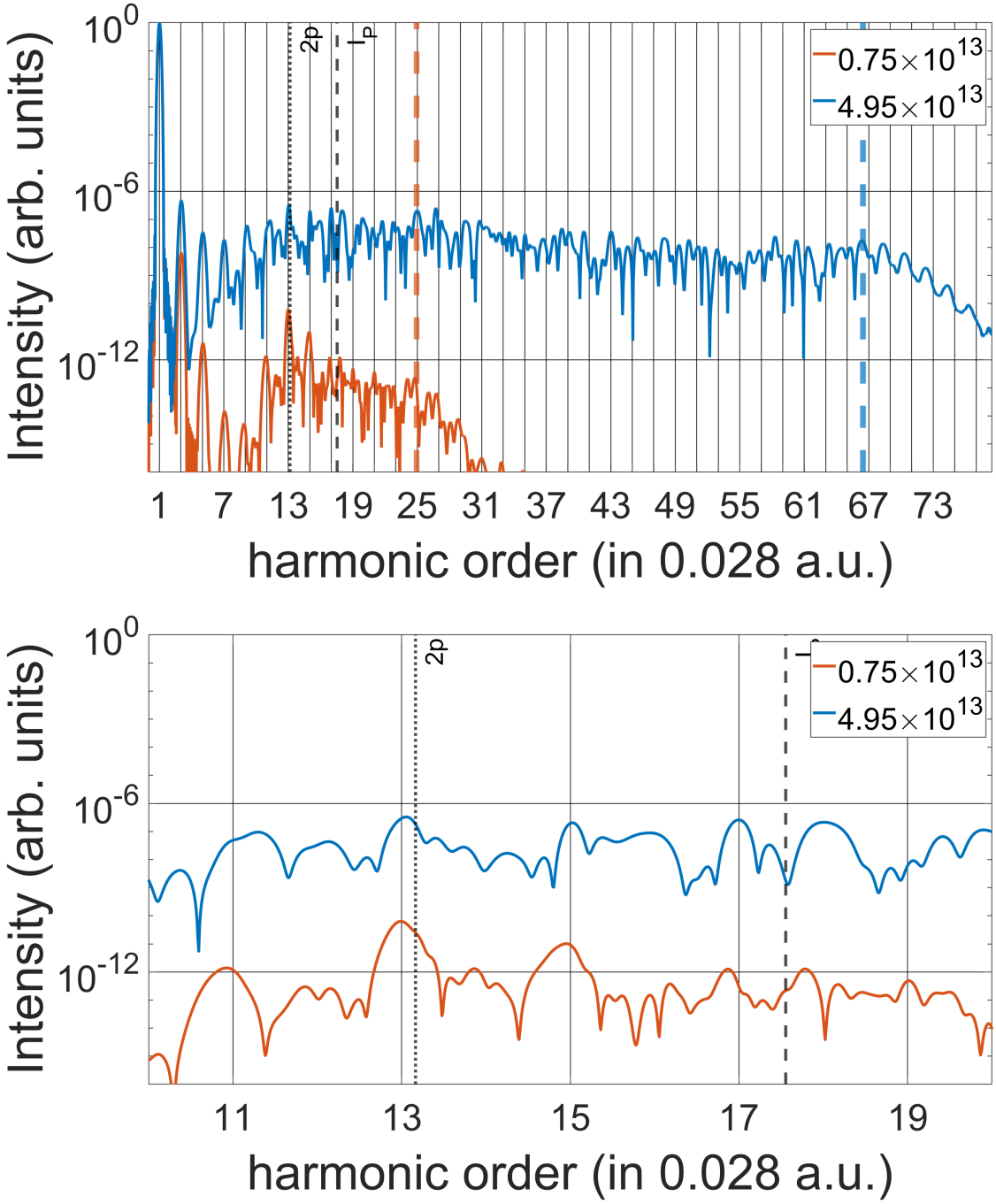

Figure 3.29: High harmonic spectra generated in atomic hydrogen. (top) Broad plateau extending to cut-offs (near 27 and 67ω, denoted by dashed lines) with many peaks appearing offset from $N\omega$; (bottom) near-threshold region exhibiting a rich structure. The hydrogen ionization threshold of 0.5 a.u. $= 17.5\omega$, where $\omega = 0.028$ a.u. corresponds to the central driver wavelength of 1600 nm. Other laser parameters: $\sin^2$ pulse of 10 optical cycles with peak intensities of 0.75×10^{13} and 4.95×10^{13} W/cm^2. Note that the intensity of the spectra are scaled by the signal at the fundamental frequency.

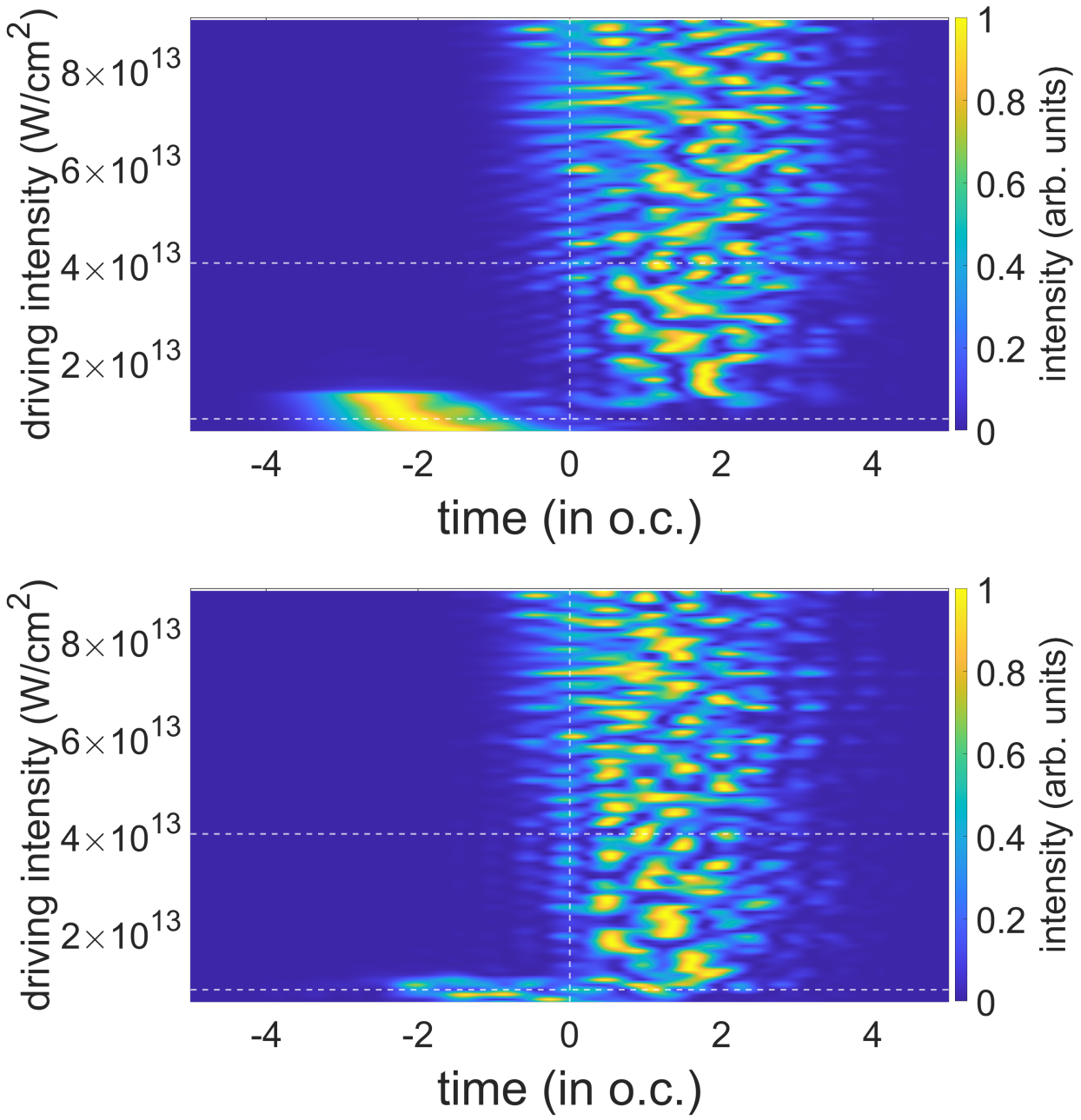

Figure 3.30: Temporal profile of radiation within 1ω of the (top) 13th and (bottom) 17th harmonics as a function of driving pulse intensity in atomic hydrogen for a 1600 nm, 10 o.c. pulse. For each intensity the results have been normalized to a maximum of 1 for sake of comparison. A vertical dashed line denotes the peak of the laser and horizontal dashed lines identify the intensities in Fig. 3.29.

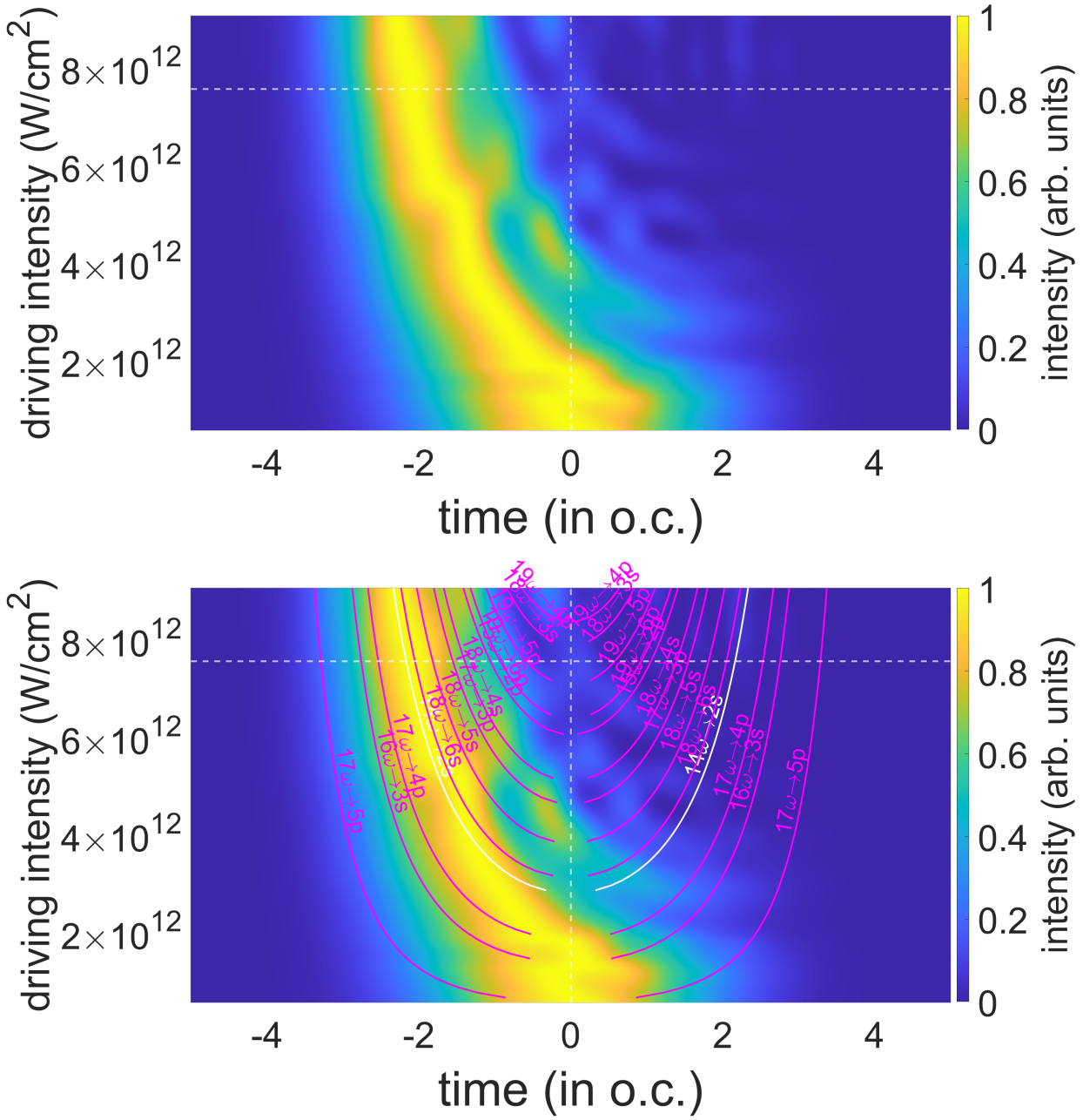

Figure 3.31: Temporal profile of radiation within 1ω of the 13th harmonic as a function of driving pulse intensity in atomic hydrogen for a 1600 nm, 10 o.c. pulse. For each intensity the results have been normalized to a maximum of 1 for sake of comparison. A vertical dashed line denotes the peak of the laser and a horizontal dashed line identifies the lower intensity in Fig. 3.29 (i.e., 0.75×10^{13} W/cm^2). Panels show identical radiation data, but the lower is overlaid with lines denoting resonance times for $12 - 14\omega$ (white) and $> 14\omega$ (magenta) resonances (there are no excluded resonances with a smaller or larger number of photons involved for these parameters) for $2s - 6p$.

3.9 Summary

To summarize, we have investigated the near-threshold region of HHG and identified resonance-enhanced radiation associated with states shifting during the pulse. For one particular case – hydrogen driven by an 800 nm, 20 o.c. sine-squared pulse of 3.8×10^{13} W/cm^2 – we have thoroughly demonstrated the process of identifying the responsible resonance ($9\omega \to 3p$) and three associated delays between the time when $3p$ shifts into resonance and the appearance of radiation. The timing of this radiation remains consistent with predictions within an appreciable variation within the parameter space. In other regimes – including more intense driving lasers, weak mid-IR pulses, and helium driven by 400 nm pulses – we have identified similar structures, demonstrating the general importance of this effect.

While certain features show agreement with an explanation based on semi-classical trajectories, others cannot be thus explained. In particular, we demonstrate a lack of expected CEP dependence – present at higher intensities and for shorter pulses – and spectral signatures which do not match the predicted shape. Through multi-parameter scans, in which the resonance time is kept fixed, we explore the consistency of the $9\omega \to 3p$ resonance enhancement. We hypothesize that breakdown of resonance predictions are associated with low values of $\frac{U_P}{\omega} (\lessapprox 1)$ and $\frac{U_P}{I_P} (\lessapprox 0.1)$, and that the pulse duration N_τ may play an important role in the timing of radiation (beyond its impact on the resonance condition).

3.9.1 Future prospects

Resonantly-enhanced near-threshold HHG offers a rich field for further investigation. In this Chapter, we have focused our attention on a particular feature – enhancement via the $9\omega \to 3p$ resonance – and noted that radiation occurs at multiple distinct delays after the resonance, unlike for other regimes investigated. If similar multiply-delayed resonance features could be identified (e.g., in helium or with mid-IR pulses), comparison could provide answers to some remaining questions:

- Do multiple delays appear at consistent delay intervals? (e.g., $0.5 + 1.25n$ o.c.)
- What parameters determine when multiple delays will generate significant radiation, versus the seemingly more common case of a single delay?
- Do falling-side resonances ever produce significant radiation at second and greater delays? (For this, we recommend investigation with longer pulses.)

There is of course, another crucial remaining question: If, as we suggest, no trajectory model is applicable at this and lower intensities, what is the mechanism of radiation? What determines the delay between resonance and radiation? Are signatures of resonance enhancement present (but perhaps less dominant) in other domains, such as:

- radiation at higher harmonics,
- from pulses with higher driving intensities, perhaps including cases where tunnel ionization is expected to play a larger role,
- in more complex systems such as molecules or atoms where multiple orbitals contribute (e.g., the $2s$ and $2p$ states of neon).

Some tools of investigation that we did not significantly pursue, but that may hold promise:

- driving lasers with more (and more continuous) variation of envelope, such as flat-top or supersine envelopes, such that resonance delays may place radiation within flatter regions of the envelope,
- "spectral profile" plots where radiation is windowed to some particular region for parameter scans,
- Floquet analysis or use of numerical basis codes, to investigate deviation from the $U_P(t)$ approximation for state shifting,
- generalized semi-classical trajectory models (cf. [41]) with multiphoton ionization conditions considering the actual predicted photon energies or states,

- tuning of state energies separate from ionization potential, through manual modification of potential parameters (see Sec. 2.2.5),
- and simulations of the response when starting in an excited or superposition state.

Chapter 4

Interpolation and Macroscopic Response

We develop a macroscopic description of high-order harmonic (HHG) radiation resulting from the interaction of atomic systems with an intense laser pulse using ab-initio solutions of the time-dependent Schrödinger equation (TDSE). After providing some background in Sec. 4.1, in Sec. 4.2 we show that for this highly nonlinear process, interpolation can been performed across laser intensity for a given wavelength, limiting the number of full time-dependent Schrödinger equation calculations to about one hundred. The impact of the phase of the driving laser on radiation is explored on the single-atom level in Sec. 4.2.2 and for macroscopic targets in Sec. 4.5. We summarize the macroscopic harmonic signal computation, which is based on the approach in [106], in Sec. 4.3. We consider the application of this efficient method for distributions of hydrogen atoms on a lattice grid (Sec. 4.3.1) and in a gas jet (Sec. 4.4) to demonstrate the successful application of the TDSE interpolation method to the thin medium or low gas density regimes that are free from longitudinal phase-matching effects. By comparing the results of the present method with theoretical predictions and against previous results, it is shown that the method based on the interpolation of ab-initio TDSE solutions leads to reliable macroscopic results. The significantly reduced computational time as compared to more sophisticated methods opens a path toward the extension of macroscopic high harmonic calculations based on ab-initio microscopic results to more complex targets and interactions. In Sec. 4.4.2, we demonstrate this via investigations of the near-threshold regime of the spectra that show that the degree of coherence of the off-harmonic radiation generated during the pulse is much lower than that of the harmonics. On the other hand, the weak

non-harmonic radiation extends to larger divergence angles than the harmonic signals providing the option for separation of the different signals in this part of the spectrum. Connecting to Ch. 3, we show in Sec. 4.4.3 that the resonance-enhanced radiation is in fact the portion of off-harmonic radiation that survives macroscopic propagation, though at relatively weaker intensity than the harmonic radiation. The general applicability of this method is shown for a variety of driving wavelengths and targets in Sec. 4.6.

4.1 Background

Proper theoretical analysis of HHG experiments requires consideration of macroscopic aspects, i.e., the coherent build-up of the (microscopic) high harmonic signals from many atoms in the generating medium. It has been shown (e.g., [14, 107]) that efficient harmonic emission depends on several macroscopic parameters of the experiment, e.g., beam shape, gas pressure, etc.. The propagation of the emitted radiation in the medium is described by Maxwell's equations. Thus, an exact description of the HHG process requires solution of Maxwell's equations coupled with the solution of the TDSE for each of the atoms at the microscopic level. Due to the large number of atoms in the medium and, hence, the large number of TDSEs to be solved, this task requires formidable computer resources (see [108–111] for further discussion). In view of the computational demands, the application range of these methods is very limited and theoretical analysis of most HHG experiments cannot be realized at this level.

Therefore, a number of models have been proposed and applied in the past to reduce the complexity of the problem (e.g., [106, 109–126]) and enable a broader investigation of the parameter space, incl. by research groups with restricted computational resources. One of these efficient approaches is based on computation of the macroscopic harmonic yield as a superposition of the fields of pointlike emitters in the medium via the discrete dipole approximation (DDA), instead of the numerical solution of the wave equation [106]. Along with an extension of the strong-field approximation (SFA+) to obtain the single-atom high harmonic spectra [53], this SFA-DDA approximation of the macroscopic harmonic build-up has been successfully applied to match experimental data

and analyze various aspects of high-harmonic generation, such as generation of bright harmonics in the keV X-ray regime [31], prediction and application of attosecond vortices from HHG [37, 127], as well as generation and application of circularly polarized harmonics [38, 103, 128]. The use of the strong-field approximation or other approximate theories at the single-atom level allows for an efficient calculation of the macroscopic harmonic yield. Although the SFA+ model provides accurate predictions for the plateau and cut-off region of the spectrum, the application of these approximative methods on the microscopic level are limited. For example, they cannot be applied for an analysis of the signal in the below- and near-threshold region of the high harmonic spectrum. This part of the spectrum, which has gained an upsurge in interest recently (e.g., [39, 95–101, 129]), is influenced by the excited state structure of the target atom, which is usually not well reproduced in approximate single-atom theories. We note that excited states play a role in the control and resonant enhancement of harmonics (see Ch. 3 and [130–135]). The limitation of approximative microscopic calculations is perhaps even more obvious with more complex targets, like molecules or nanosystems, which have recently attracted a lot of attention in experiment.

There is a gap in the theoretical analysis of HHG between full ab-initio Maxwell-Schrödinger simulations, which nowadays cannot be applied to most of the experimental conditions, and those methods based on approximative calculations, which are often limited in the accurate description of microscopic interactions. It is therefore important to develop macroscopic HHG calculations which include ab-initio microscopic calculations in an efficient way. Such methods will enable extension of macroscopic HHG studies to the analysis of the impact of more complex interactions on the spectra as well as to molecules and nanosystems.

As mentioned above, the impact of excitation on the generated near-threshold part of the spectrum is one of these more complex interactions. A TDSE result for the radiation spectrum generated in atomic hydrogen is shown in Fig. 4.1. The field-free ionization threshold corresponds to 8.77ω, where ω is the frequency of the laser pulse, and one can see the typical rich structure in the below- and near-threshold region of the spectrum. In the numerical TDSE solutions at the single-atom level, the strength of the signal in between the harmonics – which we denote as off-

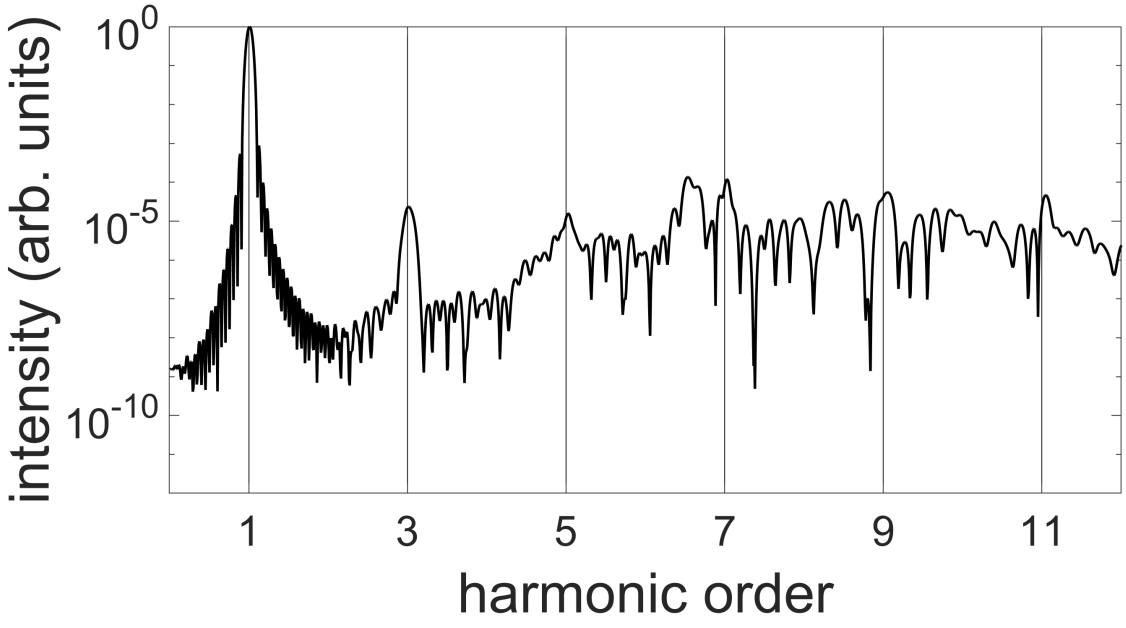

Figure 4.1: Example of single-atom high harmonic spectrum generated in atomic hydrogen, obtained via numerical solution of the time-dependent Schrödinger equation, exhibiting a rich structure in the near-threshold region of the spectrum between harmonics 5 and 12. The hydrogen ionization threshold of 0.5 a.u. $= 8.77\omega$, where $\omega = 0.057$ a.u. corresponds to the central driver wavelength of 800 nm. Other laser parameters: $\sin^2$ pulse of 20 optical cycles with peak intensity of 7×10^{13} W/cm^2. Note that the intensity of the spectrum (as well as other spectra in this Chapter) is scaled by the signal at the fundamental frequency.

harmonic radiation – appears to be as strong as the harmonic signals. Meanwhile, in experiment, off-harmonic radiation is usually much suppressed, typically showing up as weak shoulders at the side of a strong harmonic emission (e.g., [96]). Since the radiation is generated during the pulse and may therefore contain relevant information about ultrashort laser-induced electron dynamics in excited states, it is interesting to analyze at what strength it occurs in the macroscopic response and if it can be separated from the harmonic signals.

In this Chapter we present a macroscopic calculation that includes complex effects such as excitation via TDSE calculations (or other ab-initio methods). To this end, we determine the macroscopic harmonic yield as a superposition of fields of point-like emitters using TDSE results at the single-atom level. To keep the overall calculation efficient, we consider interpolation of ab-initio TDSE calculations across intensity. Having in mind that HHG is a highly nonlinear process as a function of intensity, we thoroughly show that a simple interpolation is indeed sufficient to keep the number of actual TDSE calculations to a computationally feasible range of about one hundred for the performance of a macroscopic simulation. Additionally, we demonstrate the accuracy of a simple approximation of the carrier-envelope phase effect on HHG results. The reliability of the macroscopic results is demonstrated by comparison with theoretical predictions for a lattice grid and previous results for the near-threshold regime of HHG in a gas jet under loose focusing conditions.

4.2 Interpolation

We obtain the microscopic HHG spectra as discussed in Sec. 1.4.3.3, evaluating the dipole acceleration $a(t)$ using the Ehrenfest theorem

$$a(t) = \left\langle -\frac{\partial}{\partial z} V(r) \right\rangle, \tag{4.1}$$

where $V(r)$ is the atomic interaction potential. For hydrogen, this is simply $-\frac{1}{r}$ and $a_z(t) = -\frac{z}{r^3}$. For other atoms, we consider the derivative of the full potential V_{SAE}. The complex harmonic response $a(\omega)$ is then obtained by taking the Fourier transform of the (un-windowed) dipole accel-

eration,

$$a(\omega) = \int_0^T a(t)e^{-i\omega t}dt. \tag{4.2}$$

and the harmonic spectrum $P(\omega) = |a(\omega)|^2$.

We note that the interpolation scheme and macroscopic calculation discussed below do not depend on the particular microscopic solver used – all that is needed is the final $a(t)$ or $a(\omega)$. Thus, the interpolation method can be applied with any preferred TDSE solver or any other ab-initio method. This opens the door for exploration of molecular and multielectron systems whose calculations are computationally prohibitive in combination with other macroscopic methods.

4.2.1 Interpolation across intensity

Interpolation of the TDSE solutions can be accomplished either for $a(t)$ in the time domain or for $a(\omega)$ in the frequency domain. Interpolation in the time domain has the advantage that the dipole acceleration $a(t)$ is purely real. Furthermore, any numerical calculation of the HHG spectra requires the determination of the dipole acceleration from a numerical simulation. For interpolation in the frequency domain, each numerically determined data $a(t)$ must be Fourier transformed before the interpolation can be performed. On the other hand, the information content of the harmonic signal is more efficiently stored in the frequency domain, since one may truncate the spectrum $P(\omega)$ a few harmonics after the HHG cut-off. Depending on pulse duration and numerical time step, this may decrease memory requirements by more than a factor of 10. Additionally, Fourier transformation is usually computationally more expensive than interpolation, so if results are only desired in a single domain (e.g., only spectra are considered), it is most efficient to interpolate in the desired domain.

The procedure for interpolation used is the same in the time and frequency domains. The dipole acceleration $a(t)$ (or $a(\omega)$) is numerically calculated for a set of peak intensities over a desired sampling range. For a given point in time (or frequency), the dipole acceleration (or complex spectrum) is interpolated across intensities using cubic splines with not-a-knot end conditions. The impact of the end conditions is minimized by ensuring that relevant intensities are well-contained

within the sampling range. The full dipole acceleration (complex spectrum) is then reconstructed from these slices. If required, transformation into the frequency (time) domain is completed after interpolation.

In order to evaluate the success of the interpolation procedure, we have numerically solved the TDSE for a hydrogen atom at a randomly chosen peak intensity of 9.1431×10^{13} W/cm^2 driven by a 20-cycle laser pulse at 800 nm. In Fig. 4.2, we show results of the interpolation for (a) high harmonic spectrum $P(\omega)$, (b) dipole acceleration $a(t)$, and (c) error in harmonic phase $\Phi(\omega)$. All features of both high harmonic spectrum and dipole acceleration in the exact calculation are reproduced in the interpolated results. The maximum absolute errors for these specific calculations are below 5×10^{-6} for the dipole acceleration and below 5×10^{-7} for the harmonic yield. In test calculations we have found similar results for other driver wavelengths, peak intensities, and pulse durations.

In the present work, we have chosen to evaluate exact TDSE results for a sample set of peak intensities that are equally spaced on a linear scale, though other spacing (e.g., logarithmic or Chebyshev) may be preferable in some cases. Results of test calculations suggest that Chebyshev sampling has benefits especially in other integration schemes than Monte Carlo, potentially requiring 2-3 times fewer sample points. On the other hand, it does limit the re-usability of the sample calculations for other macroscopic peak intensities.

In Fig. 4.3, we present the maximum absolute error in high harmonic spectra obtained via interpolation for two different peak intensities (other parameters as in Fig. 4.2) as a function of the sample spacing dI over the range from 1×10^{12} W/cm^2 to 2×10^{13} W/cm^2. As expected for a cubic interpolation, the error roughly scales as $O(dI^4)$ for sufficiently small dI. For larger dI, the error varies more strongly, and the error is largest when the nearest sampled intensity is far (more than 2×10^{12} W/cm^2) from the target intensity. These features are consistent for all wavelengths tested in the range of $270 - 1600$ nm. This result is of particular interest for the long wavelength regime in view of the unfavorable scaling of computation times for HHG calculations with increase of the wavelength.

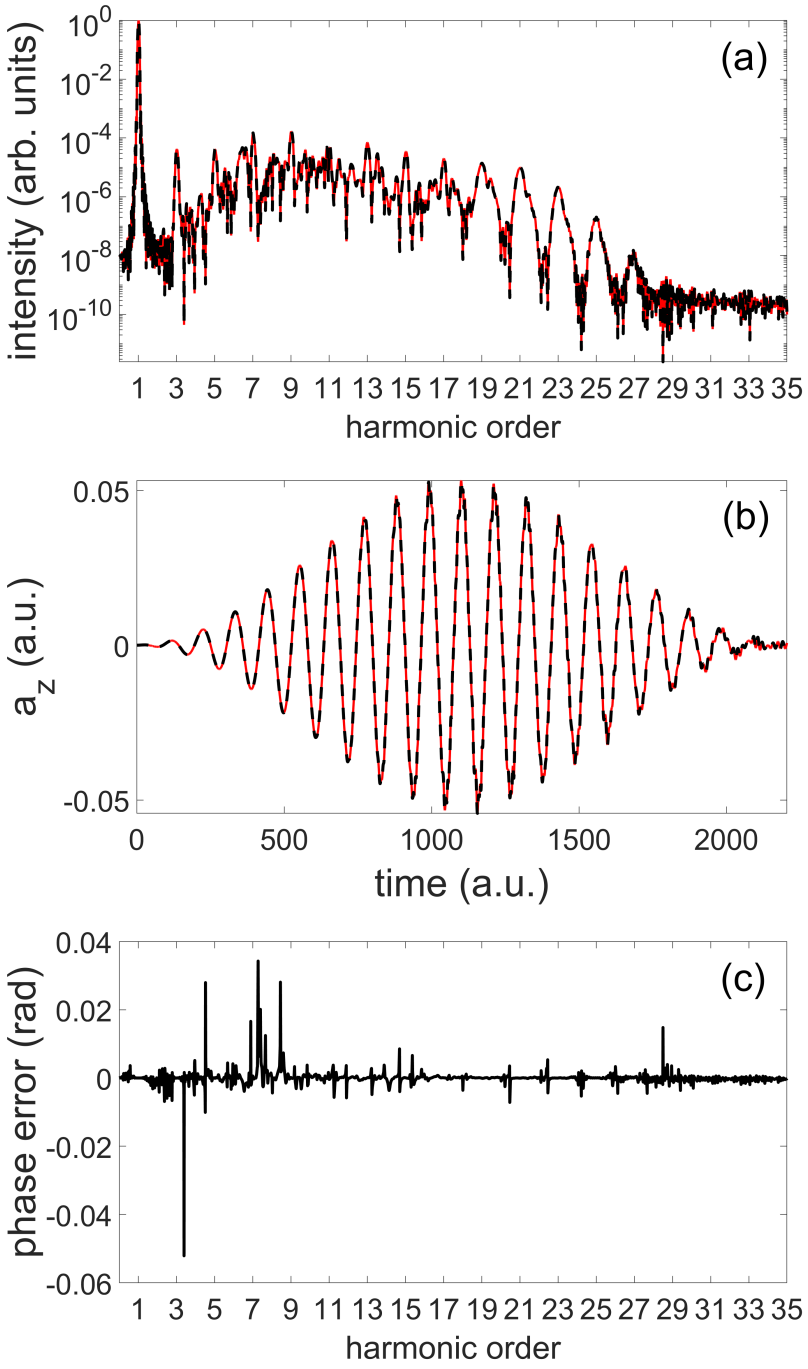

Figure 4.2: (a) Comparisons of results of interpolation (dashed lines) and exact numerical results (solid lines) for high harmonic spectrum and (b) for dipole acceleration, and (c) error in harmonic phase, generated by a $\sin^2$ pulse of 20 optical cycles at wavelength of 800 nm and peak intensity of 9.1431×10^{13} W/cm^2. Interpolation performed on data with intensities of $0.1, 0.2, 0.3, ..., 10.0 \times 10^{13}$ W/cm^2. ((a) taken from [6].)

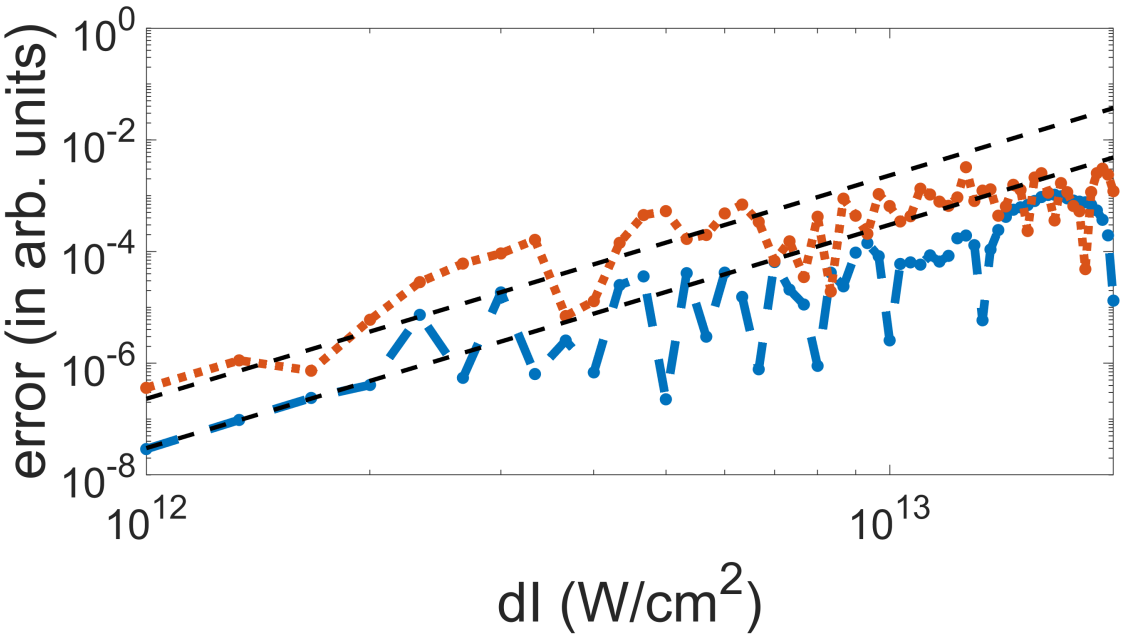

Figure 4.3: Trend of maximum absolute error in interpolated high harmonic spectrum (as compared to numerical TDSE result) as a function of the intensity sampling spacing dI (i.e., sampled intensities $dI, 2dI, \ldots, \sim 10^{14}$ W/cm^2). Shown are exemplary results at peak intensities 3.97×10^{13} W/cm^2 (blue circles with dashed line) and 9.14×10^{13} W/cm^2 (red circles with dotted line). Other laser parameters as in Fig. 4.2. Note that at sufficiently small intensity spacings, the error roughly drops as $O(dI^4)$ (black dashed lines).

While the choice of intensity sampling spacing depends on the desired accuracy, for 800 nm we have found $dI = 10^{12}$ W/cm^2 to be fully sufficient. In general, from our test calculations at other wavelengths, we have found that the spacing required relates roughly to the maximum extent of the harmonic spectra, i.e., $3.17U_P/\omega \propto I/\omega^3$. Thus, as a rule of thumb the sampling spacing for the cubic interpolation should be (in W/cm^2):

$$dI \approx \left(\frac{\omega}{0.057}\right)^3 \times 10^{12} = \left(\frac{800}{\lambda}\right)^3 \times 10^{12} \tag{4.3}$$

where ω is in a.u., while λ is in nm.

While our primary focus in this Chapter is to use the interpolation method to facilitate macroscopic HHG calculations, we note that the success of the interpolation method is interesting in itself since HHG is a highly nonlinear process and depends strongly on intensity. As we have shown, cubic interpolation produces quantitatively good agreement with exact spectra at moderate intensity sampling (and qualitatively indistinguishable spectra can be generated with coarser sampling). While perhaps not surprising from the numeric side, the implication that the results of such a highly nonlinear process can be distilled to order-100 samples for description of the whole range of relevant intensities (with saturation of ionization well before 10^{15} W/cm^2) is not *a-priori* obvious. In view of the success, it is likely that a similar technique can be applied for the dependence of HHG spectra on other parameters as well.

4.2.2 Variation of CEP

In addition to different driving intensities, it is important to consider the effects of variation of the carrier-to-envelope phase (CEP), ϕ, on the spectrum. Especially in short pulses, CEP is a parameter that controls many strong-field applications such as isolated attosecond pulse generation [136], laser-driven electron dynamics in atoms, molecules, and nanostructures [137–140], or generation of relativistic electron beams [141]. For long pulses, the impact on the microscopic spectral intensity is minimal (Fig. 4.4), but the spectral phase effects cannot be discounted in macroscopic summation.

Before proceeding, we provide a note on interpreting phase plots. Plots of phase tend to include large spikes that have little physical significance. The first reason is that phase has little meaning when the magnitude is small: $+10^{-4}$ and -10^{-4} are much the same when features of interest are on the scale of ± 1. Secondly, phase is defined modulo 2π, and smoothing out 2π jumps is not always straightforward or useful. The simplest choice of "unwrapping" phase by minimizing the difference between adjacent points leads to spectral phases spanning hundreds of radians, obscuring most features. On the other hand, restricting phases to $[0, 2\pi)$ can appear to break larger trends. For this reason, we select CEPs within a specific range that allows simpler presentation of spectral phase without manual addition of 2π's. The results are consistent for larger CEP.

In SFA, the spectral phase is given by:

$$\Phi(\omega, \phi) = \Phi(\omega, \phi = 0) + \phi H(\omega) \tag{4.4}$$

where $H(\omega)$ is the harmonic number rounded to the nearest odd integer [106]. In Fig. 4.5, we show exact TDSE results for the phase difference

$$\Delta\Phi/\phi = \big(\Phi(\omega, \phi) - \Phi(\omega, \phi = 0)\big)/\phi \tag{4.5}$$

compared to the SFA prediction $\Delta\Phi/\phi = H(\omega)$. For both intensities, we see a factor between CEP and spectral phase which does not depend on CEP (i.e., the scaled lines in Fig. 4.5 overlap):

$$\Delta\Phi/\phi = f(\omega) \tag{4.6}$$

for some function $f(x)$. For the lower intensity, there is good agreement with $f_{SFA}(\omega) = H(\omega)$. For the higher intensity, $H(\omega)$ approximates the true dependence, but the specifics are more complicated.

While not further investigated in this thesis, we do present results for a short (4 o.c.) pulse at the lower intensity (Fig. 4.6). The spectral intensity differences are larger, but mostly not impacting the harmonics themselves. The spectral phase varies more dramatically (especially in the near-threshold $6 - 10\omega$ region of interest), and in places *does* depend on the particular CEP in

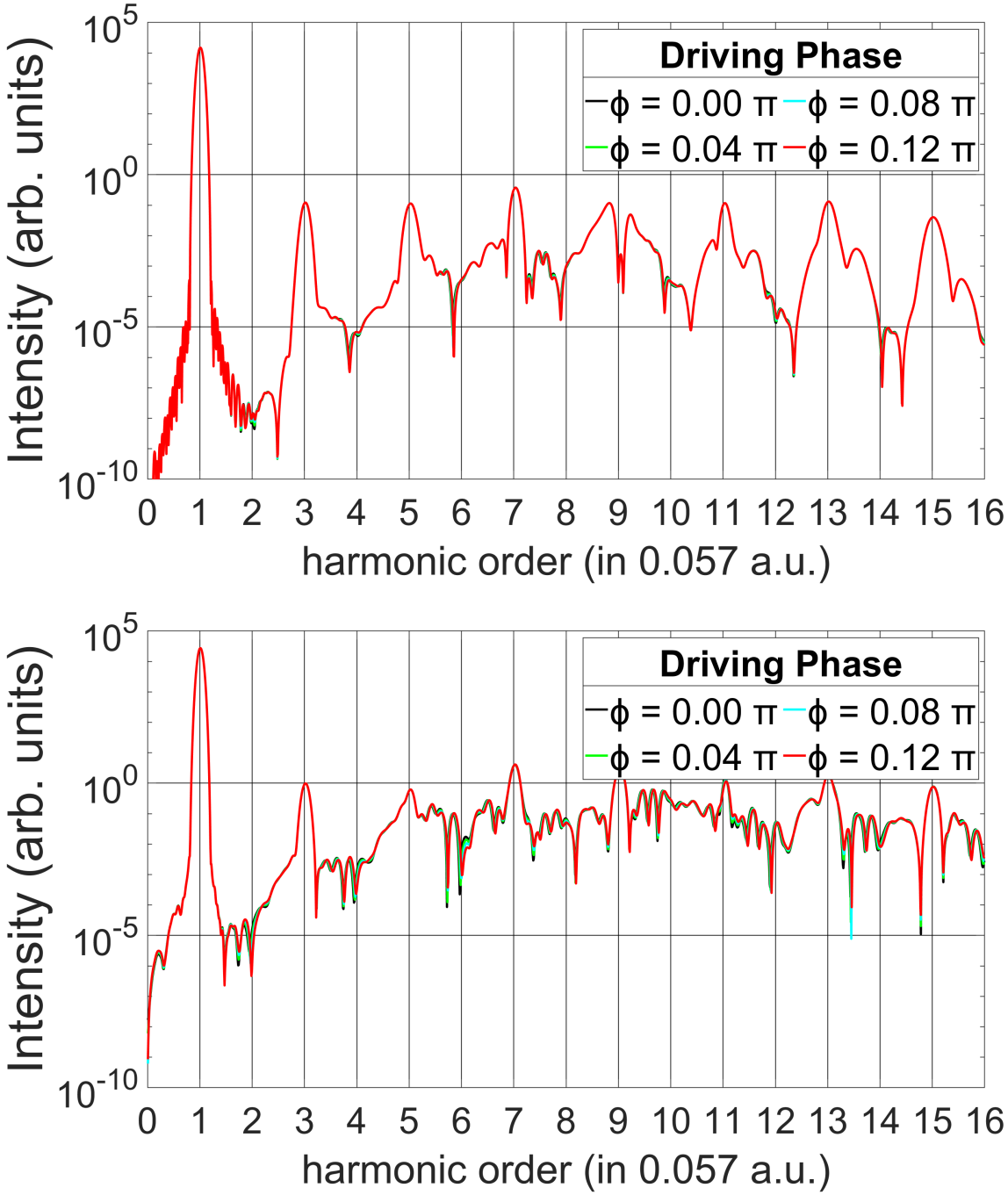

Figure 4.4: Spectra for a selection of sample CEPs, generated by a $\sin^2$ pulse of 20 optical cycles at wavelength of 800 nm and peak intensity of (top) 3.8×10^{13} W/cm^2 and (bottom) 7.0×10^{13} W/cm^2.

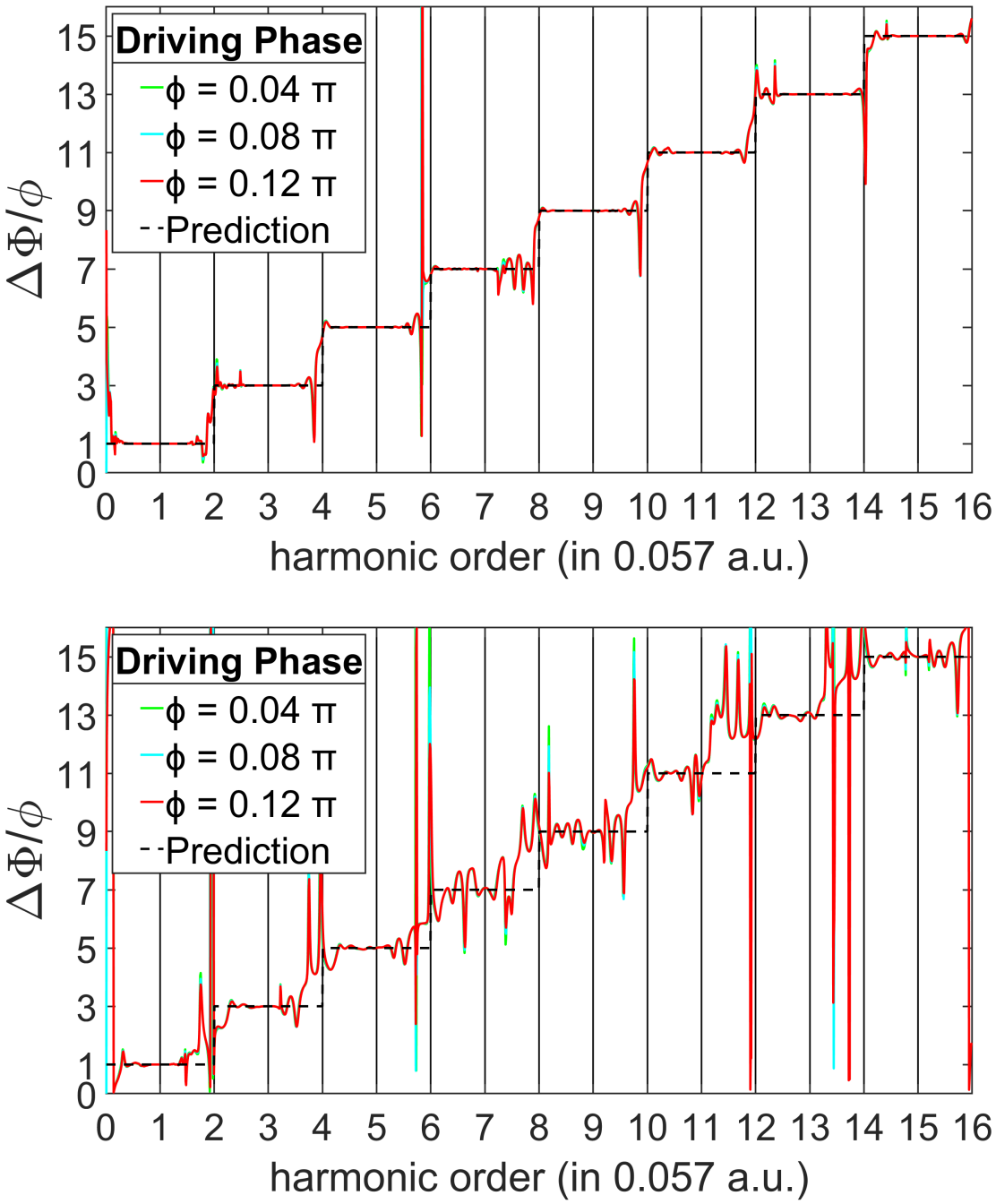

Figure 4.5: Spectral phase difference for a selection of sample CEPs, generated by a $\sin^2$ pulse of 20 optical cycles at wavelength of 800 nm and peak intensity of (top) 3.8×10^{13} W/cm^2 and (bottom) 7.0×10^{13} W/cm^2. (Top panel taken from [6].)

a way not seen for longer pulses. Still, for the majority of the spectrum, the CEP effects are similar to those for longer pulses – the radiation intensity is unaffected and the SFA approximation to the phase is good. We note parenthetically that the driving laser field was not frequency-corrected [85], leading to the harmonic blue-shift.

In Sec. 4.5, we will investigate the impact of the spatial CEP variation on the macroscopic radiation using the $\Delta\Phi/\phi = H(\omega)$ approximation. With the addition of Gouy phase, the effects are small and smooth enough that we predict the true dependence would not significantly affect results for long pulses. For highly-focused pulses where an additional focal phase [142, 143] becomes significant (see Sec. 4.5), we expect the same approximation to hold, but recommend future study involve consideration of interpolation across CEP. More careful treatment will also be needed for circularly and elliptically polarized laser pulses, as well as when multiple pulses contribute to HHG.

4.3 Macroscopic summation

To determine the macroscopic radiation signal at a far-field detector, we consider the thin medium or low gas density regimes that are free from longitudinal phase-matching effects. We define the arrangement and coordinates as follows: The driving laser propagates in the $\hat{z}$ direction, has linear polarization $\hat{y}$, and we consider only radiation polarized in this direction. The far-field detector is an arc in the xz-plane with its position defined by the angle θ from $\hat{z}$ (propagation) to $\hat{x}$. We then follow the approach used in [106], in which the macroscopic yield is obtained as the superposition of the fields generated at different points in the medium. This approximation to the full Maxwell solution relies on the dipole approximation and the assumption that generated radiation does not interact with the medium.

The spectral distribution of the total radiation generated by a number of atoms, located at $\mathbf{r}_j$ $(j = 1, 2, 3, ...)$, is given by [106]:

$$\mathbf{E}(\mathbf{r}_d, \omega) = \frac{1}{c^2|\mathbf{r}_d|} e^{-i\frac{\omega}{c}|\mathbf{r}_d|} \sum_j a_j(\omega) e^{-i\frac{\omega}{c}[\mathbf{r}_j \cdot (\hat{r}_d - \hat{z})]} \hat{\mathbf{y}}\,, \tag{4.7}$$

where $a_j(\omega)$ is the dipole acceleration in frequency domain of a single atom responding to the driving

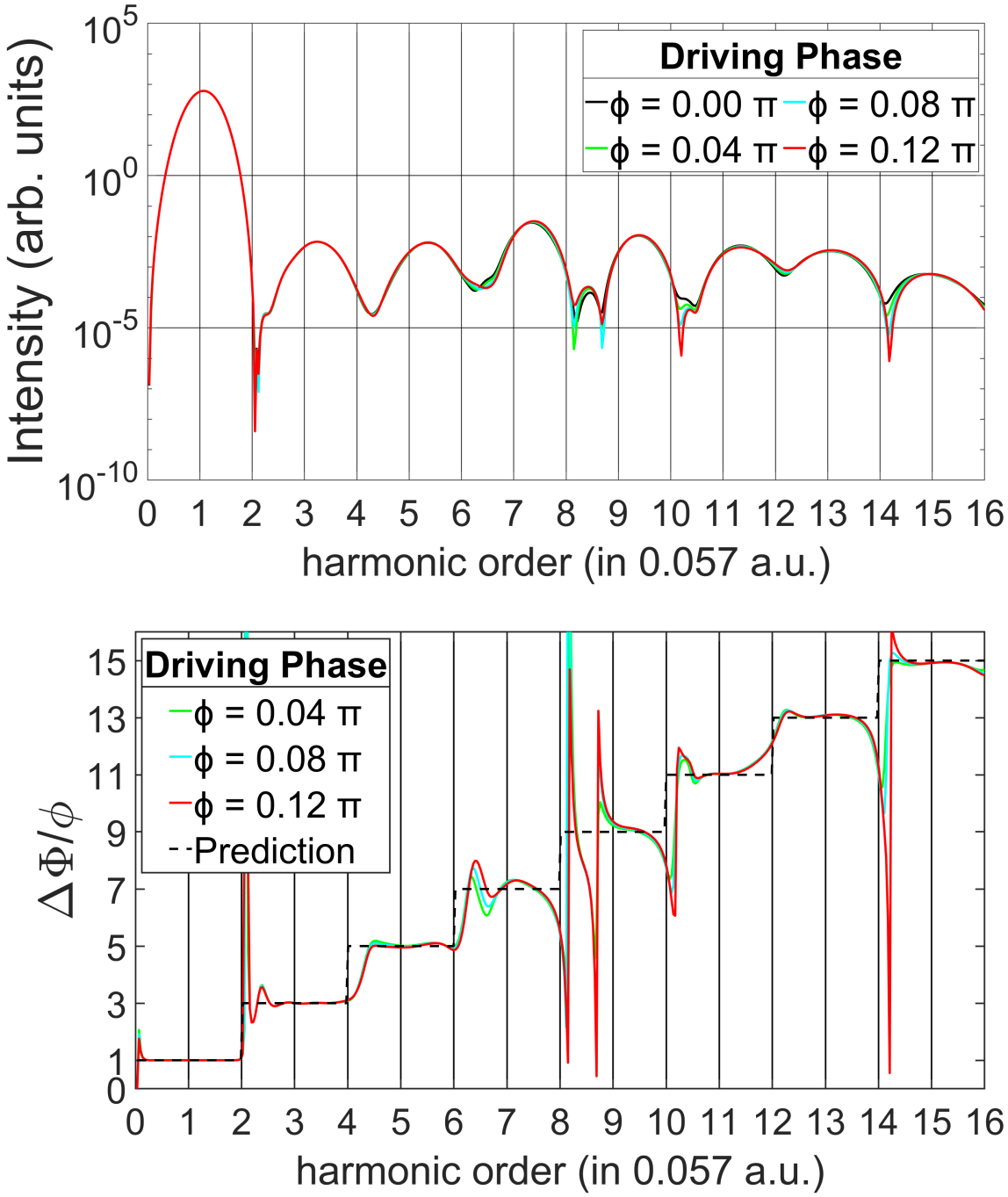

Figure 4.6: (top) Spectrum and (bottom) spectral phase difference for a selection of sample CEPs, generated by a short $\sin^2$ pulse of 4 optical cycles at wavelength of 800 nm and peak intensity of 3.8×10^{13} W/cm^2.

laser pulse. Since this is calculated without considering the delay of the driving laser reaching the radiator, $(\mathbf{r}_j \cdot \hat{\mathbf{z}})/c$, the corresponding additional phase is added. Furthermore, it has been assumed that the relative location of the detector, denoted by $\mathbf{r}_d$, is far away from the individual atoms, i.e., $|\mathbf{r}_j| \ll |\mathbf{r}_d|$ and, hence, $|\mathbf{r}_d - \mathbf{r}_j| \approx |\mathbf{r}_d| - \mathbf{r}_j \cdot \hat{\mathbf{r}}_d$ and $\frac{1}{|\mathbf{r}_d - \mathbf{r}_j|} \approx \frac{1}{|\mathbf{r}_d|}$. Since the prefactor in Eq. (4.7) universally scales the results, we drop it from the computations. As usual, radiation is reported as spectral intensities, $|\mathbf{E}(\mathbf{r}_d, \omega)|^2$.

We approximately include the effect of the Gouy phase $\zeta(z) = -\operatorname{atan}(z/z_0)$ [144], on Hth-harmonic radiation as an additional phase $H(\omega)\zeta(z)$, where z_0 is the Rayleigh range, as in [106]. As shown in the previous section, for 20 o.c. pulses this approximation holds well. Additionally, for the loose focusing geometry used below, ζ ranges up to $\approx \pm 0.2$ rad within the gas jet, and the effect on near-threshold harmonics – the main focus of the applications below – is minimal. Specifically, as seen in Sec. 4.2.2, the CEP effect is mostly restricted to a consistent additional phase scaling with harmonic number. This has the effect of adding a phase mismatch for higher harmonics, leading to suppression. Centering the gas jet off the laser focus allows for better phase matching when the Gouy and intrinsic phases compensate [106]. In Sec. 4.5, we discuss more closely the effects of Gouy phase as well as another phase term related to highly-focused laser pulses.

Using $\mathbf{r}_d = r_d\,(\cos(\theta_d)\hat{\mathbf{z}} + \sin(\theta_d)\hat{\mathbf{x}})$ and $\mathbf{r}_j = r_j\,(\cos(\theta_j)\hat{\mathbf{z}} + \sin(\theta_j)\hat{\mathbf{x}}) + y_j\hat{y}$, Eq. (4.7) can then also be written as:

$$\mathbf{E}(\theta_d, \omega) = \sum_j a_j(\omega) e^{-i\frac{\omega}{c} r_j [\cos(\theta_j) - \cos(\theta_d - \theta_j)]} \hat{\mathbf{y}}. \tag{4.8}$$

The sum in Eq. (4.7) or (4.8) can be efficiently performed if the number of atoms does not become too large. However, in a typical high-harmonic gas jet experiment, even at low-pressure densities, the number of atoms is typically of the order of 10^{12} or larger. To simplify the computation in these cases, it has been proposed [106] to perform the sum using Monte Carlo sampling, and further to split the interaction volume into discrete cells, each containing a number of radiating atoms. The atoms in the cell approximately interact with the same external field if the number of atoms in the cell is large enough to approximate their density by a continuous distribution and the size of the

cells is small enough to approximately have a uniform intensity distribution within the cell. The total field at the detector is then given by [106]:

$$\mathbf{E}(\theta_d,\omega) = \sum_j \quad n_j \quad a_j(\omega) e^{-i\frac{\omega}{c}\mathbf{r}_j\cdot[(\cos(\theta_d)-1)\hat{z}+\sin(\theta_d)\hat{x}]} \times \quad e^{-\frac{1}{2}\frac{\omega^2}{c^2}\sigma^2(1-\cos(\theta_d))}\hat{\mathbf{y}}\,, \tag{4.9}$$

where the sum goes over the number of cells in the interaction volume, $n_j = \rho(\mathbf{r_j})$ is the gas density at the center of the cell and the last term is a form factor that takes into account intra-cell interference assuming a Gaussian charge distribution in the cell. Note that the use of cells does not impact the radiation detected along the laser axis ($\theta_d = 0$).

4.3.1 Test case: Lattice grid

As a first test, we consider a set of hydrogen atoms placed in a regular lattice grid and verify that the angle-resolved far-field radiation spectra exhibit the expected interference pattern. To this end, we apply the TDSE interpolation method to a simple test model in which hydrogen atoms, initially in the ground state, are distributed uniformly on a lattice with a separation of 300 nm (typical atomic spacings in optical lattices are in the range of 256 nm - 700 nm [145, 146]). We have considered a driving laser with a central wavelength of 800 nm ($\omega = 0.057$ a.u.), a peak intensity of 9×10^{13} W/cm^2, and a sin^2 envelope of 20 cycles full width. The spatial profile of the laser is chosen to be a Gaussian beam with a beam waist of 30 μm (Rayleigh range $z_0 \approx 3500$ μm). One hundred separate TDSE calculations were performed at peak intensities in the range 0.01×10^{14} W/cm^2 to 1.00×10^{14} W/cm^2 in steps of 10^{12} W/cm^2 and the interpolation of the results is completed in the frequency domain to reduce memory requirements. Given the small number of radiators here, we sum over all atoms, without using Monte Carlo sampling or finite cells.

Considering a regular lattice geometry with atoms arranged along and perpendicular to the

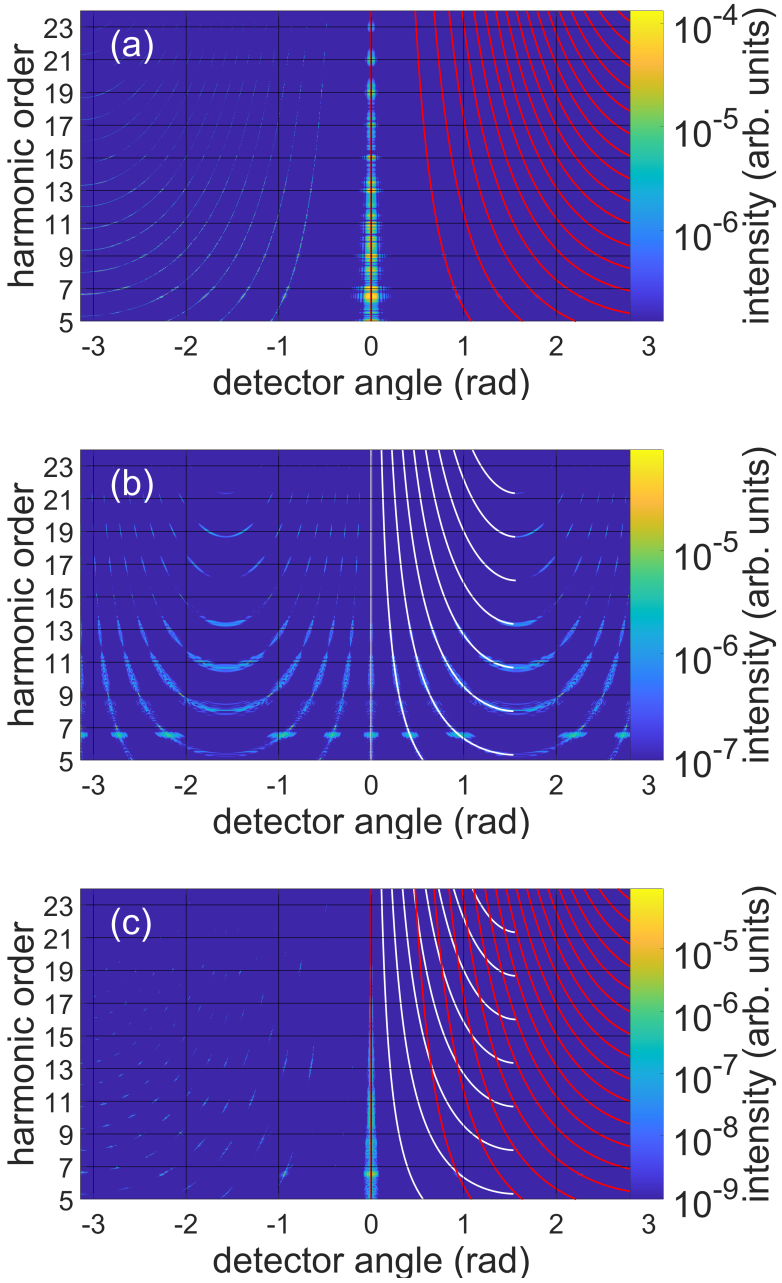

Figure 4.7: Angle-resolved macroscopic high harmonic spectra from uniformly-separated hydrogen atoms in different configurations: (a) row of 100 atoms along the propagation direction, (b) row of 100 atoms perpendicular to the propagation direction, and (c) lattice grid of 100×100 atoms in the plane spanned by the combination of (a) and (b). A Gaussian beam (beam waist 30 μm) with 20-cycle duration at 800 nm and 9×10^{13} W/cm^2 and an atom separation of $L = 300$ nm were considered. The red and white lines represent the constructive interference conditions for atoms located along and perpendicular to the propagation direction, respectively (see Eqs. (4.11) and (4.10)).

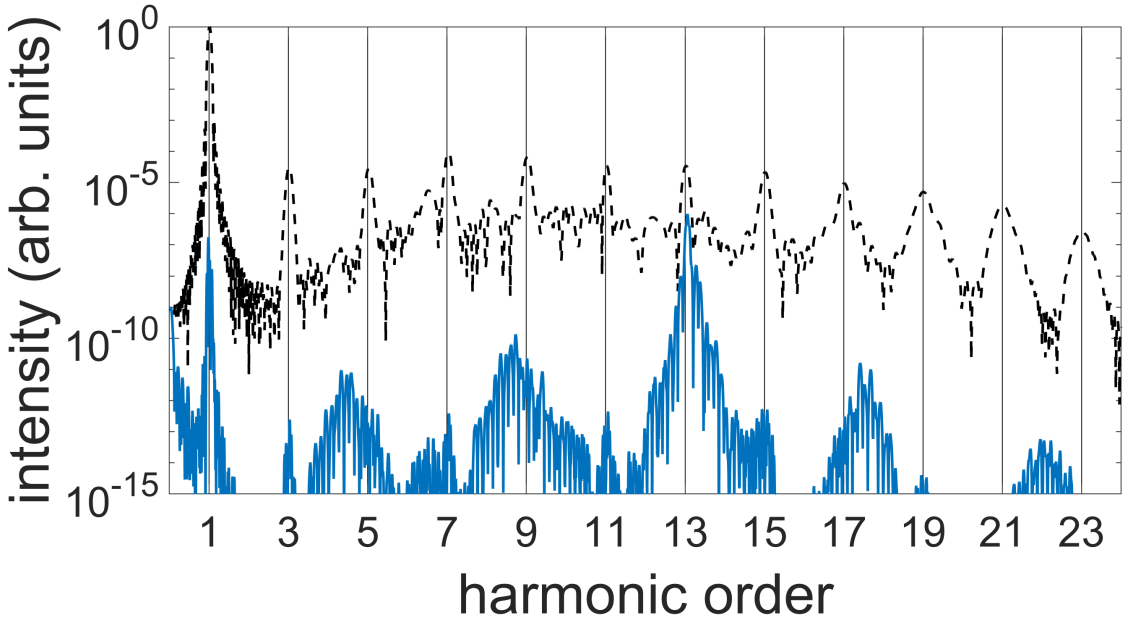

Figure 4.8: Comparison of spectra taken from the results in Fig. 4.7(c) along $\theta_d = 0.65$ rad (blue solid line) and in forward direction ($\theta_d = 0$ rad, black dashed line).

laser propagation direction, radiation from the atoms is expected to add up constructively if

$$\theta_d = \arcsin\left(n\frac{\lambda_{em}}{L}\right) \text{ and} \tag{4.10}$$

$$\theta_d = 2\arcsin\left(\sqrt{\frac{m}{2}\frac{\lambda_{em}}{L}}\right), \tag{4.11}$$

where n and m are integer numbers, L denotes the separation of the atoms and λ_{em} is the wavelength of the emitted radiation. The first (second) condition arises from the interference in emission from atoms perpendicular to (along) the laser polarization direction, and can be derived from Eq. (4.8).

Thus, we expect the process of high-order harmonic generation from uniformly spaced, independently-responding atoms to produce a particular pattern in the angle-resolved spectrum. To test the TDSE interpolation method, we have performed macroscopic calculations for 10^4 hydrogen atoms on a 100×100 lattice. The results in Fig. 4.7(c) show the complete spectrum in the forward direction (at $\theta_d = 0$) and a pattern of bright spots at other angles. As expected from the constructive interference conditions, the number of bright spots in a given detector angle range increases as the (harmonic) frequency of the emitted radiation increases (i.e., the wavelength λ_{em} decreases) and the spectra show the expected symmetries about $\theta_d = 0, \pm\pi/2$. Indeed, the bright spots occur at the vertices of curves representing the two interference conditions. To illustrate this, we show in the other panels of Fig. 4.7 the spectra resulting from configurations in which 100 atoms are positioned in a row either along (panel (a)) or perpendicular to (panel (b)) the laser propagation direction. Furthermore, the curves representing the respective interference conditions are plotted in each spectrum. It is seen that the numerical results indeed agree with the predictions based on the constructive interference conditions.

While these calculations primarily serve as a test case for the macroscopic TDSE interpolation method, we may note that optical lattices are used as platforms in ultracold atom physics to simulate quantum many-body problems (for reviews, see [147–151]). Recently, ultracold atoms have been exposed to the field of an ultrashort laser pulse to observe the response of ^{87}Rb atoms to strong fields [152], which may initiate more combined research in these fields in the future. Here, we note that the spatial separation of the bright spots in the angle-resolved spectrum generated from atoms

in a lattice potentially allows for the selection of radiation at specific higher harmonics. This is illustrated in Fig. 4.8 in which we compare the spectrum at $\theta_d = 0.65$ rad (blue solid line) with that in the forward direction (black dashed line). In the off-axis spectrum, only the fundamental exceeds 0.1% of the 13th harmonic's intensity while the rest of the spectrum is strongly suppressed.

4.4 Atomic hydrogen gas jet

In a common experimental HHG set-up, a large number of atoms in a gas jet contribute to the macroscopic signal. For this section, we therefore consider a gas jet of hydrogen atoms with a density of 10^{18} cm^{-3}. The gas jet is modeled as a cylinder aligned perpendicular to the laser propagation; the width is given by a Gaussian distribution with $\sigma = 500$ μm and is centered at the laser focus. We use the strategy to split the interaction volume in cells and utilize Monte Carlo methods for the sampling of the cell locations, discarding locations where the intensity is below a given cut-off (here, $I(\mathbf{r}_j) < 0.032 I_{peak}$) as the corresponding generated radiation does not contribute significantly to the total radiation. We have considered macroscopic high-harmonic generation from hydrogen atoms generated by a 20-cycle $\sin^2$ pulse at 800 nm, with a variety of peak intensities up to 9×10^{13} W/cm^2. As above, the spatial profile of the laser is chosen to be a Gaussian beam with a beam waist of 30 μm ($z_0 \approx 3500$ μm). One hundred microscopic TDSE calculations were performed at intensities in the range 0.01×10^{14} W/cm^2 to 1×10^{14} W/cm^2 in steps of 10^{12} W/cm^2. We note the need for single-atom calculations above the highest intensity of the macroscopic lasers considered, to allow for accurate interpolation.

4.4.1 Convergence

For the case of a gas jet, we find similar convergence behavior to the SFA+ calculations in Ref. [106]: the off-axis harmonic radiation appears to converge faster for larger cells (Fig. 4.9), and the results appear to be converged for 10^5 radiators regardless of cell size (Fig. 4.10). In general, we observe that good on-axis convergence requires a larger number of cells than required for angular convergence, at least for the near-threshold harmonics of interest in this thesis. Thus,

cell size – which has no effect for on-axis radiation – does not noticeably impact the speed of overall convergence, and we use point-like radiators for all calculations. We note that the convergence in the calculations of the response using 10^5 cells has been achieved from 100 actual TDSE calculations at sample intensities. Since the macroscopic calculations are relatively computationally inexpensive, results of this Chapter consist of calculations with 5×10^5 atomic radiators unless specified.

We must emphasize that the required number of cells is not universal, and may vary greatly for other lasers or targets. We have found that both interaction of UV laser light with helium and mid-IR lasers with hydrogen require on the order of 10^7 cells to achieve the same levels of convergence as above (see Sec. 4.6). More rapid or complex CEP variation also requires more cells for convergence (Sec. 4.5). Preliminary studies suggest alternative cell placement (e.g., quasi-random sampling) may improve convergence somewhat.

4.4.2 Near-threshold harmonics

As discussed at the outset of this Chapter, approximate single-atom methods, such as the strong-field approximation and its extensions, provide good quantitative predictions for the high-order harmonics. On the other hand, in the region near and below the ionization threshold, single-atom TDSE results and experimental data often include a structure besides the harmonic peaks, which often cannot be reproduced by approximate methods due to the incomplete description of the atomic excited state structure.

In Fig. 4.11 we compare results of (a) microscopic single-atom TDSE and (b) macroscopic TDSE interpolation calculations as a function of peak intensity for on-axis emission. In the results it is seen that at the single-atom level there is strong radiation emission at near-threshold frequencies in between the harmonics (the field-free ionization energy is at 8.77ω). The relative strength of the harmonic and off-harmonic radiation emission strongly fluctuates as a function of peak intensity. As examples, we present spectra at two different peak intensities ((c) 3.8×10^{13} W/cm^2, (d) 7.0×10^{13} W/cm^2) on the right of Fig. 4.11. While at the higher intensity (panel (d)) there is a strong single-atom 9th harmonic emission (black dashed line), the emission at the same harmonic is suppressed

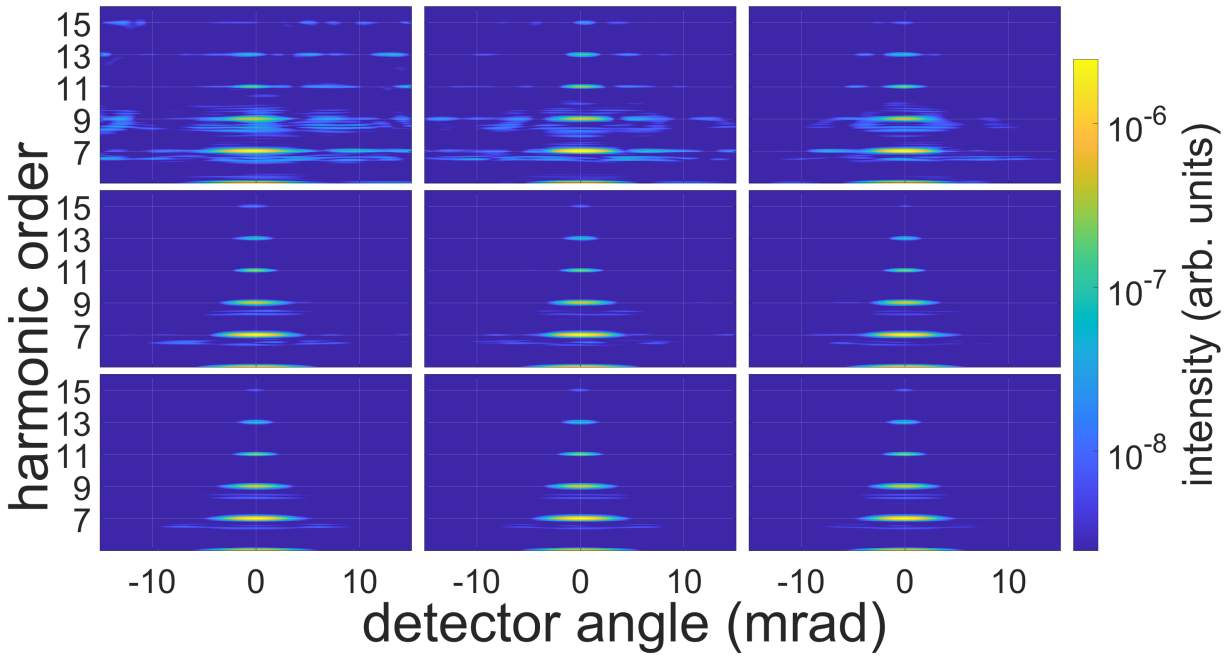

Figure 4.9: Angle-resolved macroscopic radiation spectrum for a gas jet of hydrogen atoms driven by an 800 nm laser with peak intensity 7.0×10^{13} W/cm^2 for different numbers of cells (rows) and cell sizes (columns): (top) 10^3 cells, (middle) 10^4 cells, and (bottom) 10^5 cells. (left) point-like radiators, (middle) 3 μm cells, and (right) 5 μm cells.

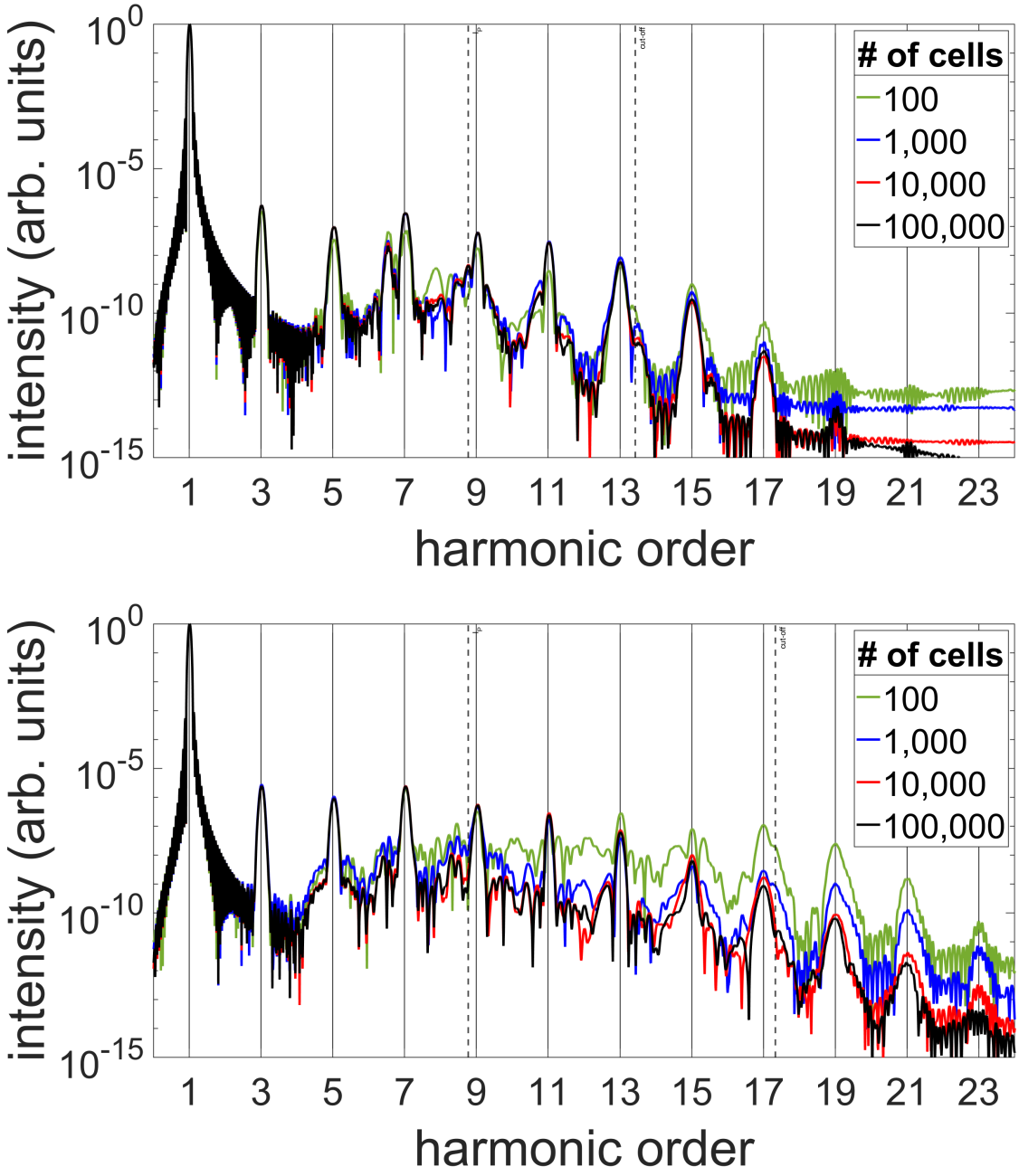

Figure 4.10: Convergence of macroscopic on-axis radiation with number of cells (cell width has no effect), generated by a $\sin^2$ pulse of 20 optical cycles at wavelength of 800 nm and peak intensity of (top) 3.8×10^{13} W/cm^2 and (bottom) 7.0×10^{13} W/cm^2. Vertical dashed lines denote the ionization potential (left line) and HHG cut-off (right line).

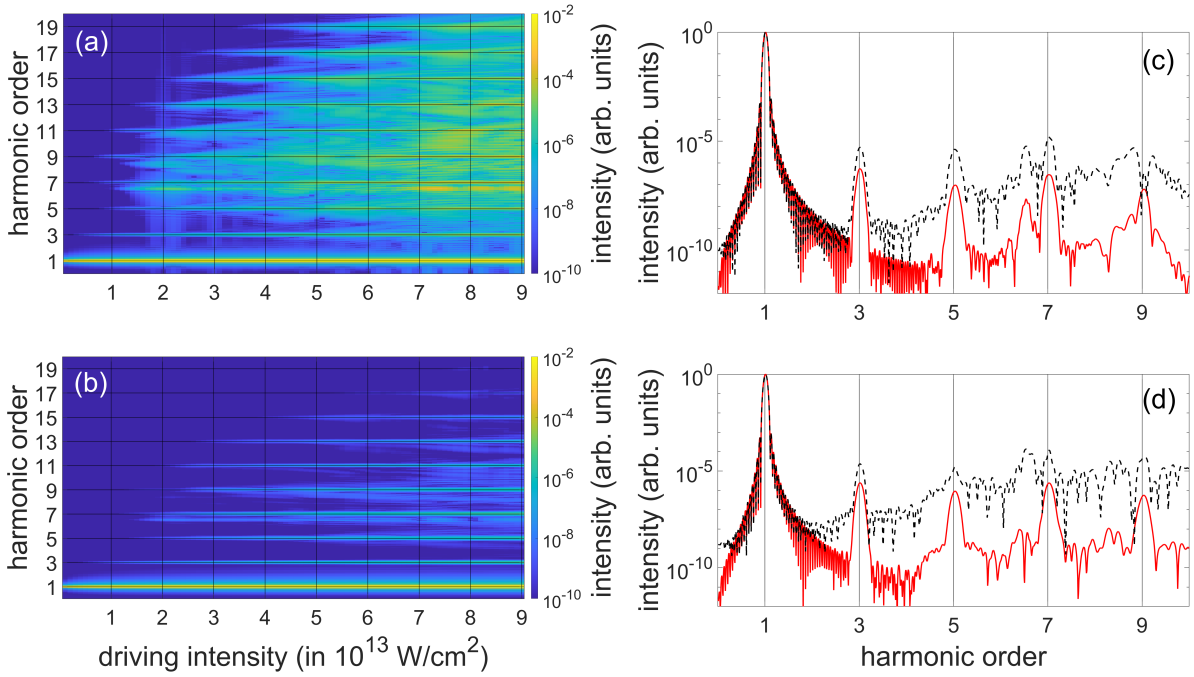

Figure 4.11: Comparison of single-atom TDSE results and macroscopic TDSE interpolation results for high harmonic generation in hydrogen atoms. On the left, the (a) single-atom and (b) macroscopic on-axis spectrum is shown as a function of peak intensity. The spectra on the right show the comparison (single atom: black dashed line, macroscopic: red solid line) at peak intensities (c) $I_0 = 3.8 \times 10^{13}$ W/cm^2 and (d) $I_0 = 7.0 \times 10^{13}$ W/cm^2.

(as compared to radiation emitted at frequencies just below the 9th harmonic) at the lower intensity (panel (c)). In general, in the near-threshold regime, the magnitude of the off-harmonic radiation yield is comparable to that of the harmonic radiation.

In contrast, the macroscopic results (panel b) show emission spectra with a much clearer structure; the harmonics are strongly enhanced as compared to radiation emission at other frequencies at all intensities. This is also evident in the macroscopic responses at the two selected peak intensities. The radiation signal in between the harmonics is suppressed by 1-2 orders of magnitude as compared to the harmonic emission. For example, the feature close to the 9th harmonic appears as a shoulder to the harmonic. Thus, in the macroscopic spectra the high harmonic peaks in the near-threshold region become as prominent as those in the rest of the spectrum, throughout the plateau to the cut-off, similar to typical observations of high-harmonic spectra in experiment (see, e.g., [96]).

The origin of the suppression of the off-harmonic radiation is related to the differences in the coherent build-up of the distinct parts of the spectrum. This can be seen from Fig. 4.12 in which we present a comparison of calculations where the interpolated single-atom TDSE results are either added up coherently (solid red line, as Eq. (4.8)) or incoherently (dashed blue line, with $P(\omega) = \sum_j |a_j(\omega)|^2$). It can be clearly seen that it is the lack of coherence of the radiation at non-harmonic frequencies that is the primary reason for the strong suppression in the macroscopic result.

Although in the on-axis spectra the off-harmonic near-threshold radiation is strongly suppressed, this part of the emitted radiation can be separated from the harmonics since it has a different angular character than the harmonic radiation (cf. Fig. 4.13). The high-harmonic lines show the expected on-axis emission, which becomes more focused in the forward direction for higher harmonic numbers. In contrast, the off-harmonic emission extends to larger divergence angles and, around some harmonics, forms halo-like patterns in the angle-resolved macroscopic spectrum. Such spatial-spectral characteristics of off-harmonic structures in the low- and high-energy part of the spectrum are in agreement with previous observations [95, 96, 153–157], showing that the present

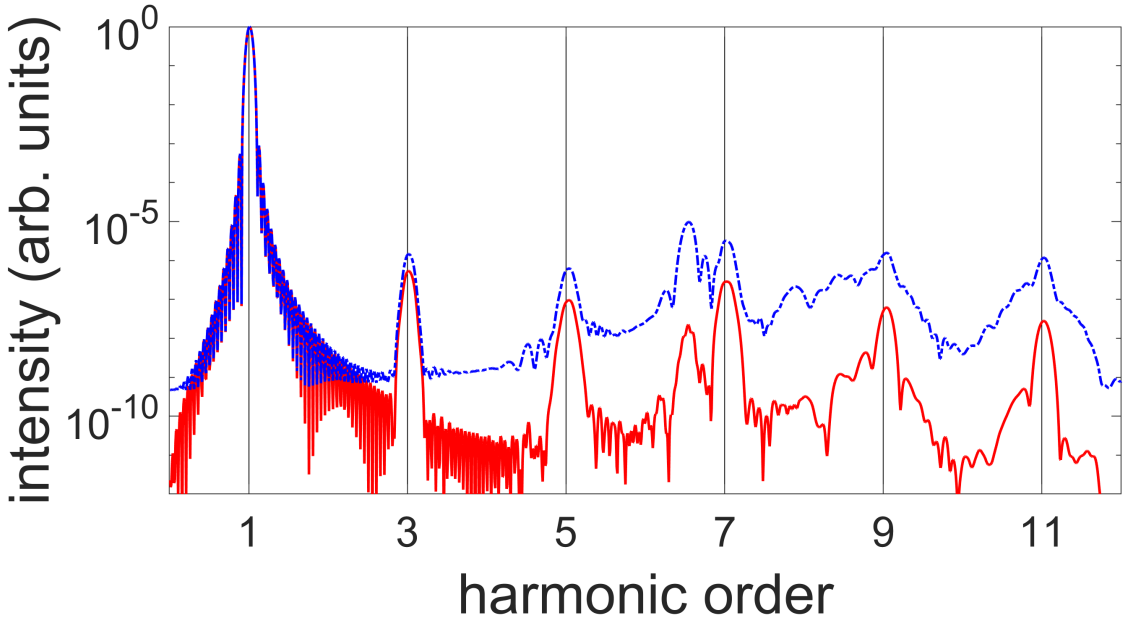

Figure 4.12: Comparison of macroscopic calculations in which the single-atom TDSE results are added coherently (solid red line) and incoherently (dot-dashed blue line) for high-order harmonic generation at $I_0 = 3.8 \times 10^{13}$ W/cm^2.

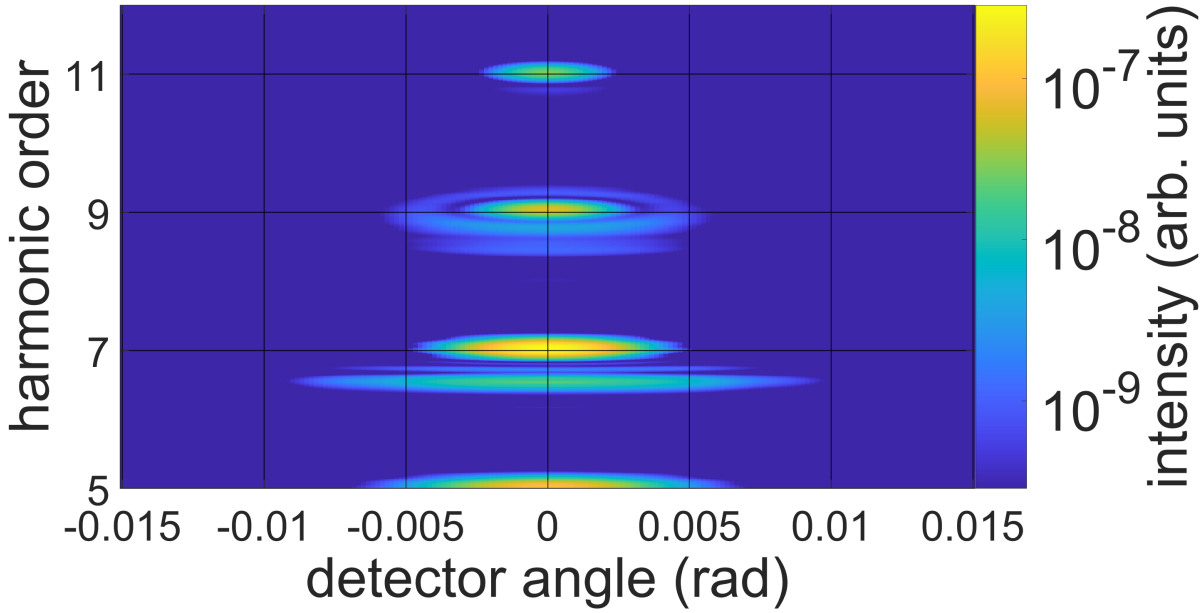

Figure 4.13: Angle-resolved near-threshold part of the macroscopic radiation spectrum for a gas jet of hydrogen atoms driven by an 800 nm laser with peak intensity 3.8×10^{13} W/cm^2.

efficient interpolation method leads to similar results and conclusions as previous sometimes more sophisticated simulations.

In Fig. 4.14, we show wavelet analysis (see Sec. 1.5.3) for the radiation (a) on-axis and (b) at 5 mrad off-axis. The on-axis radiation is dominated by consecutive odd harmonics, which – as expected – are emitted at times symmetrically about the center of the pulse. On the other hand, the off-axis wavelet, which primarily contains the non-harmonic emission, shows a different and more complex time dependence. In particular, we note that several off-harmonic features appear first near the peak of the pulse and shift downward in energy at the trailing edge. The curvature of the shift roughly scales with the field-shifted energy of the excited states, and the wavelet results thus suggest that the off-axis radiation in the near-threshold part of the radiation spectra are related to the resonance features, discussed in Ch. 3.

4.4.3 Appearance of resonance features in macroscopic response

We note that the results presented in Figs. 4.11 to 4.13 have been obtained for propagation of the wavefunction until the end of the driving laser pulse. Thus, the radiation discussed above, including the off-harmonic spectral features, has been generated during the interaction between the laser pulse and the hydrogen atom. It is therefore unlikely that the structures can be related to free induction decay following coherent excitation in the atom. Instead, as discussed in Ch. 3, we understand these features to be the result of field-shifted resonances enhancing HHG emission. By inverse Fourier transforming the macroscopic $E(\omega)$, we are able to perform the same sorts of analysis for macroscopic results as seen in Ch. 3 for microscopic results. Given the interpolation requirement of scanning intensity for any given laser parameters, it is not currently feasible to perform macroscopic scans across other parameters (e.g., λ, N_τ, Z). In the future, interpolation across multiple laser parameters may enable efficient exploration of the broader space.

In Fig. 4.15, results for radiation near 9ω as a function of intensity are given for microscopic (as Fig. 3.10) and macroscopic calculations. While the majority of off-harmonic radiation is strongly suppressed, some features survive macroscopic summation. In particular, macroscopic spectra near

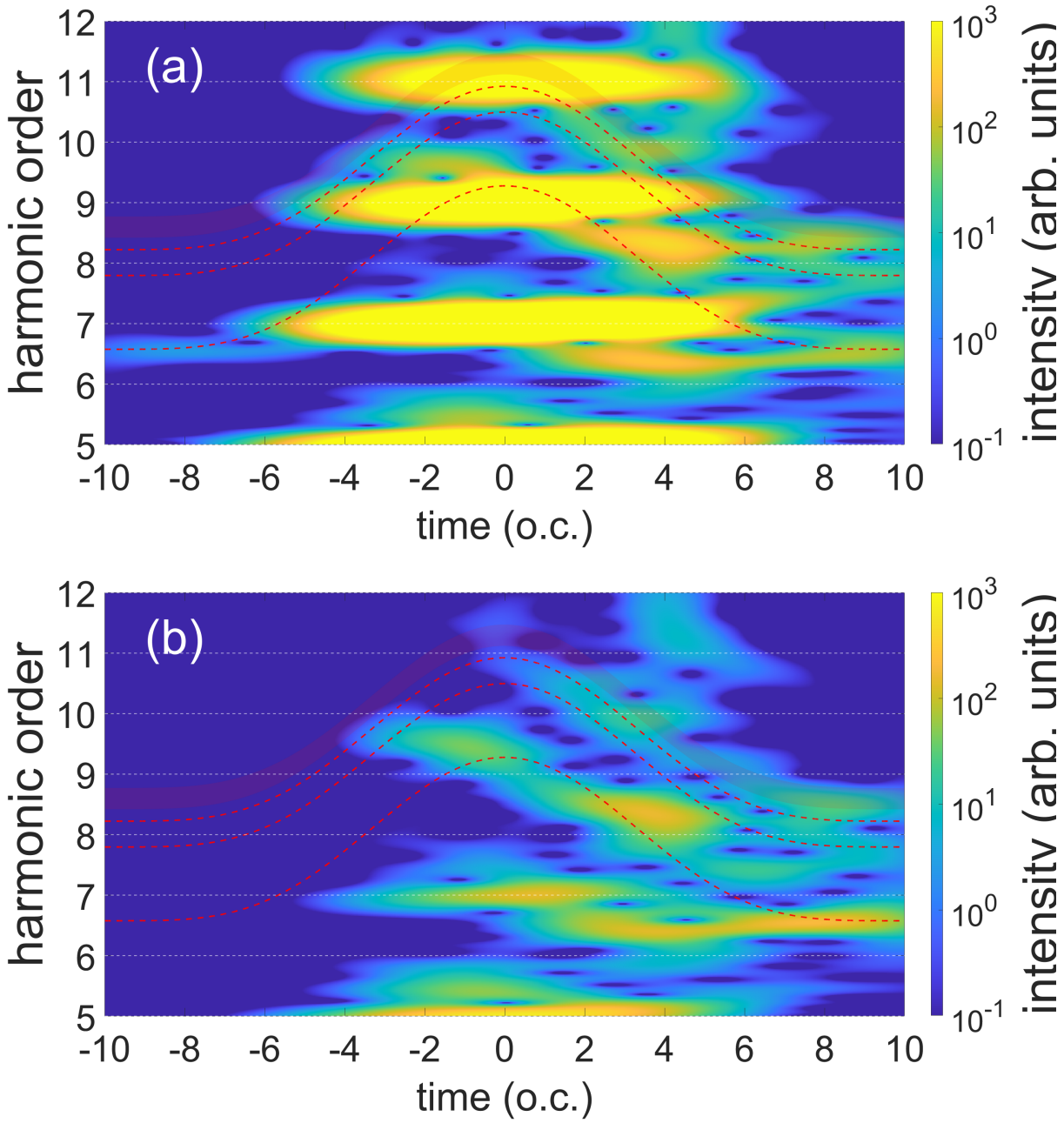

Figure 4.14: Wavelet analysis of the macroscopic radiation for a gas jet of hydrogen atoms driven by an 800 nm laser with peak intensity 7×10^{13} W/cm^2 at detection angles (a) $\theta = 0$ mrad (on-axis), and (b) $\theta = 5$ mrad. The shifted energy of the $2p, 3p$, and $4p$ states relative to the $1s$ (ground) state are denoted by red lines, while the region containing the higher Rydberg states (shifted $5p$ to threshold) are shaded in red. Wavelet parameter $\Omega_0 = 54$.

2.0×10^{13} W/cm^2 display similar radiation peaks splitting off 9ω and broad radiation in the region of field-free Rydberg energies, as seen in microscopic results. While the intensity of these macroscopic features is less than the on-harmonic radiation, it is still significant.

In Fig. 4.16, we consider temporal profiles as outlined in Sec. 1.5.1, again comparing microscopic and macroscopic radiation. The macroscopic signatures of resonantly-enhanced harmonic emission are quite prominent, with a few key differences. Firstly, radiation just after the peak of the pulse is consistently of similar strength to the strongest distinguishable resonance features. Second, resonantly-enhanced radiation occurs for intensities somewhat above the intensities predicted. Both features are explained by the range of intensities contributing to any given macroscopic result. "Normal HHG" occurring just after the peak appears consistently for wider intensity ranges than does resonantly-enhanced emission (since resonances move). And, only a small minority of atoms interact with the peak intensity; the signal is thus dominated by atoms interacting with a slightly weaker field. This also leads to a broadening (in time and driving intensity) of resonance features – for a given peak intensity, different portions of the gas jet will shift into resonance at different relative times. As a result of resonant enhancement, radiation near 9ω spans varying temporal ranges according to the driving intensity. Therefore, understanding resonant effects will be crucial to sculpting UV pulses.

4.5 Effects of macroscopic phase[1]

Nonlinear processes in ultrafast light-matter interaction are induced at high laser peak intensities and thus require the application of focused short-pulsed lasers with a broad frequency bandwidth. In contrast to above assumptions of a monochromatic Gaussian beam which experiences a Gouy π-phase shift across the focus [144], broadband pulses have a different spatial phase dependence. This more general phase distribution has been derived and studied by Porras and co-workers [142, 143]. The exact distribution depends on the so-called Porras factor, which needs to be determined for a given laser system. It creates a spatially-dependent CEP. The impact of

[1] Some results of this Section are also presented in a submitted manuscript [6].

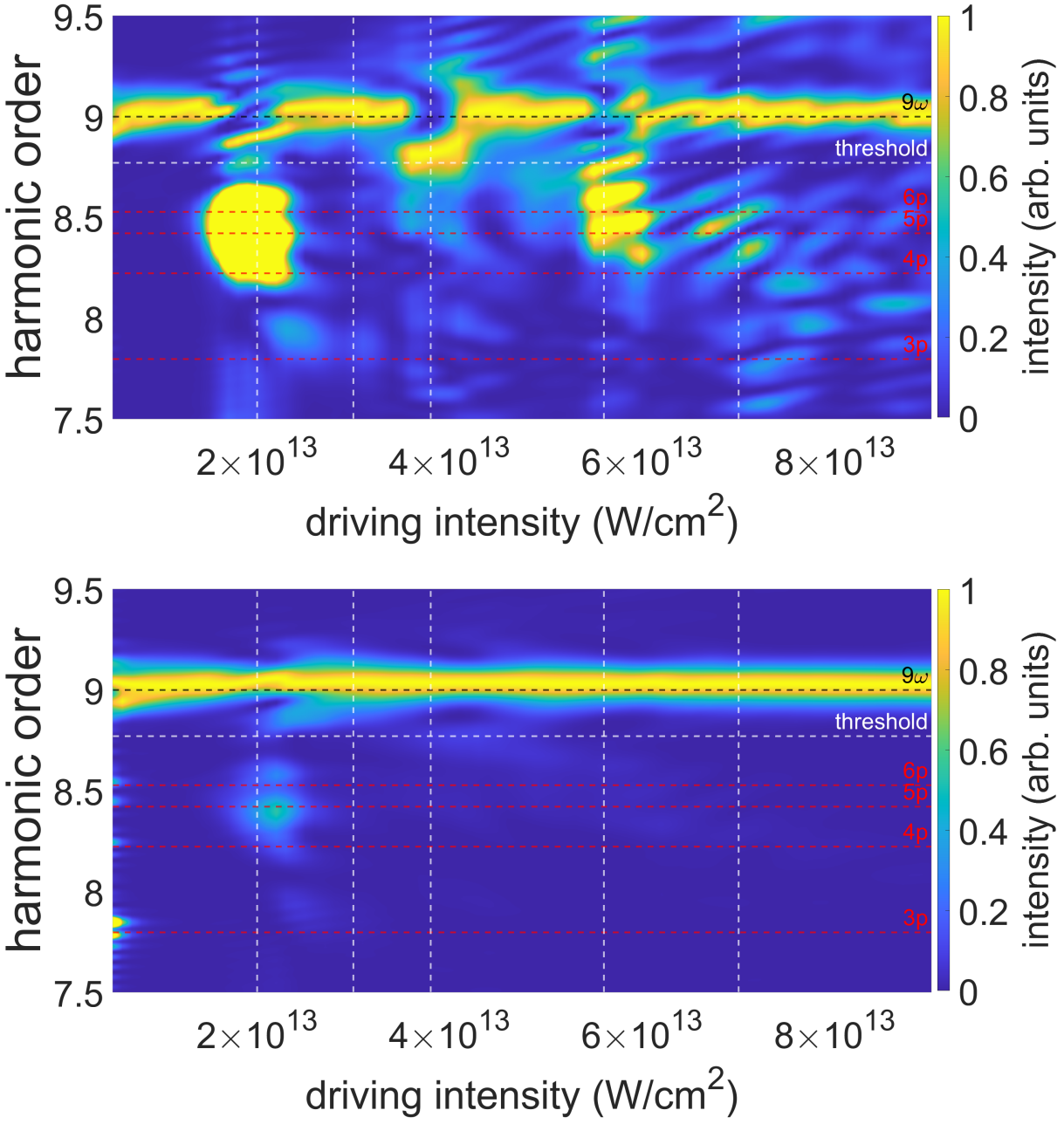

Figure 4.15: Comparison of (top) single-atom results and (bottom) on-axis macroscopic TDSE interpolation results for near-threshold HHG spectra as a function of peak intensity for an 800 nm, 20 o.c. pulse interacting with atomic hydrogen. Results for each intensity have been normalized to the maximum signal in the region between 8.75ω and 9.5ω. Horizontal red dashed lines denote field-free excited state transition energies and vertical dashed lines identify intensities selected in Sec. 3.4: 2.0×10^{13}, 3.0×10^{13}, 3.8×10^{13}, 5.6×10^{13}, and 7.0×10^{13} W/cm^2.

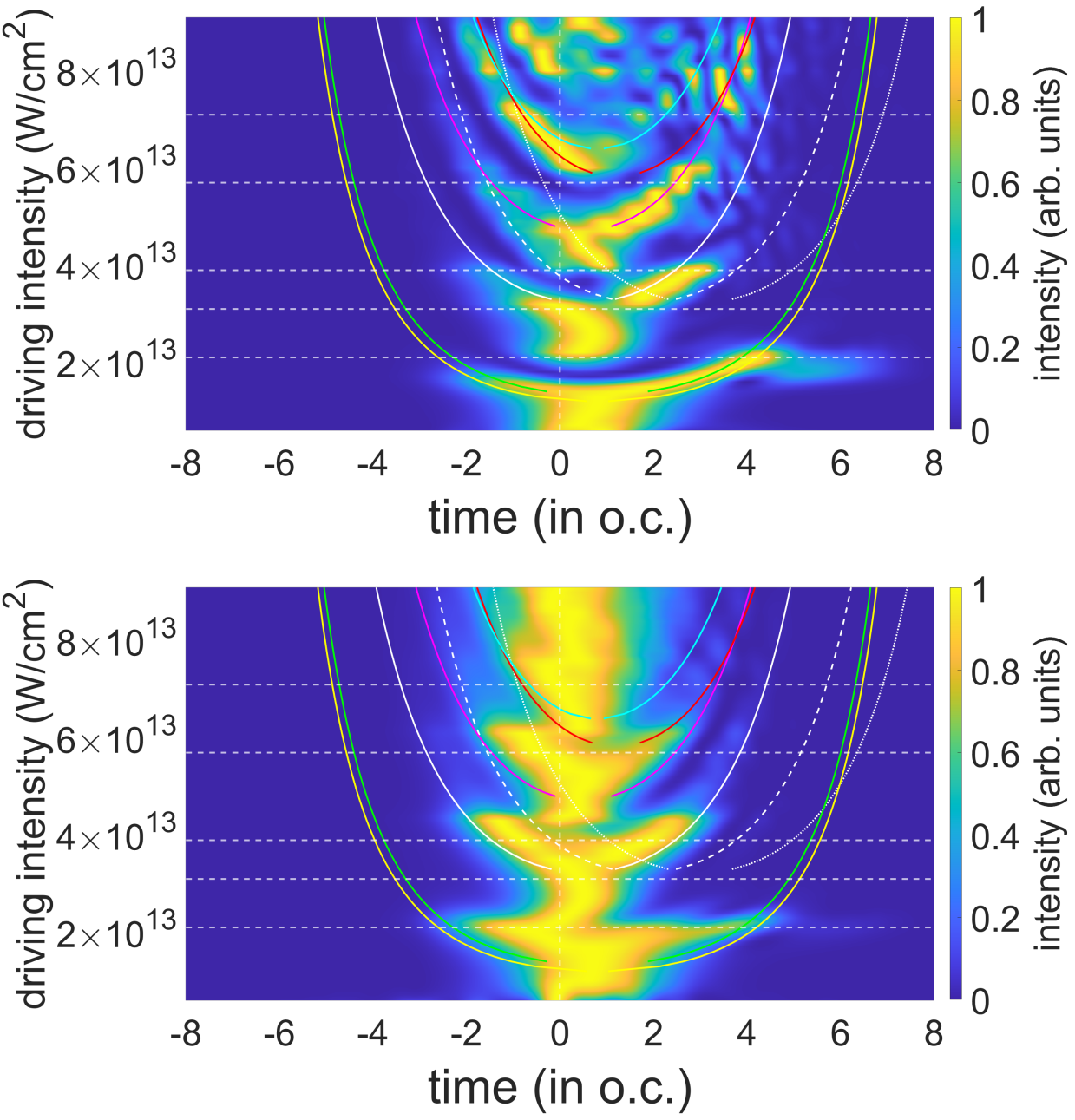

Figure 4.16: Comparison of (top) single-atom results and (bottom) on-axis macroscopic TDSE interpolation results for temporal profile of radiation within 1ω of the 9th harmonic as a function of driving pulse intensity in hydrogen for an 800 nm, 20 o.c. pulse. For each intensity, the results have been normalized to a maximum of 1 for sake of comparison. A vertical dashed line denotes the peak of the laser and horizontal dashed lines identify intensities selected in Sec. 3.4: 2.0×10^{13}, 3.0×10^{13}, 3.8×10^{13}, 5.6×10^{13}, and 7.0×10^{13} W/cm^2. Lines are drawn for delayed resonances as outlined in Table 3.1.

the focal phase on electron backscattering at nanoscale metal tips [158] and photoelectron spectra [159] in few-cycle laser pulses has been demonstrated recently.

Since in HHG the coherent addition of radiation controls the results of macroscopic summation (cf. Fig. 4.12), one can expect to observe traces of the phase distribution in the radiation. We present macroscopic high harmonic generation results that indicate significant differences in the angular resolution of the emitted harmonics, depending on the spatial phase distribution across the focus. Specifically, our results show a distinct interference pattern in the angular distribution for focal phase distributions with negative Porras factors.

The general form of the spatial phase distribution for broadband laser pulses is given by [142, 143]:

$$\Delta\Phi_F(z,r) = -\arctan\left(\frac{z}{z_0}\right) + g_0 \frac{\left[1 - 2\left(\frac{r}{w(z)}\right)^2\right]}{\frac{z}{z_0} + \frac{z_0}{z}} \tag{4.12}$$

where

$$g_0 = \left.\frac{dZ_R(\omega)}{d\omega}\right|_{\omega_0} \frac{\omega_0}{Z_R(\omega_0)} \tag{4.13}$$

is the Porras factor and

$$Z_R(\omega) = \frac{\omega W^2(\omega)}{2c} \tag{4.14}$$

is the frequency-dependent Rayleigh range ($z_0 \equiv Z_R(\omega_0)$), z and r are the positions along and transverse to the propagation of the laser, ω_0 is the central frequency of the laser, $w(z) = W_0\sqrt{1 + (\frac{z}{z_0})^2}$ is the beam radius of the center frequency, $W(\omega)$ is the frequency-dependent input waist, $W_0 = W(\omega_0)$ is the central frequency beam waist at the focus, and c is the speed of light. The first term in Eq. (4.12) is the Gouy phase for monochromatic beams, which gives a longitudinal phase dependence along the laser propagation direction, while in the transverse direction the Gouy phase is constant. The second term scales with the Porras factor g_0 and describes the difference to the Gouy phase for beams with a frequency bandwidth.

Fig. 4.17 shows a comparison of the spatial phase profile for (a) $g_0 = 0$ (Gouy phase) and (b) $g_0 = -2$. We have focused on situations with negative Porras factor, which correspond to the geometry of laser systems based on hollow-core fiber-compressors [159]. The specific value of

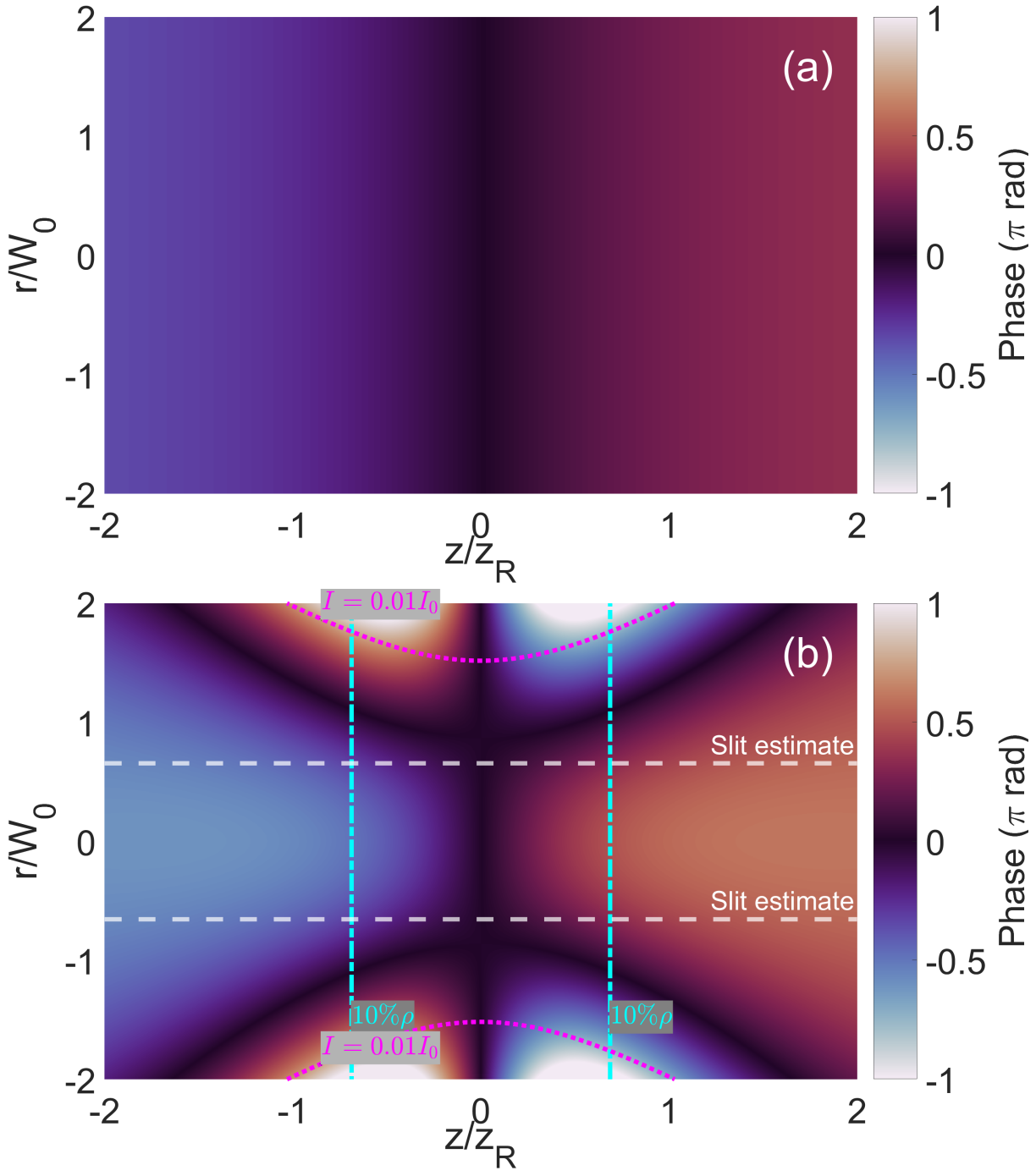

Figure 4.17: Spatial distribution of carrier-envelope phase in a focused broadband Gaussian laser pulse: (a) Gouy phase ($g_0 = 0$) and (b) focal phase with $g_0 = -2$. For the latter, reference lines are drawn showing (magenta) position where laser intensity falls below 1% of peak, (cyan) position where gas density ρ falls below 10% of peak for a gas width of $0.23z_0$, and (white) estimates of the effective slit locations based on interference patterns (0.925 times the transverse node separation near $z = 0$ in Eq. (4.12)). (Taken from [6].)

$g_0 = -2$, chosen in the majority of our studies, has been reported in a recent measurement [158]. For negative values of g_0, the 2nd focal phase term has the same sign as the Gouy phase on-axis, but changes sign at certain radial distances, which depend on g_0 and z. This implies that for the total focal phase at each off-center position along the propagation distance there are two points in the radial direction, symmetric over $r = 0$, with $\Delta\Phi_F = 0$. Furthermore, these points are in-phase with all the central points at $z = 0$ and for the location of the points $\lim_{z\to 0} r_{zero}(g_0, z) = W_0/\sqrt{2}$. One may therefore expect that such a focal phase distribution imprints an interference structure onto the angular distribution of the harmonic signals transverse to the propagation direction.

In Fig. 4.18, we present simulated angle-resolved macroscopic high harmonic spectra generated by a driving laser with a central wavelength of 800 nm ($\omega_0 = 0.057$ a.u.), a peak intensity of 7×10^{13} W/cm^2, and a sin^2-envelope of 20 cycles full width. The spatial profile of the laser has been chosen to be a Gaussian beam with a beam waist of 30 μm ($z_0 \approx 3500$ μm). We have assumed a gas jet with a Gaussian density distribution along z, centered about $z = 0$ and with a width of $\sigma_z = 800$ μm $\approx 0.23 z_0$, and constant density along x (the radial direction). Results have been obtained assuming focal phase distributions with (a) $g_0 = 0$ (Gouy phase distribution) and (b) $g_0 = -2$. In the present simulations, 10^7 single-atom results have been used to obtain each converged macroscopic HHG spectrum.

The comparison reveals a significant difference in the angular distribution of the below-threshold harmonic lines for the two phase distributions. The spectrum obtained with negative Porras factor clearly exhibits the expected interference pattern in the harmonic lines, while there is no such signature in the spectrum calculated for the Gouy phase distribution. The position of the side maxima in the interference pattern can be roughly approximated by the double-slit formula (i.e., Eq. (4.10)):

$$\theta_d(\lambda_{em}) = \arcsin\left(n\frac{\lambda_{em}}{L}\right), \tag{4.15}$$

where n is an integer, L denotes the separation of the slits perpendicular to the laser propagation direction and λ_{em} is the wavelength of the emitted radiation. The white lines in Fig. 4.18 show

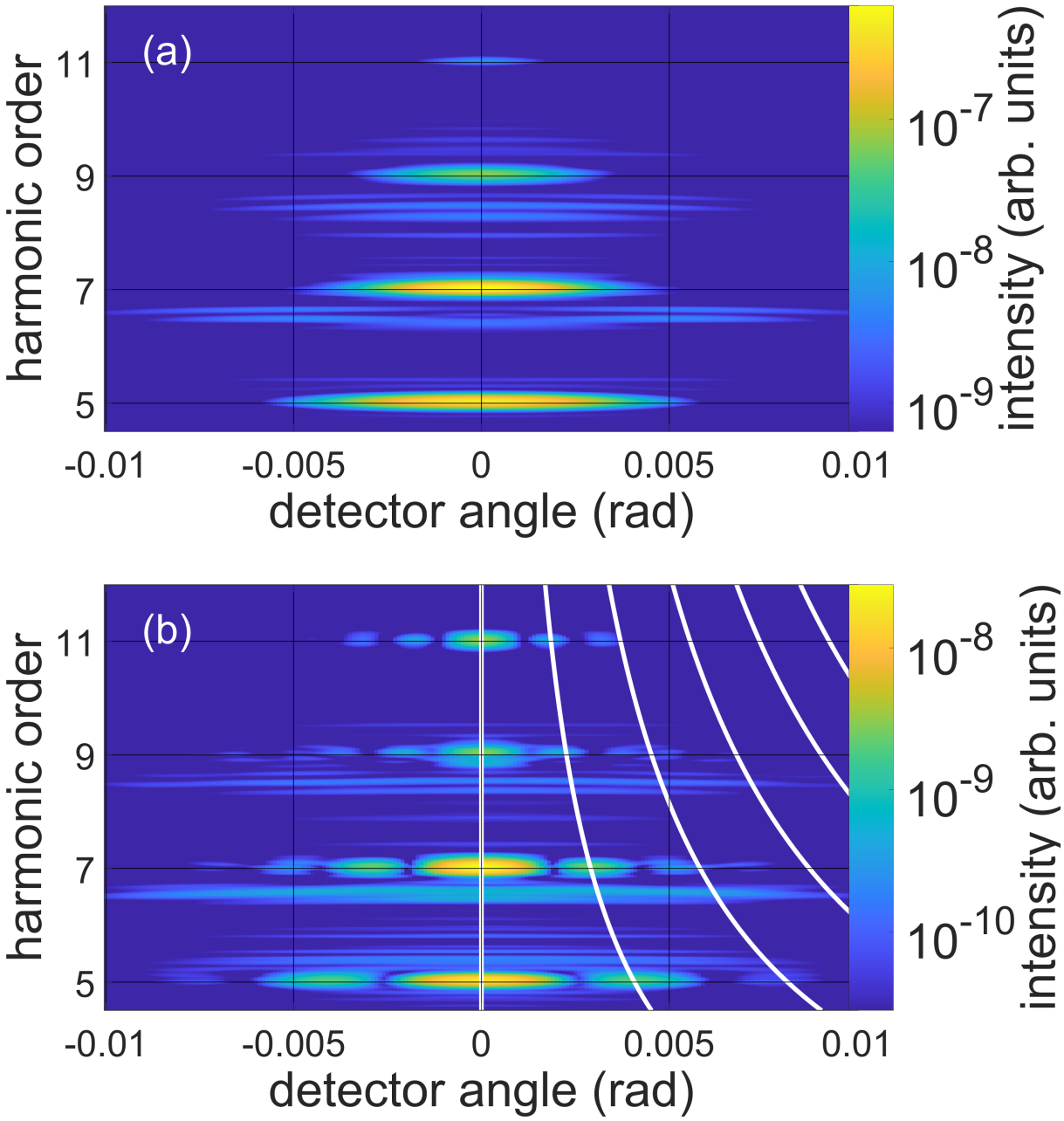

Figure 4.18: Comparison of simulated angle-resolved macroscopic high harmonic spectra using (a) Gouy phase ($g_0 = 0$) and (b) focal phase with $g_0 = -2$. Lines denote peaks of a double-slit pattern with slit separation of $0.925\sqrt{2}W_0 \approx 39\mu$m in the direction perpendicular to the laser propagation. Laser and gas jet parameters are given in the text. (Taken from [6].)

predictions for the side maxima, fitted to match the numerical data using $L = 0.925L_0$. This effective slit separation is slightly smaller than the distance between the two radial positions $L_0 = \sqrt{2}W_0$ for $\Delta\Phi_F = 0$ near $z = 0$. We further note that the off-harmonic radiation at energies in between the harmonics does not show an interference pattern. This is due to the incoherent nature of this radiation, which results from fluorescence due to resonant excitation of the hydrogen atom [160].

A key factor for the occurrence of the interference effect is that for nonzero g_0-values the phase shift equals zero at radial positions in the focus with $z \neq 0$. This raises the question of how the interference pattern depends on parameters of the set-up. Results of those studies are presented in Fig. 4.19. In the plots, we show how the positions of the first minimum (circles) and the first maximum (squares) in the interference pattern of the 7th harmonic depend on (a) the width of the central gas jet σ_z, (b) the Porras factor g_0, and (c) the beam waist W_0. Other parameters are kept the same as in Fig. 4.18.

The positions of the first two extrema remain almost unchanged for variations of the central gas jet width and the Porras factor. We note that an increase of the gas jet width leads to a decrease in the contrast between the maxima and minima in the interference pattern until for even larger jet widths, i.e., $\sigma_z > 0.5z_0$, the pattern visually disappears. This is likely due to the enhanced impact of out-of-phase contributions from locations in between the nodal points which tend to destructively interfere with the contributions from points with $\Delta\Phi_F = 0$. Within the limits for the jet widths established in Fig. 4.19(a), the position of the nodal points does not change significantly along the propagation axis. This explains the stability of the extrema over the range of jet widths. The Porras factor g_0 controls the convexity (concavity) of the curve along which the nodal points appear as a function of z. However, near the center of the focus, the change is not significant enough to impact the position of the extrema in the interference patterns for $\sigma_z \approx 0.23z_0$ (cf. Fig. 4.19(b)). On the other hand, for a variation of the laser beam width W_0 (Fig. 4.19(c)), the locations of the interference maxima approximately scale with $W_0^{-1/2}$, as expected for the simplified interpretation based on the double-slit interference pattern. Small variations from the trend are

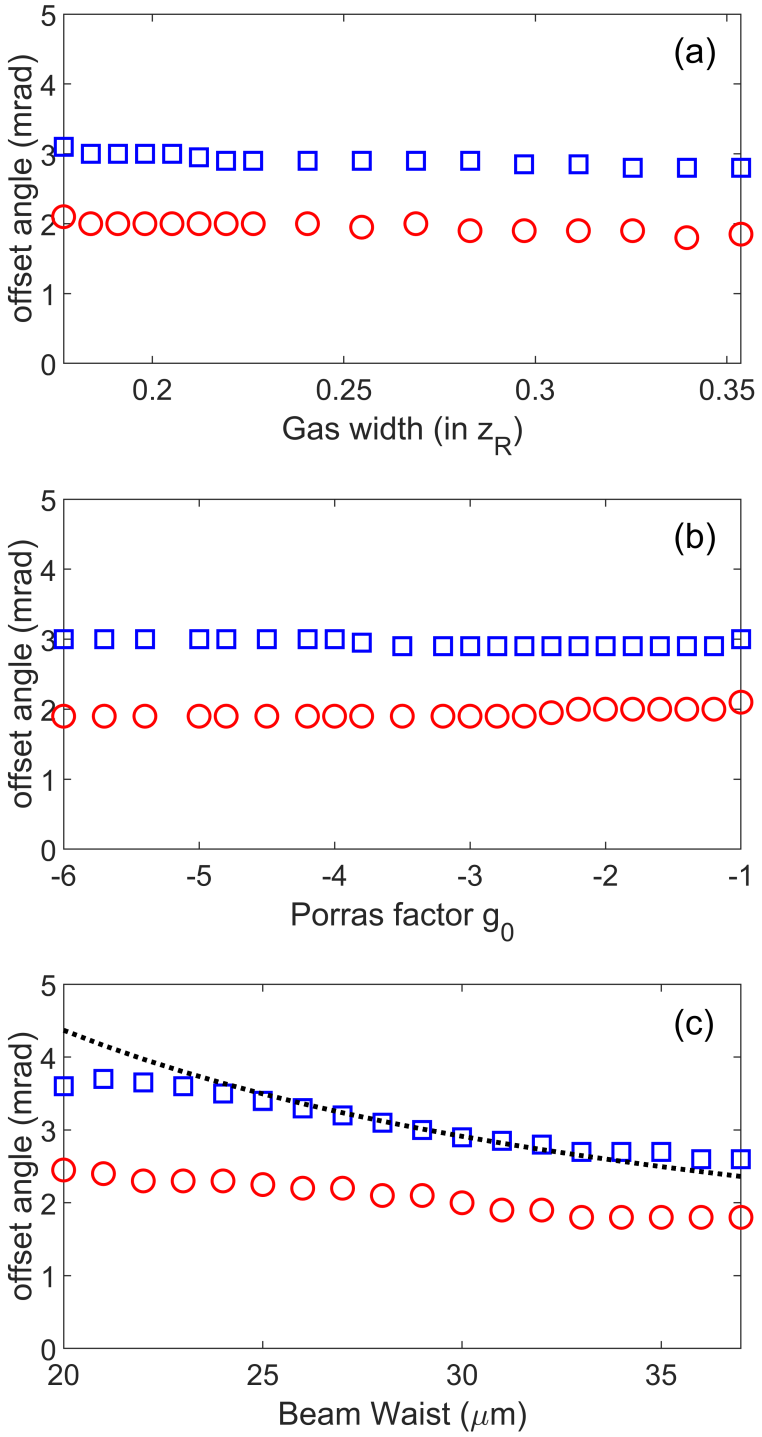

Figure 4.19: Position of first minimum (circles) and first maximum (squares) in the interference of the 7th harmonic as a function of the (a) width of the central gas jet σ_z, (b) g_0, and (c) W_0. Other parameters are kept the same as in Fig. 4.18. The line in the bottom panel shows the prediction for the first side maximum based on the double-slit formula with estimated slit separation of $0.925L_0$. (Taken from [6].)

seen at the smallest values of W_0. Since $z_0 \propto W_0^2$, this can be understood again as likely due to out-of-phase contributions from the relatively wide gas jet.

In Fig. 4.20, we demonstrate the suppression of higher harmonic radiation on-axis as a result of the macroscopic phase. As before, the single-atom response (black) has relatively equal intensity for harmonics through the cut-off, as well as for the off-harmonic radiation. Including only intensity variation and geometric phase, the macroscopic result for a (non-physical) laser with no spatial phase variation (purple) strongly suppresses most off-harmonic radiation, and decreases the intensity of the highest harmonics ($> 15\omega$) relative to the plateau. Including the Gouy phase of a monochromatic Gaussian laser (red), radiation is suppressed proportional to the harmonic order, but the structure of the off-harmonic radiation does not greatly differ. When the additional focal phase is included (green), on-axis radiation is further suppressed for higher harmonics, resulting in radiation at the cut-off 10 orders of magnitude weaker relative to the fundamental than that present in the single-atom response. When present, this additional focal phase must be considered in phase-matching.

Within the numerics of our macroscopic simulations, the focal phase is also significant. Fig. 4.21 demonstrates the increased convergence requirements when including the focal phase (bottom Panel) as compared to calculations with only the Gouy phase (top Panel). The focal phase requires orders of magnitude more cells for convergence, especially for harmonics above the threshold. We attribute this to a combination of lower radiation intensity – requiring more cells to bring the noise floor below regions of interest – and more rapid phase variation within the gas jet – requiring more cells to well-sample the phase structure.

4.6 Other investigations

In addition to our core focus of hydrogen driven by an 800 nm laser pulse, we investigated other wavelengths and targets, with parameters summarized in Table 4.1 (for example chosen intensities).

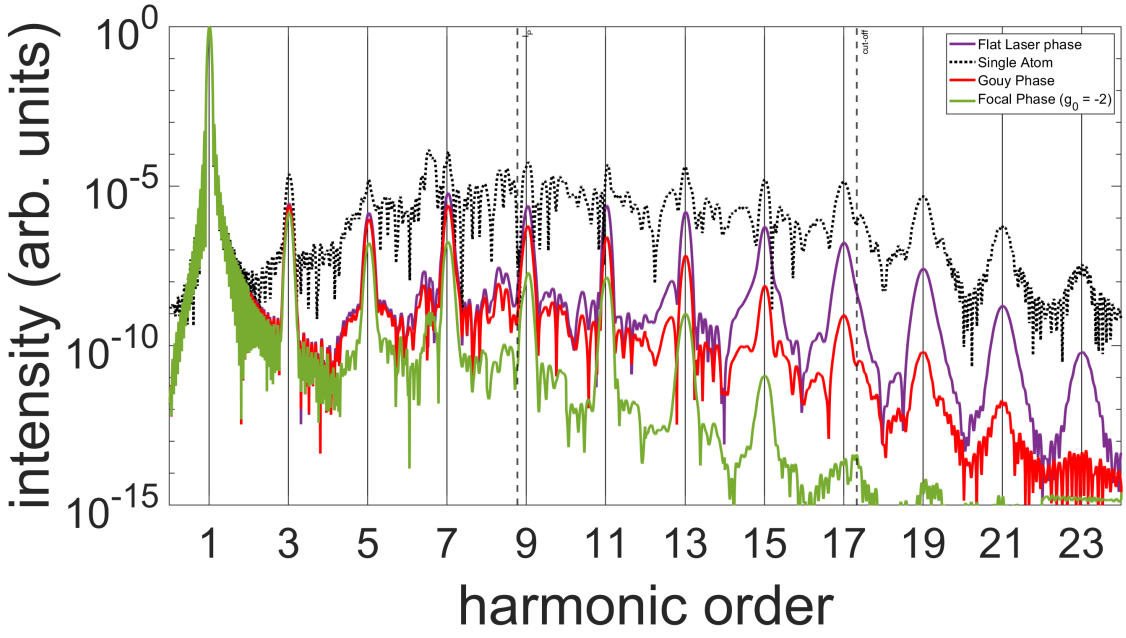

Figure 4.20: Comparison of single-atom results (black dotted) and macroscopic TDSE interpolation results for different driving laser CEP profiles: constant phase (purple), Gouy phase (red), focal phase with $g_0 = -2$ (green). For a gas jet of hydrogen atoms driven by an 800 nm laser with peak intensity 7.0×10^{13} W/cm^2.

Parameter			
Target atom	Hydrogen	Hydrogen	Helium
Wavelength (nm)	800	1600	400
Intensity (W/cm^2)	3.8×10^{13}	8.8×10^{13}	3.3×10^{14}
Duration (o.c.)	20	10	20
I_P (a.u.)	0.50	0.50	0.94
I_P/ω	8.8	17.6	8.1
U_P/ω	1.5	27.1	1.6
Keldysh γ	1.7	0.57	1.6

Table 4.1: Comparison of parameters for hydrogen driven by near-IR and mid-IR lasers and for helium driven by a 400 nm pulse. A single example intensity is chosen from the range of each set. We note that the similarity of dimensionless parameters for the 800 and 400 nm cases was by design.

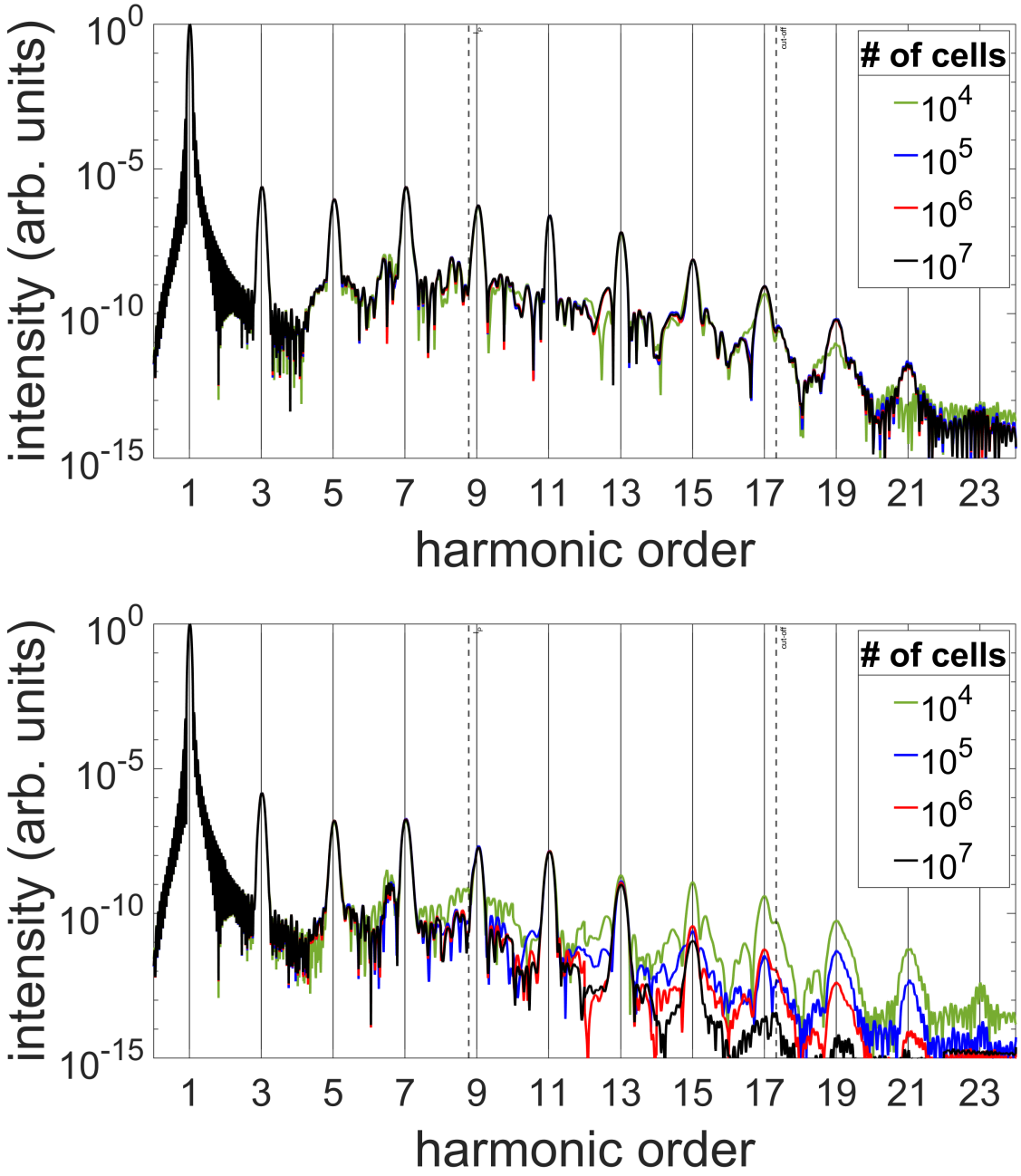

Figure 4.21: Convergence of macroscopic on-axis radiation with number of cells for (top) Gouy phase and (bottom) focal phase with $g_0 = -2$, generated by a $\sin^2$ pulse of 20 optical cycles at wavelength of 800 nm and peak intensity of 7.0×10^{13} W/cm^2. Vertical dashed lines denote the ionization potential (left line) and HHG cut-off (right line). Note different cell numbers than Fig. 4.10.

4.6.1 Hydrogen at 1600 nm

HHG driven by mid-infrared pulses has received growing interest in recent years [103–105]. Due to the scaling of the HHG cut-off ($I_P+3.17\frac{I}{4\omega^2}$) and lower probabilities of ionization (i.e., higher saturation intensities), longer driving wavelengths allow for production of bright high-harmonic supercontinua extending into keV energies [31]. Much of the research on mid-IR HHG focuses on high driving laser intensities and the resulting ultrahigh harmonics. Here, we seek to investigate the near-threshold response, where low photon energies and large U_P mean that many states cross through resonance. As previously mentioned, this spectral region cannot be approximated with the same approximation methods often used for plateau harmonics. Meanwhile, TDSE calculations become significantly more computationally expensive due to scaling of pulse duration ($\propto \lambda$) and quiver radius ($\propto \lambda^2$) as well as generally higher convergence requirements due to the relatively low intensity of the HHG signal relative to the fundamental. Efficient interpolation and macroscopic summation is thus of especial importance at longer wavelengths.

As mentioned above, we have found that longer wavelengths require finer intensity sampling to achieve commensurate convergence, and furthermore that macroscopic summation requires more cells. Therefore, the results of this Section comprise $1,000$ microscopic TDSE simulations at intensity sampling of $dI = 10^{11}$ W/cm^2, and 10^7 macroscopic cells. We note that improvements to the method will be needed in order to expand 1600 nm investigations to inclusion of focal phase – the compounded convergence requirements exceed current limits of feasibility.

In Fig. 4.22, we present a comparison of a microscopic spectrum (dot-dashed black line) and calculations where the interpolated single-atom TDSE results are either added up coherently (solid red line, as Eq. (4.8)) or incoherently (dashed blue line, with $P(\omega) = \sum_j |a_j(\omega)|^2$). As for 800 nm, the lack of coherence of the radiation strongly suppresses radiation in the macroscopic result. Unlike for the lower wavelength, the overall relative intensity of the plateau is greatly reduced, by about six orders of magnitude compared to the microscopic signal. Additionally, the suppression does not clearly select odd-harmonic radiation ($(2n+1)\omega$, denoted by vertical gridlines) compared

to peaks at other energies, except for radiation above the effective cut-off near 85ω (compared to microscopic prediction of 104ω). It thus appears that coherence is poor for all radiation in the plateau, compared to the on- vs. off-harmonic coherence differences seen at lower wavelengths. This is further supported by Fig. 4.23, where spectra resolved by angle (top) and scanning peak intensity (bottom) show similar lack of harmonic selectivity.

4.6.2 Helium at 400 nm

While atomic hydrogen serves as a straightforward and common target in theory, it is important to also consider how investigations may be extended to experimentally-accessible targets. Helium is a natural next step as both a common and useful HHG target [31] and the next simplest atom for simulations. In fact, the lack of inner orbitals is beneficial to both purposes – eliminating re-absorption of high-energy radiation and avoiding extra steps needed to address non-physical transitions to lower occupied states (see Sec. 2.2.3). In our calculations, we have used the helium SAE potential developed in this thesis (see Ch. 2).

Given the higher ionization potential of helium, we chose a lower wavelength (400 nm) and higher intensities (by a factor of about 8). This results in similar dimensionless parameters as for hydrogen driven by 800 nm lasers, as seen in Table 4.1. Interpolation and macroscopic summation are performed in the same manner as for hydrogen, with the same gas jet and laser shape parameters. While the 400 nm interpolation appears to be converged at higher intensity spacing ($\approx 8 \times 10^{12}$ W/cm^2, consistent with our rule of thumb), for the macroscopic simulations we use the same spacing as for hydrogen, i.e., $dI = 10^{12}$ W/cm^2 – the TDSE calculations had already been completed for the finer spacing and the later steps are not significantly impacted by including more points for interpolation.

Overall, we observe similar features for helium driven by 400 nm lasers as previously observed in the hydrogen results at 800 nm. In Fig. 4.24, on-axis radiation is suppressed between harmonics by coherent macroscopic summation, but significant off-harmonic peaks do remain. These features again show, in Fig. 4.25, wider angular dependence than harmonic radiation.

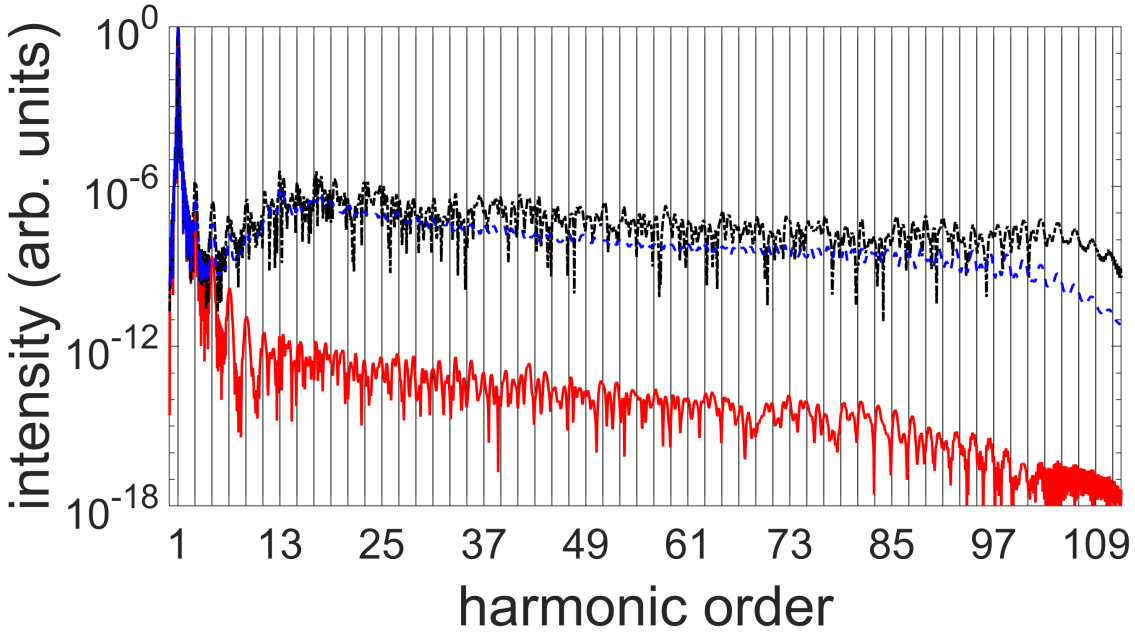

Figure 4.22: Comparison of (dot-dash black) single-atom results versus (dashed blue) incoherent and (solid red) coherent macroscopic summation, for HHG in a gas jet of hydrogen atoms driven by a 1600 nm laser pulse of 10 optical cycles with peak intensity 8.8×10^{13} W/cm^2. Note that the intensity of the spectra are scaled by the signal at the fundamental frequency.

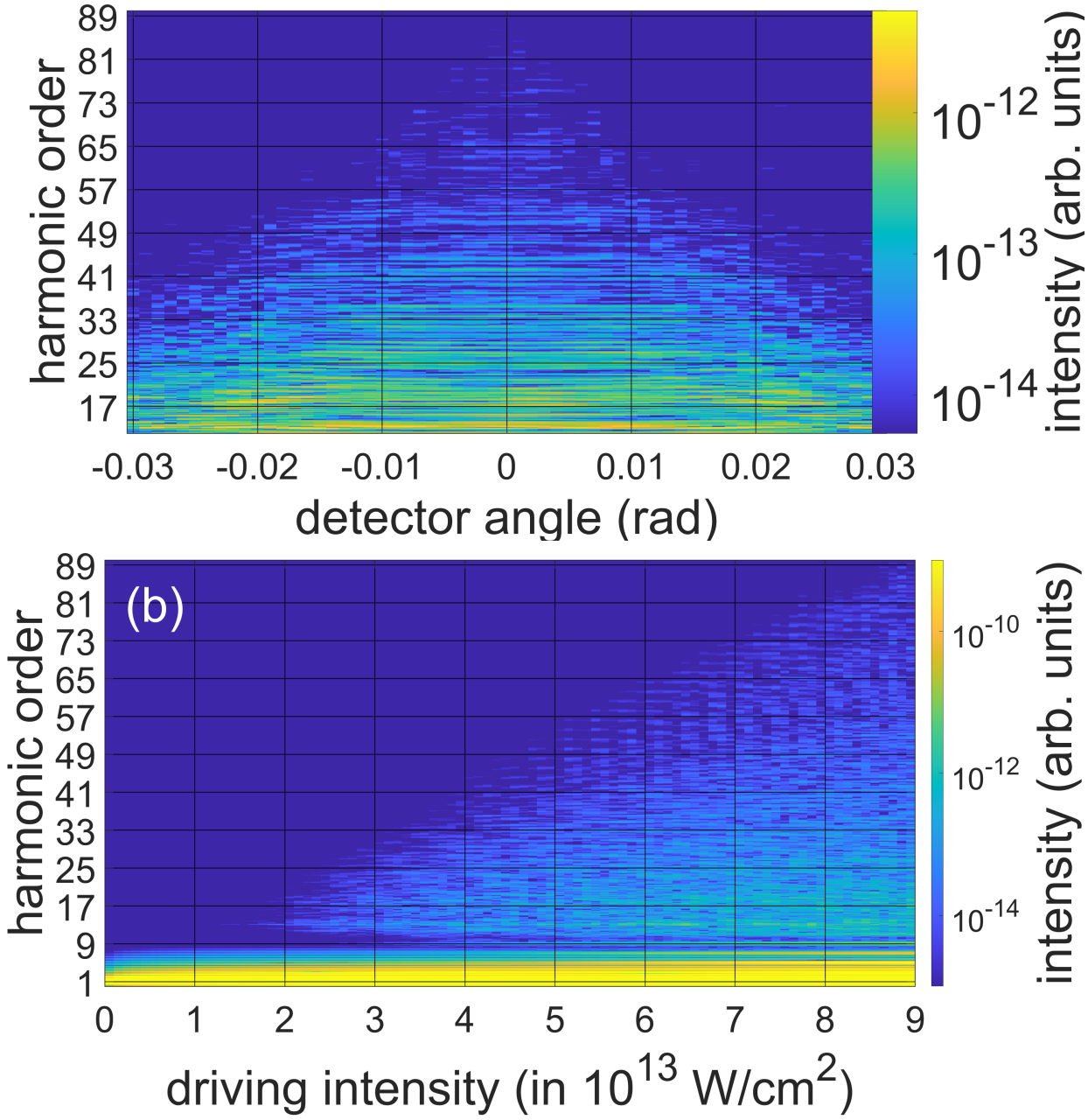

Figure 4.23: Macroscopic radiation spectra for a gas jet of hydrogen atoms driven by a 1600 nm laser. (top) Angle-resolved spectrum for a peak intensity of 8.8×10^{13} W/cm^2. (bottom) On-axis spectra shown as a function of peak intensity.

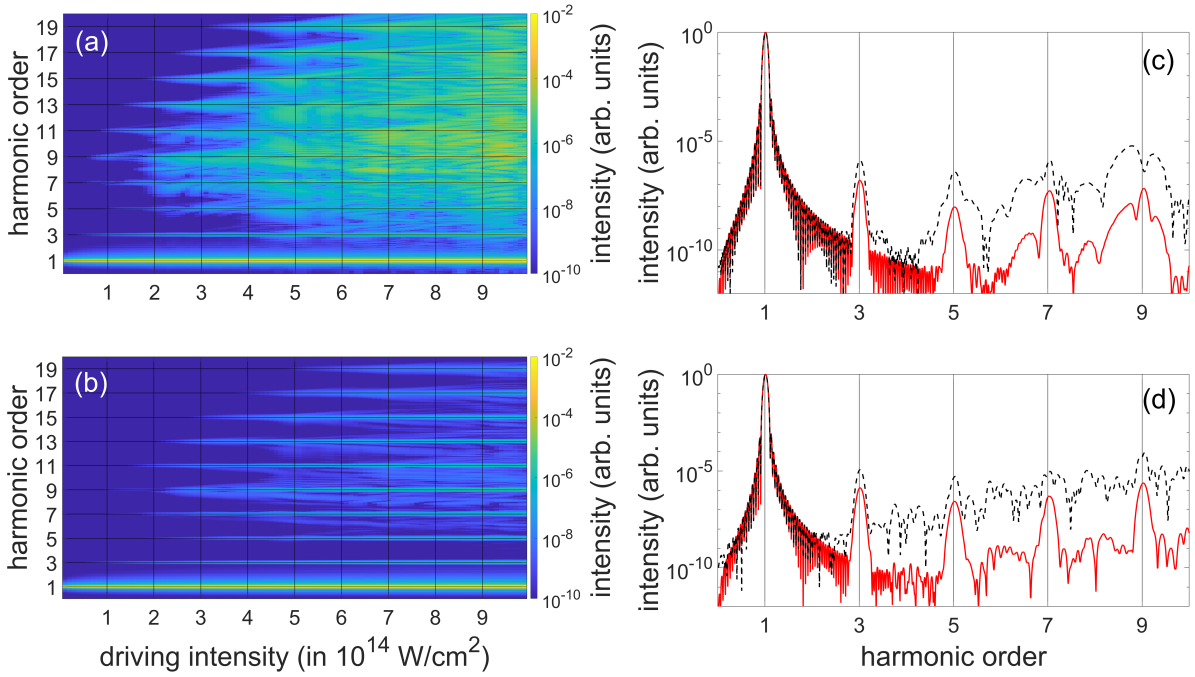

Figure 4.24: Comparison of single-atom TDSE results and macroscopic TDSE interpolation results for high harmonic generation in helium atoms. On the left, the (a) single-atom and (b) macroscopic on-axis spectrum is shown as a function of peak intensity. The spectra on the right show the comparison (single atom: black dashed line, macroscopic: red solid line) at peak intensities (c) $I_0 = 3.3 \times 10^{14}$ W/cm^2 and (d) $I_0 = 8.0 \times 10^{13}$ W/cm^2. (cf. hydrogen results in Fig. 4.11)

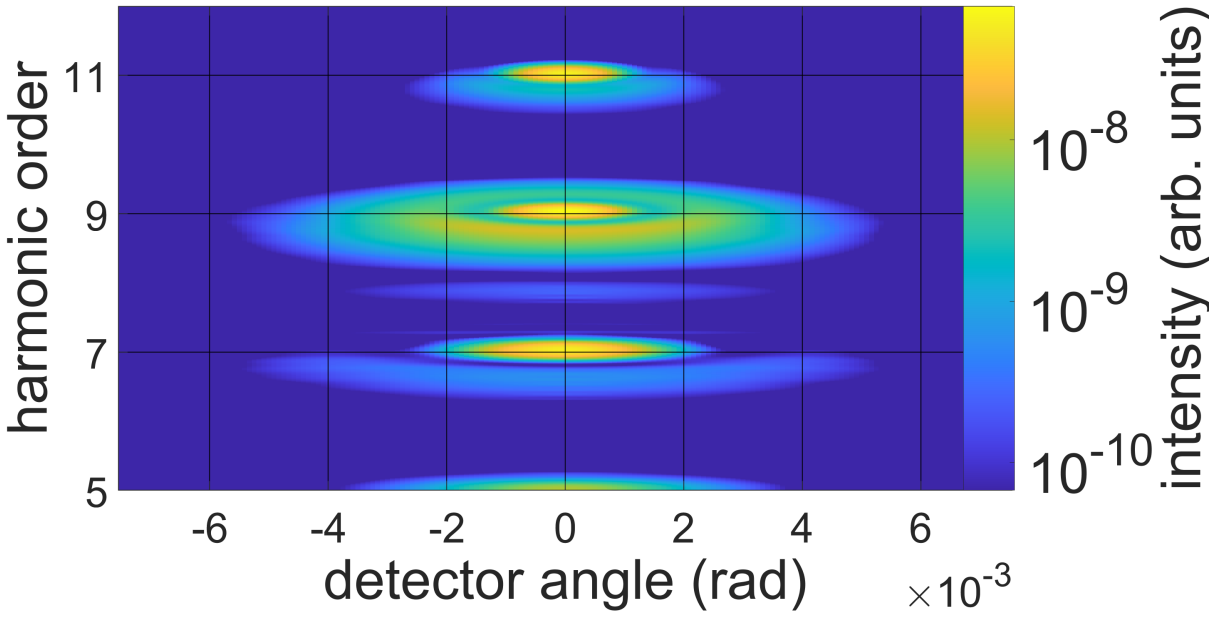

Figure 4.25: Angle-resolved near-threshold part of the macroscopic radiation spectrum for a gas jet of helium atoms driven by a 400 nm laser with peak intensity 3.3×10^{14} W/cm^2. (cf. hydrogen results in Fig. 4.13)

One difference appears in the spectrum near 9ω, Fig. 4.26. The spectrum for helium has some similar off-harmonic structures as a function of intensity in microscopic simulations (top panel). Unlike in hydrogen, however, one of these features remains dominant after macroscopic summation (bottom panel). The temporal profile intensity scans (Fig. 4.27) suggest that the same mechanism is responsible as discussed for hydrogen in Ch. 3.

4.7 Summary

To summarize, we have introduced an efficient method of generating accurate microscopic single-atom radiation data at arbitrary intensities, based on the results of a relatively small number of actual time-dependent Schrödinger equation calculations. We have shown that this interpolation scheme produces spectra matching ab-initio calculations across the entire high-order harmonic spectra, including the near-threshold regime as well as the entire plateau up to the cut-off. In the present applications, the error is found to scale with the fourth order of the intensity spacing of the initial TDSE calculations, as expected from the cubic spline method used. While we have focused on usage of the method for the hydrogen atom, it can be extended to other targets (e.g., more complex atoms, molecules, solids) as well as other calculation methods (e.g., time-dependent density functional theory).

We have then applied the interpolation method to compute the radiation response of macroscopic targets. Using a previously tested method for summing the response of microscopic radiators, we incorporated the efficiently-generated microscopic ab-initio results. This eliminates the limitations of approximative methods in the low-energy portion of the spectrum, near and below the ionization threshold. To demonstrate the reliability in using the interpolation method for accurate macroscopic HHG simulations, we have used the distribution of atoms on a uniform lattice and in a gas jet as test cases. We have shown that angle-resolved macroscopic radiation spectra can be achieved based on just one hundred ab-initio TDSE calculations. For the uniform lattice, it is shown that the numerical results match the analytical predictions for diffraction patterns.

We have used the TDSE interpolation method to explore features of near-threshold radiation

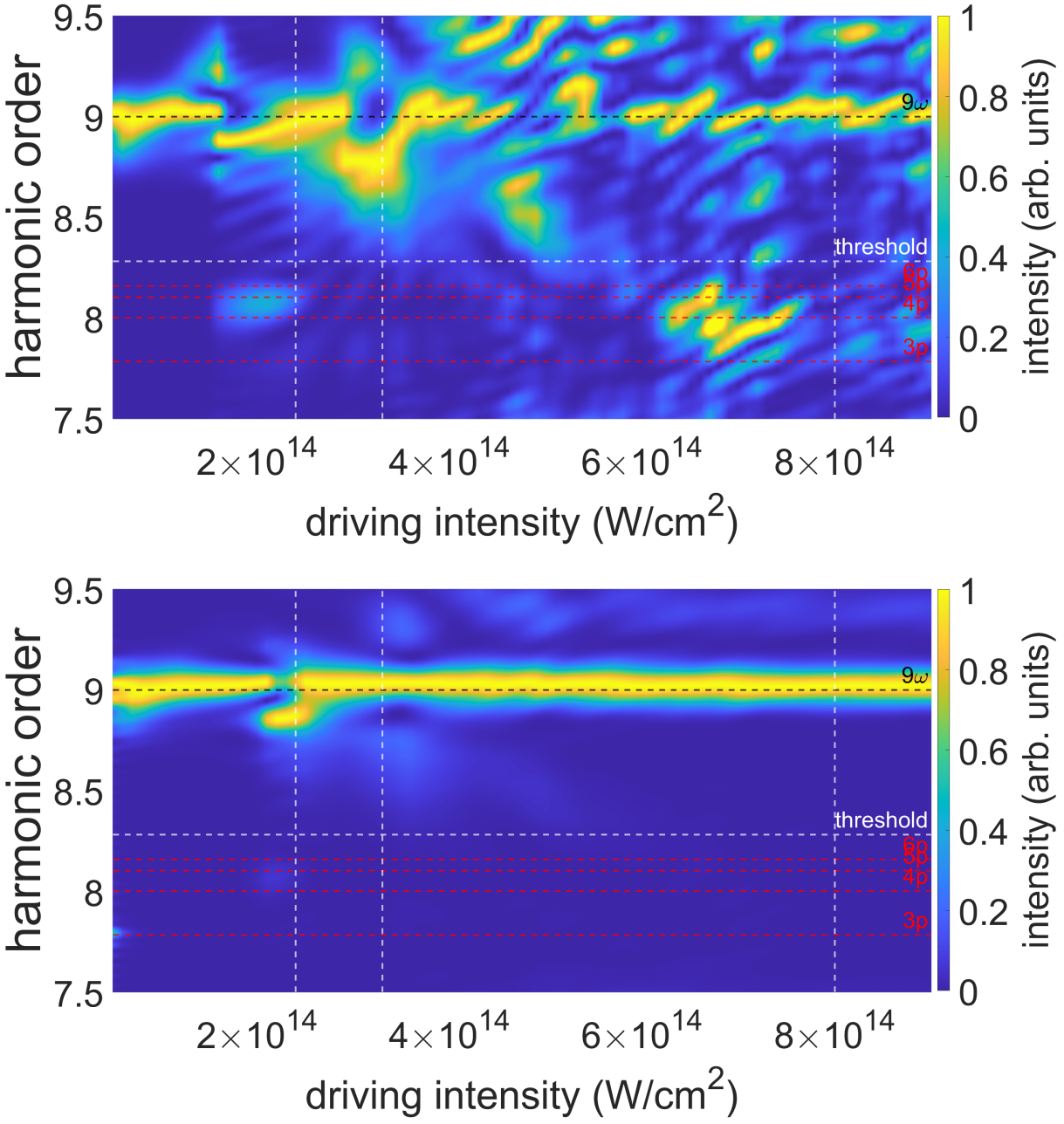

Figure 4.26: Comparison of (top) single-atom results and (bottom) on-axis macroscopic TDSE interpolation results for near-threshold HHG spectra as a function of peak intensity for a 400 nm, 20 o.c. pulse interacting with helium. Results for each intensity have been normalized to the maximum signal in the region between 8.75ω and 9.5ω. Red dashed lines denote field-free excited state transition energies, and vertical lines identify select intensities: 2.4×10^{14}, 3.3×10^{14}, and 8.0×10^{14} W/cm^2. (cf. hydrogen results in Fig. 4.15)

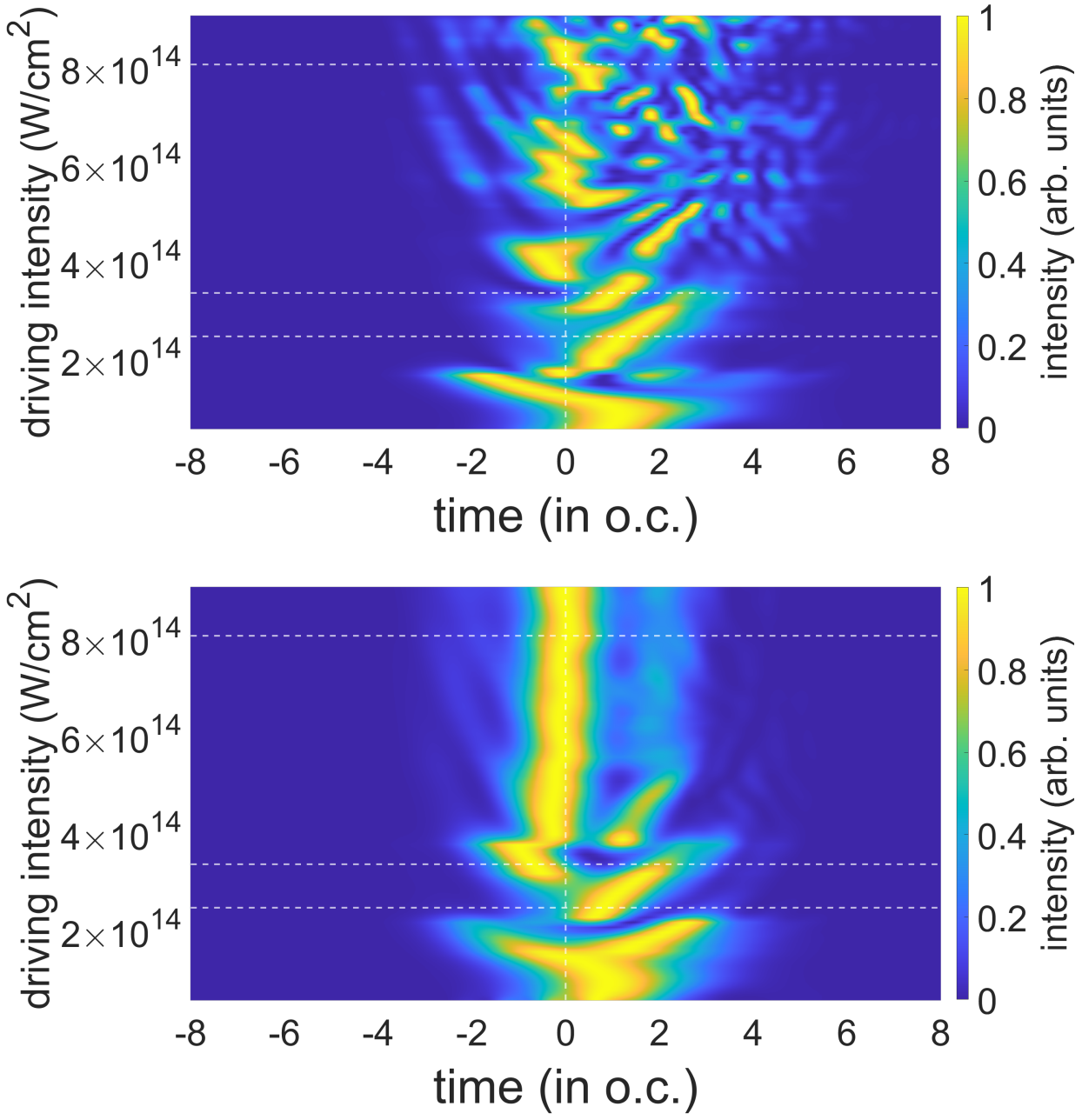

Figure 4.27: Comparison of (top) single-atom results and (bottom) on-axis macroscopic TDSE interpolation results for temporal profile of radiation within 1ω of the 9th harmonic as a function of driving pulse intensity in helium for a 400 nm, 20 o.c. pulse. For each intensity, the results have been normalized to a maximum of 1 for sake of comparison. A vertical dashed line denotes the peak of the laser and horizontal dashed lines identify select intensities: 2.4×10^{14}, 3.3×10^{14}, and 8.0×10^{14} W/cm^2. (cf. hydrogen results in Fig. 4.16)

in the macroscopic response. Most of the off-harmonic radiation features, which are present at the same strength as harmonic emission in typical single-atom calculations, are strongly suppressed in the coherent build-up of the macroscopic signals. The overall macroscopic spectra closely resemble those obtained in experiments, showing a strong emission at the odd harmonics of the driving laser frequency and a few features such as weak shoulders close to the harmonics in the near-threshold region of the spectrum (incl. the off-harmonic red- and blue-shifted structures studied in Ch. 3 – shown to arise from resonant enhancement via a Stark-shifted excited state). We have further demonstrated that these weak features have a different, i.e., wider, angular spread than the odd-harmonic radiation, in agreement with previous experimental and theoretical studies. The temporal and angular dependence both may be useful tools for tailoring pulses.

Investigating an additional focal phase term for highly-focused lasers, we find it has a large impact on both the angular structure of harmonic radiation and its intensity. Specifically, we have identified interference patterns in the angular distributions of below- and near-threshold harmonics. The interference effects are found in case of a spatial phase distribution for broadband Gaussian pulses with a negative Porras factor, while they are not present for the monochromatic Gouy phase distribution. Our analysis indicates that the interferences are due to off-center contributions that are in-phase with those at the central points in the focus.

Finally, we have briefly explored radiation in two other parameter regimes: hydrogen driven at longer-wavelengths of a mid-infrared laser, and helium driven by a shorter wavelength laser. For helium driven by 400 nm laser light, we see behavior consistent with that observed for hydrogen at 800 nm. Future work should in particular investigate intensities near 2×10^{14} W/cm^2, where off-harmonic radiation remains stronger than 9ω radiation after macroscopic summation. For the mid-IR results, efficient methods are crucial for overcoming the increasing computational complexity and costs. At this wavelength, macroscopic radiation in the HHG plateau is strongly suppressed relative to the microscopic signal, and does not demonstrate the selectivity to odd harmonics found at lower wavelengths.

Overall, the results obtained for the near-threshold region are in agreement with previous

results based on more sophisticated calculations, showing the reliability of the present method for efficiently exploring a parameter regime rich with complex features.

Chapter 5

Summary and Perspectives

This thesis investigated near-threshold high-order harmonic generation (HHG) through a variety of theoretical techniques. In Chapter 1, we provided background including a simple model of HHG ignoring the effects of target characteristics, numerical techniques for ab-initio simulation of the time-dependent Schrödinger equation (TDSE) for a single electron in an atomic potential and the electric field of a laser pulse, and strategies to analyze radiation data.

Next, in Chapter 2 we presented single-active-electron (SAE) potentials for atoms, ions, and molecules. We demonstrated the utility of these potentials for HHG as well as nonlinear polarization and ionization studies. Good agreement has been shown between results from separate SAE-TDSE and time-dependent density functional theory (TDDFT) simulations for the full HHG spectrum, driven by intense lasers across a variety of wavelengths. This comparison serves to dispute a long-standing misconception in the field, and provide a foundation for investigation of impacts of electron correlation on HHG. Additionally, we outlined a strategy to resolve a limitation of SAE-TDSE simulations in atoms where multiple orbitals may respond to the driving laser.

In Chapter 3, we investigated resonance enhancement of near-threshold HHG. We identified similar resonance effects in broad parameter regimes, including hydrogen driven by near- and mid-infrared pulses, as well as helium with 400 nm lasers. The behavior that may be explicable through semi-classical trajectory models (generally at higher intensity) has been differentiated from features that are not consistent with these models. We interpreted results through field-shifted resonance conditions and dimensionless parameters, outlining two possible regimes where the effect breaks

down: first, when a large number of resonances contribute, resulting in noisier signals and second, when perturbative and/or strongly multiphoton behavior becomes more dominant (small U_P/ω and U_P/I_P, respectively).

Finally, in Chapter 4 we introduced a method to combine efficient macroscopic simulation with ab-initio atomic methods. Specifically, we demonstrated that the intensity and CEP dependence of HHG across a wide range of parameters can be efficiently and accurately approximated through simple interpolation. Macroscopic summation then proceeds via the Discrete Dipole Approximation – a method with a proven track record in simulation of higher harmonics within the strong-field approximation – requiring only hundreds of numerical TDSE simulations. With this TDSE-DDA method, we showed that near the ionization threshold, off-harmonic radiation features are suppressed relative to harmonic radiation, but do remain at significant intensity and with a wider angular spread. Using the SAE potentials developed in this thesis, we demonstrated similar structures in helium driven by a 400 nm laser. The TDSE-DDA method can also be extended to mid-infrared lasers, where initial investigation showed dramatic suppression of HHG across driving intensities due to poor coherence – at least at the chosen set of laser and gas parameters. Finally, we considered an additional spatial phase term present in highly-focused lasers, resulting in a clear interference structure in the angular dependence of HHG.

Each of these investigations may serve as foundation for future work on understanding HHG. Therefore, we placed an emphasis throughout on explanations of process, obstacles to overcome, and future directions. For SAE potentials, there are two clear directions for the future: further careful comparison of SAE-TDSE and TDDFT results to identify dynamic multielectron effects; and, development and use of additional molecular potentials. With resonance HHG, we have identified similar effects in broad parameter regimes, but placed the majority of our focus on a feature – the impact of the hydrogen $9\omega \rightarrow 3p$ resonance on radiation near the ninth harmonic – with the distinction of producing radiation at multiple delays from the resonance. Further investigation could seek similar cases to illuminate the mechanism, further investigate the parameter boundaries between forms of HHG (trajectory-like resonance-enhanced, other resonance-enhanced, "normal"),

or turn to applications such as pulse-shaping or spectroscopy. With the TDSE-DDA method we have presented an efficient tool which may easily be extended to a large variety of investigations. These include observations of interesting effects in HHG from mid-IR pulses and those with additional focal phase terms, which certainly require further attention. Variations of target parameters such as gas composition, lattice construction, or location relative to the laser focus may reveal novel effects in the near-threshold regime. Extensions to more exotic single-radiator simulations (e.g., molecular targets or bi-elliptical driving fields) hold a great deal of promise. Finally, we have only just begun to understand the combinations of these three topics, with the helium resonance effects already showing particular promise in macroscopic simulations.

Bibliography

[1] R. Reiff, T. Joyce, A. Jaroń-Becker, and A. Becker, Single-active electron calculations of high-order harmonic generation from valence shells in atoms for quantitative comparison with TDDFT calculations, J. Phys. Commun. **4**, 065011 (2020).

[2] A. Kramida, Y. Ralchenko, J. Reader, and NIST ASD Team, NIST atomic spectra database (version 5.6.1) (2018).

[3] J. Venzke, R. Reiff, Z. Xue, A. Jaroń-Becker, and A. Becker, Angular momentum distribution in Rydberg states excited by a strong laser pulse, Phys. Rev. A **98**, 043434 (2018).

[4] T. Popmintchev, M.-C. Chen, P. Arpin, M. M. Murnane, and H. C. Kapteyn, The attosecond nonlinear optics of bright coherent x-ray generation, Nature Photonics **4**, 822–832 (2010).

[5] J. H. Heinz, R. Reiff, T. Joyce, A. Jaroń-Becker, A. Becker, and M. Kolesik, Nonlinear polarization and ionization in O_2: metastable electronic state model, Opt. Express **28**, 25022–25036 (2020).

[6] R. Reiff, J. Venzke, A. Jaroń-Becker, and A. Becker, Interference effects in high harmonic generation induced by focal phase distribution, submitted to Optics Letters (2021).

[7] H. Hertz, Ueber einen Einfluss des ultravioletten Lichtes auf die electrische Entladung, Annalen der Physik **267**, 983–1000 (1887).

[8] A. Einstein, Über einen die Erzeugung und Verwandlung des Lichtes betreffenden heuristischen Gesichtspunkt, Annalen der Physik **4**, 132–148 (1905).

[9] M. Göppert-Mayer, Über Elementarakte mit zwei Quantensprüngen, Annalen der Physik **401**, 273–294 (1931).

[10] W. Kaiser and C. G. B. Garrett, Two-photon excitation in CaF_2: Eu^{2+}, Phys. Rev. Lett. **7**, 229–231 (1961).

[11] L. Young, K. Ueda, M. Gühr, P. H. Bucksbaum, M. Simon, S. Mukamel, N. Rohringer, K. C. Prince, C. Masciovecchio, M. Meyer, A. Rudenko, D. Rolles, C. Bostedt, M. Fuchs, D. A. Reis, R. Santra, H. Kapteyn, M. Murnane, H. Ibrahim, F. Légaré, M. Vrakking, M. Isinger, D. Kroon, M. Gisselbrecht, A. L'Huillier, H. J. Wörner, and S. R. Leone, Roadmap of ultrafast x-ray atomic and molecular physics, J. Phys. B: At. Mol. Opt. Phys. **51**, 032003 (2018).

[12] K. Ueda, E. Sokell, S. Schippers, F. Aumayr, H. Sadeghpour, J. Burgdörfer, C. Lemell, X.-M. Tong, T. Pfeifer, F. Calegari, A. Palacios, F. Martin, P. Corkum, G. Sansone, E. V. Gryzlova, A. N. Grum-Grzhimailo, M. N. Piancastelli, P. M. Weber, T. Steinle, K. Amini, J. Biegert, N. Berrah, E. Kukk, R. Santra, A. Müller, D. Dowek, R. R. Lucchese, C. W. McCurdy, P. Bolognesi, L. Avaldi, T. Jahnke, M. S. Schöffler, R. Dörner, Y. Mairesse, L. Nahon, O. Smirnova, T. Schlathölter, E. E. B. Campbell, J.-M. Rost, M. Meyer, and K. A. Tanaka, Roadmap on photonic, electronic and atomic collision physics: I. light–matter interaction, J. Phys. B: At. Mol. Opt. Phys. **52**, 171001 (2019).

[13] A. McPherson, G. Gibson, H. Jara, U. Johann, T. S. Luk, I. A. McIntyre, K. Boyer, and C. K. Rhodes, Studies of multiphoton production of vacuum-ultraviolet radiation in the rare gases, J. Opt. Soc. Am. B **4**, 595 (1987).

[14] A. L'Huillier, P. Balcou, S. Candel, K. J. Schafer, and K. C. Kulander, Calculations of high-order harmonic-generation processes in xenon at 1064 nm, Phys. Rev. A **46**, 2778–2790 (1992).

[15] J. Xu, C. I. Blaga, P. Agostini, and L. F. DiMauro, Time-resolved molecular imaging, J. Phys. B: At. Mol. Opt. Phys. **49**, 112001 (2016).

[16] A. S. Alnaser and I. V. Litvinyuk, Subfemtosecond directional control of chemical processes in molecules, J. Phys. B: At. Mol. Opt. Phys. **50**, 032002 (2017).

[17] J. P. Marangos, Development of high harmonic generation spectroscopy of organic molecules and biomolecules, J. Phys. B: At. Mol. Opt. Phys. **49**, 132001 (2016).

[18] H. Yun, S. J. Yun, G. H. Lee, and C. H. Nam, High-harmonic spectroscopy of aligned molecules, J. Phys. B: At. Mol. Opt. Phys. **50**, 022001 (2017).

[19] P. Peng, C. Marceau, and D. M. Villeneuve, Attosecond imaging of molecules using high harmonic spectroscopy, Nature Reviews Physics **1**, 144–155 (2019).

[20] H. Reiss, Theoretical methods in quantum optics: S-matrix and Keldysh techniques for strong-field processes, Prog. Quantum. Electron. **16**, 1 – 71 (1992).

[21] M. V. Ammosov, N. B. Delone, and V. P. Krainov, Tunnel ionization of complex atoms and atomic ions in electromagnetic field, in High intensity laser processes, Vol. 664 (International Society for Optics and Photonics, 1986) pp. 138–141.

[22] P. Agostini, F. Fabre, G. Mainfray, G. Petite, and N. K. Rahman, Free-free transitions following six-photon ionization of xenon atoms, Phys. Rev. Lett. **42**, 1127 (1979).

[23] W. Becker, S. P. Goreslavski, D. B. Milošević, and G. G. Paulus, The plateau in above-threshold ionization: the keystone of rescattering physics, J. Phys. B: At. Mol. Opt. Phys. **51**, 162002 (2018).

[24] D. B. Milošević, G. G. Paulus, D. Bauer, and W. Becker, Above-threshold ionization by few-cycle pulses, J. Phys. B: At. Mol. Opt. Phys. **39**, R203–R262 (2006).

[25] N. B. Delone and V. P. Krainov, AC Stark shift of atomic energy levels, Physics-Uspekhi **42**, 669–687 (1999).

[26] P. Agostini, P. Breger, A. L'Huillier, H. G. Muller, G. Petite, A. Antonetti, and A. Migus, Giant Stark shifts in multiphoton ionization, Phys. Rev. Lett. **63**, 2208–2211 (1989).

[27] F. He, C. Ruiz, A. Becker, and U. Thumm, Attosecond probing of instantaneous AC Stark shifts in helium atoms, J. Phys. B: At. Mol. Opt. Phys. **44**, 211001 (2011).

[28] B. Piraux, F. Mota-Furtado, P. F. O'Mahony, A. Galstyan, and Y. V. Popov, Excitation of Rydberg wave packets in the tunneling regime, Phys. Rev. A **96**, 043403 (2017).

[29] D. G. Arbó, K. I. Dimitriou, E. Persson, and J. Burgdörfer, Sub-Poissonian angular momentum distribution near threshold in atomic ionization by short laser pulses, Phys. Rev. A **78**, 013406 (2008).

[30] Q. Li, X.-M. Tong, T. Morishita, C. Jin, H. Wei, and C. D. Lin, Rydberg states in the strong field ionization of hydrogen by 800, 1200 and 1600 nm lasers, J. Phys. B: At. Mol. Opt. Phys. **47**, 204019 (2014).

[31] T. Popmintchev, M.-C. Chen, D. Popmintchev, P. Arpin, S. Brown, S. Ališauskas, G. Andriukaitis, T. Balčiunas, O. D. Mücke, A. Pugzlys, et al., Bright coherent ultrahigh harmonics in the keV x-ray regime from mid-infrared femtosecond lasers, Science **336**, 1287–1291 (2012).

[32] M. Lewenstein, P. Balcou, M. Y. Ivanov, A. L'huillier, and P. B. Corkum, Theory of high-harmonic generation by low-frequency laser fields, Phys. Rev. A **49**, 2117 (1994).

[33] P. B. Corkum, Plasma perspective on strong field multiphoton ionization, Phys. Rev. Lett. **71**, 1994–1997 (1993).

[34] K. Kulander, K. Schafer, and J. Krause, Super-intense laser-atom physics, NATO Advanced Science Institutes Series **316**, 95 (1993).

[35] O. E. Alon, V. Averbukh, and N. Moiseyev, Selection rules for the high harmonic generation spectra, Phys. Rev. Lett. **80**, 3743–3746 (1998).

[36] S. H. Glenzer, L. B. Fletcher, E. Galtier, B. Nagler, R. Alonso-Mori, B. Barbrel, S. B. Brown, D. A. Chapman, Z. Chen, C. B. Curry, F. Fiuza, E. Gamboa, M. Gauthier, D. O. Gericke, A. Gleason, S. Goede, E. Granados, P. Heimann, J. Kim, D. Kraus, M. J. MacDonald, A. J. Mackinnon, R. Mishra, A. Ravasio, C. Roedel, P. Sperling, W. Schumaker, Y. Y. Tsui, J. Vorberger, U. Zastrau, A. Fry, W. E. White, J. B. Hasting, and H. J. Lee, Matter under extreme conditions experiments at the Linac coherent light source, J. Phys. B: At. Mol. Opt. Phys. **49**, 092001 (2016).

[37] K. M. Dorney, L. Rego, N. J. Brooks, J. San Román, C.-T. Liao, J. L. Ellis, D. Zusin, C. Gentry, Q. L. Nguyen, J. M. Shaw, et al., Controlling the polarization and vortex charge of attosecond high-harmonic beams via simultaneous spin–orbit momentum conservation, Nature Photonics **13**, 123–130 (2019).

[38] P.-C. Huang, C. Hernández-García, J.-T. Huang, P.-Y. Huang, C.-H. Lu, L. Rego, D. D. Hickstein, J. L. Ellis, A. Jaron-Becker, A. Becker, et al., Polarization control of isolated high-harmonic pulses, Nature Photonics **12**, 349–354 (2018).

[39] S. Beaulieu, S. Camp, D. Descamps, A. Comby, V. Wanie, S. Petit, F. Légaré, K. J. Schafer, M. B. Gaarde, F. Catoire, and Y. Mairesse, Role of excited states in high-order harmonic generation, Phys. Rev. Lett. **117**, 203001 (2016).

[40] L. Verlet, Computer "experiments" on classical fluids. I. thermodynamical properties of Lennard-Jones molecules, Phys. Rev. **159**, 98–103 (1967).

[41] J. A. Hostetter, J. L. Tate, K. J. Schafer, and M. B. Gaarde, Semiclassical approaches to below-threshold harmonics, Phys. Rev. A **82**, 023401 (2010).

[42] E. Shani, Analysis and numerical performance of methods of solving the time independent Schrödinger equation for simulation in strong-field physics, Master's thesis, University of Colorado Boulder (2017).

[43] D. Sorensen, Implicitly restarted Arnoldi/Lanczos methods for large scale eigenvalue calculations, in Parallel Numerical Algorithms, edited by D. Keyes, A. Sameh, and V. Venkatakrishnan (Springer, 1997) Chap. 5, pp. 119–165.

[44] O. A. Sharafeddin, D. J. Kouri, and D. K. Hoffman, Time-dependent treatment of scattering: potential referenced and kinetic energy referenced modified Cayley approaches to atom–diatom collisions and time-scale separations, Canadian Journal of Chemistry **70**, 686–692 (1992).

[45] J. Crank and P. Nicolson, A practical method for numerical evaluation of solutions of partial differential equations of the heat-conduction type, Mathematical Proceedings of the Cambridge Philosophical Society **43**, 50–67 (1947).

[46] Y. Saad and M. H. Schultz, GMRES: A generalized minimal residual algorithm for solving nonsymmetric linear systems, SIAM Journal on Scientific and Statistical Computing **7**, 856–869 (1986).

[47] C. A. Nicolaides and D. R. Beck, The variational calculation of energies and widths of resonances, Phys. Lett. A **65**, 11–12 (1978).

[48] B. Simon, The definition of molecular resonance curves by the method of exterior complex scaling, Phys. Lett. A **71**, 211–214 (1979).

[49] F. He, C. Ruiz, and A. Becker, Absorbing boundaries in numerical solutions of the time-dependent Schrödinger equation on a grid using exterior complex scaling, Phys. Rev. A **75**, 053407 (2007).

[50] L. Keldysh, Ionization in the field of a strong electromagnetic wave, JETP **20**, 1307 (1965).

[51] F. H. M. Faisal, Multiple absorption of laser photons by atoms, J. Phys. B: At. Mol. Opt. Phys. **6**, L89–L92 (1973).

[52] H. R. Reiss, Effect of an intense electromagnetic field on a weakly bound system, Phys. Rev. A **22**, 1786–1813 (1980).

[53] J. A. Pérez-Hernández, L. Roso, and L. Plaja, Harmonic generation beyond the strong-field approximation: the physics behind the short-wave-infrared scaling laws, Opt. Express **17**, 9891–9903 (2009).

[54] K. Amini, J. Biegert, F. Calegari, A. Chacón, M. F. Ciappina, A. Dauphin, D. K. Efimov, C. F. de Morisson Faria, K. Giergiel, P. Gniewek, A. S. Landsman, M. Lesiuk, M. Mandrysz, A. S. Maxwell, R. Moszyński, L. Ortmann, J. A. Pérez-Hernández, A. Picón, E. Pisanty, J. Prauzner-Bechcicki, K. Sacha, N. Suárez, A. Zaïr, J. Zakrzewski, and M. Lewenstein, Symphony on strong field approximation, Reports on Progress in Physics **82**, 116001 (2019).

[55] A. V. Oppenheim, R. W. Schafer, and J. R. Buck, Filter design techniques, in Discrete-Time Signal Processing (Prentice Hall, 1999) p. 468–471.

[56] J. M. Lilly and S. C. Olhede, Higher-order properties of analytic wavelets, IEEE Transactions on Signal Processing **57**, 146–160 (2009).

[57] J. M. Lilly and S. C. Olhede, Generalized Morse wavelets as a superfamily of analytic wavelets, IEEE Transactions on Signal Processing **60**, 6036–6041 (2012).

[58] J. M. Lilly, Element analysis: a wavelet-based method for analysing time-localized events in noisy time series, Proc. R. Soc. A. **473**, 20160776 (2017).

[59] A. Crawford-Uranga, U. De Giovannini, E. Räsänen, M. J. T. Oliveira, D. J. Mowbray, G. M. Nikolopoulos, E. T. Karamatskos, D. Markellos, P. Lambropoulos, S. Kurth, and A. Rubio, Time-dependent density-functional theory of strong-field ionization of atoms by soft x rays, Phys. Rev. A **90**, 033412 (2014).

[60] X. M. Tong and S.-I. Chu, Time-dependent density-functional theory for strong-field multiphoton processes: Application to the study of the role of dynamical electron correlation in multiple high-order harmonic generation, Phys. Rev. A **57**, 452–461 (1998).

[61] J. J. Carrera and S.-I. Chu, Ab initio time-dependent density-functional-theory study of the frequency comb structure, coherence, and dephasing of multielectron systems in the VUV-XUV regimes via high-order harmonic generation, Phys. Rev. A **79**, 063410 (2009).

[62] M. D. Perry, A. Szoke, and K. C. Kulander, Resonantly enhanced above-threshold ionization of helium, Phys. Rev. Lett. **63**, 1058–1061 (1989).

[63] K. C. Kulander and T. N. Rescigno, Effective potentials for time-dependent calculations of multiphoton processes in atoms, Comput. Phys. Commun. **63**, 523 (1991).

[64] K. C. Kulander, K. J. Schafer, and J. L. Krause, Single-active electron calculation of multiphoton process in krypton, Int. J. Quant. Chem. **40**, 415 (1991).

[65] H. G. Muller and F. C. Kooiman, Bunching and focusing of tunneling wave packets in enhancement of high-order above-threshold ionization, Phys. Rev. Lett. **81**, 1207 (1998).

[66] H. G. Muller, Numerical simulation of high-order above-threshold-ionization enhancement in argon, Phys. Rev. A **60**, 1341 (1999).

[67] M. J. Nandor, M. A. Walker, L. D. Van Woerkom, and H. G. Muller, Detailed comparison of above-threshold-ionization spectra from accurate numerical integrations and high-resolution measurements, Phys. Rev. A **60**, R1771 (1999).

[68] X. M. Tong and C. D. Lin, Empirical formula for static field ionization rates of atoms and molecules by lasers in the barrier-suppression regime, J. Phys. B: At. Mol. Opt. Phys. **38**, 2593 (2005).

[69] M. Awasthi, Y. V. Vanne, A. Saenz, A. Castro, and P. Decleva, Single-active-electron approximation for describing molecules in ultrashort laser pulses and its application to molecular hydrogen, Phys. Rev. A **77**, 063403 (2008).

[70] P. Hohenberg and W. Kohn, Inhomogeneous electron gas, Phys. Rev. **136**, B864 (1964).

[71] W. Kohn and L. J. Sham, One-particle properties of an inhomogeneous interacting electron gas, Phys. Rev. **140**, A1133 (1965).

[72] J. B. Krieger, Y. Li, and G. J. Iafrate, Exact relations in the optimized effective potential method employing an arbitrary $E_{xc}[\psi_{i\sigma}]$, Phys. Lett. A **148**, 470 (1990).

[73] X. M. Tong and S.-I. Chu, Density-functional theory with optimized effective potential and self-interaction correction for ground states and autoionizing resonances, Phys. Rev. A **55**, 3406–3416 (1997).

[74] J. P. Perdew and A. Zunger, Self-interaction correction to density-functional approximations for many-electron systems, Phys. Rev. B **23**, 10 (1981).

[75] M. A. L. Marques, A. Castro, G. F. Bertsch, and A. Rubio, octopus: a first-principles tool for excited electron–ion dynamics, Comput. Phys. Commun. **151**, 60 (2003).

[76] A. Castro, H. Appel, M. Oliveira, C. A. Rozzi, X. Andrade, F. Lorenzen, M. A. L. Marques, E. K. U. Gross, and A. Rubio, Octopus: a tool for the application of time-dependent density functional theory, Phys. Stat. Sol. B **243**, 2465 (2006).

[77] X. Andrade, D. A. Strubbe, U. De Giovannini, A. H. Larsen, M. J. T. Oliveira, J. Alberdi-Rodriguez, A. Varas, I. Theophilou, N. Helbig, M. Verstraete, L. Stella, F. Nogueira, A. Aspuru-Guzik, A. Castro, M. A. L. Marques, and A. Rubio, Real-space grids and the Octopus code as tools for the development of new simulation approaches for electronic systems, Phys. Chem. Chem. Phys. **17**, 31371 (2015).

[78] M. A. Marques, M. J. Oliveira, and T. Burnus, Libxc: A library of exchange and correlation functionals for density functional theory, Comput. Phys. Commun. **183**, 2272–2281 (2012).

[79] D. D. Johnson, Modified Broyden's method for accelerating convergence in self-consistent calculations, Phys. Rev. B **38**, 12807–12813 (1988).

[80] R. Kosloff and D. Kosloff, Absorbing boundaries for wave propagation problems, J. Comput. Phys. **63**, 363–376 (1986).

[81] K. Levenberg, A method for the solution of certain nonlinear problems, Q. Appl. Math. **2**, 164 (1944).

[82] D. W. Marquardt, An algorithm for least-squares estimation of nonlinear parameters, SIAM J. Appl. Math. **11**, 431 (1963).

[83] M. Newville, A. Nelson, T. Stensitzki, A. Ingargiola, and D. Allan, LMFIT: Non-linear least-square minimization and curve-fitting for python (2014).

[84] A. D. Bandrauk, S. Chelkowski, D. J. Diestler, J. Manz, and K.-J. Yuan, Quantum simulation of high-order harmonic spectra of the hydrogen atom, Phys. Rev. A **79**, 023403 (2009).

[85] J. Venzke, T. Joyce, Z. Xue, A. Becker, and A. Jaron-Becker, Central frequency of few-cycle laser pulses in strong-field processes, Phys. Rev. A **98**, 063409 (2018).

[86] A. D. Shiner, B. E. Schmidt, C. Trallero-Herrero, H. J. Wörner, S. Patchkovskii, P. B. Corkum, J. C. Kieffer, F. Legare, and D. M. Villeneuve, Probing collective multi-electron dynamics in xenon with high-harmonic spectroscopy, Nat. Phys. **7**, 2011 (2011).

[87] S. Pabst, L. Greenman, D. A. Mazziotti, and R. Santra, Impact of multichannel and multipole effects on the Cooper minimum in the high-order-harmonic spectrum of argon, Phys. Rev. A **85**, 023411 (2012).

[88] D. Facciala, S. Pabst, B. D. Bruner, A. G. Ciriolo, S. De Silvestri, M. Devetta, M. Negro, H. Soifer, S. Stagira, N. Dudovich, and C. Vozzi, Probe of multielectron dynamics in xenon by caustics in high-order harmonic generation, Phys. Rev. Lett. **117**, 093902 (2016).

[89] A. W. Bray, D. Freeman, S. Eckart, and A. S. Kheifets, Correlation enhancement of high-order harmonic generation in Xe, Phys. Rev. A **100**, 013404 (2019).

[90] M. Kolesik, J. M. Brown, A. Teleki, P. Jakobsen, J. V. Moloney, and E. M. Wright, Metastable electronic states and nonlinear response for high-intensity optical pulses, Optica **1**, 323–331 (2014).

[91] A. Bahl, V. P. Majety, A. Scrinzi, and M. Kolesik, Nonlinear optical response in molecular nitrogen: from ab-initio calculations to optical pulse simulations, Opt. Lett. **42**, 2295–2298 (2017).

[92] J. Venzke, A. Jaroń-Becker, and A. Becker, Ionization of helium by an ultrashort extreme-ultraviolet laser pulse, J. Phys. B: At. Mol. Opt. Phys. **53**, 085602 (2020).

[93] L. Kolanz, Anomalous ionization of atoms in the strong-field regime, Undergraduate honors thesis, Department of Physics, University of Colorado Boulder (2020).

[94] C. F. Pauletti, E. Coccia, and E. Luppi, Role of exchange and correlation in high-harmonic generation spectra of H_2, N_2, and CO_2: Real-time time-dependent electronic-structure approaches, J. Chem. Phys. **154**, 014101 (2021).

[95] D. C. Yost, T. R. Schibli, J. Ye, J. L. Tate, J. Hostetter, M. B. Gaarde, and K. J. Schafer, Vacuum-ultraviolet frequency combs from below-threshold harmonics, Nature Physics **5**, 815–820 (2009).

[96] M. Chini, X. Wang, Y. Cheng, H. Wang, Y. Wu, E. Cunningham, P.-C. Li, J. Heslar, D. A. Telnov, S.-I. Chu, et al., Coherent phase-matched VUV generation by field-controlled bound states, Nature Photonics **8**, 437–441 (2014).

[97] S. Camp, K. J. Schafer, and M. B. Gaarde, Interplay between resonant enhancement and quantum path dynamics in harmonic generation in helium, Phys. Rev. A **92**, 013404 (2015).

[98] S. Bengtsson, E. W. Larsen, D. Kroon, S. Camp, M. Miranda, C. Arnold, A. L'Huillier, K. Schafer, M. Gaarde, L. Rippe, and J. Mauritsson, Space–time control of free induction decay in the extreme ultraviolet, Nature Photonics **11**, 252–258 (2017).

[99] W.-H. Xiong, J.-Z. Jin, L.-Y. Peng, and Q. Gong, Numerical observation of two sets of low-order harmonics near the ionization threshold, Phys. Rev. A **96**, 023418 (2017).

[100] S. Camp, S. Beaulieu, K. J. Schafer, and M. B. Gaarde, Resonantly-initiated quantum trajectories and their role in the generation of near-threshold harmonics, J. Phys. B: At. Mol. Opt. Phys. **51**, 064001 (2018).

[101] H. Yun, J. H. Mun, S. I. Hwang, S. B. Park, I. A. Ivanov, C. H. Nam, and K. T. Kim, Coherent extreme-ultraviolet emission generated through frustrated tunnelling ionization, Nature Photonics **12**, 620–624 (2018).

[102] M. R. Miller, C. Hernández-García, A. Jaroń-Becker, and A. Becker, Targeting multiple rescatterings through VUV-controlled high-order-harmonic generation, Phys. Rev. A **90**, 053409 (2014).

[103] C. Hernández-García, C. G. Durfee, D. D. Hickstein, T. Popmintchev, A. Meier, M. M. Murnane, H. C. Kapteyn, I. J. Sola, A. Jaron-Becker, and A. Becker, Schemes for generation of isolated attosecond pulses of pure circular polarization, Phys. Rev. A **93**, 043855 (2016).

[104] K. Werner, M. G. Hastings, A. Schweinsberg, B. L. Wilmer, D. Austin, C. M. Wolfe, M. Kolesik, T. R. Ensley, L. Vanderhoef, A. Valenzuela, and E. Chowdhury, Ultrafast mid-infrared high harmonic and supercontinuum generation with n_2 characterization in zinc selenide, Opt. Express **27**, 2867–2885 (2019).

[105] C. Hernández-García, T. Popmintchev, M. M. Murnane, H. C. Kapteyn, L. Plaja, A. Becker, and A. Jaron-Becker, Isolated broadband attosecond pulse generation with near- and mid-infrared driver pulses via time-gated phase matching, Opt. Express **25**, 11855–11866 (2017).

[106] C. Hernández-García, J. A. Pérez-Hernández, J. Ramos, E. C. Jarque, L. Roso, and L. Plaja, High-order harmonic propagation in gases within the discrete dipole approximation, Phys. Rev. A **82**, 033432 (2010).

[107] T. Popmintchev, M.-C. Chen, A. Bahabad, M. Gerrity, P. Sidorenko, O. Cohen, I. P. Christov, M. M. Murnane, and H. C. Kapteyn, Phase matching of high harmonic generation in the soft and hard x-ray regions of the spectrum, Proceedings of the National Academy of Sciences **106**, 10516–10521 (2009).

[108] E. Lorin, S. Chelkowski, and A. Bandrauk, A numerical Maxwell–Schrödinger model for intense laser–matter interaction and propagation, Comput. Phys. Commun. **177**, 908 – 932 (2007).

[109] M. B. Gaarde, J. L. Tate, and K. J. Schafer, Macroscopic aspects of attosecond pulse generation, J. Phys. B: At. Mol. Opt. Phys. **41**, 132001 (2008).

[110] E. Lorin, M. Lytova, A. Memarian, and A. Bandrauk, Development of nonperturbative nonlinear optics models including effects of high order nonlinearities and of free electron plasma: Maxwell–Schrödinger equations coupled with evolution equations for polarization effects, and the SFA-like nonlinear optics model, J. Phys. A Math. Theor. **48**, 105201 (2015).

[111] V. V. Strelkov, V. T. Platonenko, A. F. Sterzhantov, and M. Y. Ryabikin, Attosecond electromagnetic pulses: generation, measurement, and application. Generation of high-order harmonics of an intense laser field for attosecond pulse production, Physics-Uspekhi **59**, 425–445 (2016).

[112] I. P. Christov, M. M. Murnane, and H. C. Kapteyn, Generation and propagation of attosecond x-ray pulses in gaseous media, Phys. Rev. A **57**, R2285–R2288 (1998).

[113] M. Geissler, G. Tempea, A. Scrinzi, M. Schnürer, F. Krausz, and T. Brabec, Light propagation in field-ionizing media: Extreme nonlinear optics, Phys. Rev. Lett. **83**, 2930–2933 (1999).

[114] E. Priori, G. Cerullo, M. Nisoli, S. Stagira, S. De Silvestri, P. Villoresi, L. Poletto, P. Ceccherini, C. Altucci, R. Bruzzese, and C. de Lisio, Nonadiabatic three-dimensional model of high-order harmonic generation in the few-optical-cycle regime, Phys. Rev. A **61**, 063801 (2000).

[115] N. H. Shon, A. Suda, and K. Midorikawa, Generation and propagation of high-order harmonics in high-pressure gases, Phys. Rev. A **62**, 023801 (2000).

[116] M. B. Gaarde and K. J. Schafer, Space-time considerations in the phase locking of high harmonics, Phys. Rev. Lett. **89**, 213901 (2002).

[117] V. Tosa, H. T. Kim, I. J. Kim, and C. H. Nam, High-order harmonic generation by chirped and self-guided femtosecond laser pulses. I. Spatial and spectral analysis, Phys. Rev. A **71**, 063807 (2005).

[118] T. Ruchon, C. P. Hauri, K. Varjú, E. Mansten, M. Swoboda, R. López-Martens, and A. L'Huillier, Macroscopic effects in attosecond pulse generation, New Journal of Physics **10**, 025027 (2008).

[119] V. Tosa, K. T. Kim, and C. H. Nam, Macroscopic generation of attosecond-pulse trains in strongly ionized media, Phys. Rev. A **79**, 043828 (2009).

[120] C. Jin, A.-T. Le, and C. D. Lin, Retrieval of target photorecombination cross sections from high-order harmonics generated in a macroscopic medium, Phys. Rev. A **79**, 053413 (2009).

[121] E. Lorin, S. Chelkowski, E. Zaoui, and A. Bandrauk, Maxwell–Schrödinger–plasma (MASP) model for laser–molecule interactions: Towards an understanding of filamentation with intense ultrashort pulses, Physica D: Nonlinear Phenomena **241**, 1059 – 1071 (2012).

[122] E. Lorin and A. Bandrauk, Efficient and accurate numerical modeling of a micro–macro nonlinear optics model for intense and short laser pulses, Journal of Computational Science **3**, 159 – 168 (2012).

[123] M. C. Kohler and K. Z. Hatsagortsyan, Macroscopic aspects of relativistic x-ray-assisted high-order-harmonic generation, Phys. Rev. A **85**, 023819 (2012).

[124] M. Kolesik, E. M. Wright, J. Andreasen, J. M. Brown, D. R. Carlson, and R. J. Jones, Space-time resolved simulation of femtosecond nonlinear light-matter interactions using a holistic quantum atomic model : Application to near-threshold harmonics, Opt. Express **20**, 16113–16128 (2012).

[125] P.-C. Li and S.-I. Chu, Effects of macroscopic propagation on spectra of broadband supercontinuum harmonics and isolated-attosecond-pulse generation: Coherent control of the electron quantum trajectories in two-color laser fields, Phys. Rev. A **86**, 013411 (2012).

[126] S. A. Berman, J. Dubois, C. Chandre, M. Perin, and T. Uzer, Coherent buildup of high-order harmonic radiation: The classical perspective, Phys. Rev. A **97**, 061402 (2018).

[127] C. Hernández-García, A. Picón, J. San Román, and L. Plaja, Attosecond extreme ultraviolet vortices from high-order harmonic generation, Phys. Rev. Lett. **111**, 083602 (2013).

[128] D. D. Hickstein, F. J. Dollar, P. Grychtol, J. L. Ellis, R. Knut, C. Hernández-García, D. Zusin, C. Gentry, J. M. Shaw, T. Fan, et al., Non-collinear generation of angularly isolated circularly polarized high harmonics, Nature Photonics **9**, 743–750 (2015).

[129] W.-H. Xiong, L.-Y. Peng, and Q. Gong, Recent progress of below-threshold harmonic generation, J. Phys. B: At. Mol. Opt. Phys. **50**, 032001 (2017).

[130] J. B. Watson, A. Sanpera, X. Chen, and K. Burnett, Harmonic generation from a coherent superposition of states, Phys. Rev. A **53**, R1962–R1965 (1996).

[131] E. Toma, P. Antoine, A. de Bohan, and H. Muller, Resonance-enhanced high-harmonic generation, J. Phys. B: At. Mol. Opt. Phys. **32**, 5843 (1999).

[132] M. B. Gaarde and K. J. Schafer, Enhancement of many high-order harmonics via a single multiphoton resonance, Phys. Rev. A **64**, 013820 (2001).

[133] R. Taïeb, V. Véniard, J. Wassaf, and A. Maquet, Roles of resonances and recollisions in strong-field atomic phenomena. II. High-order harmonic generation, Phys. Rev. A **68**, 033403 (2003).

[134] D. Milošević, High-energy stimulated emission from plasma ablation pumped by resonant high-order harmonic generation, J. Phys. B: At. Mol. Opt. Phys. **40**, 3367 (2007).

[135] V. Strelkov, Role of autoionizing state in resonant high-order harmonic generation and attosecond pulse production, Phys. Rev. Lett. **104**, 123901 (2010).

[136] A. Baltuška, T. Udem, M. Uiberacker, M. Hentschel, E. Goulielmakis, C. Gohle, R. Holzwarth, V. S. Yakovlev, A. Scrinzi, T. W. Hänsch, and F. Krausz, Attosecond control of electronic processes by intense light fields, Nature **421**, 611–615 (2003).

[137] I. P. Christov, M. M. Murnane, and H. C. Kapteyn, High-Harmonic Generation of Attosecond Pulses in the "Single-Cycle" Regime, Phys. Rev. Lett. **78**, 1251–1254 (1997).

[138] G. G. Paulus, F. Lindner, H. Walther, A. Baltuška, E. Goulielmakis, M. Lezius, and F. Krausz, Measurement of the Phase of Few-Cycle Laser Pulses, Phys. Rev. Lett. **91**, 253004 (2003).

[139] M. F. Kling, C. Siedschlag, A. J. Verhoef, J. I. Khan, M. Schultze, T. Uphues, Y. Ni, M. Uiberacker, M. Drescher, F. Krausz, and M. J. J. Vrakking, Control of Electron Localization in Molecular Dissociation, Science **312**, 246–248 (2006).

[140] M. Krüger, M. Schenk, and P. Hommelhoff, Attosecond control of electrons emitted from a nanoscale metal tip, Nature **475**, 78–81 (2011).

[141] D. Guénot, D. Gustas, A. Vernier, B. Beaurepaire, F. Böhle, M. Bocoum, M. Lozano, A. Jullien, R. Lopez-Martens, A. Lifschitz, and J. Faure, Relativistic electron beams driven by kHz single-cycle light pulses, Nature Photonics **11**, 293–296 (2017).

[142] M. A. Porras, Characterization of the electric field of focused pulsed Gaussian beams for phase-sensitive interactions with matter, Optics Letters **34**, 1546–1548 (2009).

[143] M. A. Porras, Z. L. Horváth, and B. Major, Three-dimensional carrier-envelope-phase map of focused few-cycle pulsed Gaussian beams, Phys. Rev. A **98**, 063819 (2018).

[144] L. G. Gouy, Sur une propriété nouvelle des ondes lumineuses, Compt. Rendue Acad. Sci. **110**, 1251–1253 (1890).

[145] M. F. Parsons, F. Huber, A. Mazurenko, C. S. Chiu, W. Setiawan, K. Wooley-Brown, S. Blatt, and M. Greiner, Site-resolved imaging of Fermionic ^{6}Li in an optical lattice, Phys. Rev. Lett. **114**, 213002 (2015).

[146] S. L. Campbell, R. B. Hutson, G. E. Marti, A. Goban, N. Darkwah Oppong, R. L. McNally, L. Sonderhouse, J. M. Robinson, W. Zhang, B. J. Bloom, and J. Ye, A Fermi-degenerate three-dimensional optical lattice clock, Science **358**, 90–94 (2017).

[147] D. Jaksch, Optical lattices, ultracold atoms and quantum information processing, Contemporary Physics **45**, 367–381 (2004).

[148] M. Lewenstein, A. Sanpera, V. Ahufinger, B. Damski, A. Sen, and U. Sen, Ultracold atomic gases in optical lattices: mimicking condensed matter physics and beyond, Advances in Physics **56**, 243–379 (2007).

[149] T. Esslinger, Fermi-Hubbard physics with atoms in an optical lattice, Annual Review of Condensed Matter Physics **1**, 129–152 (2010).

[150] M. Lewenstein, A. Sanpera, and V. Ahufinger, Ultracold atoms in optical lattices: Simulating quantum many-body systems, Oxford University Press (2012).

[151] C. Gross and I. Bloch, Quantum simulations with ultracold atoms in optical lattices, Science **357**, 995–1001 (2017).

[152] P. Wessels, B. Ruff, T. Kroker, A. K. Kazansky, N. M. Kabachnik, K. Sengstock, M. Drescher, and J. Simonet, Absolute strong-field ionization probabilities of ultracold rubidium atoms, Commun. Phys. **1**, 1–9 (2018).

[153] T. Auguste, P. Salières, A. S. Wyatt, A. Monmayrant, I. A. Walmsley, E. Cormier, A. Zaïr, M. Holler, A. Guandalini, F. Schapper, J. Biegert, L. Gallmann, and U. Keller, Theoretical and experimental analysis of quantum path interferences in high-order harmonic generation, Phys. Rev. A **80**, 033817 (2009).

[154] F. Schapper, M. Holler, T. Auguste, A. Zaïr, M. Weger, P. Salières, L. Gallmann, and U. Keller, Spatial fingerprint of quantum path interferences in high order harmonic generation, Opt. Express **18**, 2987–2994 (2010).

[155] M. Kretschmar, C. Hernández-García, D. S. Steingrube, L. Plaja, U. Morgner, and M. Kovačev, Spatial contributions of electron trajectories to high-order-harmonic radiation originating from a semi-infinite gas cell, Phys. Rev. A **88**, 013805 (2013).

[156] J. Jiang, P. Wei, Z. Zeng, J. Miao, Y. Zheng, X. Ge, C. Li, R. Li, and Z. Xu, Spatially and spectrally resolved quantum-path tracing in high-order harmonic generation, Opt. Express **22**, 15975–15981 (2014).

[157] F. Catoire, A. Ferré, O. Hort, A. Dubrouil, L. Quintard, D. Descamps, S. Petit, F. Burgy, E. Mével, Y. Mairesse, and E. Constant, Complex structure of spatially resolved high-order-harmonic spectra, Phys. Rev. A **94**, 063401 (2016).

[158] D. Hoff, M. Krüger, L. Maisenbacher, A. M. Sayler, G. G. Paulus, and P. Hommelhoff, Tracing the phase of focused broadband laser pulses, Nature Physics **13**, 947–951 (2017).

[159] Y. Zhang, D. Zille, D. Hoff, P. Wustelt, D. Würzler, M. Möller, A. M. Sayler, and G. G. Paulus, Observing the Importance of the Phase-Volume Effect for Few-Cycle Light-Matter Interactions, Phys. Rev. Lett. **124**, 133202 (2020).

[160] S. Beaulieu, S. Camp, D. Descamps, A. Comby, V. Wanie, S. Petit, F. Légaré, K. J. Schafer, M. B. Gaarde, F. Catoire, and Y. Mairesse, Role of Excited States In High-order Harmonic Generation, Phys. Rev. Lett. **117**, 203001 (2016).

[161] F. Ferray, A. L'Huillier, X. F. Li, L. A. Lompre, G. Mainfray, and C. Manus, Multiple-harmonic conversion of 1064 nm radiation in rare gases, J. Phys. B: At. Mol. Opt. Phys. **21**, L31 (1988).

[162] K. C. Kulander, Multiphoton ionization of hydrogen: A time-dependent theory, Phys. Rev. A **35**, 445 (1987).

[163] K. J. Schafer and K. C. Kulander, Energy analysis of time-dependent wave functions: Application to above-threshold ionization, Phys. Rev. A **42**, 5794 (1990).

[164] J. S. Parker, B. S. J. Doherty, K. J. Meharg, and K. T. Taylor, Time delay between singly and doubly ionizing wavepackets in laser-driven helium, J. Phys. B: At. Mol. Opt. Phys. **36**, L393 (2003).

[165] E. Cormier and P. Lambropoulos, Above-threshold ionization spectrum of hydrogen using B-spline functions, J. Phys. B: At. Mol. Opt. Phys. **30**, 77 (1977).

[166] H. Bachau, E. Cormier, P. Decleva, J. E. Hansen, and F. Martin, Applications of B-splines in atomic and molecular physics, Rep. Prog. Phys. **64**, 1815 (2001).

[167] K. C. Kulander, Time-dependent Hartree-Fock theory of multiphoton ionization: Helium, Phys. Rev. A **36**, 2726 (1987).

[168] X. Li, S. M. Smith, A. N. Markevitch, D. A. Romanov, R. J. Levis, and H. B. Schlegel, A time-dependent Hartree–Fock approach for studying the electronic optical response of molecules in intense fields, Phys. Chem. Chem. Phys. **7**, 233 (2005).

[169] J. Caillat, J. Zanghellini, M. Kitzler, O. Koch, W. Kreuzer, and A. Scrinzi, Correlated multielectron systems in strong laser fields: A multiconfiguration time-dependent Hartree-Fock approach, Phys. Rev. A **71**, 012712 (2005).

[170] M. Nest, R. Padmanaban, and P. Saalfrank, Time-dependent approach to electronically excited states of molecules with the multiconfiguration time-dependent Hartree-Fock method, J. Chem. Phys. **126**, 214106 (2007).

[171] S. Sukiasyan, C. McDonald, C. Destefani, M. Y. Ivanov, and T. Brabec, Multielectron correlation in high-harmonic generation: A 2D model analysis, Phys. Rev. Lett. **102**, 223002 (2009).

[172] D. Haxton and C. McCurdy, Ultrafast population transfer to excited valence levels of a molecule driven by x-ray pulses, Phys. Rev. A **90**, 053426 (2014).

[173] M. A. Lysaght, H. W. van der Hart, and P. B. Burke, Time-dependent R-matrix theory for ultrafast atomic processes, Phys. Rev. A **79**, 053411 (2009).

[174] O. Hassouneh, A. C. Brown, and H. W. van der Hart, Harmonic generation by noble-gas atoms in the near-IR regime using ab initio time-dependent R-matrix theory, Phys. Rev. A **90**, 043418 (2014).

[175] P. Krause, T. Klamroth, and P. Saalfrank, Time-dependent configuration-interaction calculations of laser-pulse-driven many-electron dynamics: Controlled dipole switching in lithium cyanide, J. Chem. Phys. **123**, 074105 (2005).

[176] L. Greenman, P. J. Ho, S. Pabst, E. Kamarchik, D. A. Mazziotti, and R. Santra, Implementation of the time-dependent configuration-interaction singles method for atomic strong-field processes, Phys. Rev. A **82**, 023406 (2010).

[177] P. Krause, J. A. Song, and H. B. Schlegel, Strong field ionization rates simulated with time-dependent configuration interaction and an absorbing potential, J. Chem. Phys. **140**, 174113 (2014).

[178] C. Huber and T. Klammroth, Explicitly time-dependent coupled cluster singles doubles calculations of laser-driven many-electron dynamics, J. Chem. Phys. **134**, 054113 (2011).

[179] H. Miyagi and L. B. Madsen, Time-dependent restricted-active-space self-consistent-field theory for laser-driven many-electron dynamics, Phys. Rev. A **87**, 062511 (2013).

[180] T. Sato and K. L. Ishikawa, Time-dependent complete-active-space self-consistent-field method for multielectron dynamics in intense laser fields, Phys. Rev. A **88**, 023402 (2013).

[181] T. Sato, K. L. Ishikawa, I. Brezinova, F. Lackner, S. Nagele, and J. Burgdörfer, Time-dependent complete-active-space self-consistent-field method for atoms: Application to high-order harmonic generation, Phys. Rev. A **94**, 023405 (2016).

[182] M. Brics and D. Bauer, Time-dependent renormalized natural orbital theory applied to the two-electron spin-singlet case: Ground state, linear response, and autoionization, Phys. Rev. A **88**, 052514 (2013).

[183] M. Brics, J. Rapp, and D. Bauer, Strong-field absorption and emission of radiation in two-electron systems calculated with time-dependent natural orbitals, Phys. Rev. A **93**, 013404 (2016)